A N N U A L   R E P O R T   2 0 1 7

INFN
LNGS

Annual Report 2017
Laboratori Nazionali del Gran Sasso

Cover Image: CUORE Experiment

© Yura Suvorov - LNGS-INFN

Annual Report 2017

LNGS Director	Prof. Stefano Ragazzi
Editor	Dr. Roberta Antolini
Technical Assistants	Dr. Alessia Giampaoli
	Mr. Marco Galeota

Contents

Borexino

M. Agostini[r], K. Altenmüller[r], S. Appel[r], V. Atroshchenko[h], Z. Bagdasarian[z], D. Basilico[k], G. Bellini[k], J. Benziger[o], D. Bick[d], G. Bonfini[j], D. Bravo[k,5], B. Caccianiga[k], F. Calaprice[n], A. Caminata[c], S. Caprioli[k], M. Carlini[j], P. Cavalcante[j,q], A. Chepurnov[s], K. Choi[y], L. Collica[k], D. D'Angelo[k], S. Davini[c], A. Derbin[m], X.F. Ding[t,j], A. Di Ludovico[n], L. Di Noto[c], I. Drachnev[t,m], K. Fomenko[b], A. Formozov[b,k,s], D. Franco[a], F. Gabriele[j], C. Galbiati[n], C. Ghiano[j], M. Giammarchi[k], A. Goretti[n], M. Gromov[s], D. Guffanti[t,j], C. Hagner[d], T. Houdy[a], E. Hungerford[u], Aldo Ianni[j,1], Andrea Ianni[n], A. Jany[f], D. Jeschke[r], V. Kobychev[g], D. Korablev[b], G. Korga[u], D. Kryn[a], M. Laubenstein[j], E. Litvinovich[h,i], F. Lombardi[j,2], P. Lombardi[k], L. Ludhova[z,aa], G. Lukyanchenko[h], L. Lukyanchenko[h], I. Machulin[h,i], G. Manuzio[c], S. Marcocci[t,6], J. Martyn[x], E. Meroni[k], M. Meyer[v], L. Miramonti[k], M. Misiaszek[f], V. Muratova[m], B. Neumair[r], L. Oberauer[r], B. Opitz[d], V. Orekhov[h], F. Ortica[l], M. Pallavicini[c,7], L. Papp[r], Ö. Penek[z,aa], N. Pilipenko[m], A. Pocar[p], A. Porcelli[x], G. Raikov[h], G. Ranucci[k,7], A. Razeto[j], A. Re[k], M. Redchuk[z,aa], A. Romani[l], R. Roncin[j,a], N. Rossi[j,3], S. Schönert[r], D. Semenov[m], M. Skorokhvatov[h,i], O. Smirnov[b], A. Sotnikov[b], L.F.F. Stokes[j], Y. Suvorov[j,h,4], R. Tartaglia[j], G. Testera[c], J. Thurn[v], M. Toropova[h], E. Unzhakov[m], F. Villante[j,ab], A. Vishneva[b], R.B. Vogelaar[q], F. von Feilitzsch[r], H. Wang[w], S. Weinz[x], M. Wojcik[f], M. Wurm[x], Z. Yokley[q], O. Zaimidoroga[b], S. Zavatarelli[c], K. Zuber[v], G. Zuzel[f]

The Borexino Collaboration

[a]*AstroParticule et Cosmologie, Université Paris Diderot, CNRS/IN2P3, CEA/IRFU, Observatoire de Paris, Sorbonne Paris Cité, 75205 Paris Cedex 13, France*
[b]*Joint Institute for Nuclear Research, 141980 Dubna, Russia*
[c]*Dipartimento di Fisica, Università degli Studi e INFN, 16146 Genova, Italy*
[d]*Institut für Experimentalphysik, Universität Hamburg, 22761 Hamburg, Germany*
[e]*Max-Planck-Institut für Kernphysik, 69117 Heidelberg, Germany*
[f]*M. Smoluchowski Institute of Physics, Jagiellonian University, 30348 Krakow, Poland*
[g]*Kiev Institute for Nuclear Research, 03680 Kiev, Ukraine*
[h]*National Research Centre Kurchatov Institute, 123182 Moscow, Russia*
[i]*National Research Nuclear University MEPhI (Moscow Engineering Physics Institute), 115409 Moscow, Russia*
[j]*INFN Laboratori Nazionali del Gran Sasso, 67010 Assergi (AQ), Italy*
[k]*Dipartimento di Fisica, Università degli Studi e INFN, 20133 Milano, Italy*
[l]*Dipartimento di Chimica, Biologia e Biotecnologie, Università degli Studi e INFN, 06123 Perugia, Italy*
[m]*St. Petersburg Nuclear Physics Institute NRC Kurchatov Institute, 188350 Gatchina, Russia*
[n]*Physics Department, Princeton University, Princeton, NJ 08544, USA*
[o]*Chemical Engineering Department, Princeton University, Princeton, NJ 08544, USA*
[p]*Amherst Center for Fundamental Interactions and Physics Department, University of Massachusetts, Amherst, MA 01003, USA*
[q]*Physics Department, Virginia Polytechnic Institute and State University, Blacksburg, VA 24061, USA*

[1]Also at: Laboratorio Subterráneo de Canfranc, Paseo de los Ayerbe S/N, 22880 Canfranc Estacion Huesca, Spain
[2]Present address: Physics Department, University of California, San Diego, CA 92093, USA
[3]Present address: Dipartimento di Fisica, Sapienza Università di Roma e INFN, 00185 Roma, Italy
[4]Present address: Dipartimento di Fisica, Università degli Studi Federico II e INFN, 80126 Napoli, Italy
[5]Present address: Universidad Autnoma de Madrid, Ciudad Universitaria de Cantoblanco, 28049 Madrid, Spain
[6]Present address: Fermilab National Accelerato Laboratory (FNAL), Batavia, IL 60510, (USA)
[7]Co-Spokespersons

[r]*Physik-Department and Excellence Cluster Universe, Technische Universität München, 85748 Garching, Germany*
[s]* Lomonosov Moscow State University Skobeltsyn Institute of Nuclear Physics, 119234 Moscow, Russia*
[t]* Gran Sasso Science Institute, 67100 L'Aquila, Italy*
[u]*Department of Physics, University of Houston, Houston, TX 77204, USA*
[v]*Department of Physics, Technische Universität Dresden, 01062 Dresden, Germany*
[w]*Physics and Astronomy Department, University of California Los Angeles (UCLA), Los Angeles, California 90095, USA*
[x]*Institute of Physics and Excellence Cluster PRISMA, Johannes Gutenberg-Universität Mainz, 55099 Mainz, Germany*
[y]*Department of Physics and Astronomy, University of Hawaii, Honolulu, HI 96822, USA*
[z]*Institut für Kernphysik, Forschungszentrum Jülich, 52425 Jülich, Germany*
[aa]*RWTH Aachen University, 52062 Aachen, Germany*
[ab]*Dipartimento di Scienze Fisiche e Chimiche, Università dell'Aquila, 67100 L'Aquila, Italy*

Abstract

The beginning of the Borexino experiment data taking dates back to 2007 May 15th. During more than 10 years of analysis we published results at the forefront of the measurements of the solar neutrino and geo-neutrino fluxes, and we set unprecedented limits on rare processes. This report highlights the many new results achieved by the collaborations in the year 2017 and will briefly describes the strategy for the next years.

Introduction

The Borexino experiment has the primary scientific goal of studying our star using neutrinos as sensitive probes of the physical processes that occur inside it. Borexino, thanks to the use of scintillation light is able to reconstruct the energy spectrum of the events and to have the lowest energy threshold (about 150 keV) among the solar neutrino experiments.

This report will focus on the activity that occurred in 2017 and on the recently published papers: section 1 will shortly describes the experimental apparatus, section 2 will show the latest published results, and section 3 will report about the ongoing activities on the detector and its status.

1. The Borexino Detector

Borexino is located in the Hall C of Laboratori Nazionali del Gran Sasso. The detector is made of concentric layers of increasing radiopurity (see for details e.g. [1]). Figure 1 shows the detector layout. The core of the detector is made by 300 tons of ultrapure liquid scintillator (PC plus 1.5 g/l of PPO) contained in a 125 μm thin nylon vessel of radius 4.25 m. A stainless steel sphere (SSS) filled up with $\sim$ 1000 tons of buffer liquid (PC plus DMP quencher) is instrumented with about 2200 PMTs for detecting the scintillation light. The buffer liquid shields the core scintillator from the radioactivity emitted by construction materials. The SSS is immersed in a 2000 ton water Cherenkov detector, equipped with 200 PMTs to tag muons crossing the detector and to shield the detector from the radioactivity of the experimental hall.

The light yield is about 500 photoelectrons/MeV/2000 PMTs, the position of events is reconstructed with an accuracy of about 10 cm at 1 MeV exploiting the time of flight of the scintillation
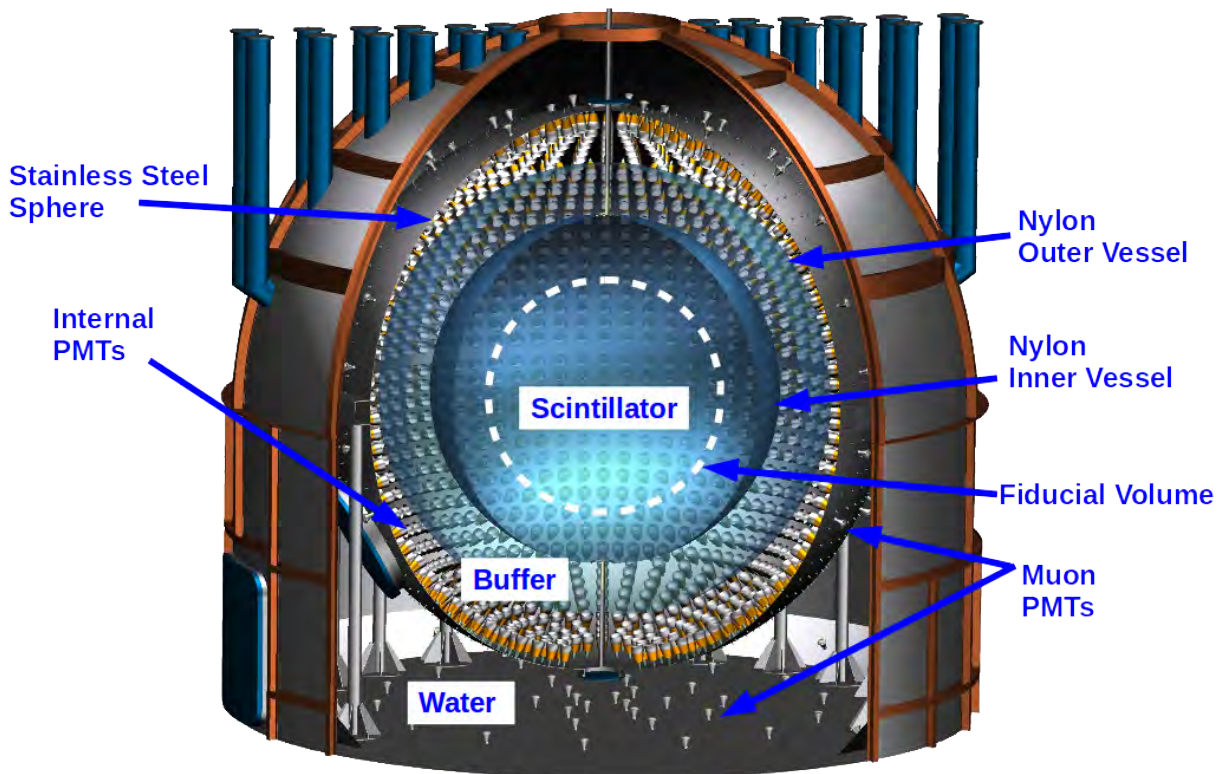
2

Figure 1: Schematic view of Borexino detector (Picture based on the original drawing, courtesy of A. Brigatti and P. Lombardi).

light, and the energy resolution scales approximately as $\sigma(E)/E = 5\%/\sqrt{(E/[MeV])}$. This sensitivity has been achieved after an accurate calibration campaign [2] carried out in 2010. Moreover the use of liquid scintillator enables a satisfactory implementation of pulse shape discrimination for α/β particles and even a challenging β^+/β^- separation [1].

The intrinsic radiopurity of the scintillator reached unprecedented levels after an intense purification campaign carried out in between 2010 and 2011. The purification campaign divides the data taking of Borexino in two periods refereed as Phase-I and Phase-II. Tab. 1 shows the record background levels in the two Borexino phases.

Thanks to its detection sensitivity, Borexino using Phase-I data made the first measurement of the interaction rate of the ^{7}Be (862 keV) neutrinos with 5% accuracy [3], exclusion of any significant day-night asymmetry of the ^{7}Be solar neutrino flux [4], first direct observation of the mono-energetic 1440 keV pep solar neutrinos and strongest upper limit of the CNO solar neutrinos flux [6], measurement of the ^{8}B solar neutrinos with a low energy threshold at 3 MeV [5]. Moreover, exploiting the first part of Phase-II data the first spectroscopical observation of pp neutrinos [7]

Contaminant	Phase-I	Phase-II
$^{14}C/^{14}C$		2.7×10^{-18} [g/g]
^{238}U		$< 9.7 \times 10^{-19}$ [g/g] (95% CL)
^{232}Th		$< 1.2 \times 10^{-18}$ [g/g](95% CL)
^{210}Po	~ 2000 [cpd/100t]	$\sim 260^*$ [cpd/100t]
^{210}Bi	~ 45 [cpd/100t]	$\sim 17.5^*$ [cpd/100t]
^{85}Kr	~ 30 [cpd/100t]	6.8 [cpd/100t] (95% CL)

Table 1: Borexino contaminant rates before and after the purification campaign. * makrs results averaged on Phase-II data December 2011 - May 2016 [14].

was achieved.

In addition Borexino detected a 5σ geo-netrino signal [8] and set strong limits on rare processes as for example the search for the electron decay, resulting $\tau > 6.6 \times 10^{28}$ y (90% CL) [9].

2. The science of Borexino in 2017

2.1. Results released in 2017

The year 2017 has been very exciting for the Borexino collaboration since new results on several topics have been released: regarding the flagship science of Borexino, the full dataset of Phase-II has been used to simultaneously measure the flux of pp, ^7Be, and pep solar neutrinos. Moreover the Phase-I and Phase-II dataset have been combined to investigate the seasonal modulation of ^7Be flux and to update the results on ^8B flux. Table 2.1 shows the updated fluxes.

Species	Rate [cpd/100t]	Flux [cm^{-2} s^{-1}]
pp	$134 \pm 10^{+6}_{-10}$	$\left(6.1 \pm 0.5^{+0.3}_{-0.5}\right) \times 10^{10}$
^7Be	$48.3 \pm 1.1^{+0.4}_{-0.7}$	$(4.99 \pm 0.11) \times 10^9$
pep	$2.43 \pm 0.36^{+0.15}_{-0.22}$	$\left(1.27 \pm 0.19^{+0.08}_{-0.12}\right) \times 10^8$
CNO	< 8.1 (95% CL)	7.9×10^8
$^8B(> 3$ MeV)	$0.22^{+0.015}_{-0.016}$	$\left(2.55^{+0.17}_{-0.19}\right) \times 10^6$

Table 2: Solar neutrino interaction rates and fluxes measured by the Borexino experiment. Rates are normalized on a mass of 100 tons and high metallicity is assumed.

Here are reported the papers published in the year 2017 by the collaboration, with a brief description of the most important results contained in them.

- *A search for low-energy neutrino and antineutrino signals correlated with gamma-ray bursts with Borexino*: A search for neutrino and antineutrino events correlated with 2350 gamma-ray bursts. No statistically significant excess over background is observed. We obtain currently the best limits on the neutrino fluence of all flavors and species below 7 MeV [10].

- *Seasonal modulation of the ^7Be solar neutrino rate in Borexino*: absence of annual modulation rejected at 99.99% C.L. The data are analyzed using three methods: the analytical fit to event rate, the Lomb-Scargle and the Empirical Mode Decomposition techniques, which all yield results in excellent agreement. [11].
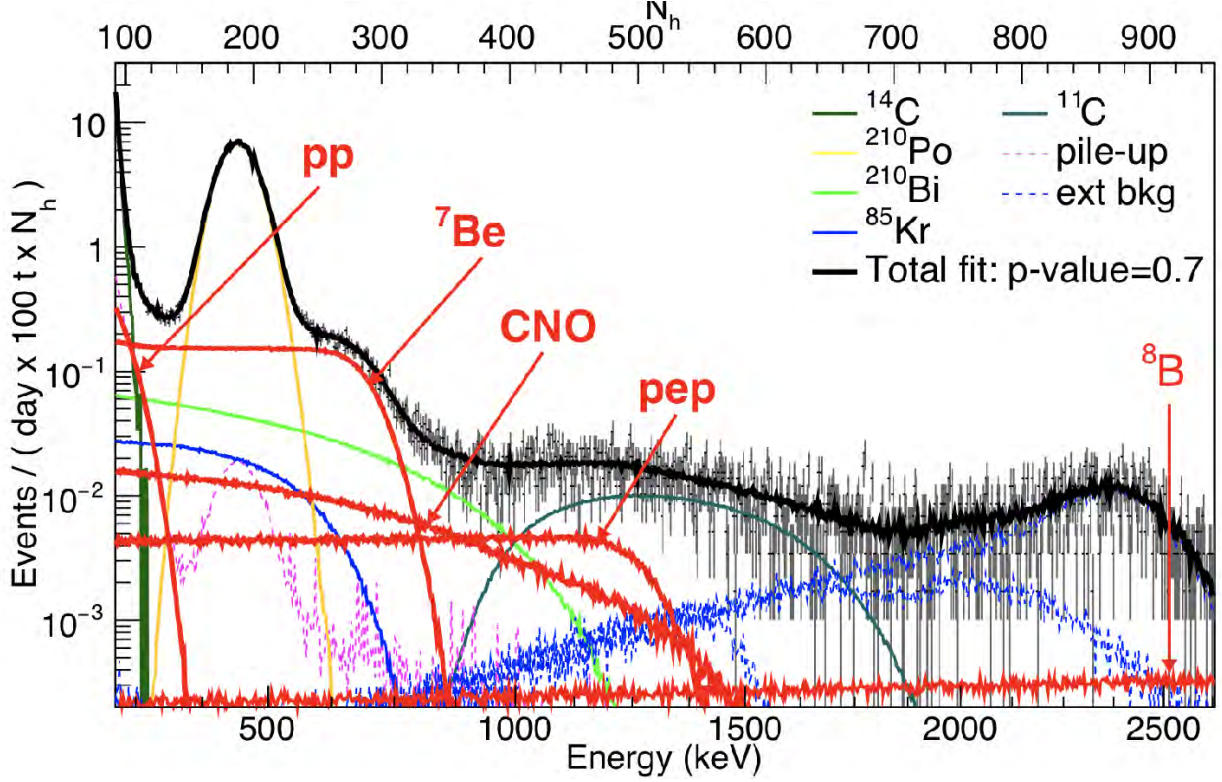
Figure 2: Example of fit of solar neutrino spectrum used to calculate the rates. Both Monte Carlo (this fit) and analytical methods are used in the analysis [14].

- *The Monte Carlo simulation of the Borexino detector*: agreement between simulations and data and techniques used for simulation of both the bulk events and events coming from construction materials are reported in this paper [12].

- *A search for low-energy neutrinos correlated with gravitational wave events GW150914, GW151226 and GW170104 with the Borexino detector*: search for correlated (gate width ± 500 s) neutrino events with black holes merger. No statistical excess found. We have obtained the best current upper limits on all flavor neutrino fluence associated with GW events, in the neutrino energy range 0.55.0 MeV [13].

- *First Simultaneous Precision Spectroscopy of pp , ^7Be, and pep Solar Neutrinos with Borexino Phase-II*: first simultaneous measurement of the interaction rates of pp, ^7Be, and pep solar neutrinos performed with a global fit to the Borexino data in an extended energy range (0.19-2.93) MeV. The interaction rate of ^7Be νs is measured with an unprecedented precision of 2.7% [14]. Figure 2.1 shows an example of the fit used to obtain the solar neutrino rates.

- *Limiting neutrino magnetic moments with Borexino Phase-II solar neutrino data*: exploiting the analytic model developed for the simultaneous spectroscopy of Phase-II data, an analysis on the shape of the electron recoil spectrum implied a limit on neutrino magnetic moment $\mu_{eff} < 2.8 \cdot 10^{-11} \mu B$ at 90% C.L. [15].
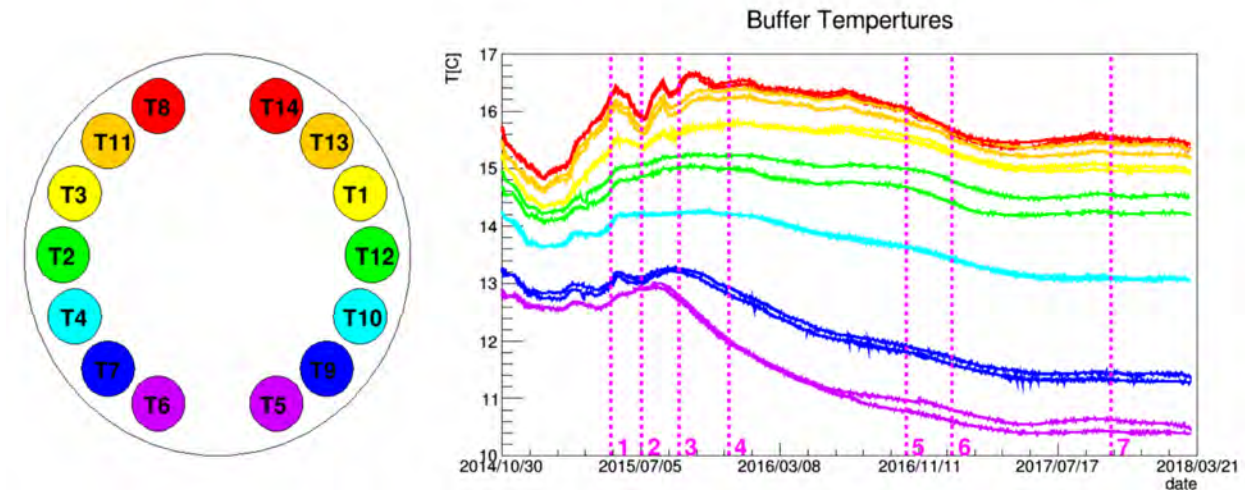
5

Figure 3: Inner Buffer temperature sensors. Vertical magenta dashed lines represent the most important operations of the thermal stabilization program: From the left to the right: 1. insulation started, 2. Water Loop turned off, 3. 5th ring insulation completed, 4. Organ Pipes and 6th ring insulation completed, 5. CR4 floor and Top Organ Pipes insulation completed, 6. Temperature Active Control System tests started and 7. Hall C active control started.

- *Improved measurement of ^8B solar neutrinos with 1.5 kt y of Borexino exposure*: about 5 time the exposure of the previous analysis, exploits a better modelization of the detector and a refinement of the background model. The uncertainty of the ^8B rate was reduced from 19% to 8% [16].

2.2. Celebration of the 10th anniversary of Borexino data taking

In September a workshop "10 years of Borexino: Workshop RECENT DEVELOPMENTS IN NEUTRINO PHYSICS AND ASTROPHYSICS" has been organized to celebrate the 10th anniversary of Borexino data taking at LNGS. In that occasion the update on ^8B rate was released.

3. Technical activities regarding the detector and status of the apparatus

3.1. Data Acquisition and Electronics

The data-taking is going on regularly with high duty-cycle. The PMT failure rate is under control and does not show any suspicious behavior. At present, 1330 PMTs are functioning with a loss of about 50 per year. In the last year thorough re-cabling implementation of the racks in the electronics hut took place. The aim of the re-cabling was to group properly the cables of the still functioning PMT, thus recovering a number of the front-end and read-out boards as spares and reducing the temperature in the electronic room, thus reducing the electronic-induced noise.

3.2. Thermal insulation

The most significant recent technical achievement is the steadied thermal condition of the detector reached as effect of the careful stabilization measures implemented by the Collaboration over the past two years. Stabilizing the movement of the scintillator is of paramount importance to try to measure CNO neutrinos. To detect CNO neutrinos it is necessary to constraint the ^{210}Bi

rate inside the detector since the spectral shape of the two signals is almost degenerate. The strategy is to constraint the rate of ^{210}Bi exploiting the secular equilibrium with ^{210}Po. However, convective motions bring inside the detector additional ^{210}Po that is not in secular equilibrium and consequently prevent us to constraint the level of ^{210}Bi in the detector. The stabilization process started with installing a 20-cm thick layer of wool-rock thermal insulator layer on the external surface of the Water Tank. This work has been completed since 2015. On November/December 2016 a final intervention was performed to further improve the insulation of the upper part of the water tank. The last action in this respect has been the switch on of the active control system realized on top of the water tank and intended to compensate for variations of the external driving temperature of the Hall, prone to the seasonal modification of the outside thermal conditions. The system consists of copper pipes where water can be circulated after being heated to the desired temperature. As a consequence of this operations all the temperature curves reported in figure 3 exhibit a very stable behavior over the period of the last months. To avoid (small) perturbations due to instabilities of the temperature of external air, in cooperation with the Laboratory staff we have proceeded to activate the control system (heater) which regulates the temperature of the inlet air in Hall C from the ventilation pipe, in order to improve the overall stability of the temperature, and thus minimize its residual impact on the detector; because the control system can only deliver heat, its effectiveness is in principle maximal during the autumn and the winter, when the external temperature decreases.

3.3. Polonium Evolution

The ^{210}Po events are selected through a high efficiency α/β pulse shape discrimination method based on a neural network approach, in which the network is trained on a large sample of ^{210}Bi and ^{210}Po fast coincidences. The ^{210}Po rate is studied in different volumes and correlated in time with the major operations performed on the detector.

Figure 4 shows the ^{210}Po rate in the so-called standard ^{210}Po fiducial volume ($r < 2.5$ m and $|z| < 1.5$ m). From the plot two important changes of regime are visible: the first, from the early summer 2015 (beginning of the insulation campaign), corresponds to the stop of the strong convective motions associated with the seasonal temperature changes; the second, from the late spring 2017, corresponds to the full stabilization of the detector (with some help also from the heating of the inlet air to Hall C started in autumn 2017).

During the first stage the top was pretty stabilized, and thus the ^{210}Po rate decayed rather regularly, while the bottom looked still affected by residual scintillator motions, which prevented the occurring of the expected decay. On the other hand, since the beginning of the second stage we have been observing a hint of decrease of the ^{210}Po , even at the bottom, especially during the Fall, and as a consequence a global enlargement of the spatial region in the detector featuring very low Polonium background. The time scale of such changes inside the Borexino detector was found to be very long, of order about 1 year.

We can take therefore advantage of the forthcoming year in order to continue the observation of the ^{210}Po behavior to try and understand if we can eventually perform a preliminary estimation of the ^{210}Po rate related to the ^{210}Bi through the secular equilibrium.

4. Conclusions

In 2017 Borexino released several results about updates of solar neutrinos fluxes, rare processes and analysis methods used by the collaboration. Moreover an aggressive strategy is going on
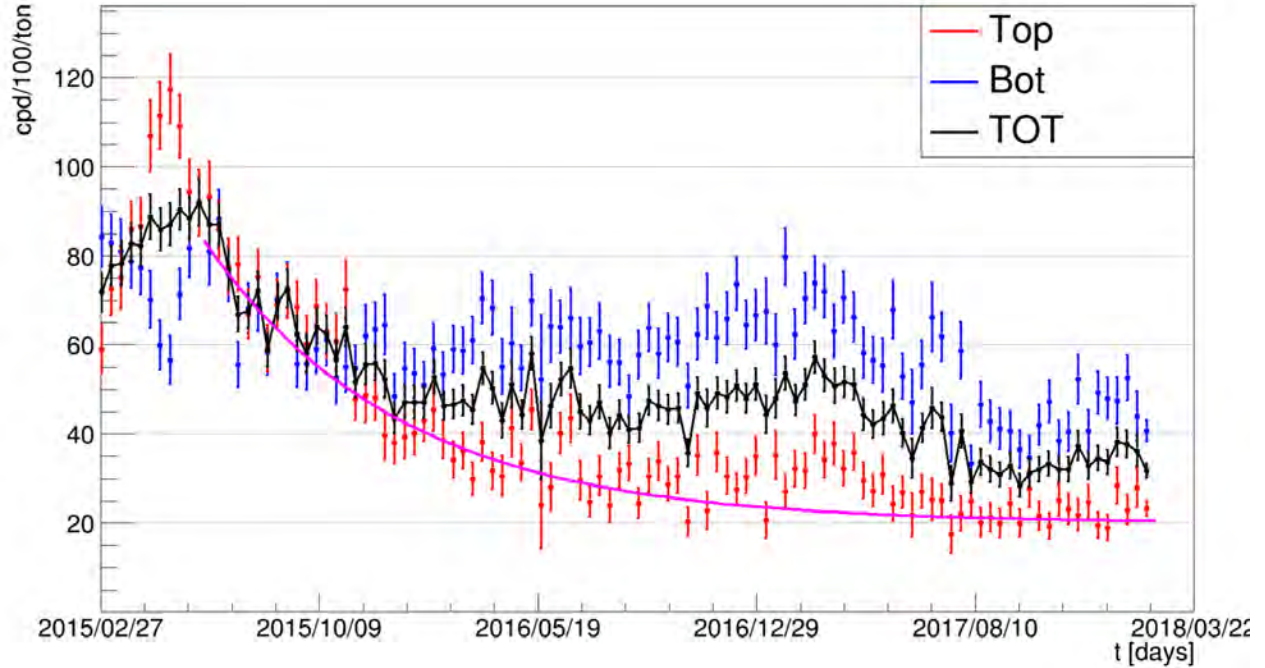
Figure 4: ^{210}Po inside the standard ^{210}Po fiducial volume. The plot show the global ^{210}Po rate (black) and top (red) and bottom (blue) separately. The magenta curve represents the theoretical ^{210}Po activity in case of pure exponential decay with a constant plateau due to a ^{210}Bi rate of 20 cpd/100t.

to avoid convecting motions inside the liquid scintillator in order to try a measurement of CNO neutrinos. The program for 2018 is continuing data taking with the detector in stable conditions in order to try to constraint the ^{210}Bi rate from ^{210}Po tagging to obtain an independent constraint of this background for the CNO analysis.

References

[1] G. Bellini *et al.* [Borexino Collaboration], Phys. Rev. D 89, 112007 (2014)

[2] H. Back *et al.* [Borexino Collaboration], JINST 7 P10018 (2012)

[3] G. Bellini *et al.* [Borexino Collaboration], Phys. Rev. Lett. 107, 141302 (2011)

[4] G. Bellini *et al.* [Borexino Collaboration], Phys. Lett. B 707, 22 (2012)

[5] G. Bellini *et al.* [Borexino Collaboration], Phys. Rev. D82:033006 (2010)

[6] G. Bellini *et al.* [Borexino Collaboration], Phys. Rev. Lett. 108, 051302 (2012)

[7] G. Bellini *et al.* [Borexino Collaboration], Nature, 512:383-386, (2014)

[8] M. Agostini *et al.* [Borexino Collaboration], Phys. Rev. D 92, 031101 (2015)

[9] M. Agostini *et al.* [Borexino Collaboration], Phys. Rev. Lett. 115 (2015) 231802

[10] M. Agostini *et al.* [Borexino Collaboration] Astropart. Phys. 86 (2017) 11 doi:10.1016/j.astropartphys.2016.10.004

[11] M. Agostini *et al.*[Borexino Collaboration] Astroparticle Physics, Volume 92, p. 21-29 06/2017

[12] M. Agostini *et al.*[Borexino Collaboration] Astroparticle Physics, Volume 97, p. 136-159 01/2018

[13] M. Agostini *et al.*[Borexino Collaboration] The Astrophysical journal, Volume 850,

[14] M. Agostini *et al.*[Borexino Collaboration] arXiv:1707.09279

[15] M. Agostini *et al.* [Borexino Collaboration] Phys.Rev. D96 (2017) no.9, 091103

[16] M. Agostini *et al.* [Borexino Collaboration] arXiv:1709.00756

The COBRA Experiment

The COBRA collaboration

Lucas Bodenstein-Dresler[a], Yingjie Chu[b], Daniel Gehre[b], Claus Gößling[a], Arne Heimbold[b],
Christian Herrmann[a], Rastislav Hodak[c], Joel Kostensalo[d], Kevin Kröninger[a], Julia Küttler[b],
Christian Nitsch[a], Thomas Quante[a], Ekaterina Rukhadze[c], Ivan Stekl[c], Jouni Suhonen[d], Jan Tebrügge[a],
Robert Temminghoff[a], Juliane Volkmer[b], Stefan Zatschler[b], Kai Zuber[b,*]

[a] TU Dortmund, Lehrstuhl für Experimentelle Physik IV, Germany
[b] TU Dresden, Institut für Kern- und Teilchenphysik, Germany
[c] CTU Prague, Institute of Experimental and Applied Physics, Czech Republic
[d] University of Jyvaskyla, Department of Physics, Finland
(* Spokesperson)

Abstract

The aim of the COBRA experiment (**C**admium Zinc Telluride **0**-Neutrino Double-**B**eta **R**esearch **A**pparatus) is to search for the existence of neutrinoless double beta-decay ($0\nu\beta\beta$-decay) and to measure its half-life. The COBRA demonstrator at LNGS is used to investigate the experimental issues of operating CZT detectors in low background mode while additional studies are proceeding in surface laboratories. The current demonstrator consists of 64 monolithic, calorimetric detectors in a coplanar grid (CPG) design. These detectors are $1\times1\times1\,\mathrm{cm}^3$ in size and are operated in an array of $4\times4\times4$ crystals. As a semiconductor material, Cadmium-Zinc-Telluride (CdZnTe or simply CZT) offers the low radioactivity levels and good energy resolution required for the search for $0\nu\beta\beta$-decay. Furthermore, CZT naturally contains several double beta-decay candidates. The most promising is ^{116}Cd with a Q-value of $2.8\,\mathrm{MeV}$, which lies above the highest prominent γ-line occurring from natural radioactivity. In 2017 the main research activity aimed to upgrade the experiment to the so-called e**X**tenden **DEM**onsrator COBRA XDEM.

1 Activities at the LNGS

1.1 The COBRA demonstrator

The COBRA collaboration currently operates a demonstrator setup consisting of 4×4×4 detectors at the LNGS. The detectors are made of CdZnTe (CZT) – a commercially available room temperature semiconductor. Due to the poor mobility of holes inside CZT, a special readout electrode has to be used to compensate for this effect. COBRA uses a so-called coplanar grid (CPG) consisting of two interlocking comb-shaped anodes held at slightly different potentials. The bias in between is referred to as grid bias (GB). This way, only one electrode collects the charge carriers created via a particle interaction in the end. A bias voltage (referred to as BV) at the order of -1 kV forces the electrons to drift towards the CPG anode. The electrode at the lower potential collects these electrons and is called the collecting anode (CA) while the other one acts as a non-collecting anode (NCA). The complete signal reconstruction relies only on the induced electron signal, that is why CZT is referred to as single charge carrier device. Details on the reconstruction can be found in [5].

Each crystal is $1.0 \times 1.0 \times 1.0$ cm^3 in size and has a mass of about 6 g. Several isotopes, which are candidates for double beta-decays, are present in CZT according to their natural abundances. An overview can be found in Table 1. The most promising are ^{116}Cd due to the high Q-value of 2814 keV and ^{130}Te because of its high natural abundance of about 34% and considerably high Q-value of 2527 keV. The results of the most recent peak search analysis for five $\beta^-\beta^-$ g.s. to g.s. transitions can be found in [6]. No signal was found, consequently, lower half-life limits could be set for the investigated double beta transitions on the order of $10^{19} - 10^{21}$ years. For the $0\nu\beta\beta$-decay of ^{114}Cd the world's leading limit was achieved.

Table 1: List of $0\nu\beta\beta$-decay candidates contained in CZT with their corresponding decay modes, natural abundances [7] and Q-values [6].

Isotope	Decay mode	Nat. ab.	Q-value [keV]
^{64}Zn	$\beta^+/EC, EC/EC$	49.17%	1095.70
^{70}Zn	$\beta^-\beta^-$	0.61%	998.50
^{106}Cd	$\beta^+\beta^+, \beta^+/EC, EC/EC$	1.25%	2775.01
^{108}Cd	EC/EC	0.89%	272.04
^{114}Cd	$\beta^-\beta^-$	28.73%	542.30
^{116}Cd	$\beta^-\beta^-$	7.49%	2813.50
^{120}Te	$\beta^+/EC, EC/EC$	0.09%	1714.81
^{128}Te	$\beta^-\beta^-$	31.74%	865.87
^{130}Te	$\beta^-\beta^-$	34.08%	2526.97

A detailed description of the COBRA demonstrator can be found in reference [8]. This publication reports on hardware aspects like the DAQ electronics as well as the experimental infrastructure to monitor and ensure a stable operation under low background conditions. The experimental setup is located on two floors referred to as the upper and lower hut. The lower hut is a clean-room like environment hosting the actual detector setup, the passive shielding and the first stage of electronics. The signals are transmitted via 20 m CAT 6 Ethernet cables to the upper hut where the main electronics and data-acquisition is located. Figure 1 shows an overview of the different shielding layers of the demonstrator in the lower hut. The outermost layer consists of 7 cm borated polyethylene acting as a shield against neutrons. Following, there is a frame of welded metal plates to prevent the first part of the readout chain to be affected by electromagnetic interferences (EMI). Inside this EMI box the custom made and actively cooled preamplifier devices are placed. The inner shielding consist of a multi-layered structure of standard lead, ultra low activity lead and copper surrounding the detectors themselves. This inner shielding is embedded into a polycarbonate box which is continuously flushed with evaporated dry nitrogen to prevent radon from diffusing into the setup.
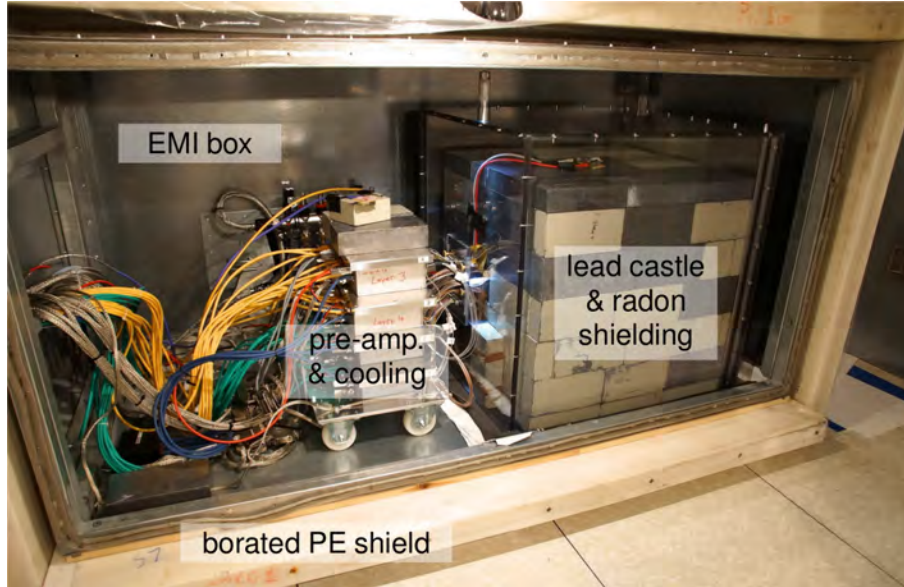
Figure 1: Overview of the experimental setup of the COBRA demonstrator. Highlighted are the different shielding layers and the first stage of the readout chain. The detectors themselves are housed within a copper nest inside the lead castle, which is sealed in a nitrogen flushed polycarbonate box.

1.2 Maintenance shifts

The overall working time spent on-site at the LNGS was about 40 man-days in 2017. Four shifts have been carried out to maintain the COBRA demonstrator and to prepare the upgrade to the extended demonstrator XDEM.

A first preparation shift was carried out in April to take care of most of the mechanical tasks. This included the construction of a new cable tree for the differential signal transmission between the lower and the upper hut. The cable route is the same as for the existing demonstrator, going from the EMI shield in the lower hut through a wall in the back of the hut and then upstairs. Both feedthroughs at the wall of the lower and upper hut had to be widened in order to hold the additional cabling. Afterwards an intensive cleaning campaign took place to restore the clean-room like conditions in the lower hut before considering to open the inner shielding of the experiment. During this shift one of the batteries inside the uninterruptible power supply (UPS) system was exchanged. The faulty battery caused a lot of signal noise on all channels since there was no filtering of the LNGS input power anymore. In this two week period before the planned maintenance, the operation of some detectors was only possible at very high trigger thresholds of several hundred keV. Furthermore, the DAQ electronics suffered from several short power shortages which are normally covered by the UPS system. As a consequence two FADCs stopped working properly, hence, the data of eight detectors could not be recorded in this time. Fortunately, the power supply of the detector array was not affected since this is backed up by a separate UPS unit in the lower hut. The situation was resolved by installing a new UPS battery in the upper hut and exchanging the faulty FADCs with spare devices. One of the FADCs could be fixed rather easily by flashing the firmware but the status of the second one seems to be unrepairable.

In order to prepare the intended low-threshold ^{113}Cd run, the coolant in the cooling system of the pre-amplifier stage was replaced from pure water to a special cooling liquid. This upgrade makes it possible to cool the first stage of electronics, which is located inside the EMI shield close to the detectors, more aggressively down to temperatures of -20°C. The effect of the improved cooling will be discussed later in section 2.1. By the end of the first shift a complete calibration of the demonstrator with the available ^{22}Na and ^{228}Th calibration sources was performed. At this time 55 out of 64 detectors were active and performed without any issues. Unfortunately it was discovered shortly afterwards that the demonstrator faced another problem with a different part of the electronics. This issue turned out to be even more dramatical than the faulty UPS battery. After three weeks of intensive remote controlled testing it was

decided that an additional shift is needed to resolve the new problem of coincident signal noise on all channels.

Right after the on-site shift in April a lot of effort was spent to identify the origin of the new noise incident via remote. A closer look into the data revealed that the overall trigger rate of all channels had increased by several orders of magnitude and that most triggered events were in coincidence. These characteristics were completely different from what had been observed before the lately completed on-site shift. The operation with a reasonably low trigger rate was only possible for arbitrary high thresholds of about 1-2 MeV, which was not sufficient for the planned measurement of the ^{113}Cd spectrum.

No indication for the root cause of the sudden appearance of this new noise problem was identified before the arrival of the shifters at LNGS. On-site, the origin was found to be related to the bias supply of the detectors inside the main electronic rack in the lower hut. It was possible to rework the custom-made converter boxes from MPOD Redel multi-pin to the Sub-D 8w8 cable standard used for the detector supply cables. After fixing the problem, the demonstrator went back to smooth operation, thus, the preparation of the dedicated ^{113}Cd could be continued.

After successfully resolving the noise problem in May, the cooling power of the pre-amplifier stage was increased to lower the overall ambient temperature. At the same time a regular evaluation of the trigger threshold for each individual channel was done to optimize the detection threshold for each detector. For a graphic representation see Figures 2 and 3.

As starting point for the anticipated ^{113}Cd low-threshold run a third shift was carried out at LNGS when stable operation and the final ambient temperature were reached. Already in the beginning of 2017 the collaboration started the purchase of two new calibration sources from the company Eckert&Ziegler. The collaboration would like to thank the LNGS staff for their advice and help with the required paper work, that minimized any delay in the delivery process. Both sources finally arrived at LNGS by the end of May. The first one is a replacement for the old ^{228}Th source (LNGS-ID: 50) due to the fading activity of only about a few 100 Bq. It was found that reasonably high statistics can be achieved with the new ^{228}Th source of about 10 kBq activity in a couple of hours compared to several days using the old one. Secondly, a ^{152}Eu source (LNGS-ID: 142) of the same geometry with 5 kBq activity was purchased that features a intense γ-line at 122 keV. This line allows for the study of the detector performance and resolution at low energies not far away from the average trigger threshold. The previous lowest available γ-line at 239 keV was coming from ^{212}Pb as part of the ^{228}Th decay chain. Both lines cover the energy range of the ^{113}Cd decay with an endpoint of about 320 keV and are of special interest for the upcoming spectral shape analysis. It turned out that it is challenging to see the low-energetic ^{152}Eu for the outermost detectors while using the calibration source at the central position within the detector array. This is mainly due to self-shielding effects of the detectors and the underlying strong Compton continuum of the higher energetic lines. To partly overcome this problem, the ^{152}Eu irradiation was repeated for two additional central positions between the two upper and lower detector layers. The benefit of this improved positioning is still under evaluation.

The last shift in 2017 aimed to exchange the instrumentation of the nitrogen dewar that is used to heat the inside of the vessel to increase the evaporation rate for a continuous flushing of the inner shield of the experiment. The system had failed several times in the past and was entirely renewed in 2016. Unfortunately the exchange of the final part was delayed due to problems with the manufacturing of parts of the instrumentation. During the installation end of December 2017 the new instrumentation was slightly damaged but could be repaired on-site. Consequently, an additional iteration of the instrumentation design was developed which will improve the overall performance of the flushing system. The installation of this new instrumentation will be done during the upgrade to the COBRA extended demonstrator in early 2018.

2   Data-taking and analysis

In 2017 roughly two months of data-taking were lost due to the incident with the faulty UPS battery and consequent noise problems. The data quality of the first six months of 2017 is still under review. The second half of 2017 was dedicated to a special low-threshold run to investigate the fourfold forbidden non-unique β^--decay of ^{113}Cd. The aim is to contribute to the scientific discussion regarding the so-called

quenching of the weak axial-vector coupling strength g_A in nuclear processes. In reference [9] it is shown that the spectral shape of this highly forbidden β-decay is especially sensitive to the effective value of g_A.

2.1 Dedicated ^{113}Cd run

More than 98% of the events recorded by the COBRA demonstrator are originating from the β-decay of ^{113}Cd. This decay was already studied with an early predecessor of the current COBRA setup what resulted in a half-life of $(8.00 \pm 0.11(\text{stat}) \pm 0.24(\text{sys})) \times 10^{15}$ years and a Q-value of $322.2 \pm 0.3(\text{stat}) \pm 0.9(\text{sys})\,\text{keV}$ [10]. Due to the long half-life the average decay rate of ^{113}Cd can be used to study the detector stability with an intrinsic monitor as was reported in [11].

After finalizing the hardware optimization for the low-threshold operation, the ambient temperature was lowered by increasing the cooling power of the pre-amplifier stage (see Figure 2). It was found that a temperature setting of $-10°$C is sufficient to reach a reasonably low temperature of about $2°$C close to the pre-amplifier boxes. The operation at this temperature should prevent immediate condensation of moisture in case of a failure of the nitrogen flushing. The temperature effect on the signal noise and detector performance was studied in [12]. Compared to room temperature, a lower operation temperature is beneficial since the thermal noise component of the signal noise is reduced while the detector resolution for CZT is optimal around $10°$C. Since there is no thermal insulation of the setup, the temperature of the lead castle housing the detectors is slightly higher than for the directly cooled preamplifier devices, but stable at about $9°$C. At the same time the trigger threshold for each channel was optimized by monitoring the overall trigger rate.
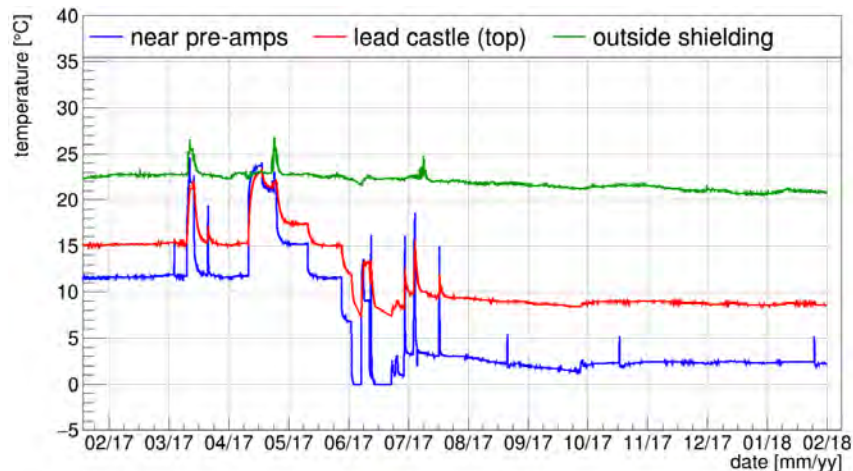

Figure 2: Temperature surveillance of the COBRA demonstrator in the lower hut. The ambient temperature outside the shielding (green) is rather constant at $22°$C. The temperature increases on short time scales indicate on-site activity at LNGS or a fail of the cooling unit due to short blackouts. The other two sensors are located inside the EMI shield (blue) and inside the radon shield (red) on top of the lead castle. This location is most representative for the actual detector temperature and was stable at $9°$C for the complete ^{113}Cd measurement.

When the thermal equilibrium for the final temperature setting was reached, a complete calibration run was performed as mentioned in section 1.2. All detectors that revealed problems during the pre-calibration or an unstable trigger rate, which hints to noise problems, were switched off. In a second iteration, detectors with a comparable high threshold were deactivated to prevent possible cross-talk effects and to ensure a stable operation. An impression of the threshold variation can be seen in Figure 3. Finally, the low-threshold ^{113}Cd run was started on July 31st. By monitoring the average trigger rate for each channel, the energy threshold for each detector was set on a weekly basis over the complete data-taking period. The data-taking was stopped in February 2018 after an exposure of more than $1\,\text{kg day}$ per single detector was reached. This allows for a single detector analysis to investigate the ^{113}Cd β-spectrum with a statistical ensemble. An overview of the analysis will be discussed in the next section.
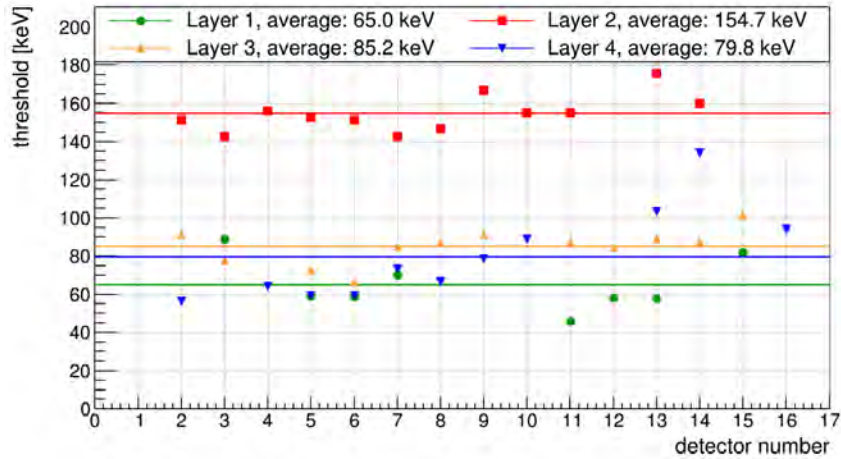
Figure 3: Threshold variation of the COBRA detectors operational in the low-threshold ^{113}Cd run. The solid lines indicate the average threshold per detector layer. Except for layer two most of the detectors could be operated with a threshold below 100 keV. Layer two suffers from the aftereffects of the noise problems that occurred in April 2017.

2.2 ^{113}Cd spectral shape analysis

The COBRA collaboration has access to a set of ^{113}Cd template spectra calculated for different nuclear frameworks in dependence of the weak axial-vector coupling strength g_A. The calculations have been carried out for $g_A \in [0.8, 1.3]$ using the *nuclear shell model* (NSM) and two further frameworks for comparison. Figure 4 illustrates the complex g_A dependency of the β-electron momentum distribution in form of a two-dimensional plot for the NSM.
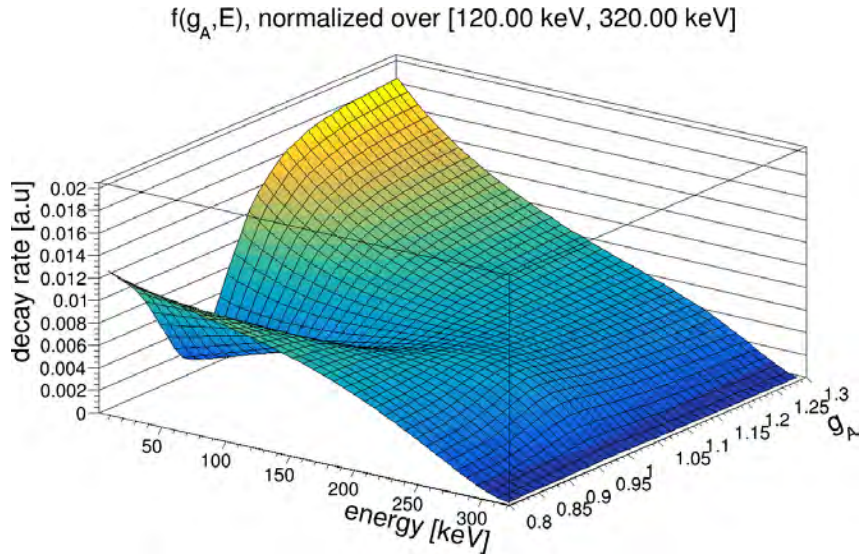

Figure 4: Two-dimensional representation of the g_A dependence of the ^{113}Cd spectral shape in the NSM. In order to compare the theoretical templates with the COBRA data, the decay rate for each g_A slice is normalized to the accessible energy range limited by the individual detector threshold and the Q-value of the decay.

In order to compare such templates with the actual COBRA data, detector effects such as a finite energy resolution, an energy dependent signal efficiency as well as the individual detector threshold have to be taken into account. This is done by folding the templates with the resolution function FWHM(E) and the

15

energy dependent detection efficiency $\varepsilon(E)$. Afterwards the templates are normalized according to the accessible energy range per detector. The detector dependent FWHM(E) is determined from calibration data using γ-lines between $122\,\mathrm{keV}$ and $2614\,\mathrm{keV}$ while $\varepsilon(E)$ is known from a Monte Carlo simulation based on GEANT4.

To achieve independence of the number of provided input templates and to compare the COBRA data for arbitrary g_A values over the whole available g_A range, an interpolation method based on so-called splines was developed [13]. A spline is a collection of several polynomial functions over a range of points referred to as *knots* (x_n, y_n). In between two neighboring knots a polynomial is defined by a set of boundary conditions. In contrast to a conventional parameter fit, no optimization process is involved since the spline is uniquely defined by the knots and the boundary conditions. Per definition all knots and so the original points of the templates are contained in the spline as well. For the interpolation the *TSpline3* class of the *ROOT* software package [14] is used, which utilizes polynomials of grade three for the spline. The final comparison of the theoretical templates and the COBRA single detector spectra is done with a χ^2 test to find the best match template and g_A value.

The data analysis is currently ongoing and will be published in 2018.

2.3 Improved pulse-shape discrimination

During the processing of the raw pulses obtained from the single detectors, several quality criteria are used to discriminate between real physical events and events triggered by electronic noise or other disturbances. These criteria have been developed to ensure a maximized signal efficiency at high energies around the Q-value of ^{116}Cd at $2.8\,\mathrm{MeV}$. In the past it has been observed that some criteria are too strict in the lower energy region, which leads to different rates of the ^{113}Cd decay compared between single detectors. Therefore, a careful review and evaluation process was done at TU Dresden. First results can be found in [15]. The data used for this study was recorded between June and September 2016 after firstly starting to lower the thresholds for the anticipated ^{113}Cd investigation. An impression for the likelihood to have one event tagged by multiple quality flags is shown in Figure 5. For each flag f, two numbers (p and s) can be calculated to quantify the level of overlapping with another flag h. The definitions are as following

$$
s_f = \frac{\text{number of events, where any other flag triggered}}{\text{total number of events flagged by } f} = \frac{N(f|h \neq f)}{N_f},
$$

$$
p_f = \frac{\text{summed number of events of all other flags}}{\text{total number of events flagged by } f} = \frac{\sum_{h \neq f} N_h}{N_f}.
$$

In the current implementation, already one flag is enough to declare an event as unphysical, which is sufficient for pulses with a rather high amplitude, hence, a high energy deposition. Currently, the implementation of a new event selection and the improvement of the existing framework is work in progress. The main idea is to evaluate each flag with respect to the uncertainty on the pulse quantities used in the flag declaration (e.g. rise time, pulse height) and to weight the single flags according to their impact.

Besides the data cleaning cuts, additional algorithms are used to reject background-like events while maintaining a high signal acceptance [2, 16]. Recently it was found that the successful discrimination between central and so-called lateral surface events (LSEs) can be combined with the developed method to distinguish between single- and multi-site events (SSEs and MSEs). This is done by using an adapted approach referred to as A/E criterion, that was originally created for Germanium-based $\beta\beta$-experiment [17]. The quantity A denotes the maximum amplitude of the current pulse and E the deposited energy by a particle interaction. The current pulse is the first derivative of charge pulse that is directly reconstructed from the raw anode signals. MSEs feature smaller A/E values compared to SSEs due to the imprints on the signal trace of the charge carriers' drift through the detector bulk. The A/E approach was successfully transferred to the COBRA CPG detector design and optimized with ^{228}Th calibration data. The decay chain of ^{228}Th features the deexcitation of ^{208}Tl with the emission of a single photon of $2.6\,\mathrm{MeV}$ energy. At this high energy pair creation is the dominant interaction process with the detector material. The kinematics of pair creation lead to distinct areas in the energy spectrum that can be used as proxies for signal-like SSEs and background-like MSEs. These areas are the single-escape peak (SEP) at $2.1\,\mathrm{MeV}$ and the double escape peak (DEP) at $1.6\,\mathrm{MeV}$. The SEP is expected to show a strong MSE fraction
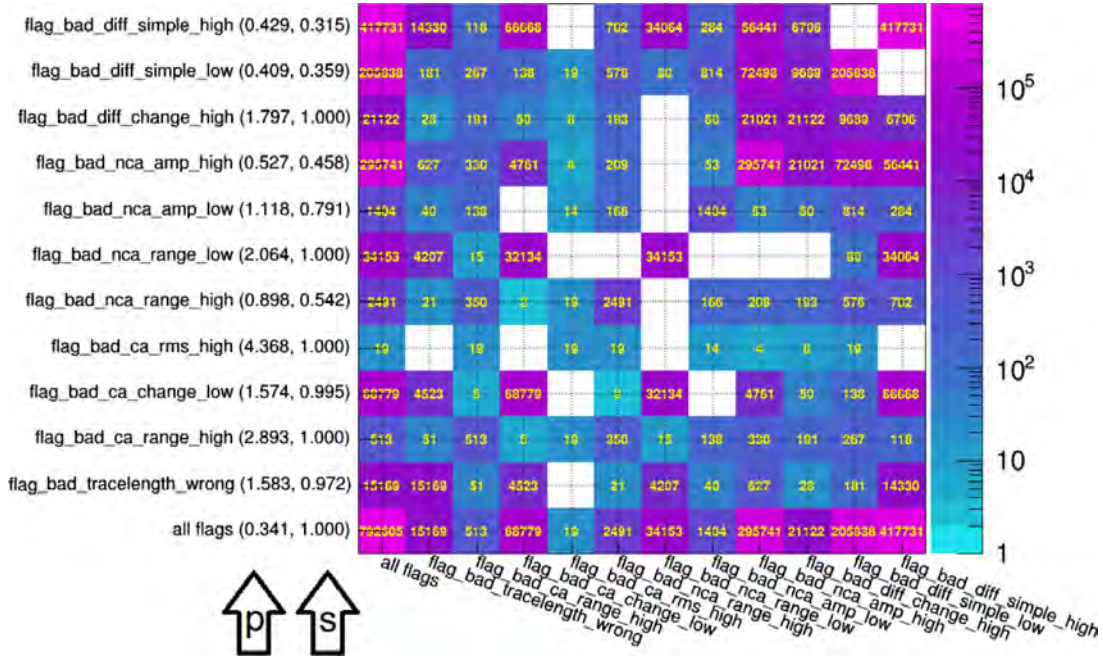
Figure 5: Impression of multi-flagged events. Every bin contains the number of counts selected by the corresponding pair of flags. On the diagonal, one can obtain the total number of counts for the given flag, whereas the histogram is symmetrical along the diagonal. The y-axis labels contain two numbers, p and s, that quantify the level of overlapping of the flag f with another flag h. It can be seen that some flag criteria show a complete overlap with another flag, which hints to some efficiency issues.

while the DEP features dominantly single-site interactions. The energy dependent fraction of multi-site interactions after the optimization procedure can be seen Figure 6 for a single detector ^{228}Th calibration.
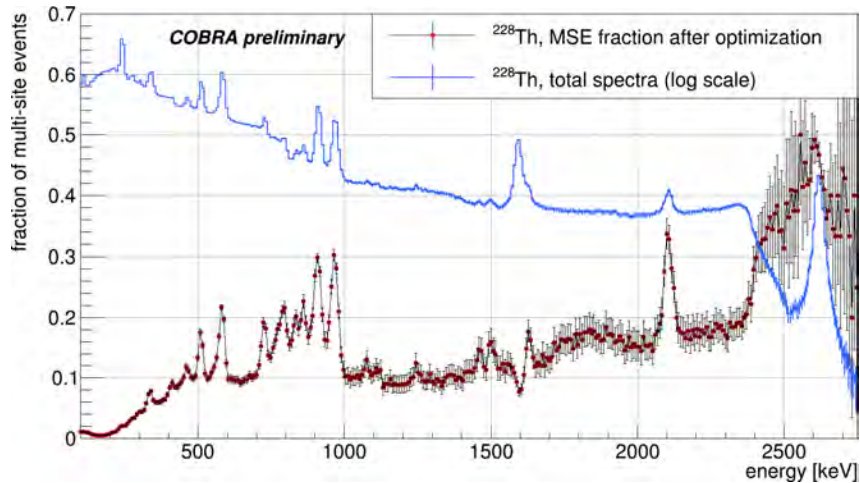

Figure 6: Fraction of identified multi-site interactions after optimization for a ^{228}Th calibration with a CZT-CPG detector [4]. For comparison, the energy spectrum of ^{228}Th in logarithmic scale is shown as well. Clearly visible is a high fraction of MSEs for the SEP at 2.1 MeV while there is only a rather small fraction of MSEs in the DEP at 1.6 MeV. Furthermore, the Compton continuum between 1 MeV and 2.3 MeV shows a comparable low MSE fraction, which is in agreement with the expectation. All γ-lines below 1 MeV show an increased MSE fraction due to the dominating process of primary Compton scattering followed by a photoelectric absorption.

For the shown calibration data the signal acceptance ε_s for the DEP and background rejection ε_b for the SEP are determined to

$$\begin{aligned} \varepsilon_s &= (94.8 \pm 1.6)\%, \\ \varepsilon_b &= (62.4 \pm 2.4)\%. \end{aligned}$$

Similar efficiencies could be reached for all LNGS detectors.

2.4 Exploration of more physics channels

Given the total amount of data of the COBRA demonstrator array, several analyses have been started on other physics channels. Within the g_A spectral shape investigation of ^{113}Cd the data selection and pulse shape discrimination have been studied in more detail at lower energies. This leads to a better filtering and slightly decreased background. At the same time an ambitious program of data partitioning was started. The goal is to identify the runs with increased background index due to a fail of the nitrogen flushing and runs that were strongly affected by electromagnetic interferences. This will lead to a data set with reduced background and a smaller set that is enriched in background. The latter is of special interest to study the background composition. Preliminary studies have shown that a background reduction up to a factor of 4.6 can be reached with this partitioning technique. In combination with the updated A/E pulse shape selection a $2\nu\beta\beta$ half-life measurement of ^{116}Cd seems to be within range. In addition, a first multi-detector analysis has been started to search for positron emitting modes and excited state transitions. Combining detectors leads to an indication of a ^{40}K background component which was barely visible in the single detector spectra. A large Monte Carlo campaign was started to explore the signature of EC/β^+ decays of ^{106}Cd for the COBRA demonstrator.

3 Preparation of XDEM installation

The COBRA collaboration is aiming to upgrade the experiment with the installation of a new prototype detector layer consisting of nine $6\,\mathrm{cm}^3$ detectors. As the new layer will be implemented into the existing setup without interfering with the current $4\times4\times4$ array, the new stage is referred to as eXtended DEMonstrator (XDEM). The upgrade will almost double the sensitive detector mass and is the first major expansion since the finalization of the COBRA demonstrator in 2013. The preparation of the XDEM installation took place in 2017 and will be summarized in the following sections.

3.1 Detector characterization

In 2017 a total of ten $6\,\mathrm{cm}^3$ CZT detectors were purchased by the COBRA collaboration. The two world-leading manufactures for CZT detectors *eV Products* (now Kromek, US) and *Redlen technologies* (Canada) were chosen based on the results obtained with very first prototypes. A detailed overview about the first detector characterization is given in [18]. Each detector is equipped with four CPGs on the anode side that are rotated by 90° and a common planar cathode electrode. This readout design is referred to as quad-CPG and overcomes the problem of too high leakage currents, which prevents the use of up-scaled versions of the $1\,\mathrm{cm}^3$ detectors. It could be shown that the interaction depth reconstruction, which is a powerful tool to discriminate background, can be transfered to this new approach [3]. In Figure 7 a comparison of the different detector designs investigated by the COBRA collaboration is shown.

The new quad-CPG detectors arrived in the middle of 2017 at TU Dortmund and were contacted and tested extensively. One improvement with respect to the treatment of the 64 detectors of the current demonstrator is the special care that was taken during the detector handling by the manufactures and in the surface laboratories. Also the packaging during the shipment was air-tight sealed, in contrast to previous orders. For the contacting a modified method was used compared to the demonstrator setup, as the electric connection is now done with the help of a highly radio-pure conductive epoxy and gold wires instead of the combination of a conductive lacquer and a conventional glue. This is a significant reduction of the number of potential background sources. The new method also allowed to contact the detectors almost completely at TU Dortmund in order to minimize the effort in the underground laboratory during
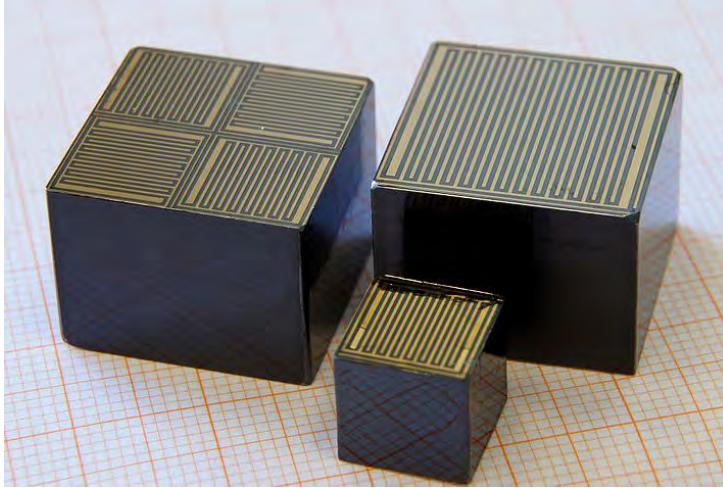
Figure 7: Picture of CPG-CZT detectors investigated by the COBRA collaboration. The $1\,cm^3$ version in the front is used in the $4{\times}4{\times}4$ array of the COBRA demonstrator. The larger $6\,cm^3$ crystals are prototypes that were studied in detail over the last two years. It was found that the up-scaled single CPG version (right) is facing problems with leakage currents limiting the achievable resolution. To overcome this problem, the anode side was segmented into four individual sectors (left) offering additional veto capabilities.

the installation. Furthermore, the contacting has been performed in a clean laminar-flow environment and the detectors were kept in a nitrogen atmosphere during storage and testing. Together with the use of the guard-ring, which has been shown to be able to reduce surface related backgrounds from α-decays by more than three orders of magnitude [1], and the beneficial surface-to-volume ratio of the larger detectors, the collaboration is confident to reduce the background index significantly compared to the demonstrator setup.
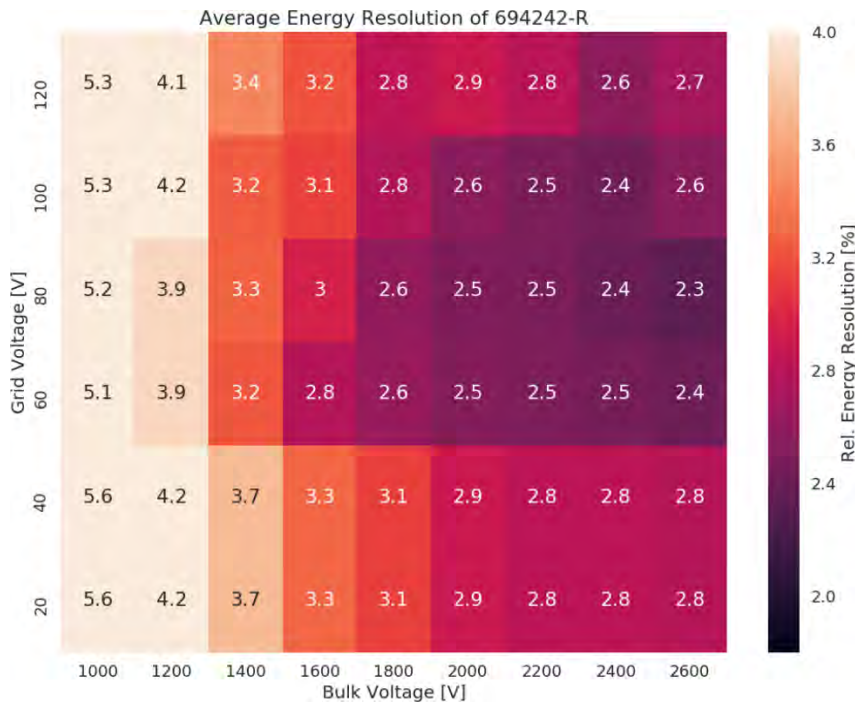

Figure 8: Characterization results of one of the new XDEM detectors. By varying the operation parameters bulk bias (BV) and grid bias (GB) an average resolution of 2.3% at 662 keV could be reached for the working point of BV/GB = 2600/80 V. This result is comparable to the achieved performance of the well-known small single CPG detectors of the demonstrator and representative for the other XDEM detectors.

The characterization of each detector included the determination of the ideal working point (combination

of grid and bulk bias, Figure 8) as well as measurements to determine the individual relative efficiency. All characterization measurements were taken in a nitrogen atmosphere to prevent any radon contamination, which turned out to be the dominant background component for the current setup. Furthermore, the electrical behavior was characterized with current-voltage (I-V) measurements and a number of different γ-sources have been used to study the energy resolution of the detectors. One of the detectors was also used for a new investigation of the guard-ring electrode with the goal to show the possibility to suppress also β-decays on the surface by cutting on the pulse height of the guard-ring electrode.

3.2 Plan for implementation

The installation of COBRA XDEM requires to rework parts of the inner passive shielding. The new detector layer will be located on top of the current demonstrator array in a new copper housing. For the innermost parts of the detector housing electro-formed OFHC copper is used that has been stored underground at the Dresden Felsenkeller laboratory for more than five years. All copper parts were electro-polished by an external company and treated according to a multi-stage cleaning procedure at LNGS prior the installation. The cable feedthroughs and routing for the calibration tube is made from certified ultra-low activity lead and arrived at LNGS in December 2017. The installation of the XDEM setup was done in March 2018 within a two week lasting shift. Some impressions of the installation are depicted in Figure 9. The nine best performing detectors were selected and put in a frame of Polyoxymethylen (POM). This frame was then put into the copper housing surrounded by one layer of ULA lead and two additional layers of standard lead. The air-tight radon cage around the lead castle had to be renewed in order to included the additional readout of the XDEM channels. The preamplifier stage including the cooling section was upgraded as well. It could be confirmed that all detector contacts are electrically working although not all channels can be read out at the time of this report. The commissioning of COBRA XDEM is ongoing but from preliminary data taken in the laboratories and at LNGS it is already clear that the new detectors will surpass the COBRA demonstrator in terms of achievable resolution and background index.
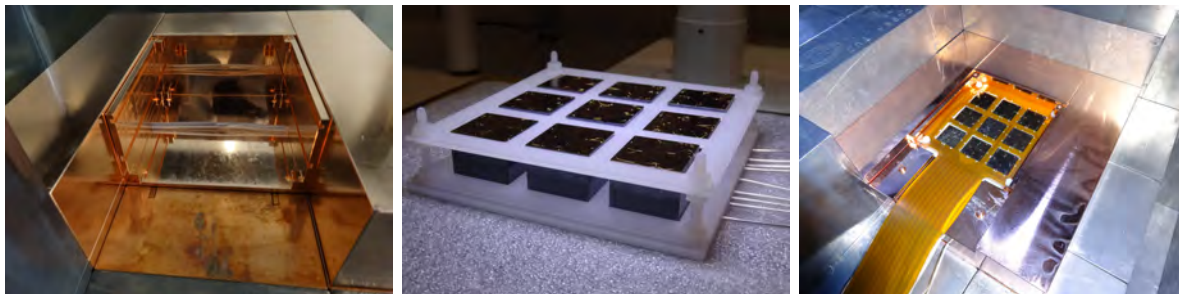

Figure 9: First impressions of the upgrade to COBRA XDEM. Left: new copper housing made from electro-polished OFHC copper and calibration routing. Middle: final XDEM detector layer consisting of a POM holder and nine $6\,\mathrm{cm}^3$ quad-CPG detectors. Right: installed XDEM detector layer within the copper nest on top of the COBRA demonstrator array.

4 Summary and outlook

The main activities of the collaboration in 2017 were the preparation and start of a dedicated ^{113}Cd measurement with the COBRA demonstrator and the preparation of the upgrade towards COBRA XDEM. The demonstrator setup was optimized for low-threshold operation to cover a maximum range of the fourfold forbidden non-unique β-decay spectrum of ^{113}Cd. The spectral shape of the β-electron distribution is highly sensitive to the effective value of the weak axial-vector coupling strength g_A involved in nuclear processes. An analysis strategy was developed to extract the best matching theoretical template for an assumed value of g_A. A dedicated ^{113}Cd run was started in July 2017 with optimized detection thresholds and operation conditions. The data-taking was stopped in February 2018 and the results of the spectral shape analysis will be published soon.

The analysis of the demonstrator data was expanded towards more physics channel with focus on the 2νββ-decay of ^{116}Cd using an advanced data partitioning. The sensitivity to more exotic double beta-decay modes such as EC/β$^+$-decays is currently studied with Monte Carlo simulations.

The collaboration purchased ten new prototype quad-CPG detectors to upgrade the experiment to COBRA XDEM. All detectors passed the quality requirements in terms of energy resolution and overall performance. From the characterization point of view the new XDEM detectors will surpass the average of the current demonstrator detectors. The nine best performing detectors were successfully installed in March 2018 at LNGS, which almost doubles the sensitive mass of COBRA. The commissioning is still ongoing and not all channels are operational at the moment, but first calibration and physics data is already looking very promising. First results and a background characterization are expected for the end of the year.

List of publications in 2017

[1] J.-H. Arling et al., *Suppression of alpha-induced lateral surface events in the COBRA experiment using CdZnTe detectors with an instrumented guard-ring electrode*, Journal of Instrumentation, Volume 12, 2017, 10.1088/1748-0221/12/11/P11025

[2] S. Zatschler, *Pulse-shape discrimination techniques for the COBRA double beta-decay experiment at LNGS*, Journal of Physics: Conference Series, Volume 888, 012076

[3] R. Temminghoff, *Investigation of the Depth Reconstruction and Search for Local Performance Variations With a Large Coplanar-Quad-Grid CdZnTe Detector*, IEEE Transactions on Nuclear Science, Volume 64, Issue 7, 2017, 10.1109/TNS.2017.2711922

[4] S. Zatschler, *Discrimination of single-site and multi-site events in CZT-CPG detectors for the COBRA experiment*, Medical Imaging Conference and Room-Temperature Semiconductor Detector Workshop (NSS/MIC/RTSD), 2016, 10.1109/NSSMIC.2016.8069958

References

[5] M. Fritts et al., *Analytical model for event reconstruction in coplanar grid CdZnTe detectors*, NIM A 708 (2013), 10.1016/j.nima.2013.01.004, arXiv:1211.6604

[6] J. Ebert et al., *Results of a search for neutrinoless double beta-β decay using the COBRA demonstrator*, Phys. Rev. C 94 (2016), 10.1103/PhysRevC.94.024603

[7] M. Berglund and M. E. Wiesner, *Isotopic compositions of the elements 2009 (IUPAC Technical Report)*, Pure and Applied Chemistry 83 (2011)

[8] J. Ebert et al., *The COBRA demonstrator at the LNGS underground laboratory*, NIM A (2016), 10.1016/j.nima.2015.10.079, arXiv:1507.08177

[9] J. Suhonen et al., *Forbidden nonunique β decays and effective values of weak coupling constants*, Phys. Rev. C 93 (2016), https://doi.org/10.1103/PhysRevC.93.034308

[10] J.V. Dawson et al., *An investigation into the ^{113}Cd beta decay spectrum using a CdZnTe array*, Nucl. Phys. A (2009), https://doi.org/10.1016/j.nuclphysa.2008.12.010

[11] J. Ebert et al., *Long-Term Stability of Underground Operated CZT Detectors Based on the Analysis of Intrinsic Cd-113 β^--Decay*, submitted to NIM A (2016), arXiv:1508.03217

[12] T. Kreße, *Investigation of the temperature behavior of CdZnTe room temperature semiconductor detectors for the COBRA experiment*, bachelor thesis, TU Dresden, 2017

[13] A. Heimbold, *Spectral shape analysis of the fourfold forbidden beta decay of Cd-113 with the COBRA experiment*, bachelor thesis, TU Dresden, 2017

[14] R. Brun and F. Rademakers, *ROOT – An object oriented data analysis framework*, NIM A (1997), Vol. 389, https://doi.org/10.1016/S0168-9002(97)00048-X

[15] R. Kantelberg, *Evaluation of the Event Selection for the Beta Decay Study of Cd-113 with the COBRA experiment*, bachelor thesis, TU Dresden, 2017

[16] M. Fritts et al., *Pulse-shape discrimination of surface events in CdZnTe detectors for the COBRA experiment*, NIM A 749 (2014), 10.1016/j.nima.2014.02.038, arXiv:1401.5844

[17] M. Agostini et al., *Pulse shape discrimination for Gerda Phase I data*, Eur. Phys. J. C 73 (2013), http://dx.doi.org/10.1140/epjc/s10052-013-2583-7

[18] J. Ebert et al., *Characterization of a large CdZnTe coplanar quad-grid semiconductor detector*, NIM A (2016), 10.1016/j.nima.2015.09.116, arXiv:1509.02361

COSINUS

G. Angloher,[a] P. Carniti,[b] L. Cassina,[b] N. Di Marco,[c] L. Gironi,[b] ,[d] C. Gotti,[b]
M. Mancuso,[a] M. Maino,[b] L. Pagnanini,[f] G. Pessina,[b] F. Petricca,[a] S. Pirro,[c]
R. Puig,[e] F. Pröbst,[a] F. Reindl,[e] K. Schäffner,[f] J. Schieck,[e] M. Stahlberg,[e]

[a] Max-Planck-Institut für Physik, D-80805 München - Germany
[b] INFN - Sezione di Milano Bicocca, Milano I-20126 - Italy
[c] INFN - Laboratori Nazionali del Gran Sasso, Assergi (AQ) I-67010 - Italy
[d] Dipartimento di Fisica, Università di Milano-Bicocca, Milano I-20126 - Italy
[e] Institut für Hochenergiephysik der ÖAW, A-1050 Wien - Austria
and Atominstitut, Vienna University of Technology, A-1020 Wien - Austria
[f] Gran Sasso Science Institute, I-67100 L'Aquila - Italy

Abstract

The COSINUS (Cryogenic Observatory for SIgnals seen in Next-generation Underground Searches) project aims to provide a model-independent cross-check of the long-standing DAMA/LIBRA claim on the observation of dark matter, by us-ing the same target material (NaI) with a different experimental approach. The use of sodium iodide (NaI) crystals, operated at cryogenic temperature as scintillat-ing calorimeters, provides both a low energy threshold for nuclear recoil events as expected from dark matter particle interactions, and the possibility to perform par-ticle discrimination. Indeed, the dual read-out of phonon and light allows to perform signal-to-background discrimination on an event-by-event basis, a unique feature in comparison to other NaI-based dark matter searches. In this report we will discuss in detail the COSINUS detector concept and we will present the performance of our first prototypes together with the results of the first measurements.

1 Introduction

Although evidence for the existence of Dark Matter (DM) is nowadays well-established on the basis of several astrophysical measurements [1], its nature still remains unknown. Among several DM theories, the Weakly Interacting Massive Particles (WIMPs) are one of the most promising DM candidates. WIMPs, with a mass in the (GeV-TeV)/c^2 range, are expected to interact with ordinary matter with cross sections similar or smaller than the weak processes.
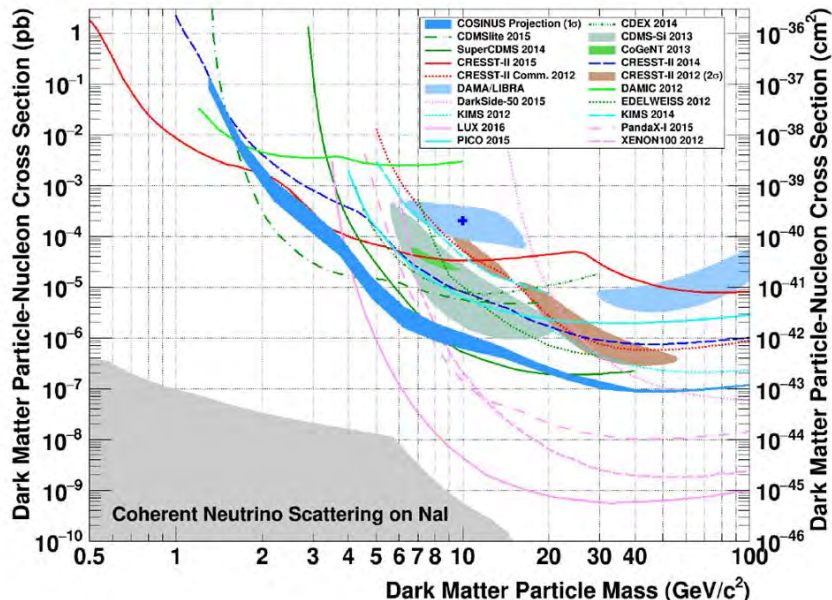
Figure 1: Projected sensitivity for a NaI-based experiment using COSINUS detector technology (solid blue band, 1 σ confidence level for spin-independent elastic dark matter nucleus scattering). Recent results from experiments using silicon and germanium targets are drawn in green, results from CRESST-II (CaWO$_4$) are depicted in red and exclusion limits using liquid noble gases in magenta. Limits drawn in cyan correspond to bubble chamber technology and experiments with CsI target. The light blue shaded regions correspond to the interpretation of the DAMA/LIBRA (NaI(Tl)) modulation signal by Savage et al. [2]. The benchmark point (blue cross) indicates the mass and cross-section chosen for the simulated WIMP contribution presented in section III of [3]. Gray-shaded regions in parameter space will be affected by coherent neutrino nucleus scattering on NaI mainly originating from solar neutrinos [4]. Figure from [3],references therein.

Direct DM search techniques are currently based on the detection of WIMPs scattering off the target nuclei and, since the expected recoil energies are well below 100 keV, an ultra-low background and highly sensitive detection apparatus is needed. At present several experimental efforts are ongoing all over the word using a variety of experimental approaches exploiting single or dual channel read-out based on the detection of scintillation light, phonon and/or charge signals induced by particles interacting in the detector target.

The analysis of present DM experiments is based on the detection of an excess of events over the expected background or on the detection of an annual modulation of the event rate caused by the seasonal variation of the Earth's velocity with respect to the dark matter halo [5]. While in the former approach the number of expected recoil events depends on the DM model assumptions, as the mass of dark matter particle, the interacting cross-section and the detector properties, a pure modulation signal can be considered model-independent.

Nonetheless, in the experimental panorama of the DM direct search the situation is

strongly controversial: recent DAMA results report a statistically robust modulation signal ($>9\sigma$) over 14 annual cycles [6] using a detector based on 250 kg of highly radiopure sodium iodide (NaI(Tl)) crystals operated at room temperature in the underground site of the Laboratori Nazionali del Gran Sasso (LNGS) in Italy. In the standard elastic scattering scenario, the DAMA/LIBRA result is not consistent with the null results of other direct search experiments (see Figure 1). Further studies are therefore needed to understand the origin of the modulation signal observed by the DAMA/LIBRA experiment and, in particular, the target dependence of the result; several R&D projects and experiments with alkali halide as target are currently running or in construction [7, 8, 9]. Among them, the COSINUS project [3] aims to develop a NaI-based detector operated at cryogenic temperature, thus exploiting both the scintillation light signal of NaI crystals and the phonon signal in a cryogenic detector. The dual channel read-out allows to perform particle identification, thus resulting in an effective suppression of the dominant β/γ background.

2 NaI-based cryogenic scintillating calorimeter

In the DM sector, the use of cryogenic scintillating calorimeters is successfully implemented in the CRESST experiment [10] while it is used by LUCIFER/CUPID$-$0 [11] for the search for neutrinoless double-beta decay.

A particle interacting in a cryogenic scintillating calorimeter produces two coincident signals: the major part of the deposited energy is converted into phonons (heat signal) while a small fraction (O(few percent)) goes into the production of scintillation light. The heat signal is therefore exploited to precisely measure the energy deposited in the target crystal and is almost independent from the particle type. The amount of scintillation light, instead, strongly depends on the particle type and can be used to perform particle identification, thus allowing the suppression of the dominant β/γ background with respect to nuclear recoil signal events. The light to phonon ratio, the so-called *light yield* (LY), is characteristic for each type of event: in particular β and γ particles produce most light and get assigned a LY$= 1$ by definition, while α-particles and neutrons show a lower LY quantified by the so-called *quenching factor* (QF).

Figure 2 shows the concept of a COSINUS detector module: a NaI target crystal is coupled via an interface (typically silicon oil) to a crystal (e.g. CdWO$_4$) carrying the Transition Edge temperature Sensor (TES) which reads the phonon signal. The crystal is inserted in a beaker-shaped light detector made from high-purity silicon. The light detector is equipped with a second TES reading the heat rise of the beaker caused by the absorption of scintillation photons. The whole detector module is operated at few milli-Kelvin. The need for the use of the CdWO$_4$ carrier crystal, is due to the hygroscopic nature and the low melting point of the NaI crystal making it impossible to evaporate the TES directly onto the NaI surface. By covering a large fraction of the NaI crystal surface, the beaker-shaped light detector exhibits a very high light collection efficiency while simultaneously serving as an active veto for external backgrounds and radioactive decays close to the surfaces of the NaI crystal and its surrounding material.

Figure 3 shows the result of simulated data for a gross exposure of 100 kg days (with
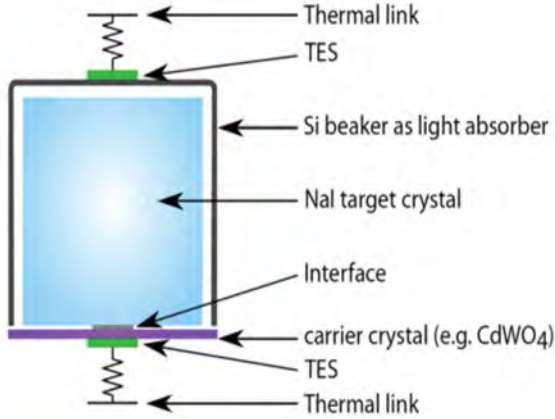
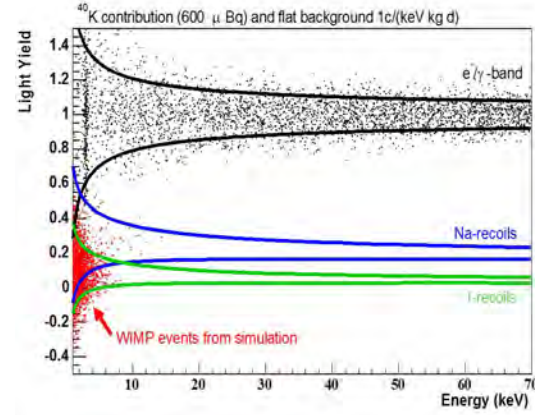Figure 2: Scheme of a COSINUS detector module.

Figure 3: Result of simulated data for a gross exposure of 100 kg days with the assumption detailed in [3] in the light yield - energy plane.

the assumption detailed in [3]) in the light yield - energy plane: black, blue and green bands correspond to electron, Na and I recoils respectively. Black dots indicate events originating from a flat background contribution of 1 c/(keV kg d) and a ^{40}K contamination with an activity of 600 μBq (corresponding to the DAMA background level) while red dots indicate Na and I scattered off by a hypothetical WIMP with a mass of 10 GeV/c^2 and a cross section of 2×10^{-4} pb (following the DAMA interpretation of Savage et al. [2]). Magenta boxes indicate the regions which may contribute to the DAMA/LIBRA energy range of positive modulation detection corresponding to 2-6 keV$_{ee}$ (where ee = electron equivalent).

3 Status and results of the COSINUS project

The first COSINUS detector prototype was realized using an undoped/pure NaI crystal with dimensions of 30x30x20 mm^3 and a weight of 66 g. The NaI is attached through a very thin layer of silicon oil to a carrier crystal made of CdWO$_4$ (diameter = 39.2mm, thickness = 1.6mm) equipped with a TES made by a thin film (200 nm) of superconducting tungsten (W-TES) produced at the Max-Planck-Institute for Physics in Munich. The cryogenic light detector consists of a sapphire wafer (diameter = 40mm, thickness $\simeq$460 μm) equipped with a TES optimized for light measurement. To increase the absorption efficiency of the blue scintillation light a 1-μm-thick layer of silicon is epitaxially grown onto the sapphire disc (SOS = Silicon On Sapphire). For the first prototype, therefore, the beaker-shaped light detector was not implemented. The whole setup is surrounded by a reflective foil [12].

The measurement was carried out in the test facility of the Max-Planck-Institute for Physics located in the underground site of LNGS, consisting of a dilution refrigerator allowing detector operation at temperatures as low as 7 mK. The TESs were read out with commercial dc-SQUID electronics (Applied Physics Systems company). The hardware-
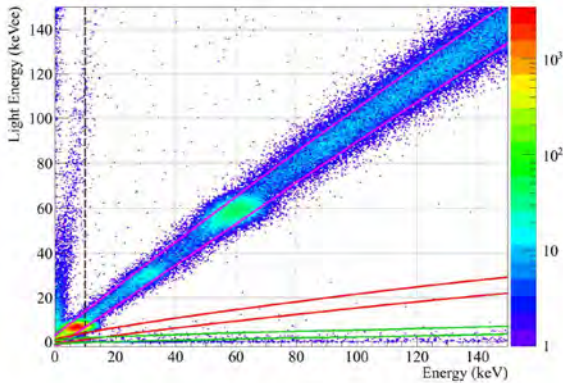
Figure 4: Data corresponding to a net exposure of 0.46 kg days of the first detector prototype in the light vs.(phonon) energy plane [12].
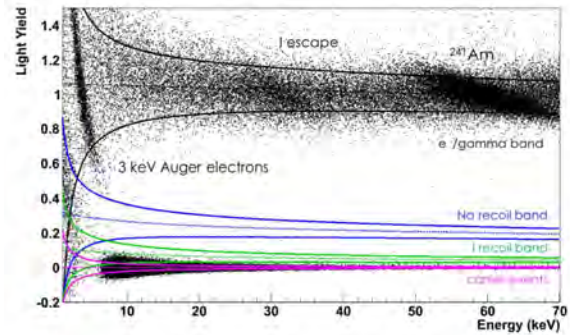

Figure 5: Data from the second COSI-NUS prototype. Lines indicate the central 80% bands for electron (black), Na (blue) and I (green) recoils respectively while the events without associated light signal are described by the magenta band [13].

triggered signals were recorded in a 328 ms window at a sampling rate of 25 kHz. Both detectors were always read out simultaneously, independent of which one triggered. The detectors were irradiated with γ-rays from an ^{41}Am source with an energy of 59,541 keV. After applying quality cuts to reject unstable detector operation, pile-up and bad pulse-shape events, a final exposure of 0.46 kg days was collected [12].

Figure 4 shows the events surviving quality cuts in the light-energy plane. A linear relation between light output and the energy deposited in the NaI crystal is clearly visible. Magenta solid lines confine the central 80% of the β/γ-band. Accounting for the QFs given in [14], red and green bands correspond to recoils off Na and I respectively, while the almost horizontal event population at very small light energies originates from particle events taking place in the CdWO$_4$ carrier crystal. The black dashed line indicates the estimate of the hardware trigger threshold of the phonon detector at 10 keV, essentially limited by the high pile-up rate observed. The energy resolution at the ∼60 keV calibration line is found to be 5.0 keV showing a significant improvement towards lower energies. By comparing the amplitude of a scintillation light pulse induced from a 59.541 keV X-ray in the NaI, originating from the ^{241}Am calibration source, to a direct hit of the light detector from a ^{55}Fe X-ray calibration source, we find that 3.7% of the energy deposited in the NaI crystal is measured as light [12].

In the second detector prototype, the beaker-shaped light detector, as foreseen for the final detector design (Figure 2), was implemented. The prototype was tested in the same facility used for the first protoytpe and, after applying the quality cuts, a total exposure of 1.32 kg days was collected. The result is shown in 5: black solid lines indicate a fit of the β/γ-band to the data with 80% bands. The mean line of the band is well modeled by a simple linear function, the width of the band includes contributions from the baseline resolutions of phonon and light detector, a Poisson-statistics term accounting for
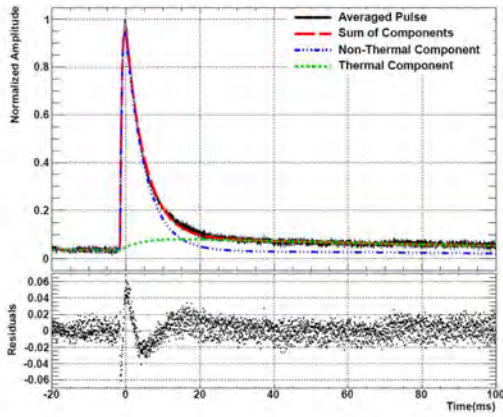
Figure 6: Top: Normalized average pulse (black) and Fit of the two-component model. Bottom: Fit residuals [13].
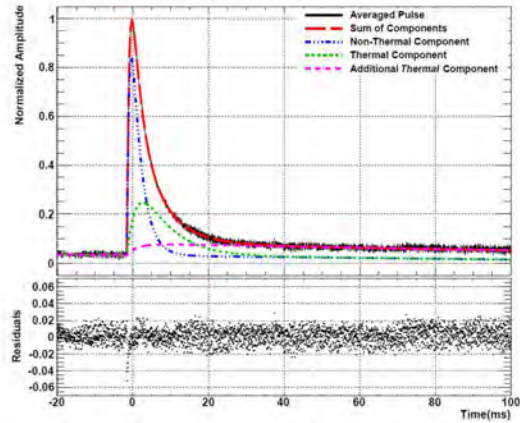
Figure 7: Top: Normalized average pulse (black) and Fit of the three-component model. Bottom: Fit residuals [13].

the quantization of the scintillation light photons and an empiric term scaling with light energy (e.g. potential position dependencies). Moreover, three characteristic structures are clearly evident: the line at ~60 keV originating from gammas from the ^{241}Am source, the so-called escape peaks from I at ~30 keV and a line at around 3 keV caused by ^{40}K Auger electrons. Na (blue) and I (green) recoil bands are calculated using the QFs of [14]. The magenta band is populated by events originating in the carrier crystal and showing a different pulse-shape than events in the NaI absorber [13].

The phonon detector was operated with a hardware trigger threshold of 8.26 ± 0.02(stat.) keV, still significantly above the COSINUS design goal of 1 keV. A baseline resolution for the phonon detector of 1.01 keV was achieved increasing to 4.5 keV at the ^{241}Am-peak at about 60 keV. With the second prototype an absolute light yield of 13.1 % was obtained. This value is roughly three times higher than that obtained with the first prototype and has been achieved thanks to the geometry of the beaker-shaped light detector [13].

Both in the measurement of the first and second COSINUS prototypes, we found that NaI exhibits a different pulse shape compared to other materials (Al_2O_3, $CaWO_4$, $ZnWO_4$, $CdWO_4$, CaF, and TeO_2) and, thus, cannot be convincingly described by the model for cryogenic particle detectors of [15]. We performed a pulse shape analysis by averaging O(100) events of the same energy deposition. We fit the averaged pulse both with the two-component model described in [15] and with a three-component fit. In the latter case, to the standard thermal and non-thermal components described in [15], we added a second thermal component. The results are shown in Figure 6 and 7 respectively: the residuals of both fits clearly show that the additional third component signifiantly improves the fit result and almost perfectly describes the measured pulse, while the two-component fit does not [12, 13]. As a result of this analysis we can conclude that the peculiarity of NaI is a long decay time of the pulse. As the decay time exceed the maximally available record window of the present DAQ we will switch to a dead-time free DAQ in the future, thus allowing to record the full tail which is a immensely useful tool to understand the origin of this third pulse component.

4 Conclusions and perspectives

The COSINUS R&D project aims at developing a NaI-based detector to solve the long-standing tension of the DAMA/LIBRA result in the panorama of direct DM searches. By using the same target material of the DAMA experiment, the target dependencies can be ruled out. Moreover, the use of a cryogenic apparatus and of a dual channel read-out, will allow to perform a signal to background discrimination on an event-by-event basis unique to NaI DM searches.

The first prototype developed by the COSINUS collaboration was the first successful measurement of a NaI crystal operated as cryogenic scintillating calorimeter measuring simultaneously the phonon and light signal from a particle interaction. The implementation of the second prototype has been the proof-of-principle measurement of the final detector design. We measured 13.1% ($\sim$40 photons/keV) of the energy deposited in the NaI as scintillation light thus exceeding the original COSINUS design goal (4 %) by more than a factor of three and proving that undoped NaI exhibits an outstandingly high light output at low temperatures. Moreover we observed a peculiar phonon pulse-shape previously not seen in numerous other materials.

At present, we are carrying out the optimization of the performances of a new detector prototype in a dedicated low-background cryostat in the underground Hall C at LNGS while the realization of further prototypes, by using high-purity both doped and undoped crystals, is foreseen. These tests together with the planned neutron test beam at the Tandem accelerator at TUM/LMU in Munich, to directly measure for the first time the QFs of a NaI crystal operated at cryogenic temperatures, will open the way for the realization of the COSINUS DM detector.

5 List of Publications

1. Results from the first cryogenic NaI detector for the COSINUS project, COSINUS Collaboration (G. Angloher et al.), JINST 12 (2017) no.11, P11007

2. The COSINUS project: Development of new NaI-based cryogenic detectors for direct dark matter search, A. Gütlein et al., 2017, Nucl.Instrum.Meth. A845

3. The COSINUS project - a NaI-based cryogenic calorimeter for direct dark matter detection, G. Angloher et al., J.Phys.Conf.Ser. 888 (2017) no.1, 012207

References

References

[1] Olive K A *et al.* (Particle Data Group) 2014 *Chin. Phys.* **C38** 090001

[2] Savage C, Gelmini G, Gondolo P and Freese K 2009 *JCAP* **0904** 010 (*Preprint* 0808.3607)

[3] Angloher G *et al.* 2016 *Eur. Phys. J.* **C76** 441 (*Preprint* 1603.02214)

[4] Gütlein A *et al.* 2015 *Astropart. Phys.* **69** 44–49 (*Preprint* 1408.2357)

[5] Drukier A K, Freese K and Spergel D N 1986 *Phys. Rev.* **D33** 3495–3508

[6] Bernabei R *et al.* 2013 *Eur. Phys. J.* **C73** 2648 (*Preprint* 1308.5109)

[7] Thompson W G (COSINE-100) 2017 Current status and projected sensitivity of COSINE-100 *TAUP 2017* (*Preprint* 1711.01488)

[8] Amare J *et al.* 2017 The ANAIS-112 experiment at the Canfranc Underground Laboratory *TAUP 2017* (*Preprint* 1710.03837)

[9] Tomei C (SABRE) 2017 *Nucl. Instrum. Meth.* **A845** 418–420

[10] Angloher G *et al.* (CRESST) 2016 *Eur. Phys. J.* **C76** 25 (*Preprint* 1509.01515)

[11] Artusa D R *et al.* 2017 *Phys. Lett.* **B767** 321–329 (*Preprint* 1610.03513)

[12] Angloher G *et al.* (COSINUS) 2017 *JINST* **12** P11007 (*Preprint* 1705.11028)

[13] Reindl F *et al.* (COSINUS) 2017 (*Preprint* 1711.01482)

[14] Tretyak V I 2010 *Astropart. Phys.* **33** 40–53 (*Preprint* 0911.3041)

[15] Pröbst F 1995 *Journal of Low Temperature Physics* **100** 69–104 ISSN 1573-7357

The CRESST dark matter search

G. Angloher [a], P. Bauer [a], A. Bento [a,b], E. Bertoldo [a], C. Bucci [c], L. Canonica [a], X. Defay [d], S. Di Lorenzo [c,j], A. Erb [d,e], F. von Feilitzsch [d], N. Ferreiro [a], A. Fuss [f,g], P. Gorla [c], A. Gütlein [f,g], D. Hauff [a], J. Jochum [h], M. Kiefer [a], H. Kluck [f,g] H . Kraus [i], J.C. Lanfranchi [d], A. Langenkämper [d], J. Loebell [h], M. Mancuso [a], V. Mokina [f,g], E. Mondragon [d], A. Münster [d], M. Olmi [c,j], C. Pagliarone [c], F. Petricca [a,†], W. Potzel [d], F. Pröbst [a], R. Puig [f], F. Reindl [a], J. Rothe [a], K. Schäffner [c], J. Schieck [f,g] V. Schipperges [h], S. Schönert [d], W. Seidel [a,‡], M. Stahlberg [f,g] L. Stodolsky [a], C. Strandhagen [h], R. Strauss [a], A. Tanzke [a], H.H. Trinh Thi [d] C. Türkoğlu [f] M. Uffinger [h], A. Ulrich [d], I. Usherov [h], S. Wawoczny [d], M. Willers [d], M. Wüstrich [a], A. Zöller [d]

[a] *Max-Planck-Institut für Physik, 80805 Munich, Germany*
[b] *Departamento de Fisica, Universidade de Coimbra, 3004 516 Coimbra, Portugal*
[c] *Laboratori Nazionali del Gran Sasso, 67010 Assergi, Italy*
[d] *Technische Universität München, Physik Department, 85747 Garching, Germany*
[e] *also at Walther-Meißner-Institut für Tieftemperaturforschung, 85748 Garching, Germany*
[f] *Institut für Hochenergiephysik der Österreichischen Akademie der Wissenschaften 1050 Wien, Austria*
[g] *Atominstitut, Vienna University of Technology, 1020 Wien, Austria*
[h] *Eberhard-Karls-Universität Tübingen, 72076 Tübingen, Germany*
[i] *University of Oxford, Department of Physics, Oxford OX1 3RH, UK*
[j] *also at GSSI-Gran Sasso Science Institute, 67100 LAquila, Italy*
[†] *Spokesperson, e-mail address: petricca@mpp.mpg.de*
[‡] *Deceased*

Abstract

The CRESST experiment is searching for dark matter particles via their elastic scattering off nuclei in a target material. The CRESST target consists of scintillating $CaWO_4$ crystals which are operated as cryogenic calorimeters at millikelvin temperatures and read out by transition edge sensors. Each interaction in the $CaWO_4$ target crystal produces a phonon signal and also a light signal that is measured by a secondary cryogenic calorimeter. The low energy thresholds of these detectors, combined with the presence of light nuclei in the target material, allow to probe the low-mass region of the parameter space for spin-independent dark matter-nucleon scattering with high sensitivity.

1   Introduction

In this era of precision cosmology we know that ordinary matter constitutes less than 5% of the matter in the Universe [1] the remaining 95% is divided by Dark Matter ($\sim$ 27 %) and Dark Energy ($\sim$ 68 %). Despite its large abundance, the nature, the origin, and the composition of Dark Matter (DM) is still unknown. Unraveling this problem is one of the major challenges of modern physics. Direct DM searches exploit a great variety of different detector technologies, all aiming to observe dark matter particles via their scattering off nuclei in their detectors. In the last few years, many direct DM projects have probed with increasing sensitivity the mass-cross section parameter space for DM-nucleus elastic scattering in the so called "WIMP mass region"[2]. Most of these experiments are suitable for DM candidates with masses $\gtrsim$ 30 GeV/c^2, where the sensitivity gain is mainly driven by the exposure. Nevertheless, a number of theoretical models favouring lighter dark matter candidates (e.g. [3, 4, 5, 6, 7]) have recently moved the interest of the community to the mass region below 10 GeV/c^2. As such light dark matter particles produce only very low-energy nuclear recoils (below keV), the challenge for their detection is to achieve a sufficiently low threshold in terms of recoil energy, with enough background discrimination at these low energies. Cryogenic experiments currently provide the best sensitivity for light dark matter particles, with the CRESST-III [30] experiment exploring the sub-GeV/c^2 dark matter particle mass regime.

2   Detector principle

Cryogenic detectors are low-temperature ($\sim$ 10 - 20 mK) calorimeters that measure the energy deposited in an absorber material by an interacting particle as an increase of temperature in an appropriate temperature sensor. Experiments based on this type of detectors developed strategies to distinguish background from a possible dark matter signal on an event-by-event base.

The CRESST target consists of scintillating CaWO$_4$ crystals (*phonon detectors*). Each interaction in CaWO$_4$ produces a phonon signal in the target crystal, yielding a precise energy measurement (approximately independent of the type of interacting particle), and a light signal that is measured by a secondary independent cryogenic calorimeter (*light detector*) allowing for particle identification [11, 12]. A phonon detector and the corresponding light detector form a so-called *detector module*.

Both, phonon and light detectors are read out via tungsten transition edge sensors (TES) and are equipped with a heater to stabilize the temperature in their operating point in the transition between normal and superconducting state. The heater is also used to inject pulses which are needed for the energy calibration and for the determination of the energy threshold.

3   The CRESST Setup at LNGS

The main part of the facility at LNGS is a cryostat, whose design had to combine the requirements of low temperature with those of low background. As can be seen in Fig. 1,

the dilution unit of the cryostat and the dewars containing cryogenic liquids do not extend into the experimental area.
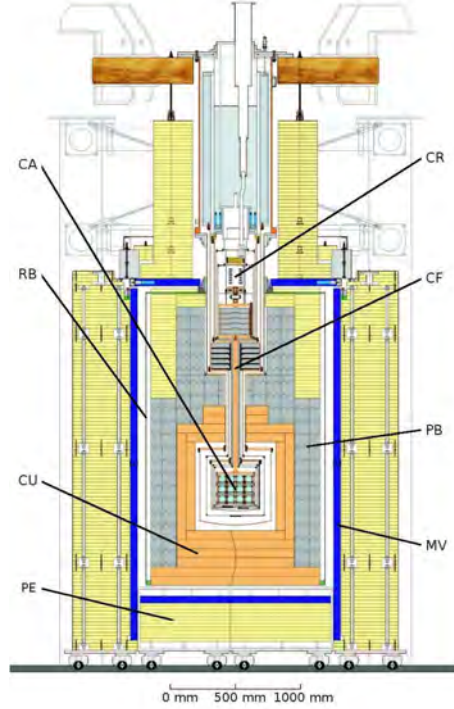

Figure 1: Schematic drawing of the CRESST setup. A cold finger (CF) links the cryostat (CR) to the experimental volume, where the detectors are arranged in a common support structure, the so called carousel (CA). This volume is surrounded by layers of shielding from copper (CU), lead (PB), and polyethylene (PE). The copper and lead shieldings are additionally enclosed in a radon box (RB). An active muon veto (MV) tags events which are induced by cosmic radiation.

The low temperatures are provided by a ^{3}He-^{4}He dilution refrigerator and transferred to the detectors via a 1.3 m long copper cold finger. The detectors are arranged in a common support structure, the so-called *carousel*, and mounted inside the *cold box* which consists of five concentric radiation shields surrounding the experimental volume and the cold finger. Two internal cold shields consisting of low-level lead are attached to the mixing chamber (~ 10 mK) and to a thermal radiation shield at ~ 77 K, respectively, in order to block any line-of-sight from the non-radio-pure parts of the dilution refrigerator to the detectors inside the cold box. The cold box is surrounded by several layers of shielding against the main types of background radiation: layers of highly pure copper and lead shield against γ-rays, while polyethylene serves as a moderator for neutrons. The inner layers of shielding are contained in a gas tight box to prevent radon from penetrating them. In addition, an active muon veto using plastic scintillator panels is installed to tag muons. The veto surrounds the lead and copper shielding and covers 98.7 % of the solid angle around the detectors, a small hole on top is necessary to leave space for the cryostat.

4 CRESST-III Detectors

The results of CRESST-II and the growing interest in the scientific community to explore DM regions different from the WIMP parameter space moved the focus of CRESST to explore the low DM mass part of the parameter space. The results from CRESST-II Phase 2 [8, 10] clearly demonstrate that the energy threshold is the main driver for exploring such region in the parameter space. This is related to the fact that the spectrum of DM interaction for a given target material becomes steeper as the mass decreases. The amount of events that drops below a given threshold thus increases for lower DM masses. As a consequence lowering the threshold of the detectors open the access to parameters space regions that are strongly suppressed for higher threshold detectors. Given the kinematics of coherent, elastic dark matter particle-nucleus scattering, extremely low thresholds of $\mathscr{O}(50 \text{ eV})$ are necessary to access dark matter particle masses of $\mathscr{O}(0.1$ GeV). In order to reach the desired threshold the CRESST-III detector layout has been optimized for low dark matter search. The new $CaWO_4$ crystal target is a cuboid of dimensions $(20\text{x}20\text{x}20)\text{mm}^3$, corresponding to a target mass of ~ 24 g, with a background level of ≈ 3 counts/(keV kg day). The thermometer design has been optimized to achieve a threshold of < 100 eV.
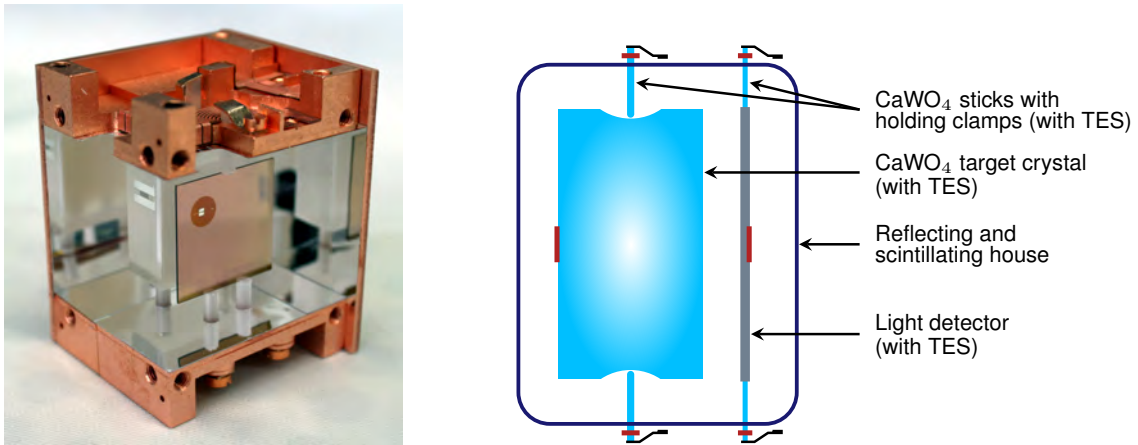

Figure 2: 24 g CRESST-III module. Left: picture of the module during preparation of Phase 1, with one of the side copper shields open. The $CaWO_4$ crystal (with the TES) and the light detector, both held by crystal sticks, are clearly visible inside the reflecting enclosure. Right : schematic sketch of the detector module.

In fig 2 a schematic view of the new CRESST module and a picture of one of the CRESST-III detectors are shown. In this optimized version of CRESST-III detector, the phonon and light detectors of each module are held by $CaWO_4$ sticks and the sticks holding the phonon detectors are equipped with TES. This novel concept for an instrumented detector holder in addition to a fully scintillating housing allow to realize a veto against events related to the crystal support. However, to minimize the need of the read out channels the sticks of each holding system are connected to a single SQUID.

4.1 Preliminary results from CRESST-III Phase 1

CRESST-III Phase 1 is an array of 10 modules, for a total mass of ~ 240 g of $CaWO_4$. Seven of these crystals are of CRESST-II quality [28] , while three are $CaWO_4$ crystal of improved quality. The latter are grown in the crystal growth facility at TUM (Technische Universität München) from raw material which was purified by an extensive chemical treatment. Each of the modules requires three read-out channels. One is connected to the phonon detector ($CaWO_4$ absorber), one to the light detector and one to the instrumented holding sticks.

The CRESST cryostat was cooled down in May 2016. The first data-taking period has started in July 2016 and since November 2016 the experiment is steadily collecting dark matter data. During October 2016 a high statistic gamma calibration has been carried out and from the end of March 2017 to half of May 2017 the dark matter data taking was interrupted again to perform a high statistic neutron calibration.

To fully exploit the potentialities of the CRESST-III modules, a data acquisition system which continuously records the detectors has been implemented, allowing the off-line application of an optimized software trigger. For CRESST-III we developed a method based on the optimum filtering technique to quantify the lowest trigger threshold achievable as a function of the acceptable amount of noise events. Applying this method, which is thoroughly described in [31], we obtain for Det-A the noise trigger rate above threshold as a function of threshold shown in fig. 3.
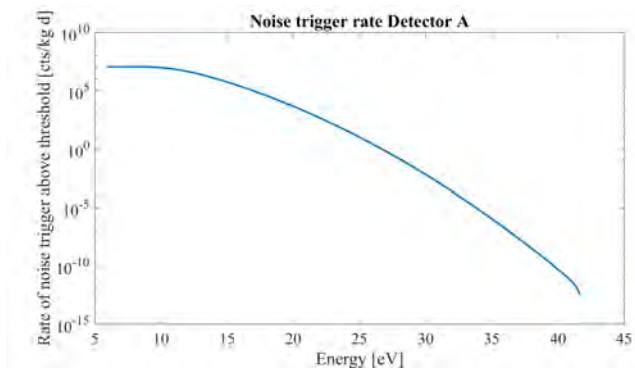
Figure 3: Noise trigger rate above threshold as function of threshold calculated for Det-A. For this detector, threshold values of 26.1 and 22.6 eV correspond respectively to 1 and 100 noise triggers per (kg day) above threshold.

This optimum filtering technique can be applied to all the other detectors and this will allow to determine the threshold for each of them. Optimum thresholds for each detector are shown in fig. 4 in which the bars identify the threshold values corresponding respectively to 1 and 100 noise triggers per (kg day) above threshold. Moreover, it can be seen that one detector has reached the design goal while the 4 other detectors have even exceeded it.

Figure 4: Thresholds evaluated for each detector using the optimum filter method. Each detector is associated to a bar which identify the threshold values corresponding respectively to 1 and 100 noise triggers per (kg day).
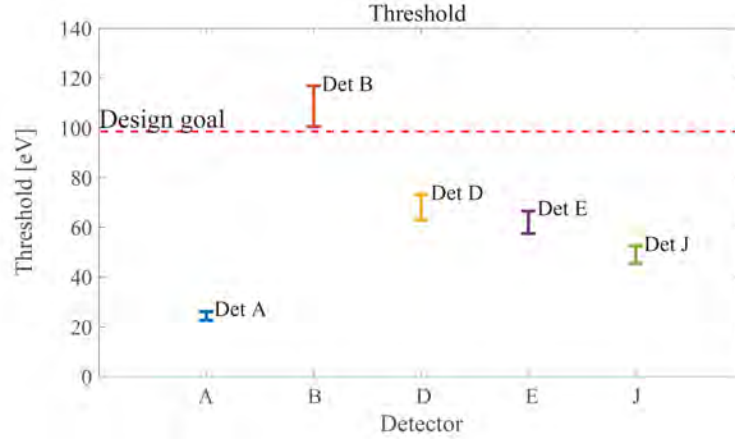
Considering the obtained thresholds the analysis started from Det-A, for which we have a total exposure of 2.39 kg days. After rate and stability cut, namely to control noise conditions and the operating point of the TES, a net exposure of 2.21 kg days is reached. For this first analysis a conservative analysis threshold of 100 eV, corresponding to the original threshold goal, was chosen.

The methods used for the analysis of the data are analogous to the ones thoroughly described and discussed in [10, 8] and references therein. A blind analysis is carried out by first defining a statistically insignificant part of the data set as a training set. Selection criteria to remove pulses for which a correct determination of the amplitude is no guaranteed are decided on the training set, not included in the final exposure, and then applied blindly without any change to the whole final data set.
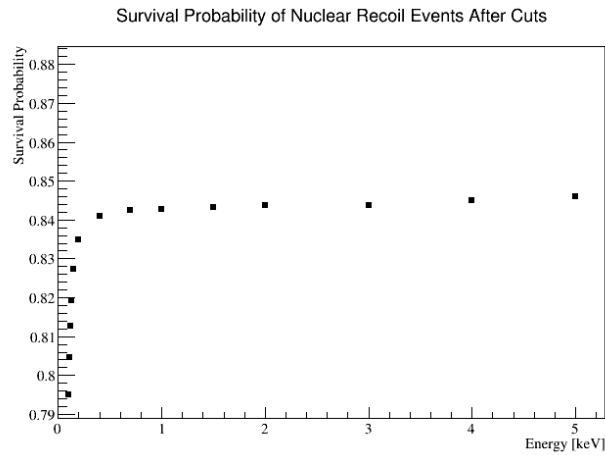

Figure 5: Cumulative signal survival probability for Det-A after all the selection criteria are applied.

For all the cuts energy dependent efficiencies are measured by applying the cuts on a set of artificial nuclear recoil events with discrete known energies created by superimposing signal templates on empty baselines periodically sampled throughout the run. the fraction of signals with a certain simulated energy passing the cuts yields the respective survival probability. In fig. 5 the cumulative signal survival probability for Det-A is shown after all selection criteria are applied. The detector has a signal survival probability of 79.5% at the analysis threshold of 100 eV.
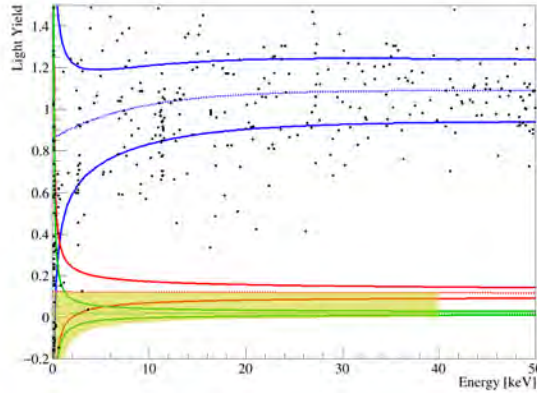

Figure 6: Det-A data in the light yield versus energy plane. The solid lines mark the 90% upper and lower boundaries of the e/γ band (blue), the band for recoils off oxygen (red) and off tungsten (green). The dark matter acceptance region is highlighted in yellow.

In fig. 6 all the events surviving the selection criteria taken with Det-A are presented in the light yield versus energy plane. The light yield is defined for every event as the ration of light to phonon signal. Electron recoils have a light yield set to one by calibration (at the calibration energy of ~ 63 keV). Nuclear recoils produce less light than electron recoils and the reduction is quantified for each target nucleus by the quenching factors, precisely known from dedicated independent measurements. In fig. 6 the solid blue lines mark the 90% upper and lower boundaries of the e^-/γ-band, with 80% of electron recoil events expected in between. From this band, with the knowledge of the quenching factors from the different nuclei present in the target material, the nuclear recoil bands for scattering off tungsten, calcium and oxygen (respectively solid green, not shown and solid red in fig. 6) are calculated analytically. The acceptance region for the dark matter analysis (yellow region in fig. 6) is defined to extend in energy between the analysis threshold of 100 eV and 40 keV and in light yield to span from the 99.5% lower boundary of the tungsten band to the center of the oxygen band, in agreement with previous analyses. The low energy spectra are shown in fig. 7: in the blue histogram all the events are considered, in the red one only the events in the acceptance region are presented. A total of 33 events are observed in the acceptance region, clustering at energies from threshold to less than 1 keV, with just one outlier at 3.7 keV. Through the Yellin optimum interval method [13, 14] a preliminary upper limit with 90% confidence level on the elastic spin-independent interaction cross section of dark matter particles with nucleons has been calculated. The exclusion limit resulting from the blind analysis reported here is drawn in solid red line in fig. 8.

.5
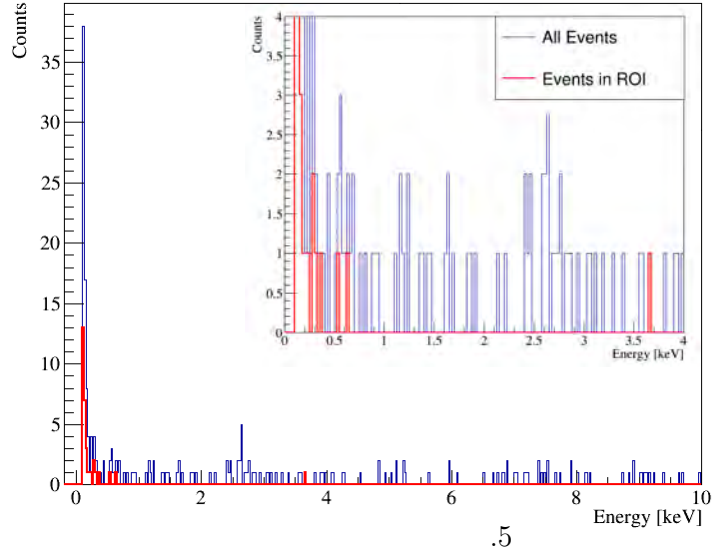
Figure 7: Low-energy spectrum of all events recorded with Det-A. The insert shows a zoom into the energy spectrum. In both the images the blue histogram shows all the events while the red histogram shows the events in the acceptance region (yellow region in fig. 6).
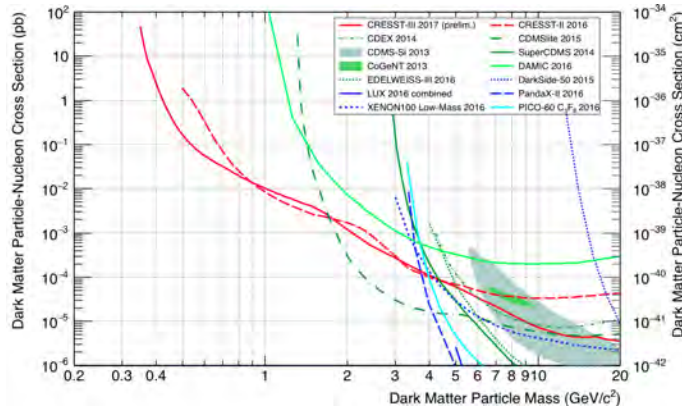
Figure 8: Parameter space for elastic spin-independent dark matter-nucleon scattering. The preliminary result from CRESST-III Phase 1 (red solid line) is compared with the limit from CRESST-II Phase 2 (red dashed line) [10]. For comparison, exclusion limits (90% C.L.) of other dark matter experiments are shown [23, 24, 22, 32, 33, 34, 35, 36, 37]. The favoured parameter space reported by CDMS-Si [17] and CoGeNT [18] are drawn as shaded regions.

Compared to the previous CRESST result [10] shown in fig. 8 as dashed red line, the reach is extended down to dark matter particle masses of 350 MeV/c^2. At 500 MeV/c^2 the cross-section sensitivity is improved by one order of magnitude while for higher masses the limit is comparable to that of the previous result, despite the very small exposure. The steep rise of the particle event rate towards lower energies observed in the acceptance

38

region below ~ 500 eV, the origin of which is presently unknown, hinders the sensitivity for low-mass searches (i.e. dark matter particle masses below $\sim$ GeV/c^2). The event at 3.7 keV is the cause of the limited sensitivity in the intermediate mass range (i.e. between ~ 1 GeV/c^2 and ~ 5 GeV/c^2). At higher masses the sensitivity scales, as expected, with exposure.

5 Conclusions and Outlook

The first results on low-mass dark matter obtained with the Phase 1 of CRESST-III confirm that a low energy threshold represents a crucial requirement for direct dark matter searches aiming to achieve sensitivity to dark matter particles with masses ~ 1 GeV/c^2 and below. With only 2.39 kg days of raw data taken with Det-A and with an analysis threshold conservatively set at 100 eV, the CRESST-III experiment improves the sensitivity of CRESST-II by one order of magnitude for a dark matter particle mass of 500 MeV/c^2 and further extends the reach of the experiment down to 350 MeV/c^2, reaffirming its leading sensitivity for light dark matter. Despite the presence of background in the acceptance region, using the full exposure of the CRESST-III experiment and further extending the lower boundary of the search energy range down to the detector threshold, a significant progress is expected in the near future in the exploration of the low mass regime.

6 List of Publications

1. F. Petricca et al., (CRESST Collaboration): First results on low-mass dark matter from the CRESST-III experiment
2017 , arXiv:1711.07692v1 [astro-ph.CO].

Acknowledgements

References

[1] P.A.R.Ade et al. (Planck Collaboration): 2014 A&A 571 A16, arXiv:1303.5076 [astro-ph.CO].

[2] P. Cushman et al.: arXiv:1310.8327 [hep-ex].

[3] T. Cohen et al.: Phys. Rev. D82 (2010) 056001, arXiv:1005.1655 [hep-ph].

[4] D. E. Kaplan et al.: Phys. Rev. D79 (2009) 115016, arXiv:0901.4117 [hep-ph].

[5] K. Sigurdson et al.: Phys. Rev. D70 (2004) 083501, arXiv:astro-ph/0406355.

[6] J. Fortin et al.: Phys. Rev. D85 (2012) 063506, arXiv:1103.3289 [hep-ph].

[7] J. Feng et al.: Phys. Lett. B 704 (2011) 534, arXiv:1102.4331 [hep-ph].

[8] G. Angloher et al., (CRESST Collaboration): Eur. Phys. J. C 74 (2014) 3184, arXiv:1407.3146[astro-ph.CO].

[9] R. Strauss et al., (CRESST Collaboration): Eur. Phys. J. C 74 (2014) 2957, arXiv:1401.3332[astro-ph.IM].

[10] G. Angloher et al., (CRESST Collaboration): Eur. Phys. J. C 76 (2016) 25, arXiv:1509.01515[astro-ph.CO].

[11] G. Angloher et al., (CRESST Collaboration): Astropart.Phys. 23 (2005) 325-339, arXiv:astro-ph/0408006.

[12] G. Angloher et al., (CRESST Collaboration): Astropart.Phys. 31 (2009) 270-276, arXiv:0809.1829[astro-ph].

[13] S. Yellin: Phys. Rev. D 66, 032005 (2002), arXiv:physics/0203002[physics.data-an].

[14] S. Yellin: Software for computing an upper limit given unknown background (02/2011) http://cdms.stanford.edu/Upperlimit/

[15] A. Brown et al.: Phys. Rev. D 85, 021301 (2012), arXiv:1109.2589[astro-ph.CO].

[16] G. Angloher et al., (CRESST Collaboration): 2012 Eur. Phys. J. C 72 (2012) 1971, arXiv:1109.0702[astro-ph.CO].

[17] R. Agnese et al., (CDMS Collaboration): Phys. Rev. Lett. 111, 251301 (2013), arXiv:1304.4279[hep-ex].

[18] C.E. Aalseth et al., (CoGeNT Collaboration): Phys. Rev. D 88, 012002 (2013), arXiv:1208.5737[astro-ph.CO].

[19] P. Agnes et al., (DarkSide Collaboration): Phys. Lett. B 743 (2015) 456-466, arXiv:1410.0653[astro-ph.CO].

[20] D.S. Akerib et al., (LUX Collaboration): 2014 Phys. Rev. Lett. 112, 091303 (2014), arXiv:1310.8214[astro-ph.CO].

[21] E. Aprile et al., (XENON100 Collaboration): Phys. Rev. Lett. 109, 181301 (2012), arXiv:1207.5988[astro-ph.CO].

[22] Q. Yue et al., (CDEX Collaboration): Phys. Rev. D 90 (2014) 091701, arXiv:1404.4946[hep-ex].

[23] R. Agnese et al., (SuperCDMS Collaboration): accepted for publication in Phys. Rev. Lett. (2015), arXiv: 1509.02448[astro-ph.CO].

[24] R. Agnese et al., (SuperCDMS Collaboration): Phys. Rev. Lett. 112, 241302 (2014), arXiv:1402.7137 [hep-ex].

[25] J. Barreto et al.: Physics Letters B 711 (2012) 264-269, arXiv:1105.5191 [astro-ph.IM].

[26] E. Armengaud et al., (EDELWEISS Collaboration): Phys. Rev. D 86 (2012) 051701, arXiv:1207.1815[astro-ph.CO].

[27] A. Gütlein et al., (CRESST Collaboration): Astropart. Phys. 69 (2015) 44-49, arXiv:1408.2357[hep-ph].

[28] A. Munster et al., (CRESST Collaboration) Jou. Cosm. and Astropar. Phys. 5 Article Number: 018 (2014)

[29] G. Angloher et al. [CRESST Collaboration], arXiv:1503.08065 [astro-ph.IM].

[30] F. Petricca et al., (CRESST Collaboration): 2017 , arXiv:1711.07692v1[astro-ph.CO].

[31] M. Mancuso et al. 2017 A method to define the energy threshold depending on noise level for rare event searches, arXiv:1711.11459 [physics.ins-det].

[32] A. Aguilar-Arevalo et al. (DAMIC Collaboration), Phys. Rev. D **94** (2016) no.8,

082006 doi:10.1103/PhysRevD.94.082006 [arXiv:1607.07410 [astro-ph.CO]].

[33] P. Agnes *et al.* [DarkSide Collaboration], Phys. Lett. B **743** (2015) 456 doi:10.1016/j.physletb.2015.03.012 [arXiv:1410.0653 [astro-ph.CO]].

[34] A. Tan *et al.* [PandaX-II Collaboration], Phys. Rev. Lett. **117** (2016) no.12, 121303 doi:10.1103/PhysRevLett.117.121303 [arXiv:1607.07400 [hep-ex]].

[35] L. Hehn *et al.* [EDELWEISS Collaboration], Eur. Phys. J. C **76** (2016) no.10, 548 doi:10.1140/epjc/s10052-016-4388-y [arXiv:1607.03367 [astro-ph.CO]].

[36] D. S. Akerib *et al.* [LUX Collaboration], Phys. Rev. Lett. **118** (2017) no.2, 021303 doi:10.1103/PhysRevLett.118.021303 [arXiv:1608.07648 [astro-ph.CO]].

[37] E. Aprile *et al.* [XENON Collaboration], Phys. Rev. D **94** (2016) no.9, 092001 Erratum: [Phys. Rev. D **95** (2017) no.5, 059901] doi:10.1103/PhysRevD.94.092001, 10.1103/PhysRevD.95.059901 [arXiv:1605.06262 [astro-ph.CO]].

CUORE

C. Alduino,[1] K. Alfonso,[2] F. T. Avignone III,[1] O. Azzolini,[3] M. Balata,[4] G. Bari,[5] F. Bellini,[6,7] G. Benato,[8]
A. Bersani,[9] M. Biassoni,[10] F. Bragazzi,[9] A. Branca,[11,12] C. Brofferio,[13,10] C. Bucci,[4] C. Bulfon,[7] A. Caminata,[9]
A. Campani,[14,9] L. Canonica,[15,4] X. G. Cao,[16] S. Capelli,[13,10] M. Capodiferro,[7] L. Cappelli,[8,17,4]
L. Cardani,[7] M. Cariello,[9] P. Carniti,[13,10] N. Casali,[7] L. Cassina,[13,10] R. Cereseto,[9] G. Ceruti,[10] A. Chiarini,[5]
D. Chiesa,[13,10] N. Chott,[1] M. Clemenza,[13,10] S. Copello,[14,9] C. Cosmelli,[6,7] O. Cremonesi,[10,*] R. J. Creswick,[1]
J. S. Cushman,[18] A. D'Addabbo,[4] D. D'Aguanno,[4,19] I. Dafinei,[7] C. J. Davis,[18] F. Del Corso,[5] S. Dell'Oro,[20]
M. M. Deninno,[5] S. Di Domizio,[14,9] M. L. Di Vacri,[4,21] V. Dompè,[4,22] A. Drobizhev,[8,17] G. Erme,[4,19]
D. Q. Fang,[16] M. Faverzani,[13,10] E. Ferri,[13,10] F. Ferroni,[6,7] S. Finelli,[5] E. Fiorini,[10,13] M. A. Franceschi,[23]
S. J. Freedman,[17,8,†] B. K. Fujikawa,[17] R. Gaigher,[10] A. Giachero,[13,10] L. Gironi,[13,10] A. Giuliani,[24]
L. Gladstone,[15] P. Gorla,[4] C. Gotti,[13,10] C. Guandalini,[5] M. Guerzoni,[5] M. Guetti,[4] T. D. Gutierrez,[25] K. Han,[26]
K. M. Heeger,[18] R. Hennings-Yeomans,[8,17] H. Z. Huang,[2] M. Iannone,[7] L. Ioannucci,[4] J. Johnston,[15] G. Keppel,[3]
Yu. G. Kolomensky,[8,17] A. Leder,[15] C. Ligi,[23] K. E. Lim,[18] Y. G. Ma,[16] L. Marini,[14,9] M. Martinez,[6,7,27]
R. H. Maruyama,[18] R. Mazza,[10] Y. Mei,[17] N. Moggi,[28,5] S. Morganti,[7] S. S. Nagorny,[4,22] T. Napolitano,[23]
M. Nastasi,[13,10] S. Nisi,[4] C. Nones,[29] E. B. Norman,[30,31] V. Novati,[24] A. Nucciotti,[13,10] I. Nutini,[4,22]
T. O'Donnell,[20] D. Orlandi,[4] J. L. Ouellet,[15] C. E. Pagliarone,[4,19] M. Pallavicini,[14,9] V. Palmieri,[3]
L. Pattavina,[4] M. Pavan,[13,10] R. Pedrotta,[11] A. Pelosi,[7] M. Perego,[10] G. Pessina,[10] C. Pira,[3] S. Pirro,[4]
S. Pozzi,[13,10] E. Previtali,[10] A. Puiu,[13,10] F. Reindl,[7] C. Rosenfeld,[1] C. Rossi,[9] C. Rusconi,[1,4] M. Sakai,[2]
S. Sangiorgio,[30] D. Santone,[4,21] B. Schmidt,[17] N. D. Scielzo,[30] V. Singh,[8] M. Sisti,[13,10] D. Speller,[18]
F. Stivanello,[3] L. Taffarello,[11] L. Tatananni,[4] F. Terranova,[13,10] M. Tessaro,[11] C. Tomei,[7] M. Vignati,[7]
S. L. Wagaarachchi,[8,17] J. Wallig,[32] B. S. Wang,[30,31] H. W. Wang,[16] B. Welliver,[17] J. Wilson,[1] K. Wilson,[1]
L. A. Winslow,[15] T. Wise,[18,33] L. Zanotti,[13,10] C. Zarra,[4] G. Q. Zhang,[16] S. Zimmermann,[32] and S. Zucchelli[28,5]

[1]*Department of Physics and Astronomy, University of South Carolina, Columbia, SC 29208, USA*
[2]*Department of Physics and Astronomy, University of California, Los Angeles, CA 90095, USA*
[3]*INFN – Laboratori Nazionali di Legnaro, Legnaro (Padova) I-35020, Italy*
[4]*INFN – Laboratori Nazionali del Gran Sasso, Assergi (L'Aquila) I-67100, Italy*
[5]*INFN – Sezione di Bologna, Bologna I-40127, Italy*
[6]*Dipartimento di Fisica, Sapienza Università di Roma, Roma I-00185, Italy*
[7]*INFN – Sezione di Roma, Roma I-00185, Italy*
[8]*Department of Physics, University of California, Berkeley, CA 94720, USA*
[9]*INFN – Sezione di Genova, Genova I-16146, Italy*
[10]*INFN – Sezione di Milano Bicocca, Milano I-20126, Italy*
[11]*INFN – Sezione di Padova, Padova I-35131, Italy*
[12]*Dipartimento di Fisica e Astronomia, Università di Padova, I-35131 Padova, Italy*
[13]*Dipartimento di Fisica, Università di Milano-Bicocca, Milano I-20126, Italy*
[14]*Dipartimento di Fisica, Università di Genova, Genova I-16146, Italy*
[15]*Massachusetts Institute of Technology, Cambridge, MA 02139, USA*
[16]*Shanghai Institute of Applied Physics, Chinese Academy of Sciences, Shanghai 201800, China*
[17]*Nuclear Science Division, Lawrence Berkeley National Laboratory, Berkeley, CA 94720, USA*
[18]*Wright Laboratory, Department of Physics, Yale University, New Haven, CT 06520, USA*
[19]*Dipartimento di Ingegneria Civile e Meccanica,*
Università degli Studi di Cassino e del Lazio Meridionale, Cassino I-03043, Italy
[20]*Center for Neutrino Physics, Virginia Polytechnic Institute and State University, Blacksburg, Virginia 24061, USA*
[21]*Dipartimento di Scienze Fisiche e Chimiche, Università dell'Aquila, L'Aquila I-67100, Italy*
[22]*INFN – Gran Sasso Science Institute, L'Aquila I-67100, Italy*
[23]*INFN – Laboratori Nazionali di Frascati, Frascati (Roma) I-00044, Italy*
[24]*CSNSM, Univ. Paris-Sud, CNRS/IN2P3, Université Paris-Saclay, 91405 Orsay, France*
[25]*Physics Department, California Polytechnic State University, San Luis Obispo, CA 93407, USA*
[26]*INPAC and School of Physics and Astronomy,*
Shanghai Jiao Tong University; Shanghai Laboratory for Particle Physics and Cosmology, Shanghai 200240, China
[27]*Laboratorio de Fisica Nuclear y Astroparticulas,*
Universidad de Zaragoza, Zaragoza 50009, Spain
[28]*Dipartimento di Fisica e Astronomia, Alma Mater Studiorum – Università di Bologna, Bologna I-40127, Italy*
[29]*Service de Physique des Particules, CEA / Saclay, 91191 Gif-sur-Yvette, France*
[30]*Lawrence Livermore National Laboratory, Livermore, CA 94550, USA*
[31]*Department of Nuclear Engineering, University of California, Berkeley, CA 94720, USA*
[32]*Engineering Division, Lawrence Berkeley National Laboratory, Berkeley, CA 94720, USA*
[33]*Department of Physics, University of Wisconsin, Madison, WI 53706, USA*

Cryogenic Underground Observatory for Rare Events (CUORE) is an experiment which aims to achieve a half-life sensitivity of 10^{26} years for neutrinoless double beta decay ($0\nu\beta\beta$) in ^{130}Te using cryogenic bolometry. $0\nu\beta\beta$ decay is one of the most sensitive probes for physics beyond the Standard Model, providing unique information on the nature of neutrinos. With this sensitivity have started to explore the inverted hierarchy region of neutrino masses. The detector consists of a close-packed array of TeO$_2$ crystals containing $\sim$206 kg of ^{130}Te in total, which has been cooled to an operating temperature of $\sim$10 mK inside a large, dedicated cryostat.

In the enclosed report we summarize the activities of the collaboration in the past year at the Laboritori Nazionali del Gran Sasso (LNGS). It has been a singular year for CUORE. We have started the primary scientific mission of the fully operational detector. During this period, the first data were collected and the scientific results of that analysis reported; CUORE currently sets the best lower limit on the half-life of $0\nu\beta\beta$ decay in ^{130}Te.

---

[*] spokeperson
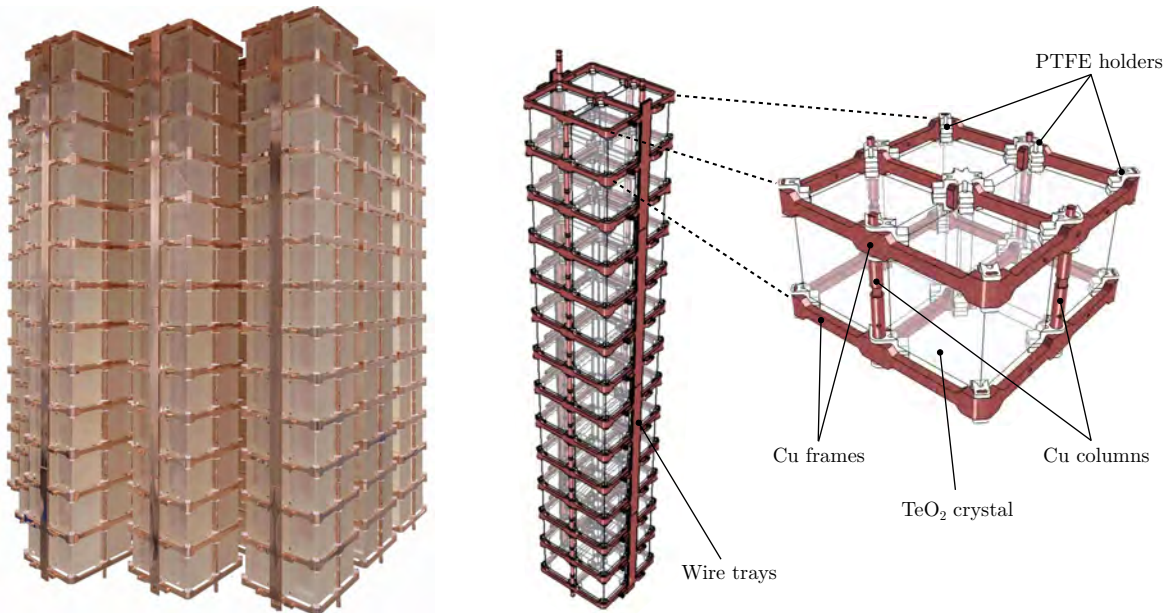[†] Deceased

I. CUORE DETECTOR OVERVIEW

FIG. 1: (Right) The completed 19-tower CUORE detector. (Left) Rendering of an individual tower with a detail of a single floor.

The CUORE detector consists of 988 ultra-radiopure TeO_2 bolometers arranged into 19 towers. Each crystal therefore serves both as source and detector of $0\nu\beta\beta$ decay in ^{130}Te. An individual CUORE tower consists of 52 crystals held inside a copper structure by Teflon (PTFE) brackets in an arrangement of 13 four-crystal floors. A picture of the assembled CUORE detector is shown in Fig. (1), together with a detailed view of an individual tower and floor.

In order to operate as a bolometer, a neutron transmutation doped (NTD) germanium thermistor and a joule heater are glued to one face of each crystal. The thermistors measure the μK-scale temperature fluctuations due to particle interactions with the crystal/absorber. The heaters deliver a fixed (and extremely precise) amount of energy to generate a pulse as similar as possible to the signal corresponding to a physical event, thus allowing to correct the detector response to the same energy deposition. These sensors are directly wire-bonded to readout ribbons held by copper trays, in turn fixed to the tower structure. All the copper components directly facing the crystals have been cleaned by following a strict protocol specifically designed and developed at the Legnaro National Laboratory (LNL). Furthermore, in order to minimize the recontamination of the components during the subsequent handling, all the towers were constructed in dedicated airtight LN_2 flushed glove boxes.

The CUORE detector cannot operate in a standard dilution refrigerator. Therefore, a custom cryogenic system had to be designed and commissioned in order to guarantee the optimal operation of the experiment for a live-time of years, satisfying a set of very stringent experimental requirements in terms of high cooling power, low noise environment and low radioactivity content.

The adopted solution consisted in a large custom cryogen-free cryostat cooled by 5 Pulse Tube refrigerators and by a high-power ^{3}He/^{4}He Dilution Unit. The CUORE cryostat comprises six nested vessels, the innermost of which encloses the experimental volume (Fig. 2). To avoid radioactive background, only a few construction materials were acceptable and over 7 tonnes of lead had to be cooled below 4 K. The different stages thermalize at about 300 K, 40 K, 4 K, 800 mK (Still), 60 mK (HEX) and 10 mK (MC). The 300 K and the 4 K vessels are vacuum-tight and enclose the Outer Vacuum Chamber (OVC) and the Inner Vacuum Chamber (IVC), respectively. The IVC contains the detector shielding lead. The lead shields include the Top Lead and the Internal Lateral and bottom Shield, the latter being made of ancient Roman lead. The Tower Support Plate holding the detector is attached to a dedicated suspension system in order to reduce the amount of vibrations and is placed right below the Top Lead. The 4 K and the 40 K vessels are externally covered with a multilayer aluminized superinsulation for the protection against thermal radiation. The IVC cool down to $\sim 50\,K$ is driven by the Fast Cooling System, which injects cold He gas inside the same IVC for a faster and more efficient cooling process. The whole cryostat is protected from the external
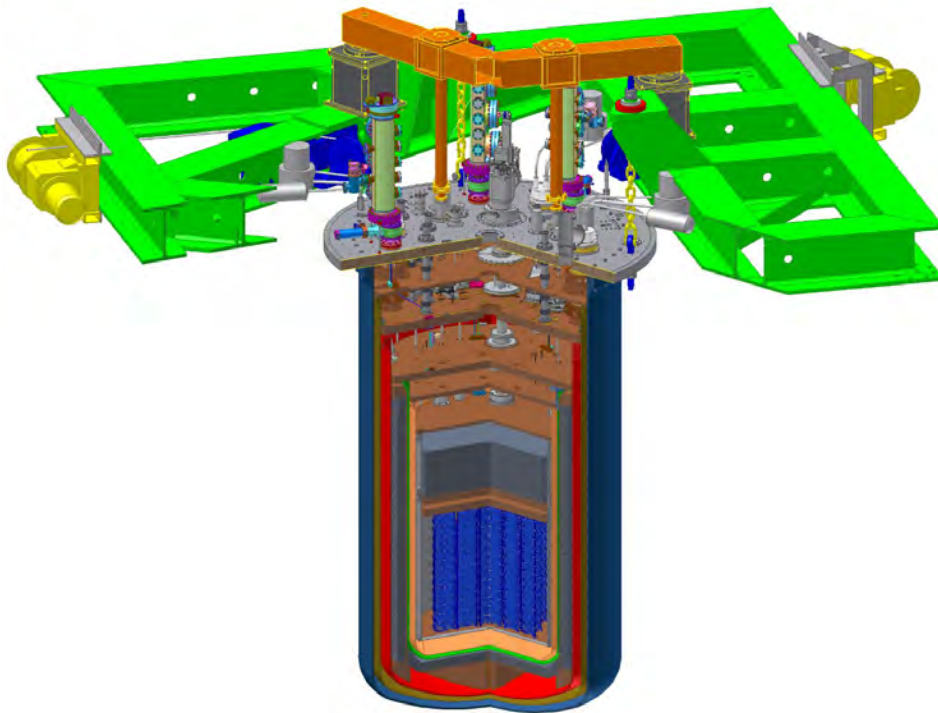
FIG. 2: Rendering of the CUORE cryostat.

radioactivity by the External Lateral and bottom Shield, a $18\,\mathrm{cm}$ polyethylene $+\ 2\,\mathrm{cm}$ $H_3BO_3 + 25\,\mathrm{cm}$ lead shield on the side and $25\,\mathrm{cm}$ lead $+\ 20\,\mathrm{cm}$ borated polyethylene shield on the bottom. In order to calibrate the detector while in operation, a dedicated system had been integrated in the cryostat, allowing for the insertion and extraction of the sources without perturbing the cryogenic environment.

II. DETECTOR CALIBRATION

The CUORE Detector Calibration System (DCS) deploys radioactive sources through the CUORE shielding and places them close to the detectors in order to calibrate each bolometer in the array. This requires moving the sources from room temperature into the $10\,\mathrm{mK}$ environment without disrupting the detector operation. Key features of this system include the active cooling through a mechanical squeezing contact at $4\,\mathrm{K}$, motion of the lightweight source string under gravity to minimize friction and frictional heating, and the construction from pure and clean materials. The detector calibration group, lead by the Yale group, completed commissioning of this system in early 2016 during Run 4 and published a detailed technical report in NIM (Nucl. Instrum. Methods A **844**, 32-44 (2017)).

After successful tests of the DCS during Run 4, we began our first calibration of the detectors in April 2017. We were able to deploy all 12 source strings, consisting of 6 inner strings between the detectors towers and 6 outer strings surrounding the detector array outside the $50\,\mathrm{mK}$ vessel, down into the cryostat to cool down the detectors. With the strings deployed, we were able to calibrate most of the detectors with only a few days of calibration time, as expected. During the year, we calibrated the detectors a total of 5 times, once before and after each dataset and once during commissioning. Each deployment took roughly 24 hours to complete after an overnight "precooling" period at the $4\,\mathrm{K}$ stage, as expected, and we observed no problems due to any thermal perturbation of the detectors during deployment (see Fig. 3). Extracting the calibration sources also went as expected, taking roughly 16 hours each time.

We did run into some issues with the calibration, namely that the gate valves between the volumes that held the source strings in between calibrations and the cryostat volume would leak upon activation. This caused some buildup of blockages in the tubes between the $300\,\mathrm{K}$ and $4\,\mathrm{K}$ volumes due to the gas freezing. While we were able to clear the blockages in most cases for the deployment of the strings, this issue became increasingly problematic. However, we were able to clear these blockages by a short warm-up of the cryostat and later replaced the leaking valves during a subsequent warm-up at the end of the year.

With the DCS, we were able to successfully calibrate the detectors after each deployment using the multiple gamma
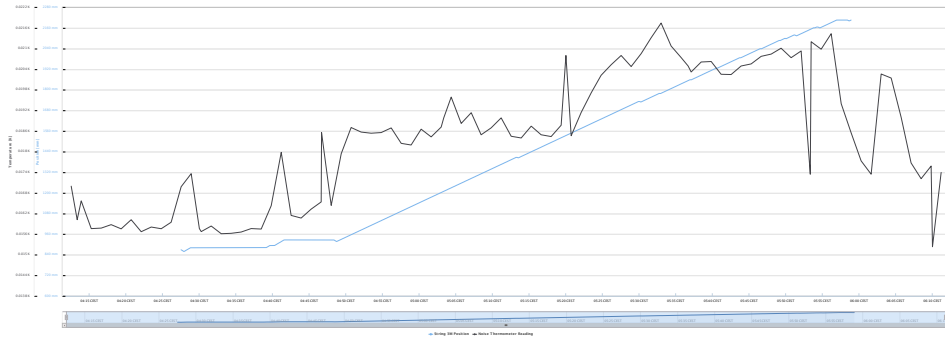
FIG. 3: Cryostat base temperature and string positions while deploying an inner string into the detector region. The blue line corresponds to the position of the source string as it is deployed, and the black line is the measurement from the noise thermometer. As we deploy inner strings, there is some heating on the crysotat which recovers quickly afterwards, so we deploy the inner strings one at a time in the detector region while moving the other strings.
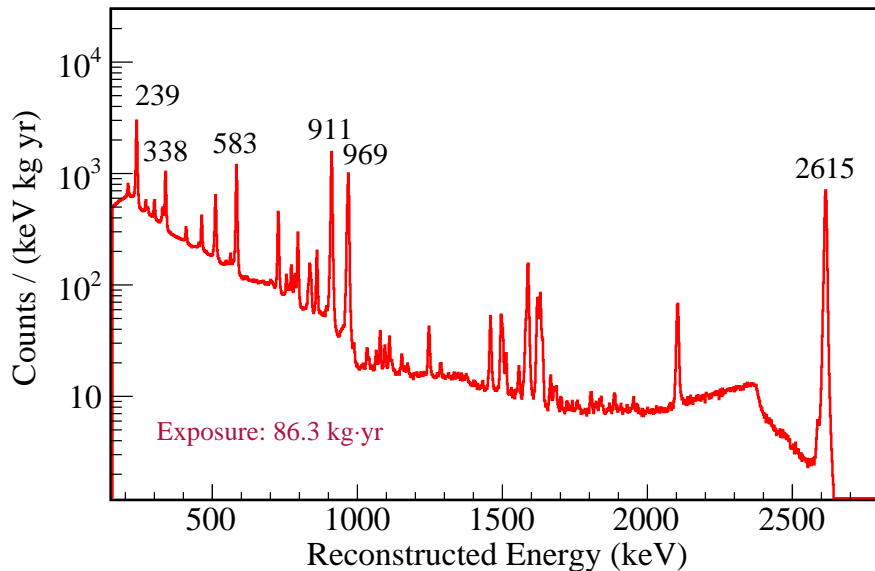

FIG. 4: Event rates for the calibration data summed over all the detectors in both datasets. By matching pulse amplitudes to the known energies of these peaks, we are able to use this calibration over a physics dataset.

peaks in the decay chain of Thorium 232, shown in Fig. 4.

III.   ELECTRONICS FRONT-END STATUS AND PERFORMANCE

The goal of the electronics is to provide an effective low-noise system for reading and monitoring CUORE detectors. It interfaces with the CUORE Data Acquisition System (DAQ) which records the data and provides a link with the slow control and data analysis tools. It was installed and is fully operative since early 2016.

Each channel consists of a chain that includes a differential voltage sensitive preamplifier, a second stage programmable amplifier and a programmable antialiasing filter. Each channel provides also the detector biasing currents. A pulser is used for detector stabilization. The amplification/biasing chains are organized in 14 racks, 78 channels per rack. Each rack contains a pair of ultra-stable and low noise linear power supplies. The pulsers are housed in 4 additional racks. The racks that include the amplification chains and the pulsers are located on the top and close to the refrigerator, inside the Faraday room, designed to shield low frequency magnetic fields. The antialiasing filters are organized in 4 additional racks in crate located just outside the Faraday cage and close to the DAQ.

The power to the whole electronics is provided by a low noise AC/DC floating system. The system ground is star-like and its center is at the DAQ. The DAQ itself is optically coupled to the computer system.

The electronics is fully programmable and monitored from the control room. The communication link is a serial CAN-bus routed on optical fibers.

Temperature stabilization of the whole detector frame is done with a Proportional Integrative (PI) SW that runs on a dedicated computer. The feedback is managed by the computer SW, which is in communication (through the optically coupled CAN-bus) with a pulser board which provides the DC output to a heater and is able to read, with 24-bit resolution, the thermometer on the detector frame. The reading/setting rate is a fraction of Hz.

IV. DATA ACQUISITION STATUS AND PERFORMANCE

The CUORE data acquisition system (DAQ) was installed in June 2016. It is composed by 64 NI-PXI-6284 digitizer boards, for a total of 1024 analog input channels. The digitizers are hosted in six PXI chassis that are contained in two rack cabinets (3 chassis each). A third rack cabinet hosts the six computers dedicated to the data readout (one per chassis) and the event builder computer. The event builder computer is also provided with communication interfaces used to control the analog components of the readout chain.

The CUORE DAQ was used intensively in 2017 showing a good performance. During the detector pre-operation and optimization phases, the automatic procedures for the characterization of the detectors (load curves resistance measurements), worked with no major problems. While they were being used, these procedures underwent some tweaking and optimization, following an iterative process with the aim of meeting the experimental needs of CUORE. Besides saving triggered events in correspondence of particle pulses, the DAQ also saves continuously the detectors' waveforms, making them accessible to the offline analysis. In calibration and physics runs the continuous data streams amount to about 120 GB/day.

V. ONLINE MONITORING

CUORE Online/Offline Run Control (CORC), developed by the University of California, Berkeley (UCB) and Lawrence Berkeley National Labs (LBNL) groups, and Slow Monitoring (SM), developed by the Massachusetts Institute of Technology (MIT) group, are high-level interfaces for monitoring the detector parameters and cryostat operations data. The underlying back-end is a Python-based web server (Pyramid) utilizing MongoDB for database storage. The last year saw many new features added to CORC and some significant code base improvements, as well as some changes to the disk format used for the database storage on the servers. For the database storage, the drive partitions on all CORC/SM machines were reformatted to XFS instead of Ext4, following MongoDB recommendations for optimal performance. Additionally a script was created that will take one of the replica set members offline periodically to perform a clone of the database for backup purposes. This script runs on the 1st and 17th of every month and 3 such back ups are kept in the event that the replica set is corrupted.

The CORC/SM page's underlying JavaScript was significantly improved as well over last year. Code in the primary files now satisfies JSHint formatting and style guides to remove potentially ambiguous or unpredictable code behavior. Additionally modern JavaScript array methods are used where possible avoiding cumbersome for-loops, and a more functional approach is taken. This provides more clarity to the code and simplifies it greatly allowing not only improved maintainability but also performance benefits. Several areas of the code were rewritten to better use the asynchronous JavaScript Promises API properly and a new charts factory was created to provide a common API for generating chart templates. Histogram computation was switched from client side to server side, greatly improving the speed of histogram generation, and allowing access to all histogram methods employed used in NumPy. In addition to code improvements, several new features were also added to CORC/SM over the last year: the ability to select portions of a run to compute summary statistics on, a towers overview page, an arbitrary time range chart for CORC variables, and an overhauled bad interval flagging page.

The ability to use an arbitrary portion of a run to compute summary statistics allows the user to view the detector colormap for subsets of the run as opposed to the whole run (e.g., the first 10 minutes vs the last 10 minutes) and can be useful for detecting changes over the duration of an entire run that may otherwise average out to an acceptable value over the course of an entire run.

The towers overview page provides 52 charts arranged in 13 rows and 4 columns (mimicking the floor and position layout of the bolometers on the run info or home pages). This provides a quick way for a shifter to examine tower-based behavior of various quantities at a glance and set appropriate bad intervals as needed. The towers page features time series, histogram and scatter plot views of various parameters. Additionally the shifter may synchronize the

charts' X or Y axes via a pair of toggle buttons allowing meaningful comparison of values across all 52 charts. This is accomplished via a custom written plugin to the Highcharts API.

The arbitrary time range plot allows the user to view a parameter across an arbitrary time range including any portion of multiple runs, allowing for long-term stability diagnostics at a glance. The interface is overhauled to include multiple checks on correct time values and to allow the user to bind time values to include specific runs, or to select an entire dataset. Additionally only valid runs are acceptable inputs to the run fields, an improvement that will be ported to other pages in the near future.

The overhauled bad interval flagging provides a pop-up modal interface for the user to more intuitively select multiple channels based on any portion and combination of tower,floor, and position. The interface allows for multiple such selections for a common bad interval and provides checks for if the user has included all channels, as well as better guards against creating an interval that has boundaries outside of the selected run. The flagging interface on the Flags page was overhauled to use a plugin called ngGrid, similar to the Runs page, and now provides pagination to avoid slowdowns from attempting to load several thousand items at once. Additionally the shifters may now edit existing flags in addition to the standard Approve/Reject options. Edited flags will be returned for approval upon successful re-submission and provide an easy way to amend an existing flag without removal and re-creation.

VI. CRYOGENY MONITOR AND CONTROL SYSTEM

CUORE Cryogeny Monitor and Control System (CMCS) is a crucial part of the whole CUORE slow control. It consists of roughly hundred LabView based Virtual Instruments (VIs), organized in a more general architecture, running on a dedicated 17 slots NI PXIe. CMCS not only acquires all the needed information coming from several different instrumentations, by dialoguing with each of them with different protocols, but also controls all the cryogenic equipment (pumps, compressor, etc.) and other vital parameters. During the year 2017, the CMCS has been regularly updated to make it more reliable, to enlarge its functionalities and monitor/control tools. For example in order to have a more robust control of the five Pulse Tubes (PTs), needed together with the Dilution Unit (DU) to keep the CUORE Cryostat at base temperature, a custom designed software (PTControl) has been developed to supervise the five PTs simultaneously on the NI PXIe. The previous configuration was running an original Cryomech software on a normal Windows OS PC, surely a less reliable option. The need to develop the PTControl was due to the fact that the Cryomech control VIs are not open access and they could not work on the PXIe that has a Real-Time OS. New diagnostic tools on the PXIe performances have been also developed and are presently running. They are monitoring the PXIe DAQ dead times, memory usage, bus status, crate modules status and CPU and hard disk performances. Finally also the Fast Cooling Monitor and Control System (FCMCS) has been updated for further use.

VII. COMPUTING INFRASTRUCTURE

We make use of six computing clusters for data analysis and Monte Carlo simulations. The Unified LNGS IT Environment (U-LITE) at LNGS is the primary computing resource for CUORE. U-LITE has 32 CPUs (64 cores) with 127 terabytes (TB) of hard disk drive (HDD) storage and 9.3 TB of fast solid-state drive (SSD) cache dedicated to CUORE. An additional 400 cores are available when not used by other experiments. CNAF, PDSF, Cori, Savio and Omega are secondary computing clusters available for Monte Carlo simulations, user analyses, code development, and other tests. The CNAF and PDSF clusters are also used to serve as backup storage for the official CUORE data. CNAF, located in Bologna, Italy, has up to 1500 cores available to CUORE and 170 TB of dedicated storage. CNAF went down in October 2017 due to a water-related accident, but it has been in recovery since March 2018. Unfortunately, this accident caused the loss of CUORE data stored at CNAF. The raw data is now in the process of being recovered from the primary repository at U-LITE. However, we did not make a backup of the data from the Monte Carlo simulations, but we are in the process of re-running the simulations. PSDF, which is part of the National Energy Research Scientific Computing Center (NERSC) located in Berkeley, California, USA, has up to 1536 cores available to CUORE and 80 TB of dedicated storage. Cori, also part of NERSC, is new a Cray XC40 supercomputer that has uses that same storage as PDSF, and CUORE has only recently taken advantage of its availability. CUORE has more than 100 TB of dedicated tape backup storage on the High Performance Storage System (HPSS) also located at NERSC. Savio is a 8040-core cluster of the University of California Berkeley, Berkeley, California, USA. So far CUORE has used Savio for re-running all the MC simulations lost on CNAF, as well as for the studies of CUORE sensitivity to $0\nu\beta\beta$ decay. The Omega cluster which has 640 cores with minimal permanent storage, is located at the Yale University in New Haven, Connecticut, USA. CUORE uses the Omega cluster exclusively for Monte Carlo simulations. The CUORE DAQ collects about 50 GB of raw data per day. The data are automatically copied from storage in the underground labs to the U-LITE computing center in the above ground labs at LNGS. From there the

collaboration begins the data analysis process. From the above ground labs the data are copied to 2 backup sites: one at the CNAF computing center in Italy and the second at NERSC HPSS in the USA.

We employ the open source relational database PostgreSQL to store and retrieve structured objects used by the data acquisition system and analysis, and the document-oriented database MongoDB to manage the diagnostics from the data analysis and the slow control. The master PostgreSQL database is located in the main surface building at LNGS and is copied, with native replication, to slave databases in the underground CUORE lab, to CNAF, and to the LBNL in Berkeley, California. The rare event where communication to the master database is lost triggers a failover and the database located in the CUORE lab becomes the master to prevent interruptions to data taking. The master MongoDB is also located in the main surface building at LNGS and is natively replicated on slave databases located in the underground CUORE lab and at LBNL with a similar failover system.

We use the version control system `Git` to manage the source code for CUORE data acquisition and analysis, simulations, control systems, as well as drafts for journal articles and reports. We host the CUORE `Git` repository on an Enterprise `GitHub` server located at the MIT that includes issue tracking and online software documentation. We have also built a website that includes both public and collaborator specific information on CUORE. The collaborator specific information includes automatically generated Doxygen software documentation, author list generators, and shift management.

VIII.   FIRST DATA FROM CUORE

The data collection is organized in runs of about one day of duration. In turn, the runs are grouped into datasets, each started and ended with a calibration and containing about one month of physics data (the data collected for the $0\nu\beta\beta$ decay).

The CUORE data taking started with dataset DS3018 at the beginning of May 2017. The detector was operated at a stable temperature of (15.0 ± 0.1) mK. The opening calibration lasted 5 days (from May 6th to May 11th), then we took physics data in a stable mode for about 24 days (until June 4th). The dataset was closed by a second calibration which lasted 4 days, from June 6th to June 10th. Dataset DS3018 was initially triggered with event windows of 5 seconds each. Later it was proven that it was possible to improve the energy resolution with event windows of 10 seconds each. Therefore, the continuous data from DS3018 were re-triggered with 10 second windows.

The final part of June and the first part of July were dedicated to the detector optimization and test runs. The data taking was retrieved at the end of July with the dataset DS3021. Again, the first and final days were devoted to the calibration (from July 30th to August 2nd and from September 4th to September 9th), while 27 days of physics data were collected (from August 4th to August 31st 2017). Given the previous experience, this second dataset was acquired directly saving event windows of 10 seconds. In addition to the longer event windows, the improved noise situation and the lower derivative trigger thresholds resulted in a better energy resolution and and higher number of channels that reached the final steps of the analysis.

In both datasets the number of active channels was 984. However, during the analysis a fraction of these had to be removed for different reasons: some of the channels where too noisy, others failed during one or more analysis steps, others did not collect a sufficient number events during the calibration and so on. In the end, after removing these problematic channels, the analysis was performed on 876 channels for dataset DS3018 and on 935 channels for dataset DS3021. Accordingly the contribution from these channels was also removed from the exposure computation yielding an exposure of TeO_2 of 37.6 kg·yr for dataset DS3018 and of 48.7 kg·yr for dataset DS3021, obtaining a total exposure of 86.3 kg·yr, more than twice the exposure of CUORE-0.

IX.   DETECTOR CHARACTERIZATION AND OPTIMIZATION

Few months during the CUORE operations in 2017 were devoted to the detector characterization and optimization. The first rough optimization occurred before the first dataset; the second period dedicated to the signal optimization was in July 2017, between the first and the second dataset. The latest optimization period occurred during fall 2017, after the end of the first data taking period, in preparation for the data taking in 2018.

The optimization consists in the tuning of all the detector parameters and the control of those environmental conditions on which we can act, keeping in mind that the final goal is to maximize the sensitivity which depends, among other factors, on the energy resolution and on the live time. We can indeed tune the detector in order to minimize the probability of having periods of unstable data taking, and at the same time improving the energy resolution.

The factors concurring to the worsening or improving of the energy resolution are countless, but most of them concur to the Signal To Noise Ratio (SNR). A bad SNR is partially due to noise sources such as electronic noise and

mechanical vibrations induced on the systems and partially due to detector parameters such as the voltage chosen to bias the sensors and the operational temperature. A good SNR allows to correctly evaluate the signal amplitude, thus obtaining a good energy resolution.

Among the factors that highly influence the quality of the data we can also find the derivative trigger thresholds and other electronics and DAQ settings. In fact, despite the experience with CUORE-0, we are dealing with a totally new system, hence the first few months were dedicated to a better understanding of the detector itself. These studies lead to a significant improvement of the data quality during the first few months after the CUORE cool down.

A. Operational temperature

Temperature scans around base temperature were performed to choose the one that optimizes the signal and at the same time allows to work with the designed NTD resistance of $\approx 100\ M\Omega$. For each temperature, a subset of channels - 3 towers - were considered for the analysis. Each one has NTDs belonging to different (neutron implantation) batches. Three temperature scans were performed: one in early March 2017 (from 9 mK to 16 mK), one in July 2017 (from 11 mK to 27 mK) and one in September 2017 (from 11 mK to 19 mK).

The first aimed to identify the working temperature and the second was perfomed to cross-check the initial choice, after some improvement on the noise and on the data-analysis software were done. From the analysis of the resolution on the baseline and on the pulsers, and the NTD resistance at working point in the first two scans, there was an hint that we could improve the resolution by working at a low temperature. However, the average NTD resistances at the working point get to values above hundreds of $M\Omega$, far off the designed value, while at higher temperatures the NTD resistances decrease to the designed range. In order to find a compromise between good resolution and NTD resistances values at working point that would well match the status of the readout electronics, the working temperature was initially set at 15 mK for the CUORE initial data-taking.
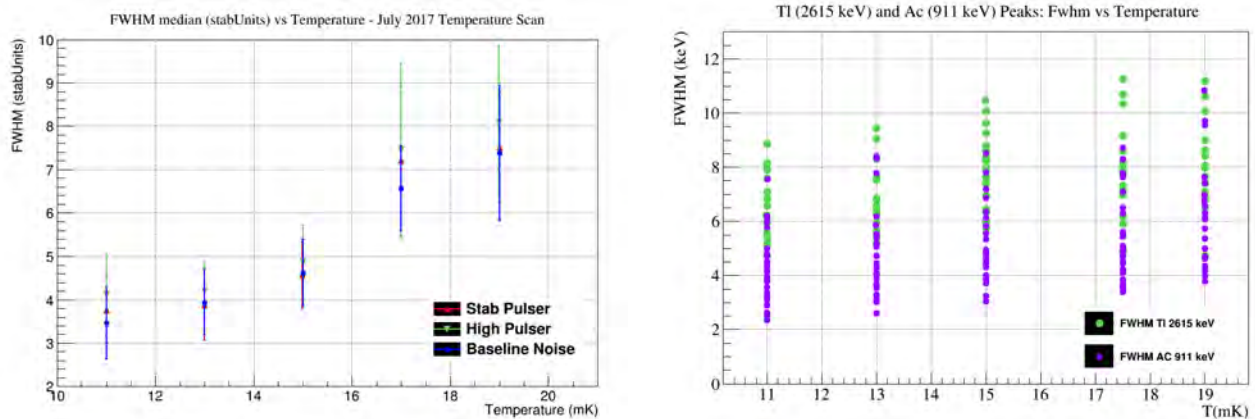

FIG. 5: (Left) Pulsers and baseline resolution (median values) in 11-19 mK temperature range. Note that the FWHM is in amplitude arbitrary units. (Right) Resolution in 11-19 mK temperature range for particle signals from Tl 2615 keV and Ac 911 keV γ lines. FWHM is in keV; each point in the plot for a given temperature corresponds to the resolution of a single channel in the three tower considered.

The third temperature scan was performed with the calibration sources deployed in order to study the resolution variation with temperature on physics events from the calibration γ lines of Tl (2615 keV) and Ac (911 keV).

Fig.5 (Left) shows the pulser and baseline resolution in the second temperature scan while Fig.5 (Right) shows the spectral line resolution during calibration in the third temperature scan. The third temperature scan confirmed indeed that lower temperatures lead to a better energy resolution for particle signals, with an average improvement of $\approx 15\%$ from 15 mK to 11 mK. For this reason the next data taking will happen at an operational temperature of 11 mK. Since the NTD working resistances at 11 mK will be higher (reaching the $G\Omega$) than the nominal values proposed for CUORE, care would be taken in setting NTDs operating conditions which would ensure a stable and uniform response in a wide energy range.

B. Load curves

For the operation of the NTDs as bolometric sensors, the application of the correct bias voltage is crucial. For this purpose, it is necessary to acquire special runs that allow to study the variation of the NTD resistance, signal amplitude and baseline noise as a function of the applied voltage. During these runs the bias voltage is varied and for each voltage configuration a fixed number of noise and pulser events are acquired.

The main goal of this procedure is to measure the characteristic I-V curve (called load curve) of the detectors. An example of load curve for one of the CUORE channel is reported in Fig. 6. From the load curve plots, it be seen that the maximum of the amplitude of the heater signals does not correspond to the same bias for which the baseline RMS gets to its minimum; this is due to competitive processes in the channel response that lower the noise for higher bias (lower NTD resistance) but at the same time reduce the thermal gain of the bolometer when more power is injected. The chosen working point is the bias voltage identified along the load curve such that it corresponds to the best SNR, which is a compromise of maximizing the signal amplitude and minimizing the noise.

Moreover we must pay attention in choosing a polarization voltage which sits at a safe distance from the inversion point of the load curve: in fact an excessive proximity to the inversion could cause pulse deformations and instabilities in the measured signal, therefore loosing the uniformity and linearity of the channel response.

For each temperature for which we want to operate, a load curve scan has to be performed in order to identify and set the NTD polarization bias to the optimal working point for each active channel.

A dedicate set of load curve runs has been taken at $15\,\mathrm{mK}$ before the beginning of the first dataset (late April 2017), to set the working points for DS3018 and DS3021, and at $11\,\mathrm{mK}$ (late December 2017) in order to choose the correct bias for the next data taking period.
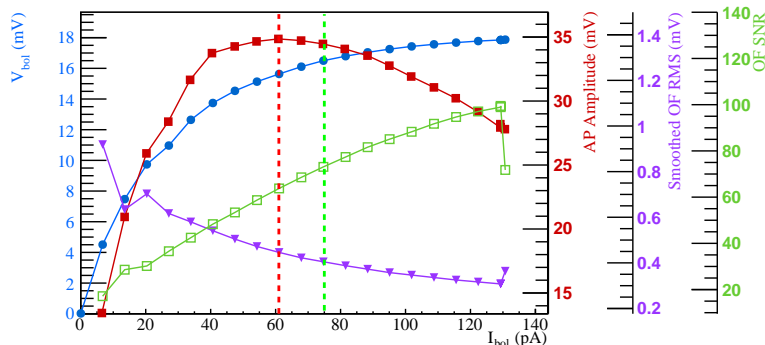

FIG. 6: Example of load curve for one of the CUORE channels: the red dotted line marks the voltage corresponding to the maximum amplitude of the signal while the green dotted line identifies the chosen working point.

C. Trigger thresholds

Given the low sampling frequency, CUORE exploits an online derivative trigger whose role is identifying particle induced pulses at all energies.

CUORE bolometers have a variety of behaviors, thus their characteristic noise is often very different. This is the reason why the parameters of the derivative trigger algorithm (in particular the thresholds) must be tuned channel by channel with an automated procedure based on the characteristic noise of the bolometer itself. The selection of the derivative trigger thresholds has been done before each one of the datasets used in the first CUORE $0\nu\beta\beta$ analysis.

Few test runs were acquired after setting the derivative trigger parameters to check the trigger efficiency for each channel. These runs are characterized by multiple heater pulses at different amplitudes in the low energy part of the spectrum. In this case we adopt a configuration with 8 different pulser amplitudes from few keV to about $1000\,\mathrm{keV}$, each one repeated in average 12 times during the duration of the run ($\sim 14\,\mathrm{hours}$). As a figure of merit for the quality of energy thresholds we used the energy corresponding at the 90% of the trigger efficiency.

Finally all the values calculated for the energy threshold at 90% trigger efficiency can be collected in the distribution of Fig. 7. This distribution gives a quantitative idea of the overall goodness of the energy thresholds. Particularly relevant is that most of the channels have an energy threshold below $150\,\mathrm{keV}$, value that has been chosen as analysis threshold during the analysis of the first two datasets.

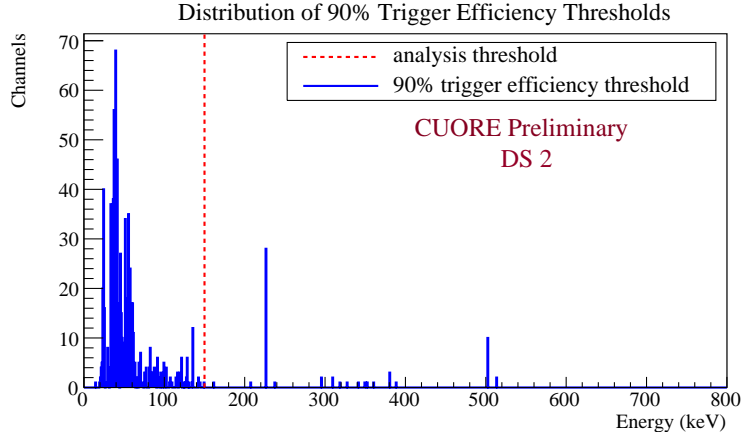Distribution of 90% Trigger Efficiency Thresholds

FIG. 7: Derivative trigger thresholds at 90% trigger efficiency for DS3021.

D. PT phase scan and noise cancellation

The Pulse Tube (PT) cryorefrigerators are one of the main source of vibrations, which are transmitted to the detector through the cryostat. The movement of the PTs rotating valves induce indeed a vibration on the cryostat at $1.4\,\mathrm{Hz}$ and its harmonics.

The superposition of these vibration frequencies emitted by the active PTs, combined with the complexity of cryostat suspension system, creates an interference pattern whose main components are modulated with periodicity as short as few tens of seconds, up to several hours. In Fig. 8 (Left) the amplitude of the most prominent noise components of one bolometer, due to the PTs is shown as a function of time: it can be noticed that the amplitude of each component modulates in time. This noise is particularly dangerous because its typical frequencies are in the same range of the signal induced by particle interactions (from 1 to $10\,\mathrm{Hz}$). In addition to a series of countermeasures adopted in order to mechanically decouple the detector from the PTs, a new custom software has been developed in order to control the velocity of the PT rotating valve, thus controlling the frequency of the induced noise. This allowed to perform a stabilization in time of the noise and to cancel out the most prominent noise contributions. Fig. 8 (Right) shows the amplitude of the main noise contributions due to the PTs, after the stabilization, but not yet in the optimal configuration.

This technique allowed to improve the bolometers performances in term of energy resolution. The noise cancellation technique, has been applied in its first rough version to DS3018 and in its final optimized version to DS3021.
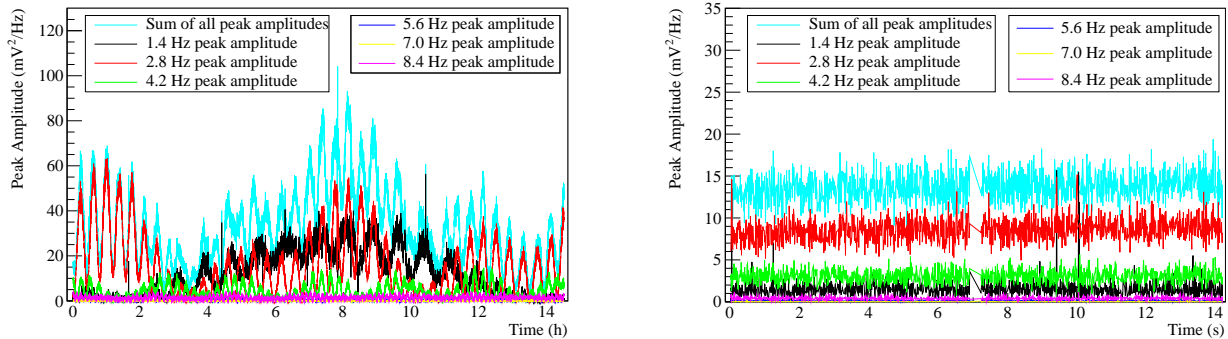

FIG. 8: (Right) Amplitude of the PT induced noise frequencies before stabilization. (Left) Amplitude of the PT induced noise frequencies after stabilization.

X. PAPERS PUBLISHED IN 2017 AND MAJOR RESULTS

In 2017, we published different physics papers with the CUORE physics results. Together with a Physical Review Letter paper presenting the first results from CUORE we published two papers related to the projected background and to the sensitivity of CUORE. These papers are detailed below in this section. Moreover, we wrote a paper presenting the analysis techniques developed to search for low energy rare events with CUORE and a paper about the possibility to study rare event processes (e.g., dark matter and axion interactions) with CUORE. Finally, we published several technical papers about CUORE related technologies and instrumentations and a physics paper related to the $2\nu\beta\beta$ analysis of the CUORE-0 data. The complete publication list is reported on Section XII.

A. First results from CUORE: A search for lepton number violation via $0\nu\beta\beta$ decay decay of ^{130}Te

This paper presents the first CUORE results referring to two month-long data collection periods which ran from May to June and August to September of 2017. By examining a total TeO$_2$ exposure of 86.3 kg yr, characterized by an effective energy resolution of (7.7 ± 0.5) keV FWHM (Fig. 9 left) and a background in the region of interest of (0.014 ± 0.002) cnts/(keV·kg·yr), we found no evidence for neutrinoless double-beta decay (Fig. 9 right). We placed a lower limit on the decay half-life of $T_{1/2}^{0\nu}(^{130}\text{Te}) > 1.3 \times 10^{25}$ yr (90% C.L.). Combining this result with those of Cuoricino and CUORE-0 experiments, we obtained the most stringent limit to date on $0\nu\beta\beta$ decay decay of ^{130}Te, $T_{1/2}^{0\nu} > 1.5 \times 10^{25}$ yr. Interpreting this result as a limit on the effective Majorana neutrino mass, we find $m_{\beta\beta} < (110 - 520)$ meV, where the range reflects the nuclear matrix element estimates employed.
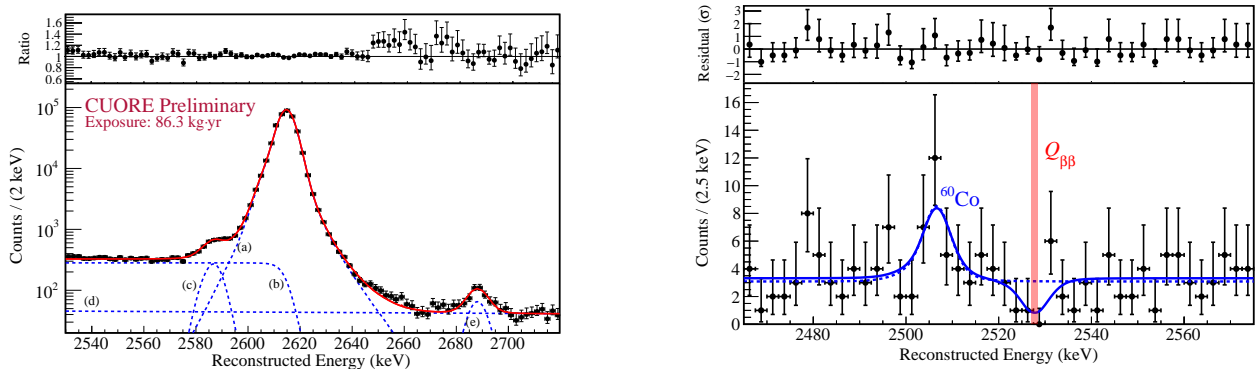

FIG. 9: Left: Fit to the 2615 keV calibration line, summed over all channels. Right: Best fit to the region of interest with residuals. This is an unbinned extended maximum likelihood fit. Each channel has a triple-Gaussian line shape with parameters determined in the fit to the 2615 keV line in the calibration spectrum.

This work was published in Physical Review Letters (PRL) and was highlighted by the editors as an Editors' Suggestion and was covered in Physics (March 26, 2018 - Physics 11, 30) along with papers from GERDA and Majorana experiments (https://physics.aps.org/articles/v11/30). Although finally published in 2018, it is reported here because it represents the culmination of the scientific work in 2017.

B. The projected background for the CUORE experiment

In this paper, published in the European Physics Journal C (EPJC), the different sources that are expected to contribute to the CUORE background are analyzed in detail. The study exploits the available data on bulk and surface contamination of CUORE construction materials and is based on the final design of the experiment. The equivalence of the CUORE and the CUORE-0 detector tower structure and materials allowed us to fully exploit the results of the CUORE-0 background model as input for the activity of all the common sources (mainly TeO$_2$ and CuNOSV bulk and surface contaminations). We developed a detailed Monte Carlo simulation to evaluate the expected background due to the various sources in the energy region where the peak signature of neutrinoless double beta decay of ^{130}Te is expected. This paper shows that the work and processes involving material selection and surface cleaning

were successful in yielding a result consistent with the CUORE target background rate of 10^{-2} cnts/(keV·kg·yr) in the region of interest (Fig. 10).
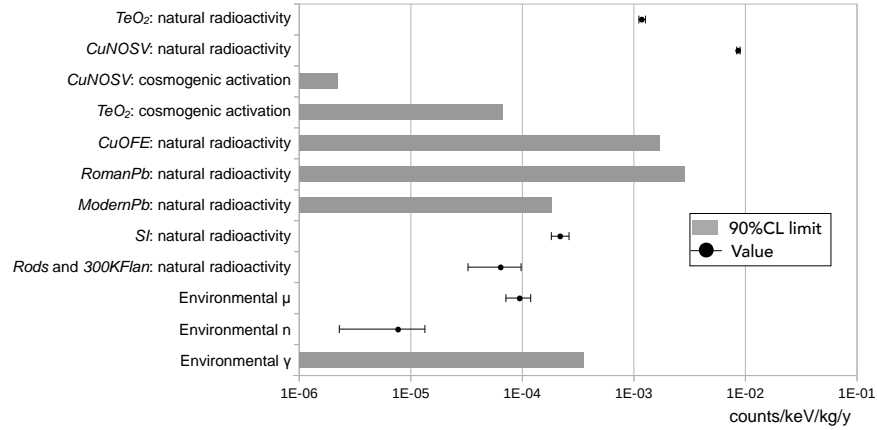
FIG. 10: Histogram representing the background rate expected in the ROI for the various components of CUORE. The grey bars indicate 90% C.L. upper limits while the dots (with 1σ uncertainties) indicate derived values. Only statistical uncertainties are indicated.

C. CUORE sensitivity to $0\nu\beta\beta$ decay decay

In this paper, published in the European Physics Journal C (EPJC), we report a study of the CUORE sensitivity to neutrinoless double beta decay. We used a Bayesian analysis based on a toy Monte Carlo (MC) approach to extract the exclusion and the discovery sensitivity to the $0\nu\beta\beta$ decay decay of ^{130}Te. We considered various background levels and energy resolutions, and analyzed the influence of the data division in subsets with different background levels. If the background level and the energy resolution meet the expectation (10^{-2} cnts/(keV·kg·yr) and 5 keV FWHM, respectively), CUORE will reach a 90% exclusion sensitivity of 9×10^{25} yr with 5 years of live time (Fig. 11). Under the same conditions, the 3σ discovery sensitivity will be 4×10^{25} yr.

FIG. 11: 90% credibility interval exclusion sensitivity for a 5 keV FWHM. The *red crosses* correspond to the median sensitivity for a background level of 10^{-2} cnts/(keV·kg·yr), while the *sm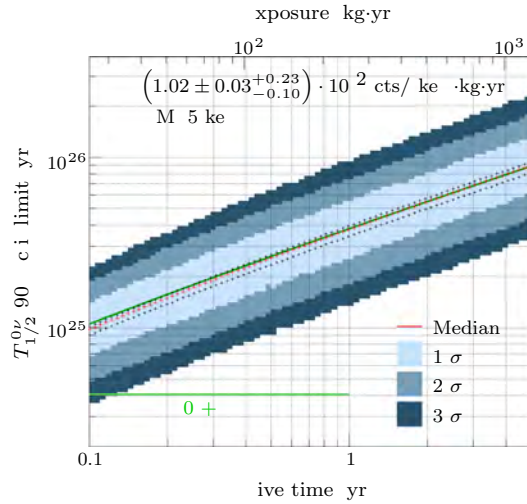aller black crosses* correspond to the median sensitivity obtained after shifting the background level up and down by an amount equivalent to its statistical and systematic uncertainty summed in quadrature. The different colored areas depict the 1σ, 2σ, and 3σ ranges of the toy-MC experiments computed for each live time. The *dark green* line shows the sensitivity estimated in a previous analysis [arXiv:1109.0494v3]. The *horizontal green line* at 4×10^{24} yr corresponds to the limit obtained with CUORE-0 and Cuoricino.

FIG. 12: (Left) Ettore Fiorini and Oliviero Cremonesi, spokesperson-emeritus and spokesperson, respectively, for CUORE cutting the ribbon at the CUORE inauguration. (Right) Carlo Bucci and Oliviero Cremonesi popping champagne in the underground lab during the inauguration Photo credit: Daniele Castri.

XI. CUORE INAUGURATION

On October 23rd, we hosted the inauguration of CUORE at LNGS. This event culminated the many-years-long work performed by members of the collaboration in order to get the first physics result from CUORE and thanked the many entities that had contributed to its success. During the event we invited scientists, media personnel, and representatives from NSF, DOE, and INFN to come to LNGS for the ceremony. The day started with a public seminar from Matteo Biassoni on the first results from CUORE which was live-streamed on the CUORE Facebook page (`https://www.facebook.com/CORECollaboration/`) and garnered nearly 700 views. Afterwards, there were remarks from the director of LNGS and representatives from INFN, DOE, and NSF, which wrapped up with comments on the history, construction, and future outlook of CUORE from multiple collaborators. The inauguration finished with a trip to the underground laboratory for a tour of the lab and the CUORE experiment with a ribbon-cutting, shown in Fig. 12 (left), followed by a short celebration with champagne, shown in Fig. 12 (right).

XII.   PUBLICATION LIST

[1] C. Alduino *et al.* (CUORE Collaboration), "Study of rare nuclear processes with CUORE", Int. J. Mod. Phys. A 33, 1843002 (2018);

[2] C. Alduino *et al.* (CUORE Collaboration), "First Results from CUORE: A Search for Lepton Number Violation via $0\nu\beta\beta$ Decay of ^{130}Te", Phys. Rev. Lett. 120, no.13, 132501 (2018);

[3] C. Alduino *et al.* (CUORE Collaboration), "Low Energy Analysis Techniques for CUORE ", Eur. Phys. J. C 77 no.12, 85 (2017);

[4] C. Alduino *et al.* (CUORE Collaboration), "CUORE sensitivity to $0\nu\beta\beta$ decay", Eur. Phys. J. C 77, no.8, 532 (2017);

[5] C. Alduino *et al.* (CUORE Collaboration), "The projected background for the CUORE experiment", Eur. Phys. J. C 77, no.8, 543 (2017);

[6] C. Alduino *et al.* (CUORE Collaboration), "Measurement of the two-neutrino double-beta decay half-life of ^{130}Te with the CUORE-0 experiment", Eur. Phys. J. C 77, 13 (2017);

[7] C. Arnaboldi *et al.*, "A front-end electronic system for large arrays of bolometers", JINST 13, no.02, P02026 (2018);

[8] K. Alfonso *et al.*, "A High Precision Pulse Generation and Stabilization System for Bolometric Experiments", JINST 13, no.02, P02029, (2018);

[9] C. Bucci *et al.*, "The Faraday room of the CUORE Experiment ", JINST 12 (2017) no.12, P12013 (2017);

[10] J. S.Cushman *et al.*, "The detector calibration system for the CUORE cryogenic bolometer array", NIMA 844, 32–44 (2017);

[11] M. Clemenza *et al.*, "Development of a multi-analytical approach for the characterization of ancient Roman lead ingots", J. Radioanal. Nucl. Chem. 311, 1495–1501 (2017);

[12] N. Moggi *et al.*, "Results from CUORE and CUORE-0", AIP Conf. Proc. 1894, 020016 (2017);

[13] D. Santone *et al.*, "The CUORE cryostat and its bolometric detector", JINST 12, no.02, C02055 (2017);

[14] L. Canonica *et al.*, "Status and prospects for CUORE", J. Phys. Conf. Ser. 888, 012034 (2017);

[15] S. Copello *et al.*, "Lowering the CUORE energy threshold", J. Phys. Conf. Ser. 888, 012047 (2017);

[16] L. Gladstone *et al.*, "The CUORE slow monitoring systems", J. Phys. Conf. Ser. 888, 012234 (2017);

[17] S Dell'Oro *et al.*, "The CUORE cryostat: a 10 mK infrastructure for large bolometric arrays", J. Phys. Conf. Ser. 888, 012235 (2017);

DAMA

Collaboration:

P. Belli[a], R. Bernabei[a,@], A. Bussolotti[a,*], R. Cerulli[a], A. Di Marco[a], V. Merlo[a], F. Montecchia[a,f], S. Ghorui[a,g], F. Cappella[b], A. d'Angelo[b], A. Incicchitti[b], A. Mattei[b,*], V.M. Mokina[b,e], V. Caracciolo[c], C.J. Dai[d], H.L. He[d], H.H. Kuang[d], X.H. Ma[d], X.D. Sheng[d], R.G. Wang[d], Z.P. Ye[d,h]

in some detector developments, by-product results and small scale experiments:

A. Addazi[i], A.S. Barabash[j], Z. Berezhiani[k,c], R.S. Boiko[e], V.B. Brudanin[l], D.M. Chernyak[e], F.A. Danevich[e], D.V. Kasperovych[e], V.V. Kobychev[e], S.I. Konovalov[j], B.N. Kropivyansky[e], M. Laubenstein[c], A. Marcianò[i], D.V. Poda[e,m], O.G. Polischuk[e], V.N. Shlegel[n], C. Taruggi[a,c], V.I. Tretyak[e], V.I. Umatov[j], Ya.V. Vasiliev[n], P. Villar[o,p], M.M. Zarytskyy[e]

[a]Dip. di Fisica, Univ. Roma "Tor Vergata" and INFN Tor Vergata, 00133 Roma, Italy.
[b]Dip. di Fisica, Univ. Roma "La Sapienza" and INFN-Roma, 00185 Roma, Italy.
[c]Laboratorio Nazionale del Gran Sasso, INFN, 67010 Assergi (Aq), Italy.
[d]IHEP, Chinese Academy of Sciences, P.O. Box 918/3, Beijing 100049, China.
[e]Institute for Nuclear Research, 03028, Kiev, Ukraine.
[f]Dip. di Ing. Civile e Ing. Informatica, Univ. Roma "Tor Vergata", 00133 Rome, Italy.
[g]Indian Institute of Technology Ropar, Ropar, India.
[h]Dep. of Physics, Jinggangshan University 343009, Jiangxi, China.
[i]Dep. of Physics & Center for Field Theory and Particle Physics, Fudan University, 200433 Shanghai, China.
[j]Institute of Theoretical and Experimental Physics, 117259 Moscow, Russia.
[k]Dip. di Fisica, Univ. L'Aquila, 67100 Coppito, AQ, Italy.
[l]Joint Institute for Nuclear Research, 141980 Dubna, Russia.
[m]CSNSM, Univ. Paris-Sud, CNRS/IN2P3, Université Paris-Saclay, 91405 Orsay, France.
[n]Nikolaev Institute of Inorganic Chemistry, 630090 Novosibirsk, Russia.
[o]Laboratorio de Física Nuclear y Astropartículas, Universidad de Zaragoza, C/ Pedro Cerbuna 12, 50009 Zaragoza, Spain
[p]Laboratorio Subterráneo de Canfranc, Paseo de los Ayerbe s.n., 22880 Canfranc Estación, Huesca, Spain
@ Spokesperson; * technical staff

Abstract

DAMA is an observatory for rare processes located deep underground at the Gran Sasso National Laboratory of the I.N.F.N. (LNGS); low background scintillators are developed and exploited. During 2017 the main experiments have been performed with: i) DAMA/LIBRA–phase2 (second phase of the second generation DAMA/LIBRA set-up with sensitive mass $\simeq 250$ kg highly radiopure NaI(Tl), upgraded in 2008, 2010 and at the end of 2012); ii) the DAMA/LXe set-up (sensitive mass: $\simeq 6.5$ kg liquid Kr-free Xenon enriched either in ^{129}Xe or in ^{136}Xe); iii) the DAMA/R&D set-up (a facility to perform relatively small scale experiments, mainly investigating double beta decay modes in various isotopes); iv) the DAMA/Ge set-up (mainly dedicated to sample measurements and to specific measurements on rare processes); some activities are also performed with the Ge-Multi, GeCris and Broad Energy Germanium detectors of the STELLA facility; v) the DAMA/CRYS set-up (a small set-up for prototype tests, detectors' qualication and small scale experiments). The main DAMA activities during 2017 are summarized in the following.

1   DAMA/LIBRA

DAMA/LIBRA (Large sodium Iodide Bulk for Rare processes) is a unique apparatus for its sensitive mass, target material, intrinsic radio-purity, methodological approach and all the controls performed on the experimental parameters (see Ref. [1, 2, 3, 4, 5, 6, 7, 8, 9, 10, 11, 12, 13, 14, 15, 16] and the 2017 publication list). It is the successor of DAMA/NaI [17, 18, 19, 20, 21, 22, 23, 24, 25, 26, 27, 28, 29], with a larger exposed mass, higher duty cycle and increased sensitivity. The main goal of DAMA/LIBRA is the investigation of the Dark Matter (DM) particles in the galactic halo by exploiting the DM model independent annual modulation signature [30, 31].

The granularity of the apparatus (25 detectors in a matrix 5×5) is an important feature to study DM and for background identification since DM particles can just contribute to events where only one of the 25 detectors fires (*single-hit* events) and not to those where more than one detector fire in coincidence (*multiple-hit* events). The apparatus has also the unique feature (as well as DAMA/NaI) that gamma calibrations are regularly performed down to the software energy threshold in the same conditions as the production runs, without any contact with the environment and without switching-off the electronics. After the phase1, at present the DAMA/LIBRA–phase2 (installed at the end of 2010) is continuosly running. The high light yield and other response features have allowed working in a safe and reliable way down to 1 keV, profiting of new photomultipliers (PMTs) of higher quantum efficiency [6] and new preamplifiers and of improvements on the electronics and DAQ. The first year was dedicated to the commissioning of the experiment.

During 2017 the data taking of a sixth full annual cycle has been carried out, analyses were progressed and a new data release foreseen during 2018.

Among the scientific goals of this running set-up we briefly mention: i) investigation with high sensitivity of the DM particle component in the galactic halo by the model independent approach known as DM annual modulation signature, with highly precise determination of the modulation parameters (which carry crucial information); ii) corollary

investigations on the nature of the candidate and on the many possible astrophysical, nuclear and particle physics scenarios; iii) investigations on other possible model dependent and/or model independent approaches to study DM particles, second order effects and some exotic scenarios; iv) improvement on the sensitivity to explore rare processes other than DM as performed by the former DAMA/NaI and DAMA/LIBRA–phase1 apparata [9, 10, 11, 29].

This requires dedicated work for reliable collection and analysis of very large exposures to reach more competitive sensitivities. As regards the DM features, see e.g. the Sect 6 of Ref. [22] and the Appendix of Ref. [2]. In particular, the latter shows how the decreasing of the software energy threshold (as in the present DAMA/LIBRA–phase2) can offer the possibility to disentangle among some of the many possible DM scenarios.

1.1 DAMA/LIBRA–phase1

The total exposure of DAMA/LIBRA–phase1 is 1.04 ton × yr in seven annual cycles; when including also that of the first generation DAMA/NaI experiment one gets 1.33 ton × yr, corresponding to 14 independent annual cycles [4].

The DAMA/LIBRA–phase1 data gave evidence for the presence of DM particles in the galactic halo, on the basis of the exploited model independent DM annual modulation signature by using highly radio-pure NaI(Tl) target, at $7.5\,\sigma$ C.L.. When including also the first generation DAMA/NaI experiment the C.L. is $9.3\,\sigma$. At present status of technology the DM annual modulation is the only model independent signature available in direct DM investigation that can be effectively exploited. All the many specific requirements of the signature are fulfilled by the data and no systematic or side reaction able to mimic the exploited DM signature is available (see e.g. Refs.[2, 3, 4, 20, 21, 22, 32, 33, 34, 35, 36, 37, 7, 8, 13] and the 2016 publication list). In addition, the compatibility with some of the scenarios available in literature and the different parameters are discussed in Refs. [21, 22, 18, 23, 24, 25, 26, 27, 28, 5, 38, 39, 14, 15], in Appendix A of Ref. [2], and in the 2017 publication list. A further large literature is available on the topics; many possibilities are open.

Various proceedings/papers about the already released DAMA/LIBRA-phase1 data have been published.

1.2 The Mirror Dark Matter analysis

Studies on DM features, second order effects, and several other rare processes are in progress with the aim to reach very high sensitivity, thanks to the progressive increasing of the exposure. In 2017 a new analysis of the DM model-independent annual modulation result obtained by DAMA/NaI and DAMA/LIBRA–phase1 in terms of mirror DM (an exact duplicate of ordinary matter from parallel hidden sector) has been published.

Two scenarios have been considered: the asymmetric Mirror DM in Ref. [15] and the symmetric one (see 2017 publication list).

In both cases, the obtained values of the $\sqrt{f}\epsilon$ (where f is the fraction of DM in the Galaxy in form of mirror atoms and ϵ is the coupling constant) parameter are well

compatible with cosmological bounds. In the analysis several uncertainties on the astrophysical, particle physics and nuclear physics models have been taken into account in the calculation.

In the framework of asymmetric mirror matter, the DM originates from hidden (or shadow) gauge sectors which have particles and interaction content similar to that of ordinary particles. It is assumed that the mirror parity is spontaneously broken and the electroweak symmetry breaking scale v' in the mirror sector is much larger than that in the Standard Model, $v = 174$ GeV. In this case, the mirror world becomes a heavier and deformed copy of our world, with mirror particle masses scaled in different ways with respect to the masses of the ordinary particles. Then, in this scenario DM would exist in the form of mirror hydrogen composed of mirror proton and electron, with mass of about 5 GeV which is a rather interesting mass range for DM particles. The data analysis in the Mirror DM model framework allows the determination of the $\sqrt{f}\epsilon$ parameter. As mentioned above, in the analysis several uncertainties on the astrophysical, particle physics and nuclear physics models have been taken into account in the calculation. The obtained values of the $\sqrt{f}\epsilon$ parameter in the case of mirror hydrogen atom ranges between 7.7×10^{-10} to 1.1×10^{-7} and they are well compatible with cosmological bounds [15]. In addition, releasing the assumption $M_{A'} \simeq 5m_p$, allowed regions for the $\sqrt{f}\epsilon$ parameter as function of $M_{A'}$, mirror hydrogen mass, obtained by marginalizing all the models for each considered scenario, have been obtained [15]; they also are well compatible with cosmological bounds.

In the symmetric mirror DM scenario (see 2017 publication list) the DM particles are expected to form bubbles in the Galaxy with diameter which could be even as the size of the solar system. The dark halo is composed by different species of mirror DM particles (different mirror atoms) and, at the present epoch, is crossing a region close to the Sun with a constant velocity, v_{halo} in the Galactic frame. The velocity distribution of the particles can be considered maxwellian; it is assumed that the halo has its own local equilibrium temperature, T. In the analysis halo temperatures in the range $10^4 - 10^8$ K have been considered. In the framework of symmetric mirror DM model (see 2017 publication list), 3 different scenarios have been considered depending on: i) the adopted quenching factors; ii) either inclusion or not of the channeling effect; iii) either inclusion or not of the Migdal effect. For each scenario, halo compositions with halo temperature in the range 10^4 - 10^8 K and halo velocity varying from -400 to +300 km/s have been considered. The results achieved for the symmetric mirror DM demonstrate that many configurations and halo models favoured by the annual modulation effect observed by DAMA correspond to $\sqrt{f}\epsilon$ values well compatible with cosmological bounds (see 2017 publication list). It is worth noting that this analysis predicts in most halo models an increase of the DM Mirror signal below 2 keV; these behaviours could be tested with the present DAMA/LIBRA-phase2.

As an example, in Figure 1, the allowed regions for the $\sqrt{f}\epsilon$ parameter as a function of v_{halo} in different scenarios are reported; in particular, the regions have been obtained by considering a composite dark halo composed by H'(20%), He'(74%), C'(0.9%), O'(5%), Fe'(0.1%) with a temperature $T = 5 \times 10^5$ K. The depicted contours correspond to different quenching factor modeling (see 2017 publication list).
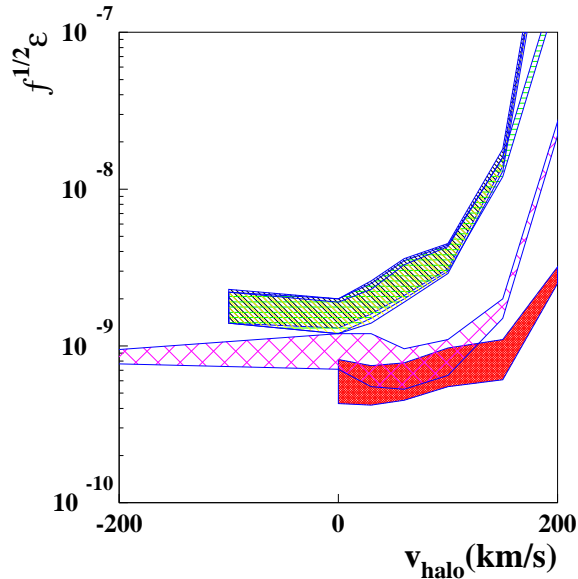
Figure 1: Symmetric Mirror Dark Matter. Example of allowed regions for the $\sqrt{f}\epsilon$ parameter as a function of v_{halo} (halo temperature $T = 5 \times 10^5$ K). The regions have been obtained by considering a composite dark halo H'(20%), He'(74%), C'(0.9%), O'(5%), Fe'(0.1%), with $v_0 = 220$ km/s and parameters in the set A of the published paper (see 2017 publication list). The five contours correspond to different quenching factor modeling.

1.3 DAMA/LIBRA–phase2 during 2017 and prospects

The upgrades performed on DAMA/LIBRA (DAMA/LIBRA–phase2) have allowed the experiment to reach a software energy threshold of 1 keV, also improving several experimental features such as e.g. the energy resolution [6].

During 2017, the data taking of DAMA/LIBRA–phase2 has continued; the 6th full annual cycle was completed and the data taking of the 7th cycle started.

The model independent data analysis of the first 6 full annual cycles of DAMA/LIBRA–phase2 has been progressed (see below Table 1). We recall that the first annual cycle was dedicated to commissioning, optimisations and data taking mainly focused to the achievement of 1 keV software energy threshold [6].

During the first 6 full annual cycles 1.3×10^8 events from sources have been collected for the energy calibrations, while 3.4×10^6 events/keV have been collected for the evaluation of the acceptance window efficiency near software energy threshold.

Some new electronic cards are in development and in test; they will allow a simplification of the electronic chain.

R&D studies towards the possible DAMA/LIBRA–phase3 are continuing; in particular, the development of new metallic PMT with high quantum efficiency has been satisfactorily carried out and some PMTs HAMAMATSU R11065-20MOD are at hand.

A multi-purpose 1 ton (full sensitive mass) set-up made of highly radio-pure NaI(Tl) was proposed in 1996 to INFN-CSN2, and the funded R&D-II, DAMA/LIBRA and R&D-III were considered as intermediate steps. As previously reported, the final design is based

Table 1: Details about the annual cycles of DAMA/LIBRA–phase2. The mean value of the squared cosine is $\alpha = \langle cos^2 \omega(t - t_0) \rangle$ an the mean value of the cosine is $\beta = \langle cos\omega(t - t_0) \rangle$ (the averages are taken over the live time of the data taking and $t_0 = 152.5$ day, i.e. June 2nd); thus, the variance of the cosine, $(\alpha - \beta^2)$, is $\simeq 0.5$ for a detector being operational evenly throughout the year.

DAMA/LIBRA–phase2 annual cycle	Period	Mass (kg)	Exposure (kg×day)	$(\alpha - \beta^2)$
1	Dec. 23, 2010 – July 29, 2011	commissioning of phase2		
2	Nov. 2, 2011 – Sept. 11, 2012	242.5	62917	0.519
3	Oct. 8, 2012 – Sept. 2, 2013	242.5	60586	0.534
4	Sept. 8, 2013 – Sept. 1, 2014	242.5	73792	0.479
5	Sept. 1, 2014 – Sept. 9, 2015	242.5	71180	0.486
6	Sept. 10, 2015 – Aug. 24, 2016	242.5	67527	0.522
7	Sept. 7, 2016 – Sept. 25, 2017	242.5	75135	0.480
DAMA/LIBRA–phase2	Nov. 2, 2011 – Sept. 25, 2017	411137 $\simeq$ 1.13 ton×yr		0.502
DAMA/NaI + DAMA/LIBRA–phase1 + DAMA/LIBRA–phase2:		2.46 ton×yr		

on the fulfilment of three additional replica of the present DAMA/LIBRA set-up and some activities were carried out in the light of related problems regarding the supplying and purifications of high quality NaI and, mainly, TlI powders and the creation of suitable protocols.

2 DAMA/LXe

In 2017 the data taking has been concluded. The set-up will be decommissioned during 2018, and the DAMA/CRYS set-up, which is presently located in an extremely small area (about 6 m^2), will be moved to the inner ground floor of the barrack. This will allow us to suitably install and operate the already built cryogenic system for DAMA/CRYS and use some components of the set-up previously available there.

Data analysis is in progress.

3 DAMA/R&D

The DAMA/R&D installation is a general-purpose low background set-up used for measurements on low background prototypes and for relatively small-scale experiments [40, 41, 42, 43, 44, 45, 46, 47, 48] and 2017 publication list.

The measurements mainly investigate 2β decay modes in various isotopes; both the active and the passive source techniques have been exploited as well as the coincidence technique. Particular attention is dedicated to the isotopes allowing the investigation of the $2\beta^+$ processes and, in particular, to resonant 2ϵ or $\epsilon\beta^+$ decay channels. The investigation of neutrino-less $2\beta^+$, 2ϵ and $\epsilon\beta^+$ processes can refine the understanding of the contribution of right-handed currents to neutrino-less 2β decay; therefore developments of experimental technique to search for 2ϵ, $\epsilon\beta^+$, and $2\beta^+$ processes are strongly required considering also that in the $2\beta^+$ investigations a gap of several orders of magnitude between theoretical expectations and experimental results is the usual situation and the better achieved sensitivities do not exceed the level of $T_{1/2} \simeq 10^{22}$ yr. Even more important motivation to search for double electron capture appears from possibility of a resonant process thanks to energy degeneracy between initial and final state of the parent and daughter nuclei. Such a resonant process could occur if the energy of transition ($Q_{2\beta}$) minus the energies of two bounded electrons on K or/and L atomic shells of daughter nucleus is near to the energy of an excited level (E_{exc}) of the daughter isotope.

Therefore, investigations on various kinds of new scintillators and preliminary works for the future measurements are also in progress within the DAMA activities.

Some of the main results during 2017 are listed in the following.

- **Investigations of 2β decay of ^{116}Cd with ^{116}CdWO$_4$ crystal scintillators (in final stage).**

  The 2β decay of ^{116}Cd has been investigated with enriched ^{116}CdWO$_4$ crystal scintillators (mass of 1162 g) over 35324 h (AURORA experiment). The half-life of ^{116}Cd relatively to the $2\nu2\beta$ decay of ^{116}Cd to the ground state of ^{116}Sn was measured with the highest up-to-date accuracy as $T_{1/2} = [2.69 \pm 0.02(\text{stat.}) \pm 0.12 \text{ (syst.)}] \times 10^{19}$ yr (one of the most accurate $2\nu2\beta$ half-life values ever measured).

  A new improved limit on the $0\nu2\beta$ decay of ^{116}Cd to the ground state of ^{116}Sn was set $T_{1/2} > 2.4 \times 10^{23}$ yr at 90% C.L., which is the most stringent known restriction for this isotope. It corresponds to the effective Majorana neutrino mass limit in the range (0.9–1.6) eV, depending on the nuclear matrix elements used in the analysis. New improved half-life limits for the different modes of $0\nu2\beta$ decay with majoron(s) emission and for the 2β transitions to the excited states of ^{116}Sn were set at the level of $T_{1/2} \simeq 10^{21} - 10^{22}$ yr. The scientific paper is under completion.

- **An experiment to search for 2β decay of ^{116}Cd to excited levels of ^{116}Sn (in preparation)**

  An experiment to search for 2β decay of ^{116}Cd to excited levels of ^{116}Sn (first of all to the 1st 0^+ 1757 keV excited level) is planned by using the highly radio-pure enriched ^{116}CdWO$_4$ crystal scintillator with mass 133 g obtained by re-recrystallization [49]. It is planned that ^{116}CdWO$_4$ scintillation detector will operate in coincidence with external gamma counters. HP Ge detectors, scintillation detectors with CdWO$_4$ crystals or some other effective radio-pure detectors can be used to detect gamma quanta expected in the transition 463 keV and 1294 keV). Then, the experiment can also profit of the higher-energy-resolution GeMulti ultra-low background HPGe gamma spectrometer.

- ^{113}**Cd and** ^{113m}**Cd beta decays (in final stage)**

  New studies of the highly forbidden ^{113}Cd and of the first forbidden ^{113m}Cd beta decays are in progress; the publication is in preparation.

- **Radioactive elements segregation in crystals (in progress)**

  Investigation to develop ultra-radio-pure scintillators for rare events searches is continuing.

- **R&D of radio-pure high quality ZnWO$_4$ for DM directionality investigations (in progress)**

  ZnWO$_4$ crystal scintillators have very interesting radio-purity [43] and a substantial dependence of scintillation response (both quenching and pulse-shape) on direction of alpha particles. This feature is expected to be also valid for heavier ions, and it can be used to search for nuclear recoils due to some particular DM candidates [50]. Four new ZnWO$_4$ crystal scintillators 50 mm in diameter and 45 mm in height (two after the first and two after the second crystallisation) were installed in the DAMA/R&D low background set-up to test the radio-purity level. The measurements and data analysis are in progress. In parallel, an R&D on deep purification methods for tungsten and on advanced quality crystals after second crystallisation is in progress in collaboration the Nikolaev Institute of Inorganic Chemistry (Novosibirsk, Russia).

- **R&D of radio-pure Gd$_2$SiO$_5$(Ce) crystal scintillators (in preparation)**

  Gd$_2$SiO$_5$(Ce) crystal scintillators, GSO(Ce), can be used to search for 2β decay of ^{152}Gd and ^{160}Gd. The ^{152}Gd is interesting due to the possibility of resonant double electron capture, while ^{160}Gd is a double beta active nucleus with one of the highest natural isotopic abundance. However, lanthanides are typically contaminated by thorium and uranium since bastnasites (minerals used to produce lanthanides) are contaminated at $\simeq 1\%$ level by uranium and thorium. We have at hand two samples of gadolinium oxide, others can be available in future, to measure radioactive contamination by actinium, since other radioactive impurities can be removed by using the methods developed in the framework of the DAMA-Kiev (Lepton Physics Department of the INR-NASU Kiev) collaboration. In case of low actinium concentration the material, after purification, can be used to produce Gd$_2$SiO$_5$(Ce) crystal scintillators for the experiment.

- **R&D of radio-pure SrI$_2$(Eu) crystal scintillators (in preparation)**

  SrI$_2$(Eu) scintillators look promising detectors to search for 2β decay of ^{84}Sr (see Ref. [51], where only 6.6 g crystal was used). SrI$_2$(Eu) scintillators show a rather high scintillation efficiency (light yield of $\simeq$ 90000 photons/MeV was reported in Ref. [52]). The idea is to develop highly radio-pure large-volume scintillators. As a first step, the purification of the europium oxide (that is expected to be the most contaminated raw material for the crystal growth) from radioactive contamination is under study, then crystal scintillators can be grown.

- **Other possible activities (in preparation)**

At the end of the present measurements, new measurements are foreseen in DAMA/-R&D; among them: developments on new enriched CdWO$_4$ depleted in ^{113}Cd, on highly radio-pure Ba compound scintillators, etc... The R&D of low background barium containing crystal scintillators to investigate double beta processes in ^{130}Ba and ^{132}Ba is continuing profiting of new scintillator detector.

DAMA/R&D is a general-purpose set-up and can assure us also in future the possibility to produce many kinds of low background measurements in an efficient way at well reduced cost.

4 DAMA/CRYS

DAMA/CRYS is a small test set-up mainly dedicated to tests on the performances of new scintillation detectors and to small-scale experiments. As mentioned above, in order to operate it more suitably and to install the already built cryogenic part, it is planned to move it in the inner part of the ground floor level of DAMA/LXe that will be dismounted during 2018 . The main activities in 2017 are briefly summarised in the following.

- **Search for the 2β decay of ^{106}Cd with the help of ^{106}CdWO$_4$ crystal scintillators (in progress)**

  An experiment to search for 2β decay of ^{106}Cd with the help of cadmium tungstate crystal scintillator enriched in ^{106}Cd at 66% (^{106}CdWO$_4$) in coincidence and anti-coincidence with two large volume CdWO$_4$ scintillation detectors in close geometry is in progress in the DAMA/CRYS set-up. The accumulated data are over 14064 hours. The possible double beta decay processes and the background components were simulated by Monte Carlo code; the data analysis is in progress. The sensitivity of the experiment is approaching the theoretical predictions for the electron capture with positron emission in ^{106}Cd: $T_{1/2} > 3 \times 10^{22}$ yr (the best previous limit was $T_{1/2} > 1.1 \times 10^{22}$ yr). The results were presented at the CNNP2017 conference in Catania, October 15-21, 2017.

- **Cryogenic system (to be installed)**

  The two parts of the cryogenic system to be installed in DAMA/CRYS (to allow also measurements of the responses of various new/improved scintillators as a function of the temperature) are ready (see comments above).

- **Realisation of high purity PbWO$_4$ crystals**

  An R&D is in progress with the Institute for Scintillation Materials ((Kyiv, Ukraine), to grow PbWO$_4$ crystals of high radio-purity and high quality light response, obtained by second recrystallisation. Archeological lead, supplied by the INR of Kiev, is used and deeply purified by the Nat. Science Center Kharkiv Institute of Physics and Technology in 2017. Among the potential applications of PbWO$_4$ crystals, there is the use e.g. as compact light-guides for experiments on rare-events, such as in case of ^{106}Cd 2β decay.

DAMA/CRYS is also a general-purpose set-up and can also assure us in future the possibility to produce many kinds of low background measurements in an efficient way at well reduced cost. Preparations of other future measurements are in progress.

5 DAMA/Ge and LNGS STELLA facility

In addition to samples measurements, the following activities have been carried out in 2017. Recent published results can be found in Ref. [53, 54, 55] and in the 2017 publication list. Improvements and preparations of other future measurements are in progress.

- **Investigation of 2β decay of ^{150}Nd to the excited levels of ^{150}Sm (in progress)**

  The experiment to search for 2β decay of ^{150}Nd to the excited levels of ^{150}Sm by using deeply purified 2.381 kg neodymium oxide samples installed in the GeMulti ultra-low background HPGe gamma spectrometer is in progress. The effect is already observed over 16375 h in coincidence with the half-life $T_{1/2} = (0.84 \, ^{+0.47}_{-0.22}) \times 10^{20}$ yr (statistical error) in agreement with the previous experiments ($T_{1/2} = 1.33^{+0.36}_{-0.23}$ (stat) $^{+0.27}_{-0.13}$ (syst)$\times 10^{20}$ yr [56] and $T_{1/2} = 1.07 \, ^{+0.45}_{-0.25}$ (stat)± 0.07 (syst)$\times 10^{20}$ yr [57]). The measurements are in progress to increase the statistics and to improve the half-life value accuracy. A paper reporting preliminary results of the experiment is in preparation.

- **Search for rare α and 2β decay of osmium isotopes (in progress)**

  The experiment to search for α decay of ^{184}Os and ^{186}Os to the first excited levels of daughter nuclei, and for 2β decay of ^{184}Os and ^{192}Os is in progress. There is an indication of α decay of ^{186}Os to the first excited level of ^{182}W with the half-life $T_{1/2} = 2.9^{+3.2}_{-1.2} \times 10^{17}$ yr, which is near to the theoretical estimations $T_{1/2} = (0.9–2.3) \times 10^{17}$ yr. Only limit ($T_{1/2} > 4.5 \times 10^{15}$ yr) is set on the half-life of ^{184}Os relatively to the α decay to the first excited level of ^{180}W. The theory predicts $T_{1/2} = (1.5–3.3) \times 10^{15}$ yr. The isotopic abundance of the ^{184}Os was accurately measured at the Curtin University (Australia) as $\delta = 0.0158(11)\%$ (2 sigma accuracy), with a precision higher than that of the Table value $\delta = 0.02(2)\%$ [58]). A next stage of the experiment is in preparation with the osmium sample placed directly inside the cryostat of the BEGe detector to improve the detection efficiency and the experimental sensitivity.

- **A first search for double beta decay of samarium, erbium and ytterbium by low background HPGe γ spectrometry (in final stage)**

  First search for 2ϵ and $\epsilon\beta^+$ decay of ^{144}Sm, ^{162}Er, ^{168}Yb and search for $2\beta^-$ decay of ^{154}Sm, ^{170}Er, ^{176}Yb to the excited levels of daughter nuclei has been realised with highly purified samarium, erbium and ytterbium oxide samples. Resonant neutrinoless double electron capture is possible in ^{164}Er, and ^{168}Yb, that makes these nuclei especially interesting. Data analysis and a paper are in preparation.

- **Purification of oxides (in progress)** The R&D of methods to purify samarium, ytterbium, erbium, europium and gadolinium oxides is in progress. Investigations on deep purification of the samples, now at hands, are continuing.

5.1 New limits on 2ϵ, $\epsilon\beta^+$ and $2\beta^+$ decay of ^{136}Ce and ^{138}Ce with deeply purified cerium sample

Cerium contains three potentially 2β active isotopes: ^{136}Ce, ^{138}Ce and ^{142}Ce. The ^{136}Ce isotope is of particular interest because it has one of the highest Q-value among the nuclides which decay $2\beta^+$.

A search for double electron capture (2ε), electron capture with positron emission ($\varepsilon\beta^+$), and double positron emission ($2\beta^+$) in ^{136}Ce and ^{138}Ce was realized with a 465 cm^3 ultra-low background HP Ge γ spectrometer over 2299 h, at the Gran Sasso underground laboratory.

Cerium oxide of 99% TREO purity grade was provided by the Stanford Materials Corporation and purified as described in [55]. However, the concentration of thorium remained rather high [55]. The contamination by thorium (along with radium) has a major impact on 2β experiments sensitivities. Thus, it was performed an additional purification of the material by using the liquid-liquid extraction method already successfully applied for a variety of rare earths purification from radioactive contamination [59]. The purification has reduced the thorium concentration in the sample by a factor of ≈ 60, that allowed to improve the sensitivity of the experiment to the 2ε, $\varepsilon\beta^+$ and $2\beta^+$ decay of ^{136}Ce by one order of magnitude (see 2017 publication list).

It should be stressed that deep purification of cerium is also motivated in the light of radio-pure crystal scintillators development. Cerium can be used to develop Ce-containing crystal scintillators (as e.g. CeF$_3$ and CeCl$_3$), and as a dopant in inorganic scintillators: Gd$_2$SiO$_5$(Ce), YAlO$_3$(Ce), LaBr$_3$(Ce), etc..

The sample of deeply purified cerium oxide with mass 627 g, encapsulated in a thin plastic container with internal sizes $\oslash 90 \times 50$ mm, was placed on the endcap of a high purity germanium (HP Ge) detector named GeCris, with an active volume of 465 cm^3, in the STELLA facility at the Laboratori Nazionali del Gran Sasso. It was used as a source of γ quanta expected in double β decay of the cerium isotopes.

The energy spectrum measured by the HP Ge detector with the CeO$_2$ sample over 2299 h is presented in Fig. 2 together with background data accumulated over 1046 h. The counting rate in the energy spectrum measured with the CeO$_2$ sample is substantially lower than that after the first stage of the material purification [55]. There is some excess in the CeO$_2$ data due to the residual contamination of the sample, mainly by radium (^{228}Ra).

The results of the CeO$_2$ sample radio-purity analysis are presented in Table 2. For the details of the analysis see 2017 publication list.

The electron capture with positron and double positron emission in ^{136}Ce should lead to the emission of annihilation γ quanta with energy 511 keV. Thus the bounds on the processes were set by analysing the annihilation γ peak in the data taking into account the 511 keV peak in the background and the contributions in this peak from the contaminants
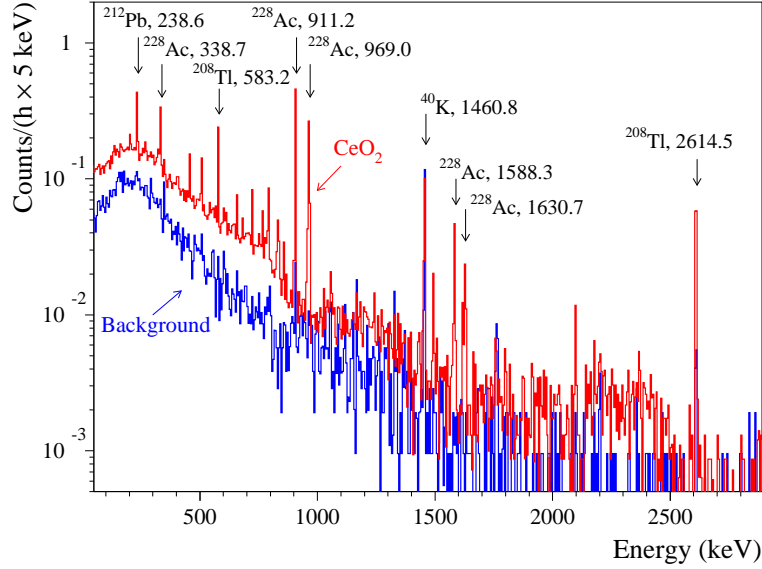
Figure 2: Energy spectra measured by the GeCris HP Ge detector with cerium oxide sample (CeO_2) over 2299 h and background accumulated over 1046 h (Background). The counting rate in the energy spectrum accumulated with the CeO_2 sample is substantially lower in comparison to the previous experiment [55] thanks to the deep purification of the material. Some excess in the CeO_2 data is mainly due to the residual contamination of the sample by radium (^{228}Ra). Energy of γ quanta are in keV.
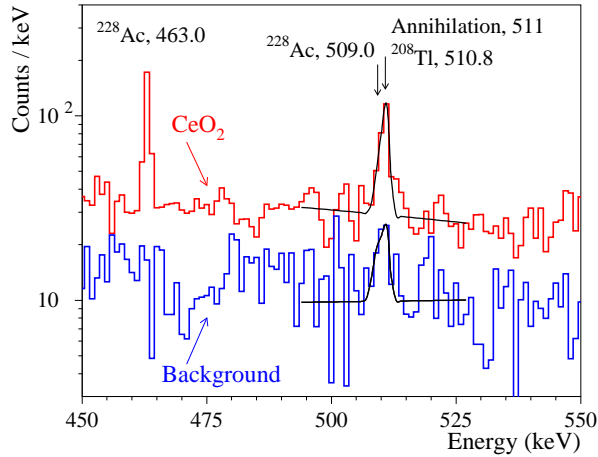

Figure 3: Energy spectrum measured with the cerium oxide sample (CeO_2) over 2299 h and background (1046 h, Background) in the vicinity of the 511 keV annihilation peak.

present in the sample. The energy spectrum measured with the CeO_2 sample and the background data in the vicinity of the annihilation peak are shown in Fig. 3.

The experiment set the best up-to-date limits on different modes and channels of double beta decay of ^{136}Ce and ^{138}Ce at the level of $T_{1/2} > 10^{17} - 10^{18}$ yr. The sensitivity of the experiment is still far from the theoretical predictions. Further improvement of the experimental sensitivity can be achieved by using enriched materials, by further reduction of the background, and by the application of cerium-containing crystal scintillators to

Table 2: Radioactive contamination of the CeO_2 before and after the two purifications. The date for the activities of the CeO_2 sample after the 2nd purification is April 12, 2016. Upper limits are at 90% C.L. and uncertainties of the measured activities are at 68% C.L.

Chain	Nuclide	Activity (mBq kg^{-1})		
		before purification [55]	after 1st purification [55]	after 2nd purification
	^{40}K	77(28)	≤ 9	≤ 4
	^{137}Cs	≤ 3	≤ 2	0.4 ± 0.2
	^{138}La	–	≤ 0.7	≤ 0.6
	^{139}Ce	–	6 ± 1	1.4 ± 0.3
	^{152}Eu	–	≤ 0.5	≤ 0.2
	^{154}Eu	–	≤ 0.9	≤ 0.08
	^{176}Lu	–	≤ 0.5	0.4 ± 0.1
^{232}Th	^{228}Ra	850 ± 50	53 ± 3	30.4 ± 0.7
	^{228}Th	620 ± 30	573 ± 17	9.8 ± 0.5
^{235}U	^{235}U	38 ± 10	≤ 1.8	≤ 0.4
	^{231}Pa	–	≤ 24	≤ 0.4
	^{227}Ac	–	≤ 3	≤ 1.4
^{238}U	^{238}U	≤ 870	≤ 40	≤ 12
	^{226}Ra	11 ± 3	≤ 1.5	≤ 0.3

increase the detection efficiency.

6 Other activities

- **Measurements of anisotropy of ZnWO$_4$ to nuclear recoils at low energy (in progress)**

In 2017 investigations on the feasibility of a directionality experiment for those DM candidates inducing just nuclear recoils have been continued; in this case the correlation of the nuclear recoils with the Earth galactic motion is exploited.

In recent years we have made extensive efforts and measurements with ZnWO$_4$ crystal scintillators, which are already interesting to investigate double beta decay of Zn and W isotopes [42, 43]. These scintillators have the particular feature to be anisotropic in the light output and in the pulse shape for heavy particles (p, α, nuclear recoils) depending on the direction with respect to the crystal axes. The response to γ/β radiation is isotropic instead. Among the anisotropic scintillators, the ZnWO$_4$ has unique features, which make it an excellent candidate for this type of research, and there is still plenty of room for the improvement of its performances. The possibility of a low background pioneer experiment to exploit deep underground the directionality approach by using anisotropic ZnWO$_4$ scintillators has been explored (see 2017 publication list).

A possible significant improvement of ZnWO$_4$ radio-purity by recrystallisation, which could be an important methodological step to advance sensitivity for the

double beta decay and DM applications (and the same procedure can be applied to $CdWO_4$ crystal scintillators too), is in progress.

In 2017 a dedicated set-up has been realised and installed at ENEA-Casaccia to quantify the anisotropy of $ZnWO_4$ crystal scintillators in the light output and in the pulse shape at keV range for heavy particles (p, α, nuclear recoils), depending on their direction with respect to the crystal axes. A neutron beam by neutron gun is used. Data are being collected at various angles. Further measurements with improved experimental performances are already scheduled.

- **Accurate measurement of the ^{212}Po half-life (in progress)**

  An experiment aiming at an accurate measurement of the ^{212}Po half-life (the Table value is $T_{1/2} = 0.299(2)$ μs) has been accomplished with the help of thorium loaded liquid scintillator and fast photomultiplier with rise time $\simeq 2$ ns. The scintillation pulse profiles have been acquired by a 3.5 GHz 40 GS/s oscilloscope. A new stage of experiment to improve the statistical error was in preparation. We expect to measure the ^{212}Po half-life with at least 2-3 times higher accuracy thanks to the fast time response of the detector. The data analysis of the first stage of the experiment is in progress.

7   Conclusions

During 2017 DAMA/LIBRA has continued to take data in the phase2 configuration and the model independent analysis of six annual cycles has been progressed.

Some new electronic cards are in development and in test; they will allow the simplification of the electronic chain.

Studies on other DM features, second order effects, and several other rare processes are in progress with the aim to reach very high sensitivity also thanks to the progressive increasing of the exposure.

Studies are under way towards possible DAMA/LIBRA–phase3 and/or DAMA/1ton (proposed since 1996).

Moreover, results on several 2β decay processes and developments on new highly radiopure scintillators for the search of rare processes have been published and are under further developments.

Finally, in 2017 all the DAMA set-ups have regularly been in data taking and various kinds of measurements have been in progress and planned for the future.

During 2017, more than 20 presentations at Conferences and Workshops (many of them by invitation) have been performed.

8 List of Publications during 2017

1. P. Belli, R. Bernabei, R.S. Boiko, F. Cappella, R. Cerulli, F.A. Danevich, A. Incicchitti, B.N. Kropivyansky, M. Laubenstein, V.M. Mokina, O.G. Polischuk, V.I. Tretyak, "New limits on 2ϵ, $\epsilon\beta^+$ and $2\beta^+$ decay of ^{136}Ce and ^{138}Ce with deeply purified cerium sample", Eur. Phys. J. A 53 (2017) 172 (DOI: 10.1140/epja/i2017-12360-0).

2. R. Cerulli, P. Villar, F. Cappella, R. Bernabei, P. Belli, A. Incicchitti, A. Addazi, Z. Berezhiani, "DAMA annual modulation and mirror Dark Matter", Eur. Phys. J. C 77 (2017) 83 [arXiv:1701.08590]

3. R. Bernabei, P. Belli, A. Di Marco, F. Montecchia, A. d'Angelo, A. Incicchitti, F. Cappella, V. Caracciolo, R. Cerulli, C.J. Dai, H.L. He, H.H. Kuang, X.H. Ma, X.D. Sheng, R.G. Wang, Z.P. Ye, "DAMA/LIBRA results and perspectives", EPJ Web of Conferences 136 (2017) 05001 (DOI: 10.1051/epjconf/201713605001).

4. P. Belli, "Preface", Int. J. Mod. Phys. A 32, 1702001 (2017).

5. R. Bernabei and A. Incicchitti, "Low Background Techniques in NaI(Tl) set-ups", Int. J. Mod. Phys. A 32, 1743007 (2017).

6. R. Cerulli, "Low background techniques toward a $ZnWO_4$ directionality experiment", Int. J. Mod. Phys. A 32, 1743009 (2017).

7. R. Bernabei, P. Belli, F. Cappella, V. Caracciolo, R. Cerulli, F.A. Danevich, A. d'Angelo, A. Di Marco, A. Incicchitti, V.M. Mokina, D.V. Poda, O.G. Polischuk, C. Taruggi, V.I. Tretyak, "$ZnWO_4$ anisotropic scintillator for Dark Matter investigation with the directionality technique", EPJ Web of Conferences 136 (2017) 05002 (DOI: 10.1051/epjconf/201713605002).

8. R. Bernabei, P. Belli, S. d'Angelo, A. Di Marco, F. Montecchia, A. d'Angelo, A. Incicchitti, F. Cappella, V. Caracciolo, R. Cerulli, C.J. Dai, H.L. He, H.H. Kuang, X.H. Ma, X.D. Sheng, R.G. Wang, Z.P. Ye, "Recent results from DAMA/LIBRA-phase1 and perspectives", Astronomical and Astrophysical Transactions (AApTr) 30 (2017) 71.

9. P. Belli, "The Dark Universe and the detection of Dark Matter", J. of Phys.: Conf. Series 866 (2017) 012016 (doi:10.1088/1742-6596/866/1/012016) .

10. R. Bernabei, P. Belli, S. d'Angelo, A. Di Marco, F. Montecchia, A. d'Angelo, A. Incicchitti, D. Prosperi, F. Cappella, V. Caracciolo, R. Cerulli, C.J. Dai, H.L. He, H.H. Kuang, X.H. Ma, X.D. Sheng, R.G. Wang, Z.P. Ye, "Recent results from DAMA/LIBRA and perspectives", in the volume of Proc. of the 17th Lomonosov Conference on Elementary Particle Physics, World Scie Ed. (2017) pages 280-286; ISBN: 978-981-322-455-1 ; DOI:10.1142/9789813224568_0044.

11. R. Bernabei, P. Belli, R. Cerulli, A. Di Marco, V. Merlo, F. Montecchia, F. Cappella, A. d'Angelo, A. Incicchitti, V. Caracciolo, C. J. Dai, H. L. He, H. H. Kuang, X. H. Ma, X. D. Sheng, R. G. Wang, and Z. P. Ye, "Results and perspectives of DAMA/LIBRA", AIP Conf. Proc. 1894, 020003 (2017); doi: 10.1063/1.5007628.

12. O.G. Polischuk, A.S. Barabash, P. Belli, R. Bernabei, F. Cappella, V. Caracciolo, R. Cerulli, D.M. Chernyak, F.A. Danevich, S. d'Angelo, A. Incicchitti, D.V. Kasperovych, V.V. Kobychev, S.I. Konovalov, M. Laubenstein, V.M. Mokina, D.V. Poda, V.N. Shlegel, V.I. Tretyak, V.I. Umatov and Ya.V. Vasiliev, "Investigation of 2β Decay of ^{116}Cd with the Help of Enriched ^{116}CdWO$_4$ Crystal Scintillators", AIP Conf. Proc. 1894, 020018 (2017) (doi: 10.1063/1.5007643).

13. P. Belli, R. Bernabei, V.B. Brudanin, F. Cappella, V. Caracciolo, R. Cerulli, F.A. Danevich, A. Incicchitti, D.V. Kasperovych, V.V. Kobychev, V.M. Mokina, O.G. Polischuk, V.I. Tretyak, and M.M. Zarytskyy, "Search for double beta decay in ^{106}Cd in the DAMA/CRYS set-up", AIP Conf. Proc. 1894, 020005 (2017) (doi: 10.1063/1.5007630).

14. R. Bernabei, P. Belli, A. Di Marco, F. Montecchia, A. d'Angelo, A. Incicchitti, F. Cappella, V. Caracciolo, R. Cerulli, C. J. Dai, H. L. He, H. H. Kuang, X. H. Ma, X. D. Sheng, R. G. Wang, and Z. P. Ye, "Highlights on signals from Dark Matter particles", EPJ Web of Conf. 164 (2017), 01013 [doi: 10.1051/epjconf/201716401013].

15. R. Bernabei, "Particle dark matter direct detection", in the volume The Fourteenth Marcel Grossmann Meeting, edited by World Scientific co. (2017) 203-214 [ISBN-10: 9813226595 and ISBN-13: 978-9813226593].

16. P. Belli, "Results and strategies in dark matter detection", in the volume The Fourteenth Marcel Grossmann Meeting, edited by World Scientific co. (2017) 681-692 [ISBN-10: 9813226595 and ISBN-13: 978-9813226593].

17. R. Bernabei, P. Belli, A. Di Marco, F. Montecchia, A. d'Angelo, A. Incicchitti, F. Cappella, V. Caracciolo, R. Cerulli, C. J. Dai, H. L. He, H. H. Kuang, X. H. Ma, X. D. Sheng, R. G. Wang, and Z. P. Ye, "DAMA/LIBRA-phase1 results and perspectives of the phase2", in the volume The Fourteenth Marcel Grossmann Meeting, edited by World Scientific co. (2017) 2402-2407 [ISBN-10: 9813226595 and ISBN-13: 978-9813226593].

18. A. Addazi, P. Belli, R. Bernabei, A. Marciano', "Testing Non-commutative Spacetimes and Violations of the Pauli Exclusion Principle with underground experiments", submitted for publication [arXiv:1712.08082v1].

References

[1] R. Bernabei et al., Nucl. Instr. and Meth. A 592 (2008) 297.

[2] R. Bernabei et al., Eur. Phys. J. C 56 (2008) 333.

[3] R. Bernabei et al., Eur. Phys. J. C 67 (2010) 39.

[4] R. Bernabei et al., Eur. Phys. J. C 73 (2013) 2648.

[5] P. Belli et al., Phys. Rev. D 84 (2011) 055014.

[6] R. Bernabei et al., J. of Instr. 7 (2012) P03009.

[7] R. Bernabei et al., Eur. Phys. J. C 72 (2012) 2064.

[8] R. Bernabei et al., Int. J. of Mod. Phys. A 28 (2013) 1330022 (73 pages).

[9] R. Bernabei et al., Eur. Phys. J. C 62 (2009) 327.

[10] R. Bernabei et al., Eur. Phys. J. C 72 (2012) 1920.

[11] R. Bernabei et al., Eur. Phys. J. A 49 (2013) 64.

[12] R. Bernabei et al., Eur. Phys. J. C 74 (2014) 2827.

[13] R. Bernabei et al., Eur. Phys. J. C 74 (2014) 3196.

[14] R. Bernabei, et al., Eur. Phys. J. C 75 (2015) 239.

[15] A. Addazi, et al., Eur. Phys. J. C 75 (2015) 400.

[16] DAMA coll., issue dedicated to DAMA, Int. J. of Mod. Phys. A 31 (2016).

[17] P. Belli, R. Bernabei, C. Bacci, A. Incicchitti, R. Marcovaldi, D. Prosperi, DAMA proposal to INFN Scientific Committee II, April 24th 1990.

[18] R. Bernabei et al., Phys. Lett. B 389 (1996) 757; R. Bernabei et al., Phys. Lett. B 424 (1998) 195; R. Bernabei et al., Phys. Lett. B 450 (1999) 448; P. Belli et al., Phys. Rev. D 61 (2000) 023512; R. Bernabei et al., Phys. Lett. B 480 (2000) 23; R. Bernabei et al., Phys. Lett. B 509 (2001) 197; R. Bernabei et al., Eur. Phys. J. C 23 (2002) 61; P. Belli et al., Phys. Rev. D 66 (2002) 043503.

[19] R. Bernabei et al., Il Nuovo Cim. A 112 (1999) 545.

[20] R. Bernabei et al., Eur. Phys. J. C18 (2000) 283.

[21] R. Bernabei el al., La Rivista del Nuovo Cimento 26 n.1 (2003) 1-73.

[22] R. Bernabei et al., Int. J. Mod. Phys. D 13 (2004) 2127.

[23] R. Bernabei et al., Int. J. Mod. Phys. A 21 (2006) 1445.

[24] R. Bernabei et al., Eur. Phys. J. C 47 (2006) 263.

[25] R. Bernabei et al., Int. J. Mod. Phys. A 22 (2007) 3155.

[26] R. Bernabei et al., Eur. Phys. J. C 53 (2008) 205.

[27] R. Bernabei et al., Phys. Rev. D 77 (2008) 023506.

[28] R. Bernabei et al., Mod. Phys. Lett. A 23 (2008) 2125.

[29] R. Bernabei et al., Phys. Lett. B408 (1997) 439; P. Belli et al., Phys. Lett. B460 (1999) 236; R. Bernabei et al., Phys. Rev. Lett. 83 (1999) 4918; P. Belli et al., Phys. Rev. C60 (1999) 065501; R. Bernabei et al., Il Nuovo Cimento A112 (1999) 1541; R. Bernabei et al., Phys. Lett. B 515 (2001) 6; F. Cappella et al., Eur. Phys. J.-direct C14 (2002) 1; R. Bernabei et al., Eur. Phys. J. A 23 (2005) 7; R. Bernabei et al., Eur. Phys. J. A 24 (2005) 51; R. Bernabei et al., Astrop. Phys. 4 (1995) 45.

[30] K.A. Drukier et al., Phys. Rev. D 33 (1986) 3495.

[31] K. Freese et al., Phys. Rev. D 37 (1988) 3388.

[32] R. Bernabei et al., AIP Conf. Proceed. 1223 (2010) 50 (arXiv:0912.0660).

[33] R. Bernabei et al., J. Phys.: Conf. Ser. 203 (2010) 012040 (arXiv:0912.4200); http://taup2009.lngs.infn.it/slides/jul3/nozzoli.pdf, talk given by F. Nozzoli.

[34] R. Bernabei et al., in the volume Frontier Objects in Astrophysics and Particle Physics (Vulcano 2010), S.I.F. Ed. (2011) 157 (arXiv:1007.0595).

[35] R. Bernabei et al., Can. J. Phys. 89 (2011) 11.

[36] R. Bernabei et al., Physics Procedia 37 (2012) 1095.

[37] R. Bernabei et al., arXiv:1210.6199; arXiv:1211.6346.

[38] A. Bottino et al., Phys. Rev. D 85 (2012) 095013.

[39] A. Bottino et al., arXiv:1112.5666.

[40] R. Bernabei et al., Astropart. Phys. 7 (1997) 73; R. Bernabei et al., Il Nuovo Cim. A 110 (1997) 189; P. Belli et al., Astropart. Phys. 10 (1999) 115; P. Belli et al., Nucl. Phys. B 563 (1999) 97; R. Bernabei et al., Nucl. Phys. A 705 (2002) 29; P. Belli et al., Nucl. Instrum. and Meth. A 498 (2003) 352; R. Cerulli et al., Nucl. Instrum. and Meth. A 525 (2004) 535; R. Bernabei et al., Nucl. Instrum. and Meth. A 555 (2005) 270; R. Bernabei et al., Ukr. J. Phys. 51 (2006) 1037; P. Belli et al., Nucl. Phys. A 789 (2007) 15; P. Belli et al., Phys. Rev. C 76 (2007) 064603; P. Belli et al., Eur. Phys. J. A 36 (2008) 167; P. Belli et al., J. Phys. G 38 (2011) 015103; D. Poda et al., Radiation Measurements 56 (2013) 66.

[41] P. Belli et al., Nucl. Instrum. and Meth. A 615 (2010) 301.

[42] P. Belli et al., Nucl. Phys. A 826 (2009) 256; P. Belli et al., Phys. Lett. B 658 (2008) 193.

[43] P. Belli et al., Nucl. Instrum. and Meth. A 626-627 (2011) 31.

[44] P. Belli et al., Phys. Rev. C 85 (2012) 044610.

[45] P. Belli et al., J. Phys. G: Nucl. Part. Phys. 38 (2011) 115107.

[46] A.S. Barabash et al., JINST. 6 (2011) P08011.

[47] P. Belli et al., Eur. Phys. J. A 50 (2014) 134.

[48] P. Belli et al., Phys. Scripta 90 (2015) 085301.

[49] A.S. Barabash, P. Belli, R. Bernabei, Yu.A. Borovle, V. Caracciolo, R. Cerulli, F.A. Danevich, A. Incicchitti, V.V. Kobychev, S.I. Konovalov, M. Laubenstein, V.M. Mokina, O.G. Polischuk, O.E. Safonova, V.N. Shlegel, V.I. Tretyak, I.A. Tupitsyna, V.I. Umatov, V.N. Zhdankov, Nucl. Instr. and Meth. A 833 (2016) 77.

[50] F. Cappella et al., Eur. Phys. J. C 73 (2013) 2276.

[51] P. Belli et al., Nucl. Instrum. and Meth. A 670 (2012) 10;

[52] N.J. Cherepy et al., Applied Physics Letters 92 (2008) 083508.

[53] P. Belli et al., Nucl. Instr. and Meth. A 572 (2007) 734; P. Belli et al., Nucl. Phys. A 806 (2008) 388; P. Belli et al., Nucl. Phys. A 824 (2009) 101; O. P. Barinova et al., Nucl. Instrum. and Meth. A 607 (2009) 573; P. Belli et al., Eur. Phys. J. A 42 (2009) 171; P. Belli et al., Nucl. Phys. A 846 (2010) 143; P. Belli et al., Nucl. Phys. At. Energy 11 (2010) 362; P. Belli et al., Nucl. Phys. A 859 (2011) 126; P. Belli et al., Phys. Rev. C 83 (2011) 034603; P. Belli et al., Eur. Phys. J. A 47 (2011) 91; P.

Belli et al., Phys. Lett. B 711 (2012) 41; P. Belli et al., Nucl. Instrum. and Meth. A 704 (2013) 40; P. Belli et al., Phys. Rev. C 87 (2013) 034607; S. Das et al., Nucl. Instrum. and Meth. A 797 (2015) 130.

[54] P. Belli et al., Eur. Phys. J. A 49 (2013) 24.

[55] P. Belli et al., Nucl. Phys. A 930 (2014) 195.

[56] A.S. Barabash et al., Phys. Rev. C 79 (2009) 045501.

[57] M.F. Kidd et al., Phys. Rev. C 90 (2014) 055501.

[58] J. Meija et al., Isotopic compositions of the elements 2013 (IUPAC Technical Report), Pure Appl. Chem. 88 (2016) 293.

[59] O.G. Polischuk et al., Purification of lanthanides for double beta decay experiments, AIP Conf. Proc. 1549 (2013) 124.

DarkSide: Liquid Argon Search for Dark Matter

(The DarkSide Collaboration)

(Spokesperson: Cristiano Galbiati)

DarkSide-50 has provided the strongest low-massWIMP dark matter limits. The analysis is based on the ionization signal, for which the DarkSide-50 time projection chamber is fully efficient at $0.1\,\mathrm{keV}_{ee}$. The observed rate in the detector at $0.5\,\mathrm{keV}_{ee}$ is about $1.5\,\mathrm{event/keV}_{ee}/\mathrm{kg/d}$ and is almost entirely accounted for by known background sources. We obtain a $90\,\%$ C.L. exclusion limit above $1.8\,\mathrm{GeV}/c^2$ for the spin-independent cross section of dark matter WIMPs on nucleons, extending the exclusion region for dark matter below previous limits in the range 1.8–$6\,\mathrm{GeV}/c^2$.The DarkSide collaboration has made many large strides during the last year. It has gained formal approval of the DarkSide-20k experiment, which will be a $30\,\mathrm{t}$ liquid argon time projection chamber hosted at LNGS, by all funding agencies that will be contributing to the construction and operations support of the project. This includes the efforts to extract and purify the underground argon, which will be the detector target, with major progress being made at the site of the Aria cryogenic distillation column, including delivery of the top, bottom and first batch of central modules of the first column. Development of the first silicon photomultiplier photodetector module is well underway and will be completed during 2018, along with the first batch of modules which will make-up the first motherboard and thus fundamental unit of the detector.

I. DARKSIDE-50 RESULTS

The DarkSide Collaboration proposed DarkSide-50 with the goal of delivering a zero-background multi-year campaign of dark matter searches and to assess the suitability of the two-phase LAr TPC technology for larger scale dark matter searches.

The DarkSide Collaboration recently completed a major milestone of its program by publishing results from a 532-day campaign with DarkSide-50 [1]. The outcome of the dark matter search is a null result (see Figure 1), giving the current best upper limit using argon (see Figure 2). The promise of a zero-background result has been delivered.
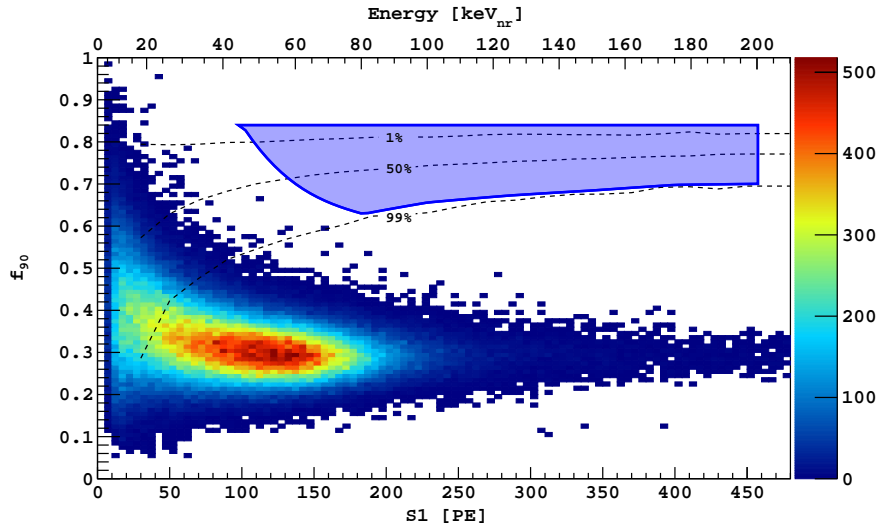

FIG. 1.   DarkSide-50 532-live-day high-mass WIMP search. Observed events in the f_{90} vs. S1 plane surviving all cuts in the energy region of interest. The solid blue outline indicates the DM search region. The 1%, 50%, and 99% f_{90} acceptance contours for nuclear recoils, as derived from fits to our ^{241}AmBe calibration data, are shown as the dashed lines.

The assessment of the suitability of the two-phase LAr TPC technology for larger scale dark matter searches is now complete: the DarkSide Collaboration is able to extrapolate that the DarkSide-20k experiment recently approved for construction by INFN, NSF, and LNGS, will operate with zero-background from instrumental sources (1.6 nuclear recoil events are expected in $100 \, \mathrm{t} \, \mathrm{yr}$ from neutral current interactions due to atmospheric neutrinos).

The extremely low background of DarkSide-50 reached since the start of operations with UAr has also allowed us to obtain a second, very significant result, which could not have been anticipated at the time of the proposal for the experiment. The analysis of very-low energy events, characterized by the presence of the sole ionization events, allowed to perform the most significant search for low-mass dark matter, resulting in world-best limits for masses below $8 \, \mathrm{GeV}/c^2$ [2] (see Fig 3). The same analysis stream also produced very competitive limits for the scattering of dark matter into electrons [3].

With its result on low-mass dark matter searches, the DarkSide Collaboration set itself from the competition by delivering the result that surpassed all competing technologies by the largest margin (averaging one order of magnitude and ranging up to two orders of magnitude) in any mass range. The DarkSide Collaboration will now move forward to exploit the lowest background ever achieved in the low energy range for a study of seasonal oscillations, featuring an energy threshold more than one order of magnitude lower than the competitors.

With its result on the search of traditional dark matter, the DarkSide Collaboration projects that the DarkSide-20k experiment will deliver a leading result in dark matter searches and, thanks to the complete suppression of instrumental background, will set itself apart from Xe-based experiments. Additional papers related to DarkSide-50 that were published during the 2017 year included [4–8].
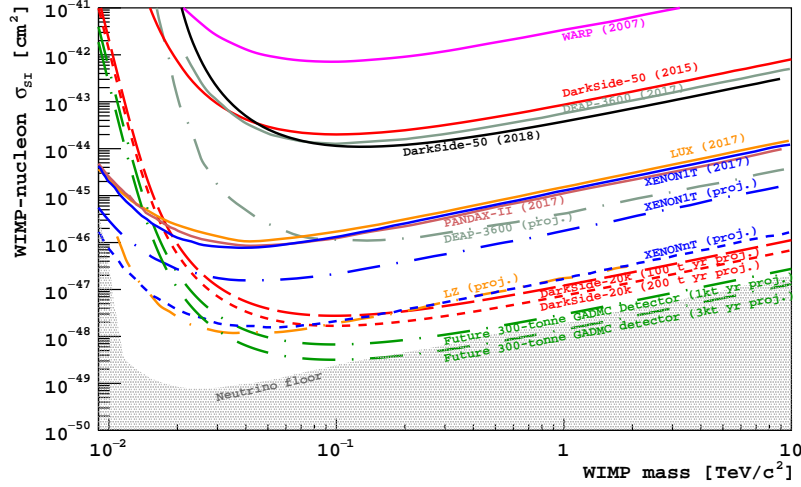

FIG. 2. DM spin-independent cross-section vs. mass limits and sensitivities from previous argon-based results (including the DarkSide-50 532-live-day limit), current best limits produced by xenon-based experiments, and expected future sensitivities (dashed and/or dotted lines).
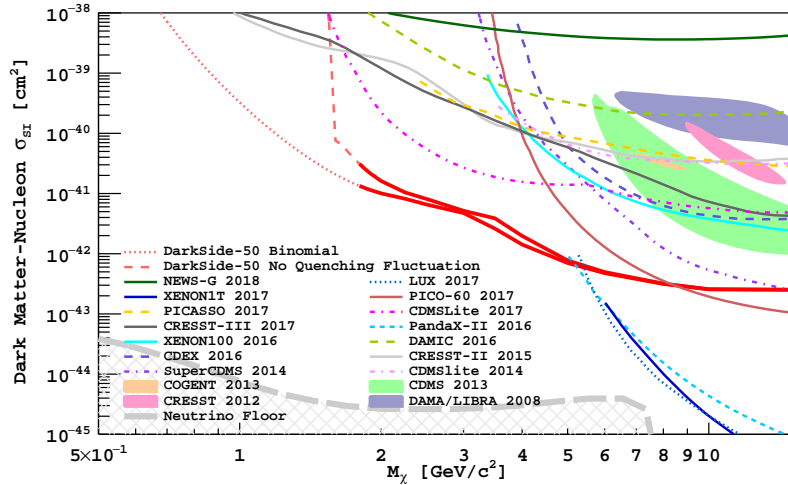

FIG. 3. Results from DarkSide-50 high-mass WIMP search. 90 % upper limits for the binomial fluctuation model (red solid line, continued as dotted) and the model with zero fluctuation in quenching (red solid line, continued as dashed) on spin-independent dark matter-nucleon cross sections from DarkSide-50 in the range above $1.8\,\mathrm{GeV}/c^2$.

II. DARKSIDE-20K AND A GLOBAL LIQUID ARGON PROGRAM

The DarkSide (DS) Collaboration unites researchers from currently operating LAr direct dark matter searches to build the DS-20k detector, designed to be experimental-background free and featuring the best sensitivity to high-mass WIMP dark matter among all experiments that are currently approved and foreseen to operate within the next 5-10 years (see Figure 2). The DS-20k detector is also complementary to the next generation xenon-based detectors, since a possible observation of WIMPs with two different targets could allow scientists to fully confirm the detection and to disentangle the correlation between mass and cross-section. The DS-20k experiment aims at a significant improvement in sensitivity, a factor of at least >50 with respect to recent results, reaching $1.2 \times 10^{-47}\,\mathrm{cm^2}$ for WIMPs of $1\,\mathrm{TeV}/c^2$ mass. This goal will be achieved using a LAr time projection chamber (LAr TPC) with an active (fiducial) mass of $32\,\mathrm{t}(29\,\mathrm{t})$, for a total exposure of $100\,\mathrm{t\,yr}$ to be accumulated in a run lasting $5\,\mathrm{yr}$. Thanks to its exceptionally low instrumental background, DS-20k could extend its operations to a decade, increasing the exposure to $200\,\mathrm{t\,yr}$ and reaching a sensitivity of $7.4 \times 10^{-48}\,\mathrm{cm^2}$ for WIMPs of $1\,\mathrm{TeV}/c^2$ mass.

DS-20k was jointly proposed to the US NSF, the Italian INFN, and the host laboratory, LNGS, in December 2015. The experiment was first reviewed by a joint panel charged by the Italian INFN and the US NSF. The joint review was made possible for NSF by statute NSF-14-1999 "Dear Colleague Letter - International Activities within the Physics Division - Potential International Co-Review", following approval by the US State Department. Following the first joint review, the experiment has also been separately reviewed by the "Commissione Nazionale Seconda" of INFN, by the "Comitato Tecnico Scientifico" of INFN, by the "Comitato Scientifico" of LNGS, and by the "Particle Astrophysics – Experiment" panel of NSF. Following all reviews, the experiment was approved by INFN and LNGS in April 2017 and by NSF in October 2017. Following a meeting of participating international funding agencies and laboratories held at the Embassy of Canada in Rome in September 2017, the experiment is officially supported by three participating underground laboratories: the host laboratory LNGS, Laboratorio Subterráneo de Canfranc (LSC), and SNOLab. Future reviews of the progress of the now approved experiment will involve the tight coordination of the Directorates of all three laboratories.

University groups from Poland, Russia, Spain, and Switzerland are already funded for work on DS-20k by their funding agencies. University groups from France, Germany, and UK are currently participating with the DS Collaboration through support from internal resources and are preparing proposals to each of their funding agencies.

Canadian groups have recently joined the DS Collaboration, in September 2017. Funding for large scale extraction of low-radioactivity argon is already available from CFI in Canada. Funding for R&D is available for DEAP-3600 from NSERC in Canada and a further request for development work on DS-20k and the future larger detector will be submitted at the end of 2017. An internal proposal for support to the DS-20k activities and for capital funds was submitted to TRIUMF in October 2017 and a decision is expected by the end of the 2017 calendar year. A proposal to the Canadian CFI for additional capital funds will be submitted to the next competition, expected in 2019.

Scientists from the four world-leading LAr dark matter projects (ArDM at LSC, DS-50 at LNGS, DEAP-3600 and MiniCLEAN at SNOLab) have agreed to join forces to carry out DS-20k as a single next-generation LAr experiment at LNGS [9]. The same inclusive group of scientists also signed a Letter of Intent signaling their interest to continue the collaboration beyond DS-20k to build a larger experiment, with a fiducial mass of a few hundred of tonnes, capable of collecting an exposure of $1000\,\mathrm{t\,yr}$ with the ability to remove (by discrimination, veto tagging, etc.) all backgrounds except NRs induced by atmospheric and diffuse supernova background neutrinos. The location and laboratory for this final experiment of our program are still to be debated within the collaboration. The same group of scientists also agreed to form the Global Argon Dark Matter

Collaboration (GADMC), a consortium of all institutes active in the development of argon dark matter experiments. The GADMC will:

- Oversee the open access to currently operating LAr dark matter experiments (DS-50 and DEAP-3600) and their science data, to the benefit of all participating institutions,
- Coordinate the contributions to DS-20k at LNGS, the single, next generation LAr dark matter effort at the scale of a few tens of tonnes,
- Coordinate the contributions to the future LAr dark matter effort to build a detector at the scale of a few hundred of tonnes.

After the approval of DarkSide-20k, in September 2017, in consideration of the increased awareness of the potential impact of LNGS operations on the surrounding environment, including the two acqueducts serving the L'Aquila and Teramo districts, and in compliance with Art. 15 Capo III of D. Lgs. 81/2008, which mandates consideration of all technical means available for the elimination and/or mitigation of safety and environmental risks on work sites, the LNGS Directorate requested that the DarkSide Collaboration consider the possibility of developing an alternate plan for the veto detectors, and in particular the possibility of eliminating the large batch of organic liquid scintillator that was part of the baseline design [9].

The DarkSide Collaboration responded by developing a design that relies on a plastic scintillator veto (PSV) to substitute the the liquid scintillator veto (LSV), originally envisioned as the veto for the neutrons from fission and (α,n) reactions in the DarkSide-20k detector materials, whose design was developed on the basis of the experience with the DarkSide-50 LSV [10]. We anticipate that the PSV may reach the same level of rejection of neutrons originated by fission and (α,n) reactions in the DarkSide-20k construction materials. We acknowledge that some R&D is necessary to complete the design of the PSV. In recognition of the need for R&D, we opted to eliminate the single largest source of neutrons remaining in the DarkSide-20k detector after elimination of the cryogenic PMTs in favor of SiPM-based cryogenic photosensors: the DarkSide-20k cryostat and its multi-layer insulation (MLI). The elimination of the DarkSide-20k cryostat and the accompanying MLI is accomplished by operating DarkSide-20k and its PSV within a large outer cryostat (OC) with a AAr fill, outfitted as a liquid argon scintillator veto (LArSV) for cosmic rays and cosmogenics. After long and detailed consultations within the Collaboration and in cooperation with the CERN Neutrino Platform group, we selected as the ideal candidate for the OC an exact replica of the two twin cryostats built at CERN in support of the ProtoDUNE program. In this configuration, the OC and accompanying MLI are substituted by a thin, ultra-low background copper vessel (CV), serving as the containment vessel of the UAr. There will be no temperature differential across the CV. The pressure differential across the CV will be limited to 100 mbar in all phases of filling and operation of DarkSide-20k.

Following the substitution of the OC and MLI with the ultra-low background CV, we anticipate that the neutron budget of DarkSide-20k will be so low that strict adherence to the material selection prescriptions and rigorous screening of all materials could provide guarantee a background-free condition even without the use of the PSV. Development and construction of a high-efficiency PSV remains a top priority for DarkSide-20k. First, the adoption of the PSV is necessary to maintain in the ability to identify and count neutrons, which proved crucial and essential for the success of DarkSide-50. Second, the presence of a high-efficiency PSV will also mitigate the criticality of the material screening program: it will provide extra insurance on the ultimate delivery of a background-free experiment, even in presence of limited discrepancies in the outcome of the material selection process.

In early reviews of the new plan for the veto detectors, we identified a possible risk in the limited ability of testing the DarkSide-20k LAr TPC prior to the complete fill of the OC with a large inventory of AAr. The risk was mitigated by implementing an important modification to the OC: the DarkSide-20k TPC will be assembled within the OC and will be suspended to a removable cap closing the top surface of the OC; upon completion of the assembly, without disconnecting any of the

electric and/or hydraulic service lines of DarkSide-20k, the DarkSide-20k TPC and the supporting cap will be removed from the OC; the DarkSide-20k TPC will be inserted in a smaller cryostat, closed at the top with the same cap, thus permitting a dedicated test in its final configuration prior to committing to the start of filling of the OC with its large AAr inventory.

Development of the new design for the DarkSide-20k veto detectors is proceeding rapidly, in strong cooperation with the CERN Neutrino Platform group, and with full compliance insofar with the requirements that the new design deliver the same or better physics performance, that the cost fit within the same budget envelope, and that the impact of schedule be not prejudicial for the competitiveness of the experiment.

The mitigation strategy followed by the DarkSide Collaboration for DarkSide-20k will be even more effective. In addition to all applicable mitigating actions envisioned at CERN for ProtoDUNE, we plan to take advantage of the unique strategy for UAr and AAr purification developed in DarkSide-50, which relies on drawing argon from the both phases of both detectors and to transform the liquid into gaseous phase prior to purification in a high-temperature Zr getter. All of the argon, both in the gaseous and liquid phases, is drawn from the top of the detector, as detailed later in Sec. VII. All lines at the bottom of the cryostat identified in the preliminary safety assessment of ProtoDUNE are therefore removed. The need for an automated valve at the bottom of the cryostat is removed, and the passive cryostat will have no solution of continuity in its insulation at the bottom. There are no LAr recirculation pumps, only GAr displacement pumps. In case of a rupture of piping at the top of the detector, the reaction time for turning off the drawing of the liquid phase can be much shorter than the 20 s quoted for ProtoDUNE.

In consideration of elements described above, the outstanding results anticipated for DarkSide-20k and detailed above are only possible due to the pulse shape discrimination (PSD) capabilities of argon, procurement of isotopically pure argon from an underground source, use of a comprehensive vetoing scheme (PSV and LArSV), and use of large photosensitive areas covered by silicon photomultipliers (SiPMs). A very strong discrimination of electron recoils (ERs) from nuclear NRs was demonstrated in DS-50 using PSD [11], and a supplementary analysis of Monte Carlo simulated data for DS-20k predicted an ultimate rejection factor $>3 \times 10^9$ [9]. This will allow us to completely discriminate the ERs. In addition, work to procure the target for DS-50 demonstrated that underground argon (UAr) can be obtained with an ^{39}Ar content that is suppressed by a factor of more than 1400, with respect to atmospheric argon (AAr), drastically reducing the expected number of ER events to be discriminated against. The remaining neutron background will be tagged by the PSV with high efficiency. DarkSide-20k and its PSV will be operated within a OC, a replica of the two twin ProtoDUNE cryostats, with a AAr fill, outfitted as a LArSV for cosmic rays and cosmogenics. Both the PSV and the LArSV will be operated with SiPM-based cryogenic photosensors nearly identical to those outfitting DarkSide-20k.

III.   DETECTOR OVERVIEW

The DarkSide-20K experiment will be located at the Hall-C of the Gran Sasso National Laboratory (LNGS) in Italy. It consists of two detectors: the inner detector and the veto detector. The inner detector is a Time Projection Chamber (TPC) filled with underground argon, and the veto detector is a cubic detector directly from the Proto-DUNE experiment (reference), filling with atmospheric argon. Figure 4 shows a 3D drawing of the DarkSide-20K experiment, the inner detector is placed at the middle position of the veto detector, and the veto detector is located in Hall-C of LNGS; next to the veto detector, there is a stainless steel cryostat prepared to test the inner detector after assembly, and before the hoisting. The detailed information about the inner detector, as well as the cryogenics systems of both inner detector and veto detector will be explained.
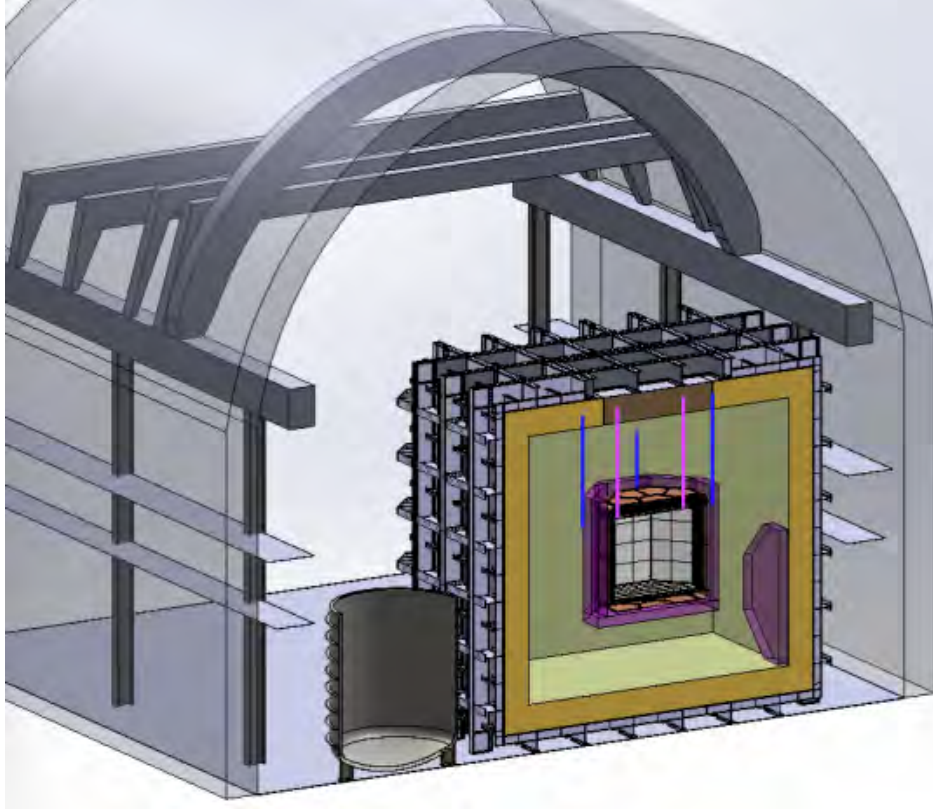
FIG. 4. A 3D drawing of the DarkSide 20K experiment.

IV.   OUTER CRYOSTAT

The new concept is to host both the inner active detector vessel and the veto detector in a large liquid argon cryostat. The advantage is to keep the inner detector vessel, which will host the depleted liquid argon, immersed in a bath of liquid argon and therefore cancelling all hydrostatic pressure and the thermal insulation requirements. This allows to minimize the material of the inner vessel and therefore to limit the possible radio-contaminations very close to the active detector. In this case most of the structural and possibly radioactive material is moved far away from the inner vessel by at least 2 m. The main liquid argon bath will define the thermal conditions of the inner vessel and will provide additional shielding. The walls of the outer cryostat will include a neutron moderator which will thermalise the cosmogenic neutrons and the ones raising from the rock.

The design concept of this outer vessel is based on the experience matured with the construction of similar vessels for the DUNE longbaseline neutrino experiment. The adopted technique is the one of the LNG (Liquified Natural Gas) carriers and vessels, which has proven over many years its solidity and reliability. Characteristics of this are the passive thermal insulation, and the inner wall (cold membrane) with its corrugated layout, which is designed to allow contraction and expansion of the main liquid volume.

Two vessels of the same size as the one proposed here have been constructed at CERN and will be brought into operation in the second half of 2018. The experience gained there in the design, construction and operation will be fully translated to this new project. For that reason, the same mechanical constraints, dimension and thermal properties have been kept. The main difference is in the inner detector access and support system, which will now require a top cap plug on its roof. Even this feature was tested with the construction and operation of a first demonstrator for the DUNE project.

82

The cryostat itself consists of two main parts: a warm and a cold structure. The main function of the warm structure is to deal with the hydrostatic pressure coming from the liquid. The internal cold structures insulate the vessel towards the outside and provide the containment of the liquid argon. All services and cryogenics penetrations for the DarkSide-20k LAr TPC detector are placed on the roof of the cryostat. The outer cryostat is a selfsupporting structure sitting on the floor of the experimental area, without any particular external structural requirement.

V. INNER VESSEL

Due to the employment of a LAr veto, there is no need to use a double-walled, vacuum insulated cryostat for the containment of the inner detector and the UAr. In particular, the pressure difference between the liquid AAr shield and the liquid UAr inside the inner vessel can be compensated by the excellent thermal conductivity of the copper, and is hence foreseen to be very small. Therefore, a thin-wall, octagonal cross-sectional copper inner vessel can be made using reinforcement by support ribs. This removes the by far largest contributor of the neutron background in the overall DarkSide-20k exposure, reducing the contribution from the inner vessel by three orders of magnitude.
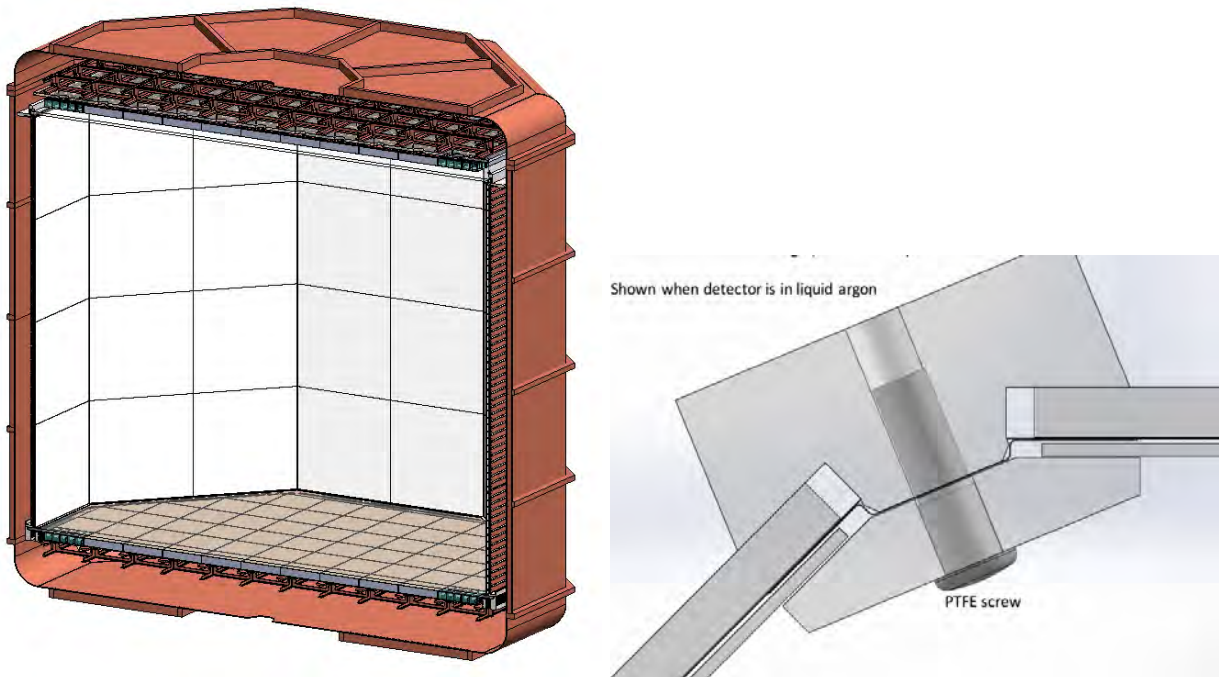
VI. TPC

FIG. 5. **Left:** 3D model of the DarkSide-20k LAr TPC. **Right:** Cross-sectional view of the reflector panel corner joints.

According to the size and the shape, a 3D model of the TPC is shown on the left side of Figure 5. The active LAr volume is defined by a transparent conductive indium-tin-oxide (ITO) cathode at the bottom, a grid just below the liquid surface, separating the electron drift and extraction region, and a reflecting surface with an octagonal footprint on the sides. The thin argon gas electroluminescence

region above the liquid surface is bounded by a flat diving bell shaped ITO electrode at the top. A field cage is mounted at the external side of the reflecting region to generate a uniform drift region. Interactions in active LAr volume generate prompt scintillation light, that gives the S1 signal. A high voltage is applied between the cathode and grid to produce a vertical electric field to drift the ionization electrons created at the interaction site upward. An independently-adjustable potential between the grid and anode creates the fields to extract the electrons into the gas and accelerate them to create the secondary scintillation, called electroluminescence, which gives the S2 signal. Both the S1 and S2 signals are detected by the top and bottom arrays of PDMs which view the active LAr volume through large acrylic windows. This design maximizes the light yield and follows the same concept of S2 generation as was successfully utilized in DarkSide-50. The cathode and anode planes require octagonal windows with a width of roughly 2.5 m, and since there are no available ultra-high-purity fused silica plates of this size, UV-transparent acrylic is the material of choice.

The S1 signal is distributed roughly equally over both arrays, while the S2 signal, emitted in the gas pocket, is concentrated in the top array and within a few SiPM tiles around the transverse position of the ionization drift, thus yielding a precise x-y location. The drift time (the time between the S1 and S2 signals) determines the z-location of the event in the TPC.

DarkSide-50 TPC employed a thick, modified high reflectivity PTFE as the material of the reflection panels, which performed very well. Considering scaling the DarkSide-50 PTFE reflector panel up to the size required for DarkSide-20k, about 2000 kg of the PTFE will be used. Such a large mass of PTFE would cause this to be the dominate neutron source provided by (α, n) reactions in the carbon and flourine rich PTFE. In addition, DarkSide-50 found that the PTFE panels are the major source of Cherenkov events, and this background could become significantly large if the PTFE panels are scaled up to the DarkSide-20k size. In order to retain the high reflectivity and reduce the neutron background and Cherenkov events, DarkSide-20k will use Enhanced Specular Reflector (ESR) foil as the TPC reflector.

ESR is a thin layer foil which has reflectivity for 420 nm light, up to 98 %, with a thickness of only 65 μm. To hold the ESR foil in place and maintain its flatness during the operations, two pieces of UVT acrylic sheets are used to sandwich the ESR foil in the middle. The acrylic sheet facing to the active LAr volume is 1 mm thick, while the thickness of the backside acrylic sheet is 4 mm thick. The surface facing the active LAr volume of each 1 mm thick acrylic sheet is coated with TPB to shift the wavelength of the argon scintillation light to 420 nm, in order to maximize the light reflection and collection.

There are two different kinds of ESR-acrylic sandwiches, the flat assembly and the corner assembly, the detail views of these two assemblies are shown on the right side of Figure 5. Each ESR-acrylic sandwich assembly is fixed by several PTFE screws, with the screw heads facing to the active volume. In order not to lose any light, each head of the PTFE screw is coated with TPB. Some space is left between the acrylic and the ERS to allow venting of any gas during filling of the LAr, and also to allow LArto fill the space and reduce the chances for total internal reflection of light within the ESR-acrylic sandwich. The flat assemblies and the corner assemblies are mounted on the field cage, which is holding by another set of acrylic structures, by the PTFE screws, but the corner assemblies and the flat assemblies are not directly connected to each other in order to accommodate the shrinkage when the assemblies are immersed in the LAr.

In order to get rid of any gaps in the ESR reflector that may appear during the cooling and shrinking, the ESR foils are overlapped at every joint between the sandwich assemblies. In the vertical direction, the movement caused by the shrinkage is coherent, since the vertical supporting structures of the TPC are all made of acrylic. So, only the radial shrinkage has to be considered and precautions taken to make sure things move in the correct relative way. This radial shrinkage will cause the vertical overlapping sides of the ESR to move away from each other, due to the different coefficients of thermal expansion between the ESR foil and the acrylic. Thus, these sides

of the ESR foils have to be overlapped more by counting the shrinkage between each sandwich assemblies, especially between the flat and the corner assemblies. Works to optimize this design and to understand the optics are now being carried out at UCLA and UC Davis and will converge on the final design soon.

Differing from the HVFT used in DarkSide-50 TPC, the HVFT for DarkSide-20k has to go through the LAr veto detector and deliver the HV into the inner detector. Since the vacuum seal of the feedthrough is made by cryo-fitting, the seal cannot survive in LAr. Therefore, the feedthrough of DarkSide-20k has to be more then 6 m long to allow the cryo-fitted vacuum seal to be sitting in a room temperature environment. The vacuum seal of the feedthrough has already been demonstrated by the DarkSide-50 feedthrough.

Considering the hosting and the assembly, the entire HVFT will be divided into two parts: a flexible part and an inflexible part. The flexible part comes from the outside of the veto detector and goes all the way down to the copper vessel of the inner detector. The cryo-fitted vacuum seal is sitting near the top port of the flexible part, and at the bottom of the flexible part, there is a male banana connector and a copper-sealed CF flange, for the future connection to the inflexible part. The inflexible part of the HVFT is very similar to that used in DarkSide-50, the only difference is there is no sealing on the inflexible part. A female banana connector and a CF flange are made as the top port of the inflexible part to connect with the flexible part, for electric conduction and vacuum seal.

VII. CRYOGENICS

Two cryogenics systems have to be built for the DarkSide-20k experiment, due to both the inner detector and the veto detector all need to be filled with LAr. Compared to the cryogenics system of the DarkSide-50 experiment, which has a total of (153 ± 1) kg of argon, the cryogenics system of the DarkSide-20k inner detector must be able to efficiently purify and maintain 47 t of UAr for the inner detector, and 682 t of AAr for the veto detector. The principle of the LAr cryogenics system has been fully demonstrated in the DarkSide-50 experiment, which is characterized as good inner pressure stability, high purification capability, and long term cooling power maintaining ability. More specifically, the pressure stability in the cryostat is designed to have fluctuation within $\pm$ 0.1 psi, but in reality, the pressure stability is maintained within 0.023 psi over a period of more than two years. The purified LAr has an oxygen contamination less than 0.01 ppb, which results in a ≥ 5 ms electron lifetime. The ability to maintain long term cooling power keeps the system immune to any kind of power failure (including the failure of the UPS system), as recently demonstrated during a total LNGS blackout with the DarkSide-50 system. The features of the DarkSide-50 cryogenics system will be fully implemented into the DarkSide-20k cryogenics systems, not only simply scaled the argon volume up, but also upgraded based on experience and lessons learned.

The liquid argon handing systems of the inner detector and the veto detector are isolated, since they are filled with UAr and AAr respectively. The UAr is delivered and initially stored in five cryogenic shipping and storage containers in liquid phase. Each of the containers contains 10 t of LAr and a liquid nitrogen tank used to continually re-condense the UAr as it boils off. At the top of each LAr tank, there is a condenser connected to the liquid nitrogen tank, which can provide a certain cooling power to maintain the UAr in liquid phase during shipping and storing. After the five cryogenics containers arrive at the Hall-C of LNGS, the argon tanks nitrogen tanks are connected to the UAr loop and the nitrogen loop of the cryogenics system, respectively. The AAr, to be filled into the veto detector, will be directly delivered by a LAr truck and stored in a LAr reserve tank.

The condenser box is one of the key components of the DarkSide-20K cryogenics system. Apart from the condenser itself, the condenser box has five heat exchangers to efficiently pre-cool the argon

gas by cold nitrogen gas and argon gas. The radon trap is placed into the condenser box between the coldest heat exchanger and the second coldest heat exchanger to maximize the function. A 3D drawing of the condenser box is shown in Figure 6, while a liquid nitrogen condenser, which has the same size of the design, has already been fabricated and tested at UCLA. All of these parts will be connected by stainless steel tubes with 1" OD, 0.035" wall to allow the system working at the circulation speed up to 1000 stdL/min.
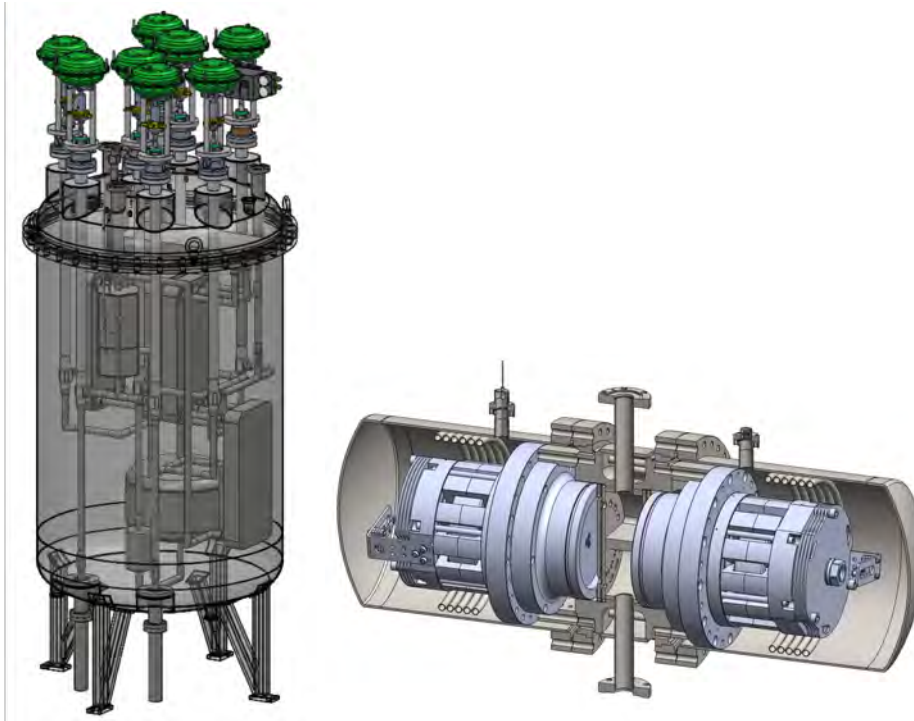

FIG. 6. **Left:** A 3D drawing of the inner detector condenser box. **Right:** The section 3D drawing of the DarkSide-20K argon gas circulation pump.

The cryogenics systems of the inner detector and the veto detector require gas circulation speeds of up to 1000 stdL/min and 10000 stdL/min, respectively, during the initial fast circulation. To achieve such a high circulation speed, flexibility of the operations, as well as the ease of the pump development, two circulation pumps are placed in parallel in each cryogenics system, and each pump provides a circulation rate up to 500 stdL/min and 5000 stdL/min for the inner detector and the veto detector, respectively. According to the successful demonstration of the QDrive pump working in the DarkSide 50 cryogenics system, the gas circulation pump of DarkSide-20K uses the similar design, and it is relying on two components: linear motors and reed valves. The design of the argon gas circulation pump for the inner detector of DarkSide-20K is shown on the right side of Figure 6, two linear motors are placed face to face oppositely, to counteract the vibration produced during the motor operation. At the end of the cylinder of each motor, there is a reed valve to control the gas flow during the motor moving in the two different travel directions. This design has already been fabricated and will soon undergo the full testing at CERN.

VIII. VETO DESIGN

In the present design of the experiment the role of the former water Cherenkov and liquid scintillator detectors is replaced by argon contained in the outer cryostat and by a plastic scintillator.

Previous studies have shown that radiogenic neutrons are the most dangerous background. These neutrons are emitted with an energy spectrum slightly depending on the material and extending up to some MeV: they may enter the LAr TPC and perform elastic scattering with the UAr target. They loose a small amount of energy after each interaction due to the large mass ratio between Ar nuclides and neutrons, but they typically produce a signal in the TPC that mimics a dark matter interaction. During their random walk these neutrons have a chance to exit the TPC and enter in the external veto detector. We plan to install a layer of plastic scintillator of 30 cm thickness around the TPC to act at once as neutron moderator and neutron veto. Organic plastic scintillators are made by a fluorescent material suspended in a solid polymer base; they contain a large number of Hydrogen atoms so that they are excellent neutron moderators. Neutron thermalized in the plastic scintillator are then captured by H (with the emission of a 2.2 MeV γ-ray) or by others nuclides with high cross capture cross section purposely mixed with the plastic scintillator. As in the previous design, if a signal candidate to be a WIMP is identified within a proper volume of the TPC, we then look at the veto detectors signals to check if it is instead due to neutrons. We then search for a signal in the plastic scintillator due to the neutron thermalization (prompt signal, the typical time delay with respect to the LAr TPC signal is of 200 ns) and for the one following the neutron capture (delayed signal, because it happens on a time scale of several µs after the LAr TPC signal).

The design of the plastic scintillator veto is first driven by the expected neutron rejection efficiency obtained with the Monte Carlo simulation assuming our best estimate about the radioactive contamination of the materials. We have then selected as baseline option the one that minimizes the need of R&D and that can be built as much as possible on the base of known technologies. Our G4DS-based Monte Carlo simulations predict that the neutron rejection efficiency of a veto detector based on a simple, undoped plastic scintillator, is insufficient. However, the use of a plastic scintillator offers the ability to dope it with a neutron capturing isotope uniformly mixed in the scintillator, as well as easily allows a design of a segmented detector where plastic scintillator sectors are interleaved with layers of neutron capturing material.

Our current baseline design calls for a simple plastic scintillator interleaved with Gd foils. Gd has the highest known cross section for capture of thermal neutrons, emitting a few γ-rays with a total energy of several MeV's, well above the ^{14}C end point. In a preliminary design under development, the plastic scintillator sectors are vertical bars with a typical squared section 10×10 cm^2, mounted around the LAr TPC at a minimal distance, totaling a three layers of bars as required to provide the 30 cm thickness of plastic scintillator mentioned above. The resulting structure is best described as a polygonal cage with inner radius of 200 cm and outer radius of 230 cm. The length of each bar is still being optimized, and in the scenario of a 2 m length the total number of vertical scintillating bars is of 600. A similar number of additional bars, mounted horizontally, are used to cover the bottom and the top of the LAr TPC. In this preliminary design, the bars are optically independent and wrapped within a reflective material. The Gd is in form of foils covering the bars or in form of Gd$_2$O$_3$ directly deposited on the reflector. We find that a thickness of only 25 µm of Gd is sufficient to absorb any thermal neutrons impinging on it. The total mass of Gd required is of about 1 % of the total mass of the scintillator. In this design, the light generated in each bar would be collected by two SiPM-based PDMs nearly identical to those developed for the DarkSide-20k LAr TPC, directly coupled to the two bases of the bar. We would plan to use the same PDMs designed for the LAr TPC, with minimal changes in the supporting mechanics to optimize the optical coupling between the scintillator and the SiPM tile. The total anticipated number of tiles is of about 2500. The number of external readout channels and corresponding fiber optics and penetrations can be significantly lower thanks to ability to add the signal from a few PDMs into a single signal.

We are planning to start performing specific tests to optimize the details of the design and the light collection efficiency of the scintillator bars in liquid argon. The few data available about the optical properties of plastic scintillator at cryogenic temperature they suggest that we should not expect significant changes compared to room temperature, but direct verification is mandatory.

IX. PHOTO-ELECTRONICS

The need for a reliable photosensor characterized by low intrinsic radioactivity and optimal performance at 87 K, led the DarkSide Collaboration to select the SiPMs as cryogenic photosensors to be operated in LAr. A long R&D started years ago in collaboration with the "Fondazione Bruno Kessler" (FBK). We tested several generations of FBK SiPM technologies have been tested with the aim of improving both the photosensor performance and the reliability at cryogenic temperature. The NUV-HD SiPMs were optimized to offer the highest quantum efficiently to photons with wavelength in the range 380-420 nm, while the so called "Low Field" (NUV-HD-LF) configuration showed a dark count rate at cryogenic temperature two orders of magnitude smaller than that of the standard field SiPMs. Further optimization of the poly-silicon quenching resistor behavior at 87 K allowed to improve the SiPM performance, comfortably fulfilling the DarkSide experiment requests:

At the beginning of 2017 the DarkSide collaboration demonstrated that, in spite of the high SiPM capacitance, a large area SiPM tile ($50 \times 50 \, mm^2$) can be successfully readout by a single electronic channel, preserving a signal to noise ratio (SNR) larger than 13. Each SiPM tile, made by 24 rectangular ($7.9 \times 11.7 \, mm^2$) SiPMs, coupled with a Front End Board (FEB), makes a Photo-Detector Module (PDM). The PDM has dimension $50 \times 50 \, mm^2$ and relies on an acrylic structure to cope the mechanic stress foreseen by cryogenic thermal cycles.

At the beginning of 2018 we built the first full Photo Detector Module (PDM), the equivalent of a PMT, based on SiPMs. The next foreseen milestone is the construction of the first SQB motherboard, equipped with 25 PDMs, a steering module for voltage distribution and opto-link driver for signal transmission through optical fibers.

The first $24 \, cm^2$ read-out with a single channel measurements were performed using the available NUV-HD-LF SiPMs, with area$10 \times 10 \, mm^2$. The number of SiPMs available was enough to mount three full tiles. Signals collected from the detector were analyzed using a digital filtering technique, using an optimal filter with $\tau = 400 \, ns$ (see Fig. 7), improving the signal to noise ratio and timing resolution. The SNR was obtained by dividing the difference between the mean values of the single and of the two-PE peak, divided by the standard deviation of the noise, obtained by extrapolating to zero the nth-PE peak. The measured SNR for the tiles was 10.5 to 13.8, well above the requirement. With these results, all specifications detailed in Ref. [9] for SiPMs and PDMs are now all successfully fulfilled.

The construction of the first PDM is one of the most important steps in the roadmap of the DarkSide-20k photo-electronics. A PDM is made of a SiPM tile, a Front End Board (FEB) and an acrylic mechanical structure. The PDM mechanics has to be fully compatible with the motherboard (MB) mechanics, expected to host up to 25 PDMs, allowing the easy replacement of any single PDM mounted on the MB.

Recently FBK produced an improved SiPM version, NUV-HD-LF 2018 edition, characterized by a triple concentration of their special dopant, offering a wider over-voltage operation range and effectively reducing the fraction of events with after-pulses. A SiPM run produced with this new technology was delivered at the beginning of January and tested shortly later by the DarkSide Collaboration. This was the first FBK run providing rectangular SiPMs ($7.9 \times 11.7 \, mm^2$), as requested by the DarkSide-20k tile geometry.

The SiPM run yield at warm temperature was quite high, of about 65 %, while at cryogenic temperature it dropped to 30 %. A first characterization was performed dicing a SiPM wafer and testing few tens of SiPMs in LN_2. These measurements showed that the I-V curves have a wide over-voltage region were SiPMs can comfortably work and a good break-down voltage uniformity. We selected 24 SiPMs with uniform I-V characteristics to make the first tile equipped with rectangular, NUV-HD-LF 2018 edition SiPMs. The PCB was manufactured with Arlon, the cleanest substrate we have identified insofar.
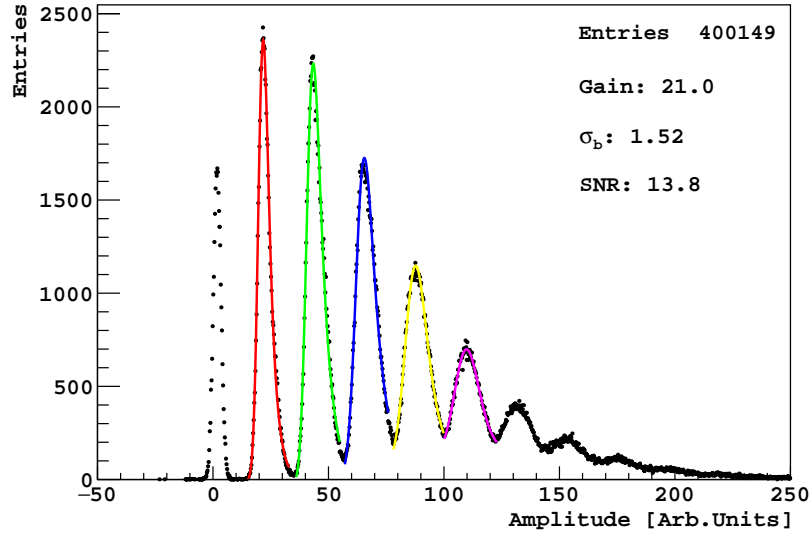
FIG. 7. Amplitude spectrum of the photoelectron peaks for the tile with 24 SiPMs (NUV-HD-LF 2016 edition).

The left side of Fig. 8 shows a snapshot of the first PDM. This tile implemented few changes with respect to the previous versions, including a new layout with the SiPM voltage divider on the backside of the PCB and power supply filtering by appropriate capacitors. The wafer dicing and the SiPM bonding was made at Princeton University, using a cryogenic epoxy on the SiPM backside, and a wire bonding procedure on the top. The tile was coupled with a FEB, whose design was basically the same we used at the beginning of 2017, with slight modifications with respect to the previous versions, to take advantage of a new cryogenic summing amplifier, OPA 838, with improved performance. The first PDM was assembled at LNGS during the first week of March and shortly after it experienced 10 thermal cycles, to verify its mechanical stability. As expected the thermal cycles did not show any issue. A full characterization of the SiPMs used to equip the first PDM is ongoing, to quantify the fraction of after-pulse events, the Dark count rate and the break-down voltage uniformity. A first preliminary measurement was performed by immersing the PDM in Liquid Nitrogen: the data analysis gave a SNR larger than 24, a factor of 2 better than the tiles equipped with the NUV-HD-LF 2017 edition SiPMs and the FEB produced in 2017, whose results were shown at the LNGS Scientific Committee meeting of April 2017.

The right side of Fig. 8 shows the filtered amplitude spectrum of the first PDM: the low after-pulse behavior of the new FBK NUV-HD-LF 2018 edition SiPMs is evident from the modest tail following each peak. The PDMdescribed above makes use of low radioactivity components: a broad screening campaign was made, including capacitors, resistors, electronic chips, metallic clips, and connectors. The radioactivity of all the PDM components, excluding the plastic of the two connectors between the tile and the FEB, and the connector between the FEB and the MB strips, is estimated at the level of about $1\,\mathrm{mBq/PDM}$. This is already a good result, compatible with the DarkSide radioactivity budget. Nevertheless, we are committed with an R&D to further decrease this number. The most important contribution to the above background comes from the Arlon substrates, whose screening gave an α activity of about $100\,\mathrm{mBq/kg}$. We are presently developing a fused silica substrate, that would drastically reduce this background. As far as the connector plastic is concerned, we are developing an acrylic equivalent of the plastic connector housing.
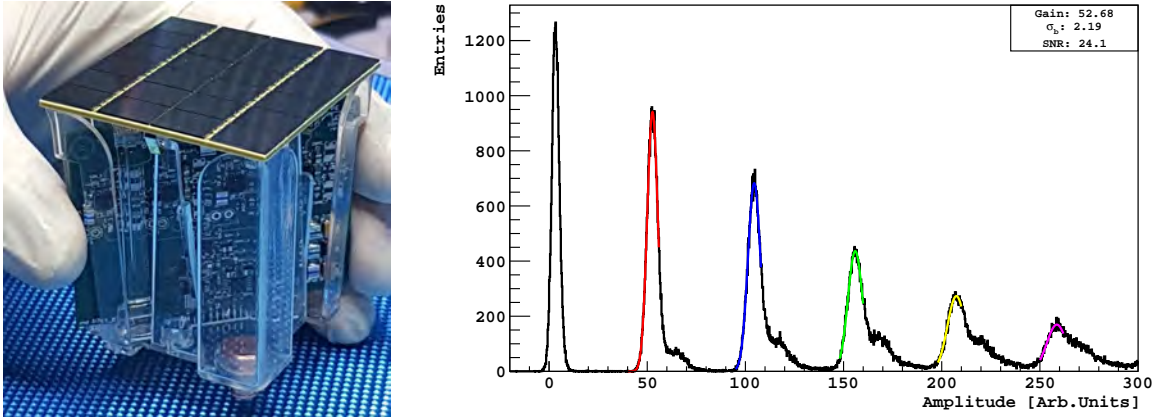
89

FIG. 8. **Left:** Snapshot of the first PDM. **Right:** Amplitude spectrum of signals of the first PDM (NUV-HD-LF 2018 with triple dopant concentration, preliminary result).

X. ARGON PROCUREMENT AND PURIFICATION

The UAr extraction and purification chain is one of the key points of the DarkSide-20k project, as well as the long term objectives of the Global Argon Dark Matter Collaboration that has begun to take shape. The Urania project makes up the effort to design and build a plant for extracting argon from the CO_2 from the Doe Canyon wells in Cortez, CO, USA, install and commission that plant on location in Colorado, and then actually do the extraction of the 50 t of argon required for DarkSide-20k. There is currently an advance conceptual design of the argon extraction plant, and a call for a bid for tender is set for 2018 for the final engineering and construction of the plant.

One of the last major decisions that needs to be folded into the plant design concerns the specific design of PSA plant that will perform the fine separation of CO_2 from the gas stream. A test plant was built at Università degli Studi di Napoli, to test various sorbents for use in the PSA to determine the most efficient, while being immune to poisoning from the other various components within the gas stream (CH_4, N_2, hydrocarbons, etc.). The test plant is now undergoing commissioning and results from the first round of sorbent are expected early in 2018.

The PNNL group has recently confirmed the presence of an air infiltration in the feed gas, which allows 30 ppm of air to be fed into the gas stream that not only supplied the pilot-plant which extract argon for DarkSide-50, but has been decided to be the input stream for the Urania plant. The long term gas analyzer (LOGAN), which PNNL installed at the Doe Canyon Facility to monitor the gas composition, was able to see that the composition of air at one point in the gas process was about 50 % with the other 50 % being CO_2. Taking this discovery by the PNNL group into consideration, and accounting for the amount of cosmogenic production of ^{39}Ar in the UAr during the storage and transportation before being inserted into DarkSide-50, it is a possibility that a fraction (or the majority) of ^{39}Ar observed in DarkSide-50 is of atmospheric origin. If we can mitigate the air infiltration completely, and manage the argon in the most efficient way possible, in terms of the length of time it sits above ground, then the potential for the reduction factor of ^{39}Ar to be greater than that measured in DarkSide-50 is quite high.

Additionally, the PNNL group is using LOGAN to make long-term measurements of the gas stream. both before and after tthe current helium removal. By doing this, we can determine how the composition of helium changes in the feed gas of Urania and determine if we will need to either continuously take into account small traces of helium, or if there are times when there are large fluctuations helium, and how often they occur. Already it has been seen that the helium content can fluctuate on a continuous basis, but at a very small scale, while there are large spikes in the helium concentration more than a few times per month. The Urania team will be working

90

to understand how we can receive warning of these helium spikes, and how we can then mitigate the problem from shutting down Urania operations.

The Urania Project has started to reshape into a much bigger effort with the joining of multiple Canadian groups to the team. Recent discussions have initiated the process of deciding how to best utilize the currently available funding from Canada, and how to then allocate the responsibilities and work load across the expanding effort, so to best utilize the resources the project will have available. There was a high level meeting held at the beginning of November in Ottawa, Canada, consisting of members of all three major players in the Urania Project (Canadian, Italian, and US Groups). At this meeting the financial responsibilities for the Urania project were decided, although based around discussions leading up to the meeting. Finally, it has been brought up that the Urania project also needs to look to the future, since the long term goal of the Global Argon Dark Matter Collaboration is to build a multi-hundred tonne detector, and so many hundred of tonnes of UAr will be required. The Urania team has begun to think about this effort and how the long term program may look, and this will evolve over conversations leading into the November meeting, however, this will not interfere with the effort being put towards the Urania project and the production of the $50\,\mathrm{t}$ of UAr required for DarkSide-20k.

The construction of Aria is ongoing. Cryostat modules are individually manufactured, then leak and pressure tested at the manufacturer under the guidance of a DarkSide team. The first 11 cryostat modules have been completed to date: these include the top module with the condenser, the bottom module with the reboiler, and the central modules with serial numbers 1 and 21 through 28 (note: the installation of Seruci-I will start from the bottom of the column, module 28). Upon completion, cryostat modules are shipped to CERN for the final leak test.

The CERN-based leak tests aim to validate the tightness of the internal process lines and external vacuum envelop of each fully assembled cryostat. So-called "global" leak tests were employed extensively on LHC cryostats. The same method is adopted for the Aria modules. Specifically, the CERN tests consist of leak-tightness at room temperature of individual modules (as defined in a CERN-Princeton Agreement (KN3155) and in the annexed technical document). There are a number of reasons for these tests to be performed at CERN: there are similarities between the LHC and Aria cryostats, and CERN has significant expertise and experience in high sensitivity leak testing of cryostats and in independent validation of complex assemblies prior to underground installation, not to mention the availability at CERN of specialized leak-testing equipment.

All the 11 cryostat modules completed so far have passed the final test at CERN, and have been validated and certified to comply with the design requirements: no leaks detected (rate increase $<10^{-9}\,\mathrm{mbar\,L/s}$) after reaching a stable baseline of the order of $10^{-9}\,\mathrm{mbar\,L/s}$ for the internal lines, and no leaks detected (rate increase $<10^{-9}\,\mathrm{mbar\,L/s}$) after reaching a stable baseline of the order of $10^{-8}\,\mathrm{mbar\,L/s}$ for their vacuum envelopes.

There are several hundred internal welds on the complex boiler and condenser modules. For this reason it was decided to proceed to a further test on the bottom module. The boiler module was chosen to be thermally cycled to $87\,\mathrm{K}$, followed by a repetition of the room temperature leak test. The tightness of the boiler module after thermal cycling to $87\,\mathrm{K}$ provides good confidence in the manufacturer's build quality (note: the bottom module was the first to be manufactured). It was therefore decided not to perform a thermal cycle on the other modules.

The 11 modules manufactured so far are ready for shipping to Carbosulcis. An agreement has been reached with INFN-Central Administration and Cagliari Custom Office. Completion of the procedure for the transfer of the modules to INFN is expected in October 2017, and in sequence the transfer of the first batch of modules to Sardinia is expected within the end of 2017. Production of the remaining 19 modules is due to resume in September 2017. Tests at CERN will resume shortly afterwards and will also be performed on 29 bellows sleeves of $0.7\,\mathrm{m}$ diameter required to join all modules on site in Sardinia.

Carbosulcis has completed at the end of August 2017 the refurbishment of the mine shaft that

will host Seruci-I. This very complex procedure required the careful removal and elimination of kilometers of tubing, piping, and electrical conduits. The refurbished winze, with its motors dating to the 1950's, is performing flawlessly. Carbosulcis is now switching its focus on procurement of the stainless steel platforms to be installed in the mine shaft to support the Seruci-I cryogenic distillation column.

The Aria group is also performing detailed simulations on the possible use of nitric oxide (NO) in the limited height Seruci-0 equipment, such as to extrapolate performance on argon separation for the Seruci-I column.

XI. READOUT

A larger TPC with as much as 8280 PDMs is being considered. This will offer several advantage for the physics reach of DarkSide-20k including the increased self shielding to external and radiogenic neutron backgrounds and additional sensitive volume for WIMP searches. The larger number of channels (+60%) would not alter significantly the DAQ design. as described above, with the exception of a modest increase in the bandwidth needed to connect the digitizer board to the HLST. However, it will constitute a significant cost increase, due to the extra digitization channels needed, beside the obvious cost increase due SiPMs, cold electroniscs, and optical connections for the analog signals.

Several mitigation strategies are thus considered. One possibility arises from the better than expected SNR of the latest SiPMs production with triple-doping, allowing higher gain of the SiPMs for the same level of dark count rate and after pulsing. It is then conceivable to further sums the signal from e.g. two adjacent PDMs, reducing thus the cost for the readout electronics by almost a factor two. Further studies are on-going to study the performance of such a scheme and to optimize the readout channel layout.

The new Veto design will require several photo-sensors operating in the LAr bath surrounding the TPC vessel, that will share as much as possible the same characteristic as the TPC PDMs. The number and placement of these detector element are not finalized yet but it is assumed that a number of O(1000) additional channels should be added to the DAQ system. This constitutes an increase of a factor 10 with respect to the old design, but on the other hand, the possibility to have the very same signal processing in the backend electronics providing the analog-to-digital conversion constitutes a significant simplification. Given the established performance of the DarkSide-20k photo-sensors and front-end electronics it is not expected that Veto detector would cause significant changes in the basic design highlighted above

The basic readout element of the proposed DarkSide-20k DAQ is a multi channel board hosting several fast ADCs linked to a large FPGA for digital signal processing and a host CPU for control, monitor and data formatting using as an output channel 1 Gbit/s to 10 Gbit/s ethernet connection to an external computer. The development of such board is an ongoing project at CAEN firm from Viareggio, Italy. The basic layout and components have been selected and is expected that first specimen of these boards will be available for testing at the end of 2018.

Specialized firmware is to be provided for noise filtering, basic data formatting and zero suppression in the FPGA. Possibility for custom trigger algorithm at the single board level is being also explored allowing for coincidence of discriminated hits. This FPGA has more than 650k logic elements. It is expected that about 40% of those will be available for the customized algorithms. The CPU will have direct access to DDR4 readout memory available also to the FPGA. On the ARM cpu an embedded version of the Linux OS will run allowing easy development and deployment of custom s/w for data processing and reduction as well as trasnmission over tcp/ip on the available 1GBE port. A similar, lab scale, project is being developed within Rome LABE (Electronic Lab). In this case a first prototype is currently under test and there is the possibility of an early testing
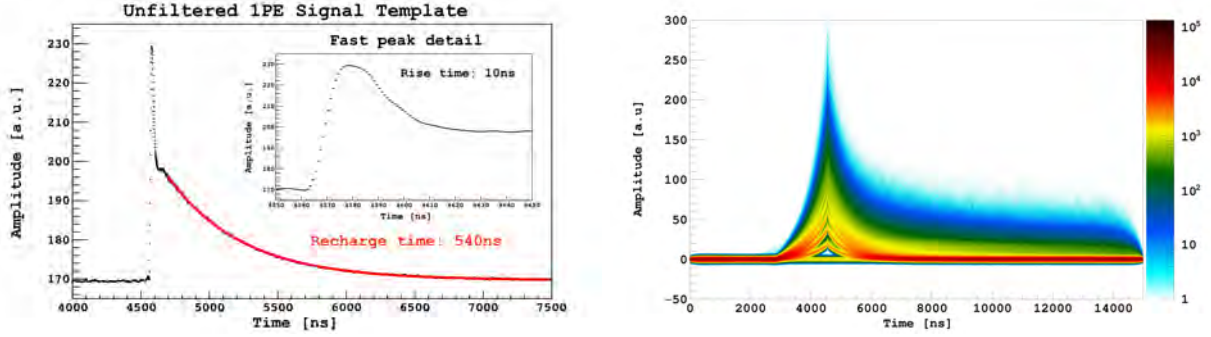
FIG. 9. **Left:** template of the 1 PE 24 cm^2 response. The measured rise time from 10% to 90% of the pulse height is 10 ns, the total duration of the fast peak is approximatively 40 ns and the measured recharge time is $\tau_{SCR} = 540$ ns. **Right:** persistence plot of 2×10^5 optimally filtered waveforms. More than 5 orders of photo-electrons are distinguishable. To the right of the primary peaks after-pulse events manifest themselves for several microseconds.

of some of elements of the readout scheme.

To eliminate excessive electronic noise per channel a matched filtering algorithm has been implemented to process the waveforms. The optimally filtered waveform is obtained convolving the digitized signal of the PDM with the time-reversed template of the single photo-electron response. The template necessary to perform the filtering is directly extracted from data. The left panel of Fig. 9 shows the 1 PE output of the SiPM tile used to reach the SNR and timing performances required. In the right panel of the same figure the result of the filtering process is plotted. The raw waveforms acquired with a 1 GS/s CAEN V1751 digitizer board in LNGS lab have been processed and time-aligned using as reference the leading edge of the laser trigger pulses. Several orders of photo-electrons are well identifiable.

Given the quasi-exponential shape of the template, the convolution process has the effect of a first order low-pass filter with cutoff frequency of $1/2\pi\tau_{SCR}$ on the baseline noise. This, together with the estimation of the SNR and of the 1 PE resolution obtained fitting the amplitude spectrum allows to make the estimation of the expected rate of fake hits after the matched filter use. Having set the discriminator threshold to 0.5 PE, the resulting rate of baseline induced hits is negligible (NR $< 10^{-3}$Hz/channel), whereas the signal detection efficiency is practically 100%. In these experimental conditions the only noise contribution expected is due to the SiPMs dark rate and their correlated noises. The use of a matched filtering technique, in addition to the SNR boost, also improves the timing resolution of the detector. This is just partly due to the reduction of the baseline noise. The maximum amplitude of the filtered waveform corresponds to the maximal superposition of the input waveform with the signal template, meaning that the whole information contained in the charge (*i.e.* the integral) of the SiPM pulse is used to form the filtered maximum. The time jitter for the 1 PE filtered waveforms is 16 ns, sufficiently good to effectively exploit the liquid argon pulse shape discrimination power. Very preliminary tests with the newer SiPM produced in recent FBK test runs with higher doping are even more promising showing the potential for better performance in terms of SNR and time resolution than discussed here.

The implementation of the matched filter algorithm on a Red Pitaya demonstrator is currently being carried out in the INFN section of Bologna. Preliminary tests of the system have been performed on a small LAr TPC at LNGS at the beginning s of 2018 with positive result. In the next step the online filter will be implemented in test boards that will be provided by CAEN soon that will emulate all the functions of the future DAQ board.

TABLE I. Expected β/γ and nuclear recoil (NR) backgrounds expected during the full DarkSide-20k exposure, based on current data and Monte Carlo simulations. The center column gives the total number of single-scatter events within the energy region of interest (ROI) before the application of the fiducial and veto cuts and the PSD. The right-most column is the total number of events surviving the veto cut, fiducial volume cut, and PSD. Internal β/γ background does *not* include the ^{39}Ar depletion expected from Aria.

Background	Events in ROI $[5 \ \mathrm{yr}]^{-1}$	Background $[100 \, \mathrm{t} \, \mathrm{yr}]^{-1}$
Internal β/γ's	3.1×10^8	0.06
Internal NRs	$\ll 10^{-3}$	$\ll 10^{-3}$
e^--ν_{pp} scatters	3.4×10^4	$\ll 10^{-3}$
External β/γ's	$<5 \times 10^4$	$\ll 10^{-3}$
External NRs (OC)	-	<0.07
Ext. NRs (TPC, PSV)	2.8	<0.015
Cosmogenic β/γ's	3×10^5	$\ll 0.01$
Cosmogenic NRs	-	<0.06
ν-Induced NR	2.7	1.6

XII. BACKGROUND SIMULATIONS

The background sources can be divided into three broad categories: 1) "Internal background" – ionizing events due to radioactive contamination and neutrino interactions in the active argon itself; 2) "External background" – ionizing events originating from radioactivity in the TPC, in the CV, in the surrounding AAr, in the PSV, in the OC, and in the rocks surrounding Hall C of the underground LNGS laboratory; 3) "Cosmogenic background" – ionizing events originating from the residual cosmic ray flux in Hall C.

As has already been discussed, the design of DarkSide-20k strongly reduces many of these backgrounds by features such as the use of UAr as a target material, the dual-phase LAr TPC design, and the nested detector system. To ensure that the science goals are achieved, the DarkSide Collaboration will implement a thorough system of controls based on background modeling, process and materials development, and materials radiopurity assay. The scope and prioritization of these activities will be informed by experience with DarkSide-50 [11, 12], collaborators' experience with other experiments, and the experience of the low-background community in general. A full background model of the detector has been built from the G4DS Monte Carlo simulation and is under continuous refinement. The model will lead to radiological and environmental limits for all aspects of the project, and will allow identification of materials, systems, and processes that pose the greatest risks. Much is already understood about the radiopurity of materials, techniques for removing low-level radioactive contamination, and methods for avoiding contamination (*e.g.*, from exposure to radon or dust).

The current state of the background estimates for the proposed 100 t yr exposure of DarkSide-20k is summarized in Tab. I.

XIII. RED

The ReD project has as its main objective the development of advanced calibrations for the new optical readout with electronic and nuclear recoils. Thanks to the support hereby guaranteed by INFN CSN2 we have built the LAr TPC and carried out the first runs with radioactive sources.

In the present configuration, the detector design closely follows that used in SCENE. The active volume is contained within a 46 mm diameter, 112 mm tall, PTFE support structure lined with 3M Vikuiti$^{\mathrm{TM}}$ enhanced specular reflector and capped by fused silica windows. The LAr is viewed

through the windows by two SiPM $50 \times 50\,\text{mm}^2$ tiles. The windows are coated with ITO, allowing for the application of electric field, and copper field rings mounted on the PTFE structure maintain field uniformity. All internal surfaces of the detector are evaporation-coated with TPB. A hexagonal stainless steel mesh is fixed at the top of the active LAr volume and electrically grounded to provide the drift field (between the bottom window and the mesh) and the extraction and amplification fields (between the mesh and the top window).

In 2017 the LAr TPC has been equipped with a SiPM custom tile manufactured by FBK placed on the bottom plane and readout with standard DarkSide-20k FEB; a second tile will be made as soon as the SiPMs are available. For the current run, the top plane optical readout is provided by a commercial SensL SiPMs array SensL-ArrayC-60035-64P and custom FEB. Gas pocket and HV commissioning were made up to drift field values (over $1.2\,\text{kV/cm}$) above the requirements for the experiment.

The commissioning runs allowed us to compare the light yield obtained with the photo-sensors demonstrating a similar or better performance of the FBK tiles with respect to that made with SensL SiPMs. Quenching measurements of the scintillation light were carried out according to the drift field (from $0\,\text{kV/cm}$ to $1\,\text{kV/cm}$) for electron-recoils at different energies using standard gamma calibration sources. The reconstruction code has been tested and improved for the next data taking campaign.

The commissioning of the TPC in double phase is currently under way with a new data acquisition software implemented by the INFN Roma 1 and INFN Napoli groups. The new code, based on a recent project for the PADME experiment at LNF, has demonstrated to be stable and more easily supported for future ReD developments due to its simplicity with respect to older legacy DAQ code previously used, and is almost ready to be adopted as a baseline.

The new dedicated cryogenic system is under construction. The delivery of the new cryostat will enable the neutron beam measurements. To this purpose, a d-d neutron gun provided by Temple University was installed and commissioned in Naples.

At the same time, the LNS beam line is being set up, with the design and procurement of the custom scattering chamber, whose blueprint has recently been finalized. The scattering chamber is optimized for the $p(^7\text{Li},^7\text{Be})n$ primary reaction (primary ^7Li beam delivered by the TANDEM at LNS). When delivered, the scattering chamber will mounted on the "70 deg" beam line at LNS and equipped with a Si detector in order to tag the associated ^7Be. The scattering chamber features a thin exit window ($0.4\,\text{mm}$ of aluminum) at about $25°$, in order to minimize parasitic neutron interactions on the path to the LAr TPC.

A full stand-alone Geant4-based simulation of the ReD set up has been written and validated, which was used for the preliminary feasibility studies and for the optimization of the set-up for the $p(^7\text{Li},^7\text{Be})n$ measurement at LNS. For instance, the outcome of the simulation was used as input for the design of the scattering chamber and to select the distance between the TPCand the liquid scintillator neutron detectors, as a fair trade-off between angular resolution and counting rate. The simulation has been also extended in order to simulate the energy and angular spectrum of neutrons from the d-d reaction, $e.g.$ from the Temple University neutron gun, or for a possible measurement at LNS with a dedicated d beam. In parallel, the ReD Monte-Carlo was fully incorporated into G4DS, an extensive Geant4-based modular framework in use for DarkSide-50 and DarkSide-20k. G4DS includes a rich set of particle generators and tuned physical processes, and, in particular, full optical propagation of photons produced by scintillation in LAr and by electroluminescense in GAr. The implementation for the ReD Monte Carlo consists of precise LAr TPC and cryostat

models, as well as a model for the liquid scintillator counters.

[1] P. Agnes et al. (The DarkSide Collaboration), arXiv:1802.07198v1 (2018).
[2] P. Agnes et al. (The DarkSide Collaboration), arXiv:1802.06994v1 (2018).
[3] P. Agnes et al. (The DarkSide Collaboration), arXiv:1802.06998v1 (2018).
[4] P. Agnes et al. (The DarkSide Collaboration), JINST **12**, P01021 (2017).
[5] P. Agnes et al. (The DarkSide Collaboration), JINST **12**, P10015 (2017).
[6] P. Agnes et al. (The DarkSide Collaboration), JINST **12**, T12004 (2017).
[7] P. Agnes et al. (The DarkSide Collaboration), JINST **12**, P12011 (2017).
[8] P. Agnes et al. (The DarkSide Collaboration), Nucl. Inst. Meth. A (2018).
[9] C. E. Aalseth et al. (The DarkSide Collaboration), Eur. Phys. J. Plus **133**, 131 (2018).
[10] P. Agnes et al. (The DarkSide collaboration), JINST **11**, P03016 (2016).
[11] P. Agnes et al. (The DarkSide Collaboration), Phys. Lett. B **743**, 456 (2015).
[12] P. Agnes et al. (The DarkSide Collaboration), Phys. Rev. D **93**, 081101 (2016).

GERDA

M. Agostini[o], A.M. Bakalyarov[m], M. Balata[a], I. Barabanov[k],
L. Baudis[s], C. Bauer[g], E. Bellotti[h,i], S. Belogurov[l,k],
A. Bettini[p,q], L. Bezrukov[k], T. Bode[o], V. Brudanin[e],
R. Brugnera[p,q], A. Caldwell[n], C. Cattadori[i], A. Chernogorov[l],
V. D'Andrea[a], E.V. Demidova[l], N. Di Marco[a], A. Domula[d],
E. Doroshkevich[k], V. Egorov[e], R. Falkenstein[r], A. Gangapshev[k,g],
A. Garfagnini[p,q], C. Gooch[n], P. Grabmayr[r], V. Gurentsov[k],
K. Gusev[e,m,o], J. Hakenmüller[g], A. Hegai[r], M. Heisel[g],
S. Hemmer[q], R. Hiller[s], W. Hofmann[g], M. Hult[f],
L.V. Inzhechik[k], J. Janicskó Csáthy[o], J. Jochum[r], M. Junker[a],
V. Kazalov[k], Y. Kermaidic[g], T. Kihm[g], I.V. Kirpichnikov[l],
A. Kirsch[g], A. Kish[s], A. Klimenko[g,e], R. Kneißl[n],
K.T. Knöpfle[g], O. Kochetov[e], V.N. Kornoukhov[l,k], V.V. Kuzminov[k],
M. Laubenstein[a], A. Lazzaro[o], M. Lindner[g], I. Lippi[q],
A. Lubashevskiy[g,e], B. Lubsandorzhiev[k], G. Lutter[f], C. Macolino[a],
B. Majorovits[n], W. Maneschg[g], M. Miloradovic[s], R. Mingazheva[s],
M. Misiaszek[c], P. Moseev[k], I. Nemchenok[e], K. Panas[c],
L. Pandola[b], A. Pullia[j], C. Ransom[s], S. Riboldi[j],
N. Rumyantseva[m,e], C. Sada[p,q], F. Salamida[i], C. Schmitt[r],
B. Schneider[d], J. Schreiner[g], O. Schulz[n], B. Schwingenheuer[g],
S. Schönert[o], A-K. Schütz[r], O. Selivanenko[k], E. Shevchik[e],
M. Shirchenko[e], H. Simgen[g], A. Smolnikov[g,e], L. Stanco[q],
L. Vanhoefer[n], A.A. Vasenko[l], A. Veresnikova[k], K. von Sturm[p,q],
V. Wagner[g], A. Wegmann[g], T. Wester[d], C. Wiesinger[o],

M. Wojcik[c], E. Yanovich[k], I. Zhitnikov[e], S.V. Zhukov[m],
D. Zinatulina[e], A.J. Zsigmond[n], K. Zuber[d], G. Zuzel[c]

^{a} INFN Laboratori Nazionali del Gran Sasso and Gran Sasso Science Institute, Assergi, Italy
^{b} INFN Laboratori Nazionali del Sud, Catania, Italy
^{c} Institute of Physics, Jagiellonian University, Cracow, Poland
^{d} Institut für Kern- und Teilchenphysik, Technische Universität Dresden, Dresden, Germany
^{e} Joint Institute for Nuclear Research, Dubna, Russia
^{f} European Commission, JRC-Geel, Geel, Belgium
^{g} Max-Planck-Institut für Kernphysik, Heidelberg, Germany
^{h} Dipartimento di Fisica, Università Milano Bicocca, Milan, Italy
^{i} INFN Milano Bicocca, Milan, Italy
^{j} Dipartimento di Fisica, Università degli Studi di Milano e INFN Milano, Milan, Italy
^{k} Institute for Nuclear Research of the Russian Academy of Sciences, Moscow, Russia
^{l} Institute for Theoretical and Experimental Physics, Moscow, Russia
^{m} National Research Centre "Kurchatov Institute", Moscow, Russia
^{n} Max-Planck-Institut für Physik, Munich, Germany
^{o} Physik Department and Excellence Cluster Universe, Technische Universität München, Germany
^{p} Dipartimento di Fisica e Astronomia dell'Università di Padova, Padua, Italy
^{q} INFN Padova, Padua, Italy
^{r} Physikalisches Institut, Eberhard Karls Universität Tübingen, Tübingen, Germany
^{s} Physik Institut der Universität Zürich, Zurich, Switzerland

Abstract

The GERmanium Detector Array (GERDA) experiment is searching for the neutrinoless double beta decay ($0\nu\beta\beta$) of the isotope ^{76}Ge. High-purity germanium crystals enriched in ^{76}Ge, simultaneously used as source and detector, are directly deployed into ultra-pure, cryogenic liquid argon, which acts both as cooling medium and shield against the external radiation. The second phase of the experiment is taking data since end of 2015 with 20 additional kg of custom-made BEGe-type Germanium detectors and an active LAr veto. The data release of June 2017 showed no evidence for a possible signal: the lower limit for the half-life of ^{76}Ge is $8.0 \cdot 10^{25}$ yr at 90% CL. The very low residual background found at the Q-value of the decay, about 10^{-3} cts/(keV·kg·yr), makes GERDA the first experiment in the field to be background-free for the complete design exposure of 100 kg·yr.

1 Introduction

The neutrinoless double beta decay ($0\nu\beta\beta$) is a hypothetical lepton-number-violating nuclear transition predicted by several extensions of the Standard Model of particle physics. Its detection would prove that neutrinos have a Majorana mass component and that lepton number is not conserved, thus providing a possible answer to the matter-antimatter asymmetry in the Universe and the origin of neutrino masses.

Searches for $0\nu\beta\beta$ are ongoing in a number of experiments around the world using different nuclei as ^{76}Ge, ^{136}Xe and ^{130}Te. The experimental signature of $0\nu\beta\beta$ is a peak in the distribution of the energy sum of two electrons at the Q-value of the decay ($Q_{\beta\beta}$). Typically only a few signal counts per kg per year are expected: a very strong suppression of all background sources and a high energy resolution are therefore required.

2 The GERDA experiment

The GERDA experiment, located at the underground Laboratori Nazionali del Gran Sasso (LNGS) of INFN in Italy, operates bare high-pure germanium detectors (HPGe) in liquid argon (LAr), which cools the detectors to their operating temperature of about 90 K and shields them from external radiation.

Figure 1 shows the setup of the experiment: the 64 m^3 LAr cryostat is contained in a 590 m^3 water tank, filled with ultra-pure water and equipped with photomultipliers, thus acting both as Cerenkov veto and additional shield. On the top of the water tank a clean room with a glove box and a lock is used for the assembly of HPGe detectors into strings.

The HPGes are arranged in an array of 6 strings hosting detectors enriched in ^{76}Ge (^{enr}Ge): 7 coaxial detectors from the former Heidelberg-Moscow and IGEX experiments, and 30 newly developed Broad Energy germanium (BEGe) detectors featuring superior pulse shape discrimination performance. The detector array is complemented with a central string instrumented with three coaxial detectors made from germanium of natural isotopic composition.

In Phase II, the cylindrical volume around the detector strings is instrumented with a curtain of wavelength-shifting fibres read out at both ends with 90 silicon photomultipliers (SiPMs). Sixteen low-background photomultipliers (PMTs) are mounted below and above of the HPGe array.

All Ge detectors are connected to low radioactivity charge sensitive amplifiers. The charge signal traces are digitized with a 100 MHz sampling rate and a total window of 160 μs. Data are stored on disk and analyzed offline.

3 Data taking and event selection

GERDA is taking data since 2011. Data from the first phase of GERDA (Phase I) gave no positive indication of the $0\nu\beta\beta$ decay with an exposure of about 21.6 kg·yr and a background index at the $Q_{\beta\beta}$= (2039.061 ± 0.007) keV of 10^{-2} cts/(keV·kg·yr). A lower limit on the half-life of the process of $T_{1/2}^{0\nu}$> 2.1 · 10^{25} yr (90% C.L.) was set.

The second phase (Phase II), is ongoing since December 2015 and initial results were released in June 2016 with 10.8 kg·yr of total exposure and a background index of 10^{-3} cts/(keV·kg·yr) [1]. In June 2017 new data collected up to April 15th 2017 have been fully validated and analyzed for a total exposure of 34.4 kg·yr of ^{enr}Ge (18.2 kg·yr from BEGe detectors and 16.2 kg·yr from coaxial detectors) [2].

The offline data analysis flow foresees a blind approach: events with a reconstructed energy in the interval $Q_{\beta\beta}$±25 keV are not analysed but only stored on disk. After the entire analysis procedures and parameters have been frozen, these blinded events are processed.

Unphysical events, originating from electrical discharges or bursts of noise, are rejected by a set of multi-parametric cuts based on the flatness of the baseline, polarity and time structure of the pulse. Physical events at $Q_{\beta\beta}$ are accepted with an efficiency greater than 99.9% while no unphysical event survives the cuts above 1.6 MeV.

In 92% of $0\nu\beta\beta$ decays occurring in the active detector volume, the total $0\nu\beta\beta$ energy is detected in that detector. Therefore multiple detector coincidences are discarded as background events. In order to discriminate time-correlated decays from primordial radioisotopes, such as the radon progenies ^{214}Bi and ^{214}Po, two consecutive candidate events within 1 ms are rejected. Candidate events are also rejected if a muon trigger occurred within 10 μs before a germanium detector trigger or if any of the LAr light detectors record a signal of amplitude above 50% of the expectation for a single photo-electron within 5 μs from the germanium trigger.
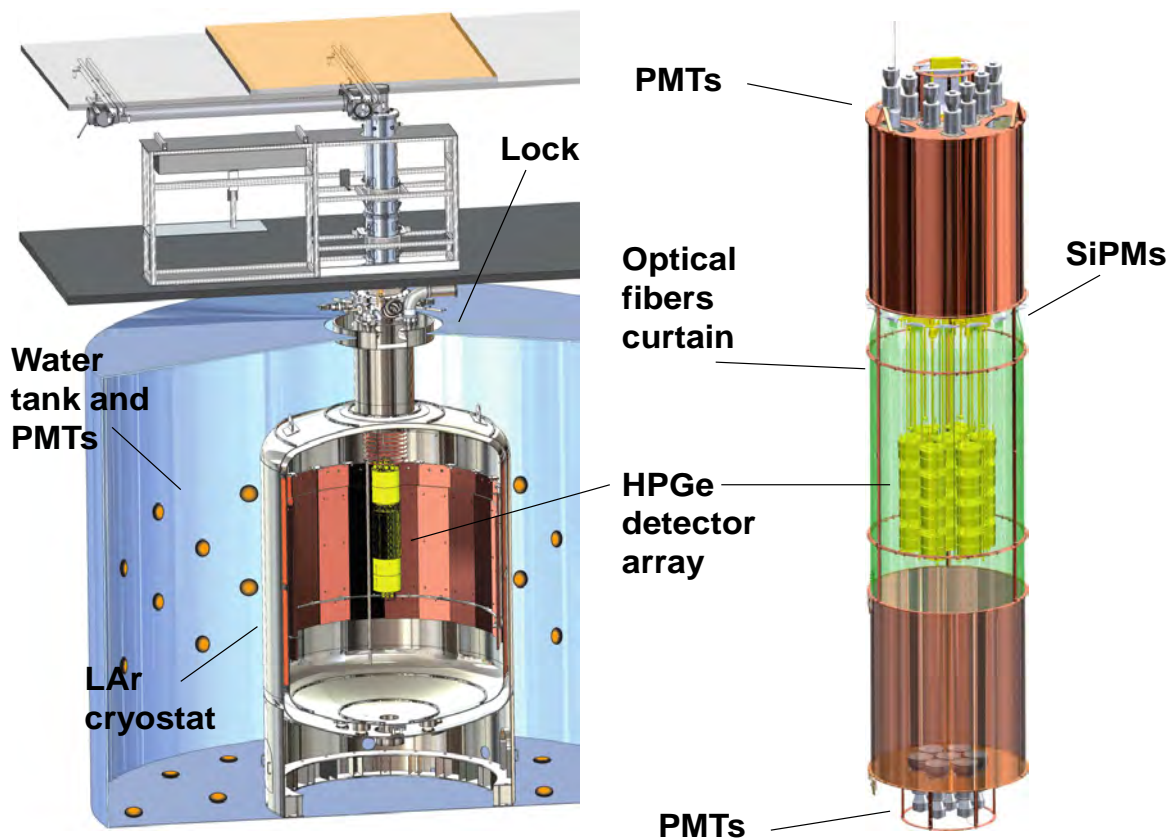
Figure 1: Schematic layout of the GERDA setup. The zoom in the right-hand side of the figure displays the inner part of the setup.

The deposited energy is reconstructed with an improved digital filter optimized for each detector and each calibration. The energy scale and resolution is set by taking weekly calibration with ^{228}Th sources. The stability of the scale is continuously monitored by injecting charge pulses (test pulses) with a rate of 0.05 Hz and, weekly, by checking the shift of the position of the 2615 keV γ line between two consecutive calibration (Fig. 2a). The average resolution at $Q_{\beta\beta}$, evaluated by using the calibration data, is shown in Fig. 2b; for coaxial detectors the width of the strongest γ lines in the physics data (1460 keV from ^{40}K and 1525 keV from ^{42}K) is found to be 0.5 keV larger than expected, probably due to gain instabilities in the corresponding readout channels between calibrations. The effect is accounted for by including a correction term; the average resolution at $Q_{\beta\beta}$ is 3.90(7) keV and 2.93(6) keV FWHM for the ^{enr}Ge coaxial and BEGe detectors, respectively.

Due to the short range of electrons in germanium ($\sim$1 mm), $0\nu\beta\beta$ decays produce a localized energy deposit. The time profile of the Ge current signal can be used to disentangle $0\nu\beta\beta$ decays (single-site events, SSE) from background events such as γ-rays, which mainly interact via Compton scattering with an average free path of $\sim$1 cm (multi-site events, MSE), or external α/β-rays, which deposit their energy on the detector surface. The geometry of the BEGe detectors allows the application of a simple mono-parametric Pulse Shape Discrimination (PSD) technique based on the maximum of the detector current pulse A normalized to the total energy
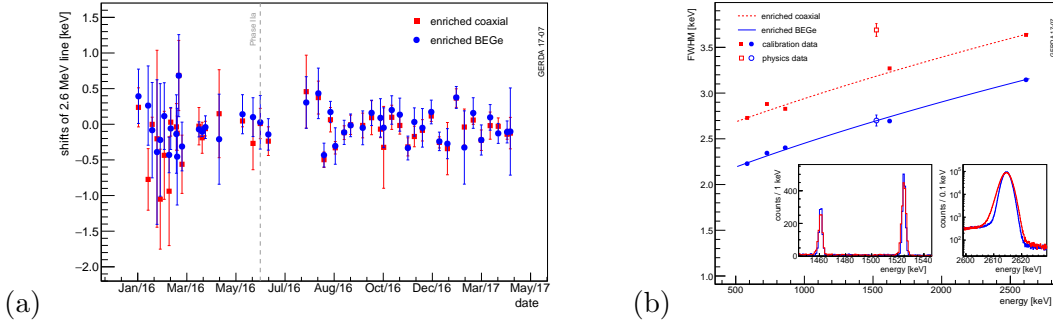
Figure 2: (a) Average shift of the 2615 keV γ-ray line between consecutive calibrations. The error bars represent the standard deviation of the shifts of the individual detectors. (b) Average energy resolution for γ lines observed in calibration data and in physics data, for the BEGe and coaxial detectors. The inset displays a zoom of the γ lines at 1460 keV (^{40}K) and 1525 keV (^{42}K) in physics data, and a zoom of the 2615 keV line from calibration data.

E. The cut on A/E allows to reject $> 90\%$ of (γ-like) MSEs and basically all α-like surface events, with a $0\nu\beta\beta$ selection efficiency of $(87 \pm 2)\%$. For coaxial detectors two neural network algorithms (ANN) are applied to discriminate SSEs from MSEs and from α surface events with a combined selection efficiency for $0\nu\beta\beta$ decays of $(79 \pm 5)\%$.

4 Statistical analysis and results

In June 2017, data from the BEGe detectors taken between June 1, 2016 and April 15, 2017 has been unblinded, providing an additional exposure of 12.4 kg·yr with respect to [1]. Two extra events passing all selection cuts are found in the blinded energy region; both of them being more than 15 keV away from $Q_{\beta\beta}$ (namely $> 10\sigma$) they cannot be attributed to $0\nu\beta\beta$ decay. Due to a recently identified background population not efficiently rejected by ANN PSD, data from coaxial detectors (11.2 kg·yr) were not unblinded. It will be unblinded in a future data release, when a new cut is developed to suppress this background. The background in the signal region is 10^{-3} cts/(keV·kg·yr) for BEGe detectors and 2.7×10^{-3} cts/(keV·kg·yr) for coaxials. The energy spectra around $Q_{\beta\beta}$ for Phase I, Phase II coaxial detectors and Phase II BEGe detectors (after all cuts) are shown in Fig. 3.

The total exposure available for analysis is (471.1 ± 8.5) mol·yr of ^{76}Ge. Both a frequentist and a Bayesian analysis, based on an unbinned extended likelihood function described in the Methods Section of Ref. [1], is performed. The fit function is a flat distribution for the background and a Gaussian centered at $Q_{\beta\beta}$ with a width according to the resolution for a possible $0\nu\beta\beta$ signal. The signal strength S $= 1/T_{1/2}^{0\nu}$ is calculated for each data set (both for Phase I and Phase II, for coaxial and BEGe detector respectively) according to its exposure and efficiency while the inverse half-life 1/T is a common free parameter. The analysis accounts for the systematic uncertainties due to efficiencies and energy resolutions, and to a possible offset in the energy scale. The limit on the half-life of ^{76}Ge is $T_{1/2}^{0\nu}> 8.0 \cdot 10^{25}$ yr (90% CL) (frequentist) and $T_{1/2}^{0\nu}> 5.1 \cdot 10^{25}$ yr (Bayesian), while the median sensitivity for the 90% CL lower limit of $T_{1/2}^{0\nu}$ is $5.8 \cdot 10^{25}$ yr (frequentist) and $T_{1/2}^{0\nu}> 4.5 \cdot 10^{25}$ yr (Bayesian) [3].
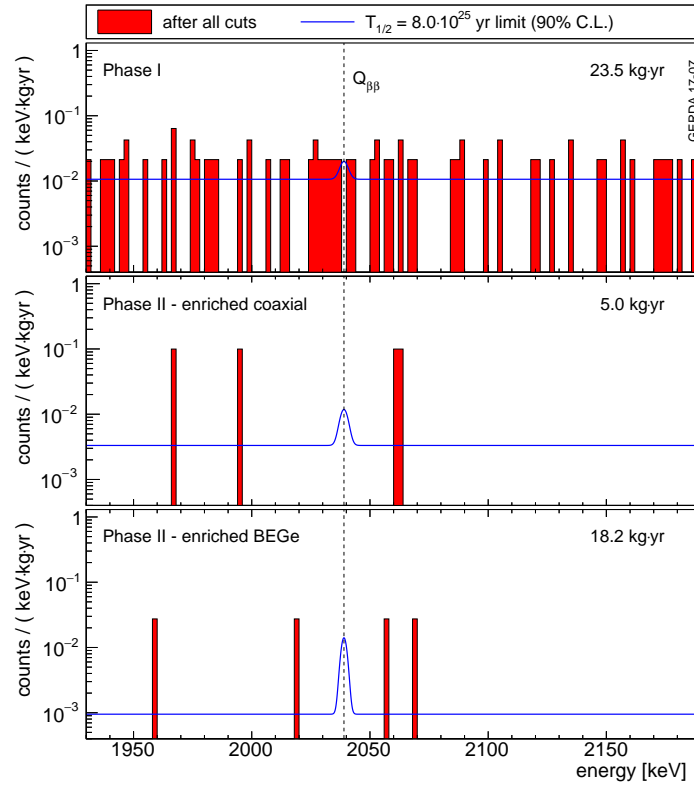
Figure 3: Energy spectra around $Q_{\beta\beta}$ for Phase I, Phase II coaxial detectors and Phase II BEGe detectors after all cuts. The binning is 2 keV. The blue lines show the hypothetical $0\nu\beta\beta$ signal for $T_{1/2}^{0\nu} = 8.0 \cdot 10^{25}$ yr, sitting on the constant background.

5 Conclusions

The GERDA experiment is currently taking data. The ambitious design goal for the background level of 10^{-3} cts/(keV·kg·yr) was fulfilled, thus, making GERDA the first "background-free" experiment for the whole design exposure; the sensitivity is therefore expected to grow linearly with the exposure and the median sensitivity is expected to reach 10^{26} yr within 2018. At present, thanks to the powerful pulse shape discrimination of BEGe detectors and to the detection of the argon scintillation light, GERDA has reached the world-best background index (BI) at $Q_{\beta\beta}$ if weighted with the energy resolution of the detectors.

The excellent performances in terms of background index and energy resolution motivates a future extension of the program in a medium term time scale. The LEGEND collaboration aims to build a 200 kg enriched germanium experiment using the GERDA cryostat. Such an experiment would remain background-free up to an exposure of 1000 kg·yr provided the background can be further reduced by a factor 5-10; thus LEGEND-200 [4] would allow to reach a half-life of 10^{27} yr. The 200 kg project is conceived as a first step towards a more ambitious 1-ton experiment that would allow to reach a sensitivity of 10^{28} yr, thus, fully covering the inverted hierarchy region in ten years of data taking.

6 Other works

6.1 Limits on uranium and thorium bulk content in Gerda Phase I detectors.

Internal contaminations of ^{238}U, ^{235}U and ^{232}Th in the bulk of high purity germanium detectors are potential backgrounds for experiments searching for neutrinoless double beta decay of ^{76}Ge. The data from Gerda Phase I have been analyzed for alpha events from the decay chain of these contaminations by looking for full decay chains and for time correlations between successive decays in the same detector. No candidate events for a full chain have been found. Upper limits on the activities in the range of a few nBq/kg for ^{226}Ra, ^{227}Ac and ^{228}Th, the long-lived daughter nuclides of ^{238}U, ^{235}U and ^{232}Th, respectively, have been derived. With these upper limits a background index in the energy region of interest from ^{226}Ra and ^{228}Th contamination is estimated which satisfies the prerequisites of a future ton scale germanium double beta decay experiment [5].

6.2 Pulse shape discrimination studies with a dedicated setup.

Pulse shape discrimination is an important handle to improve sensitivity in low background experiments. A dedicated setup was built to investigate the response of high-purity germanium detectors to single Compton scattered events. Using properly collimated γ-ray sources, it is possible to select events with known interaction location. The aim is to correlate the position dependent signal shape with geometrical and electrical properties of the detector. The design and the performance of the setup with a first look on data are reported in [6].

6.3 Mitigation of ^{42}Ar/^{42}K background for the GERDA Phase II experiment.

Background coming from the ^{42}Ar decay chain is considered to be one of the most relevant for the GERDA experiment, which searches for the neutrinoless double beta decay of ^{76}Ge. The sensitivity strongly relies on the absence of background around the Q-value of the decay. Background coming from ^{42}K, a progeny of ^{42}Ar, can contribute to that background via electrons from the continuous spectrum with an endpoint at 3.5 MeV. Research and development on the

suppression methods targeting this source of background were performed at the low-background test facility LArGe . It was demonstrated that by reducing ^{42}K ion collection on the surfaces of the broad energy germanium detectors in combination with pulse shape discrimination techniques and an argon scintillation veto, it is possible to suppress ^{42}K background by three orders of magnitude. This is sufficient for Phase II of the GERDA experiment [7].

6.4 Pulse shape discrimination performance of Inverted Coaxial Ge detectors.

The characterization of two inverted coaxial Ge detectors in the context of being employed in future ^{76}Ge neutrinoless double beta decay experiments has been studied in [8]. It is an advantage that such detectors can be produced with bigger Ge mass as compared to the planar Broad Energy Ge (BEGe) or p-type Point Contact (PPC) detectors that are currently used in the Gerda and Majorana Demonstrator $0\nu\beta\beta$decay experiments respectively. This will result in a lower background for the search of $0\nu\beta\beta$decay due to a reduction of detector surface to volume ratio, cables, electronics and holders which are dominating nearby radioactive sources. The measured resolution near the ^{76}Ge Q-value at 2039 keV is 2.3 keV FWHM and their pulse-shape discrimination of background events are similar to BEGe and PPC detectors. It is concluded that this type of Ge-detector is suitable for usage in ^{76}Ge $0\nu\beta\beta$decay experiments.

References

References

[1] Agostini M *et al.* (GERDA) 2017 *Nature* **544** 47

[2] Agostini M *et al.* (GERDA) 2017 Searching for neutrinoless double beta decay with GERDA *15th International Conference on Topics in Astroparticle and Underground Physics (TAUP 2017) Sudbury, Ontario, Canada, July 24-28, 2017* (*Preprint* 1710.07776) URL http://inspirehep.net/record/1632043/files/arXiv:1710.07776.pdf

[3] Agostini M *et al.* (GERDA) 2018 *Phys. Rev. Lett.* **120** 132503 (*Preprint* 1803.11100)

[4] Abgrall N *et al.* (LEGEND) 2017 *AIP Conf. Proc.* **1894** 020027 (*Preprint* 1709.01980)

[5] Agostini M *et al.* (GERDA) 2017 *Astropart. Phys.* **91** 15–21 (*Preprint* 1611.06884)

[6] von Sturm K, Belogurov S, Brugnera R, Garfagnini A, Lippi I, Modenese L, Rosso D and Turcato M 2017 *Appl. Radiat. Isot.* **125** 163–168

[7] Lubashevskiy A *et al.* 2018 *Eur. Phys. J.* **C78** 15 (*Preprint* 1708.00226)

[8] Domula A, Hult M, Kermaidic Y, Marissens G, Schwingenheuer B, Wester T and Zuber K 2018 *Nucl. Instrum. Meth.* **A891** 106–110 (*Preprint* 1711.01433)

LUNA: Laboratory for Underground Nuclear Astrophysics

M. Aliotta[a], D. Bemmerer[b], A. Best[c], A. Boeltzig[d], C. Broggini[e], C. Bruno[a], A. Caciolli[f], F. Cavanna[g], L. Csedreki[i], T. Chillery[a], G. F. Ciani[d], P. Corvisiero[g], T. Davinson[a], R. Depalo[f], G. D'Erasmo[i], A. Di Leva[c], L. di Paolo[h], Z. Elekes[j], F. Ferraro[k], E. M. Fiore[i], A. Formicola[h], Zs. Fülöp[j], G. Gervino[l], A. Guglielmetti[m], C. Gustavino[n], Gy. Gyürky[j], G. Imbriani[c], M. Lugaro[o], P. Marigo[f], V. Mossa[i], M. Junker[h], I. Kochanek[h], R. Menegazzo[e], F. R. Pantaleo[i], V. Paticchio[i], R. Perrino[p], D. Piatti[f], P. Prati[k], L. Schiavulli[i], K. Stöckel[b], O. Straniero[q], T. Szücs[j], M. P. Takács[b], D. Trezzi[m], A. Valentini[i], S. Zavatarelli[g]

SPOKESPERSON: P. PRATI

[a]University of Edinburgh, Edinburgh, United Kingdom
[b]Helmholtz-Zentrum Dresden-Rossendorf, Dresden, Germany
[c]Università degli Studi di Napoli "Federico II", and INFN, Napoli, Italy
[d]Gran Sasso Science Institute (GSSI), L'Aquila, Italy
[e]INFN, Padova, Italy
[f]Università degli Studi di Padova and INFN, Padova, Italy
[g]INFN, Genova, Italy
[h]Università degli Studi di Bari and INFN, Bari, Italy
[i]INFN, Laboratori Nazionali del Gran Sasso (LNGS), Assergi (AQ), Italy
[j]Institute for Nuclear Research (MTA ATOMKI), Debrecen, Hungary
[k]Università degli Studi di Genova and INFN, Genova, Italy
[l]Università degli Studi di Torino and INFN, Torino, Italy
[m]Università degli Studi di Milano and INFN, Milano, Italy
[n]INFN, Roma, Italy
[o]Monarch University Budapest, Budapest, Hungary
[p]INFN, Lecce, Italy
[q]Osservatorio Astronomico di Collurania, Teramo, and INFN Napoli, Italy

Abstract

Aim of the LUNA experiment is the direct measurement of the cross section of nuclear reactions relevant for stellar and primordial nucleosynthesis. The year 2017 was dedicated to experiments on the ^{2}H(p,γ)^{3}He, ^{6}Li(p,γ)^{7}Be and ^{13}C(α,n)^{16}O reactions. Data analysis to extract the cross section at astrophysical energies for the processes ^{22}Ne(p,γ)^{23}Na, ^{23}Na(p,γ)^{24}Mg and ^{18}O(p,γ)^{19}F reactions was also completed. Relevant progresses have been achieved in the development of the LUNA-MV project carried out in the same period of the LUNA activities and new progresses were obtained.

1 The ^{6}Li(p,γ)^{7}Be reaction

The ^{6}Li(p,γ)^{7}Be reaction takes part in Big Bang Nucleosynthesis and contributes to lithium depletion during the pre-main sequence phase of stellar evolution. Its cross section is poorly constraint at the energies of astrophysical interest, especially since the discovery of a resonance at center of mass energy of 195 keV [1].
A new direct measurement of the ^{6}Li(p,γ)^{7}Be cross section was started at LUNA in December 2016. First a feasibility test was performed, in which the experimental setup was mounted and tested, then seven weeks of data taking were performed between March and September 2017. The experimental setup consisted in a scattering chamber with water-cooled target holder, an HPGe detector mounted in close geometry at 55° from the beam direction and a silicon detector mounted at 145° used to detect charged particles from the competing reaction ^{6}Li(p,α)^{3}He. At LUNA, the ^{6}Li+p excitation function was measured on six different targets of three different types: evaporated lithium oxide targets, evaporated lithium tungstate targets and an infinitely thick lithium chloride target. All targets were enriched in ^{6}Li at the 95% level. The proton beam energy range between 80 and 400 keV was explored, spanning completely the energy range of the new tentative resonance. Target stability was periodically checked by measuring the reaction yield at a reference energy. All targets proved to be stable against beam irradiation (target deterioration was always < 20%).
The targets used for the LUNA measurements have been characterized at the Helmholtz-Zentrum Dresden-Rossendorf (HZDR) using two independent techniques: Nuclear Reaction Analysis (NRA, 1 week of beam time in July 2017) and Elastic Recoil Detection Analysis (ERDA). Combining the results from the two techniques it is possible to obtain a complete characterization of the targets: while ERDA provides the abundances of different light elements in the target, NRA provides a more detailed distribution of the ^{6}Li as a function of the depth. Figure 1 shows typical ^{6}Li+p peaks as observed with the HPGe detector irradiating a 130 μg/cm^2 thick lithium tungstate target and a scan obtained at HZDR for the same target. The data analysis to extract the cross section from the measured yield is presently ongoing.

2 The ^{2}H(p,γ)^{3}He reaction

The primordial abundance of deuterium, (D:H)$_{obs}$, is presently known with good accuracy, (D:H)$_{obs}$= (2.53 $\pm$ 0.04) 10^{-5} [3], while the corresponding (D:H)$_{BBN}$ obtained from the BBN calculations, (D:H)$_{BBN}$ = (2.65 $\pm$ 0.07) 10^{-5} [4], is affected by a 3% uncertainty due to the insufficient knowledge of S$_{12}$ in the relevant energy interval. Only a single dataset of S$_{12}$ is available in the relevant energy range [?] and, according to the Authors, it is affected by a systematic error of 9%. The situation is even worst when considering a 20% discrepancy of that data with the theoretical previsions [5]. For all these reasons an experimental effort to measure the cross section with 3-5% accuracy is needed.
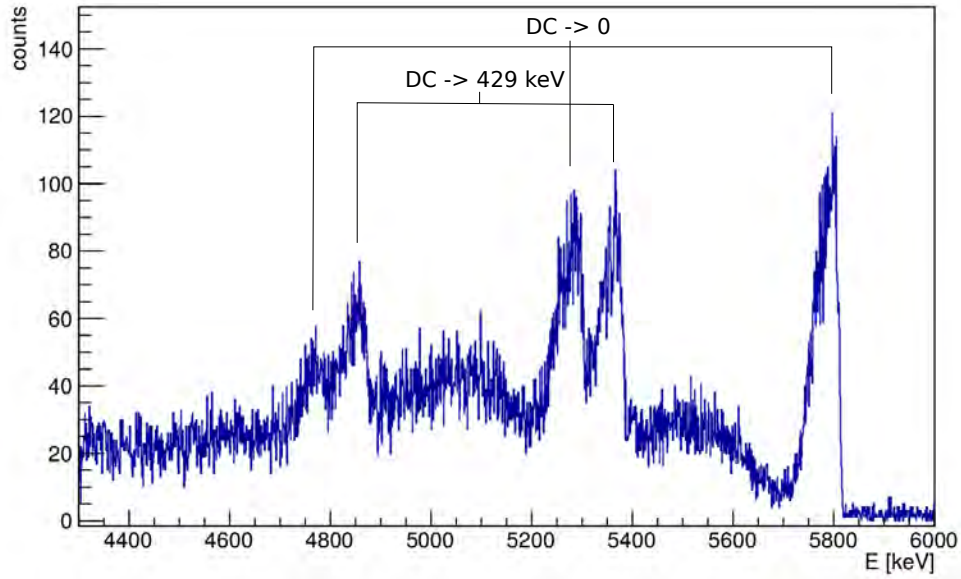
Figure 1: ^{6}Li(p,γ: detail of the in-beam γ spectrum measured by a HpGe detector. (left) and a typical resonance scan (right) to characterize the target depth and deterioration.
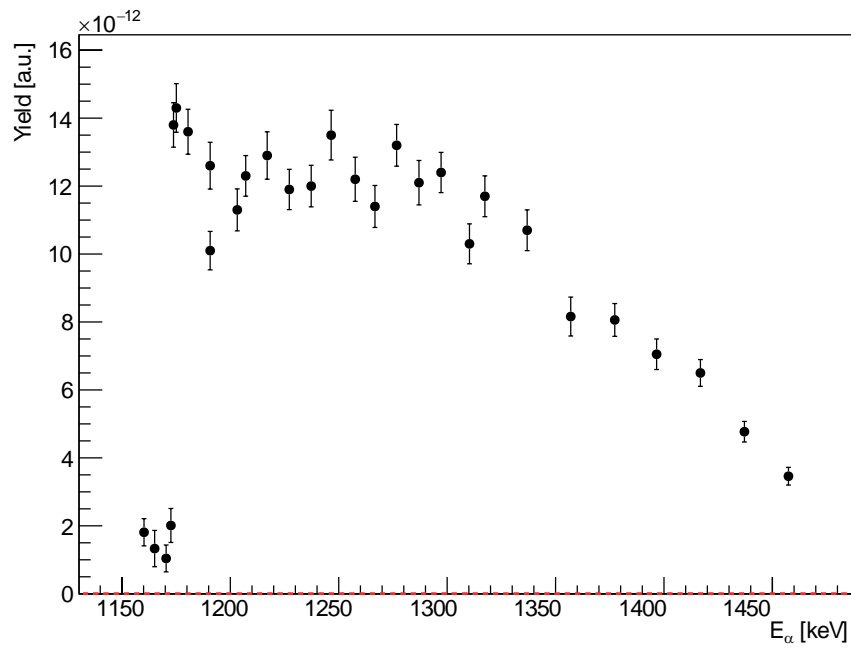

Figure 2: ^{6}Li(p,γ: a typical resonance scan (right) to characterize the target depth and deterioration.

The ^{2}H(p,γ)^{3}He experiment at LUNA consists of two main phases characterized by different setups. The former is a windowless gas target filled with deuterium surrounded by a 4π BGO detector [2]. The data taking as well as the analysis of this phase have been concluded and the results will be published as soon as also the second phase will be over. The set up of this latter phase consists of a 137% HPGe detector in close geometry with the interaction chamber. With this setup the angular distribution can be inferred by exploiting the high energy resolution of the detector and the Doppler effect responsible for the broad energy distribution of the detected gamma rays coming from different directions inside the extended gas target. The ^{2}H(p,γ)^{3}He photons have an energy of about 5.5 MeV, far away from the energy of the commonly used radioactive sources. Thus, for determining the setup efficiency a different technique based on the well-known resonant reactions ^{14}N(p,γ)^{15}O and on ^{60}Co radioactive decay has been used. In order to reduce the systematic error due to the summing correction, the set-up efficiency has been measured exploiting the coincidence between two γ-rays emitted in cascade (from source as well as from reaction) and detected by two different germanium detectors, the main detector (Ge1) and a second one used as the acquisition trigger (Ge2). Whenever Ge2 detects an event 1, it enables Ge1 that can thus detect photon 2 emitted in cascade: the ratio of the observed photons with respect to the number of triggers provides the Ge1 efficiency. In case of ^{60}Co, for each radioactive decay process, two photons, 1 = 1.17 MeV and 2 = 1.33 MeV, are produced. In the case of the resonant capture, several decay branches are able to provide two photons in cascade of energies up to 6.7 MeV, even higher than the ^{2}H(p,γ)^{3}He reaction. This method allows fixing precisely the detector energy response (fig. 3).

To measure the cross section we did a scan in the energy range of interest (30 keV $<$ E$_{cm}$ $<$ 300keV) with 30-50 keV steps; two runs were performed for each energy: one with deuterium gas inside the scattering chamber, the other with ^{4}He in order to evaluate the beam induced background contribution and the eventual deuterium implantation. The data taking has been completed, the analysis is ongoing.

3   The ^{22}Ne(p,γ)^{23}Na reaction

The ^{22}Ne(p,γ)^{23}Na reaction is important for hydrogen burning in AGB stars, novae and possibly also the simmering phase preceding type Ia supernovae. Its reaction rate at the relevant temperatures is controlled by a number of resonances and by the direct capture component. This reaction has been studied at LUNA in two phases.

The first phase (with two HPGe detectors placed at 55° and 90° with respect to the beam direction) is now completed and results have been reported in two different papers [6, 7]. Three resonances (156.2, 189.5, and 259.7 keV) have been directly observed for the first time and for other three (71, 105, and 215 keV,) improved upper limits on the strength were given. The LUNA result reduces greatly the uncertainties compared to NACRE [8] and STARLIB [9] and changes the central value. The impact of the new LUNA data has been evaluated into AGB stellar models showing a drastic reduction of the uncertainties on the element abundances [10]. A second phase, characterized by a high efficiency setup (4π BGO), described in details in [11], provided a reduction of the upper limit of the 71 keV and 105 keV resonances by a factor of 25 and 100, respectively. We have also measured the direct capture component at 4 energies, between 200 and 360 keV.
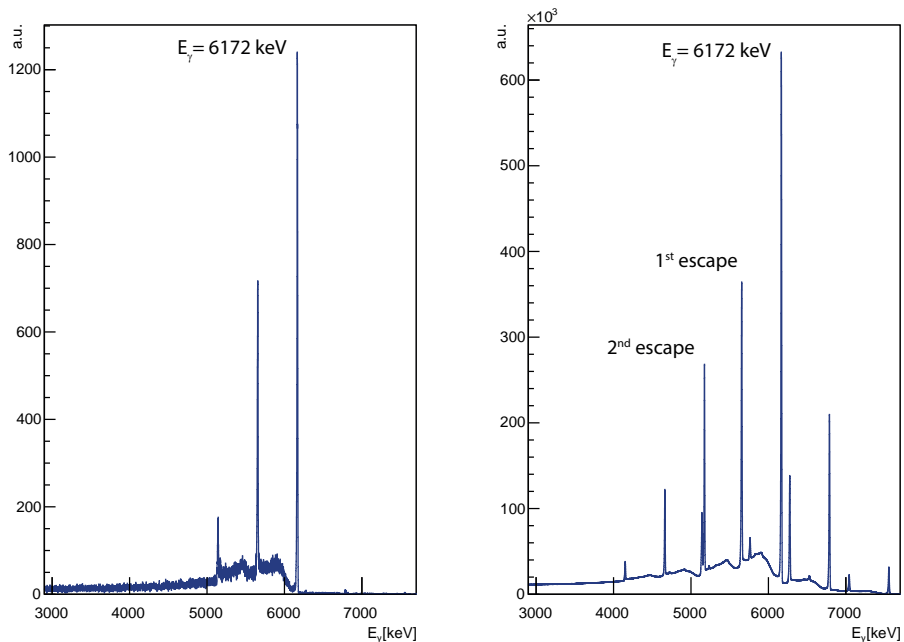
Figure 3: $^{14}\text{N}(p,\gamma)^{15}\text{O}$ Resonance spectra: left the one acquired in coincidence configuration, right the one acquired in inclusive configuration

4 Study of the $^{22}\text{Ne}(\alpha,\gamma)^{26}\text{Mg}$ reaction

This reaction is a competitor to the $^{22}\text{Ne}(\alpha,\text{n})^{25}\text{Mg}$ neutron source for the astrophysical s-process. In the energy range of LUNA400, only $^{22}\text{Ne}(\alpha,\gamma)^{26}\text{Mg}$ is energetically possible: the $^{22}\text{Ne}(\alpha,\text{n})^{25}\text{Mg}$ channel opens only above the reaction threshold of $E_\alpha > 564$ keV. The study of $^{22}\text{Ne}(\alpha,\text{n})^{25}\text{Mg}$ is part of the LUNA-MV science case.

There is a possible resonance in $^{22}\text{Ne}(\alpha,\gamma)^{26}\text{Mg}$ at $E_\alpha = 395$ keV, which is presently only constrained by indirect data, with reported upper limits in the 10^{-9} - 10^{-13} eV range. If confirmed at the 10^{-9} eV level, the 395 keV resonance would effectively shut down the $^{22}\text{Ne}(\alpha,\text{n})^{25}\text{Mg}$ neutron source for temperatures below 300 MK, affecting a wide range of astrophysical s-process scenarios.

Using an enriched ^{22}Ne gas target and the experimental setup from the $^{22}\text{Ne}(p,\gamma)^{23}\text{Na}$ experiment with the 4π BGO, an attempt has been made to observe or disprove the existence of such a resonance. The preliminary analysis of the first data shows no additional beam-induced background, confirming the sensitivity of the setup, and no resonance signal. The feasibility test has proven that an upper limit on the resonance strength of 10^{-10} eV can be achieved. Further improvements, with a new borated polyethylene shielding are foreseen and will be implemented during the beam-time of March-May 2018.

5 The $^{13}\text{C}(\alpha,\text{n})^{16}\text{O}$ reaction

The $^{13}\text{C}(\alpha,\text{n})^{16}\text{O}$ reaction is the major neutron source in low mass AGB stars: the temperature of interest is around 1 - 2 10^8 K which translates into an effective energy range between 120 and

250 keV.

In this last year two main milestones have been achieved and successfully completed: the final configuration of the neutron detector and the study of ^{13}C targets. The ^{3}He LUNA counters, an array composed of 18 counters, have been characterized in terms of internal background, and arranged in the final configuration inside a polyethylene moderator, at the moment installed in the beam line of the LUNA 400kV accelerator. In Figure 2 is shown the comparison between LUNA counters, and Notre Dame counters (this array has been used in a campaign to characterize the neutron flux of some international deep underground laboratories [12]): the complete analysis of the runs gave an activity of 1.6 10^{-6} alpha cm^{-2} s^{-1}, and 6 10^{-5} alpha cm^{-2} s-1, for the LUNA and the Notre Dame counters, respectively. This means that the intrinsic activity of the new LUNA counters is a factor of 37 lower, which is a key feature for a successful measurement of the low energy ^{13}C(α,n)^{16}O cross section. An extensive production of evaporated targets enriched in ^{13}C at 99% on tantalum backing has been done in MTA-ATOMKI, Debrecen. The target characterization has been performed using the reaction ^{13}C(α,n)^{16}O. Figure 4 shows a sample of the thick-target γ-ray yield curve of the E$_{R,lab}$ = 1748 keV resonance. The sharp front edge is determined by the convolution of the beam resolution and the natural width of the resonance; this is followed by a constant plateau. The ^{13}C atoms are nearly homogeneously distributed from the surface to a depth of 4-5 keV at half maximum. The high energy tail is due to the effects of energy straggling of the proton beam. The reproducibility and the thickness of the targets have been confirmed by several measurements.

Last commitment was the developing of the target chamber: it has been completely commissioned, and a new the target holder is built in a way to mount three targets at the same time and to select one of them for the measurement without breaking the vacuum system of the target chamber. The complete experimental setup, presently in operation at LUNA, is shown in Figure 5.

The steps for the next semester include: to finalize the PSD analysis and the submission of the relative paper, to complete the cross section measurements in the low energy range, to perform the efficiency measurements of the detector setup above ground in the MTA-ATOMKI laboratory. Data taking will continue in different runs at least to the end of 2018.

6   LUNA MV

The LUNA MV accelerator will provide intense beams of H$^+$, ^{4}He$^+$, ^{12}C$^+$ e ^{12}C^{++} in the energy range: 350 keV - 3.5 MeV. The procedure related to the accelerator supply is under the responsibility of the RUP (Responsible of the Procedure), G. Imbriani (University and INFN Neaples) while the designer and DEC (Executive Work Director) is M. Junker (INFN-LNGS).The technical coordinator (TC) for all the activities related to site preparation is L. Di Paolo, a LNGS engineer. Di Paolo is also GLIMOS and RAE for the LUNA-MV project. The LUNA Spokesperson, P. Prati (University and INFN-Genoa), is also the LUNA-MV Principal Investigator. The budget allocated to the project derives from a grant of the Italian Ministry of Research (MIUR) for a total of 5.3 M.

A proposal for the scientific program at LUNA-MV has been submitted to LNGS and INFN in July 2016. The proposal considers only the first five year of operation of the future LUNA-MV accelerator even if the scientific life of the new laboratory will be much longer (likely not less than 30 years). The scientific case for such five-year period is detailed in the proposal: briefly the plan is to measure the cross section of four processes: ^{14}N(p,γ)^{15}O (the bottleneck of the CNO cycle, already studied at LUNA in the past but still uncertain due to a high energy discrepancy), ^{12}C+^{12}C (the key process for Carbon burning), ^{13}C(α,n)^{16}O and ^{22}Ne(α,n)^{25}Mg
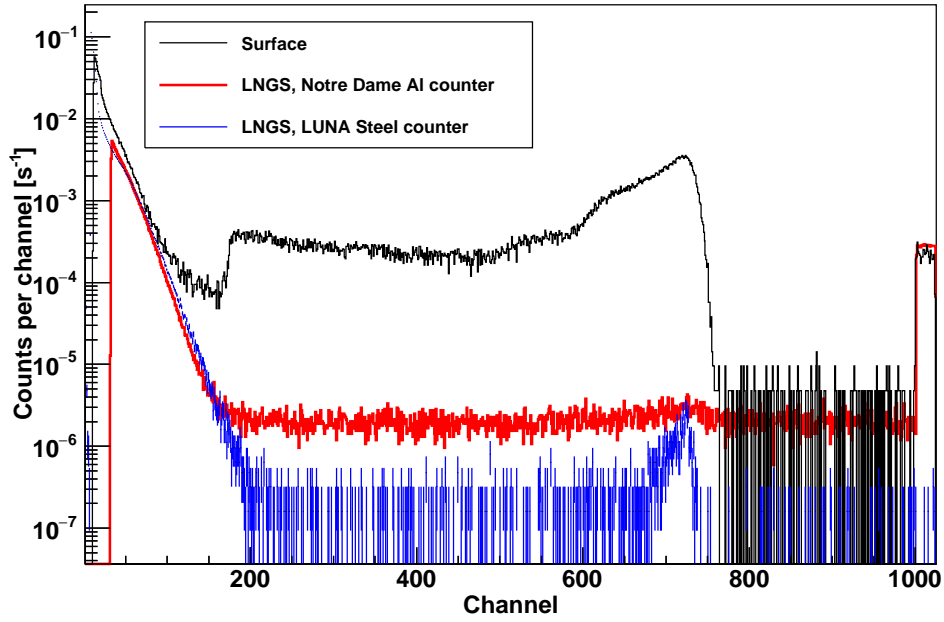
Figure 4: Background spectra measured at surface and deep underground at LNGS by standard (red) and low intrinsic activity (blue) ^{3}He counters. The latter have been selected to build the new LUNA neutron detector.
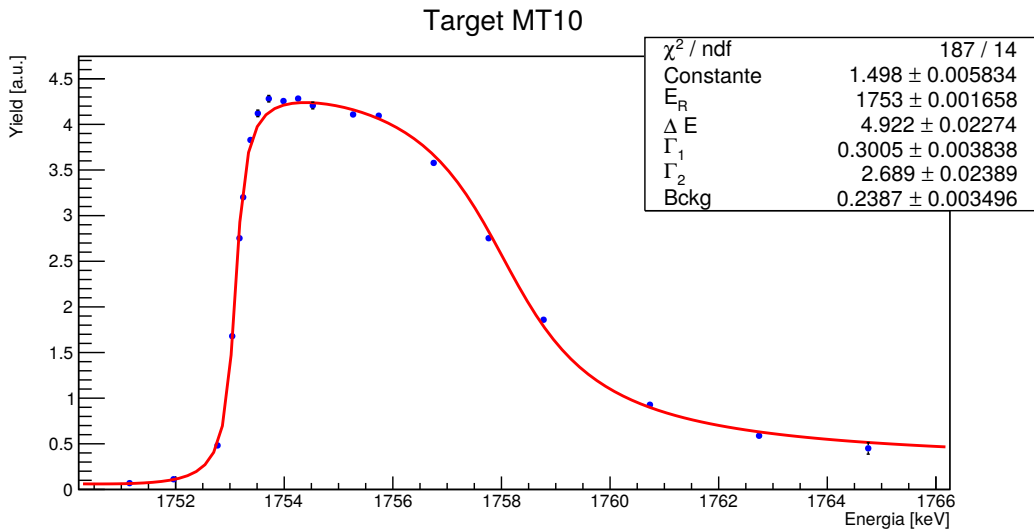

Figure 5: Thick-target γ-ray yield curve of the $E_{R,lab} = 1748$ keV resonance for one of the ^{13}C-LUNA targets.
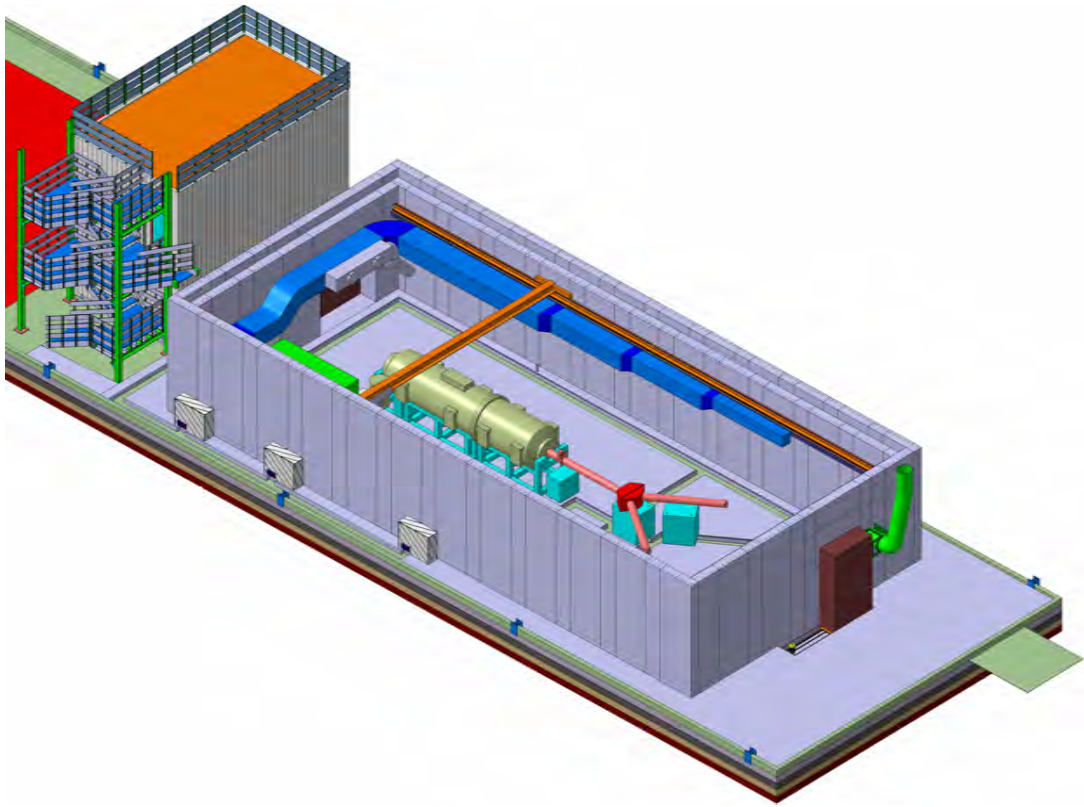
Figure 6: Rendering of the LUNA-MV experimental hall. The accelerator and the two beam lines are visible

(the two neutron sources for nucleosynthesis beyond Iron with the s-process). To successfully complete the scientific program in the given period, two beam lines must be built (actually, one of the two will be delivered by HVE as part of the accelerator tender) and equipped for experiments with solid and gas targets A lay-out of the whole plant is given in Figure 1. A fifth process, $^{12}C(\alpha,\gamma)^{16}O$, is as well universally recognized to have outstanding importance and it is definitively included in the LUNA scientific goals. Due to the high complexity and cost, the LUNA Collaboration proposes to postpone the study of $^{12}C(\alpha,\gamma)^{16}O$ to the second five-year period at LUNA-MV.

Project status at September 2017

The project goal is to install the new LUNA-MV accelerator in the North part of Hall-B of LNGS. While the accelerator construction is in progress at HVEE, INFN is committed to prepare all the other parts of the new facility i.e. a shielded room for the accelerator and two beam lines, an underground building to host the control room and other technical services, all the technological plants. Furthermore, at the time of the accelerator delivering at LNGS, INFN must also have obtained the authorization ("Nulla Osta di categoria B") to run the machine. Presently, as better described in the following, the facility must be ready to receive the accelerator by December 2018. The whole process can (and has been) splitted in several items that are discussed separately in the following:

1. **Accelerator and contract between INFN and HVEE**

   The construction of the accelerator is in progress at HVEE. A protocol for the in-house acceptance tests (that will be coordinated by A. Di Leva, University and INFN Naples) has been discussed with HVEE. Such tests are foreseen for June 2018. Since (see below), INFN and HVEE agreed to deliver the accelerator in LNGS at January 2019. After the accelerator deployment at LNGS, a period of six months will be dedicated to set-up, commissioning and final acceptance tests. The whole activity described in the contract between INFN and HVEE must be completed within June 2019 and the party responsible of any delay is subjected to the payment of penalty clauses.

2. **Construction of the accelerator room**

   The LUNA-MV accelerator will be completely closed by a shielding made by 80 cm concrete wall in all the directions (roof included), see Figure 1. The design work to fix the shielding thickness necessary to maintain the neutron flux outside the accelerator room at the level of 10-7 n cm-2 s-1 has been described in previous reports. The constructive design, including the mounting procedure (see Figure 2), has been defined by an external Engineer and a dedicated tender has been closed in May 2017 with the selection of the Society Vibrocementi which offered the lowest price. The construction works in Hall B should start in May 2018 and be concluded within July 2018.

3. **Construction of the control room**

   The control room (see Figure 3) will be hosted inside a two-floor building located at the South side of the shielded accelerator area.

The building has been entirely designed by the LNGS technical division and the tender to select the provider has been closed on September 18th, 2017. The beginning of the works will be anyway delayed till the conclusion of the construction of the accelerator room. The present estimate fixes the delivering of the control room within October 2018.

4. **Technological plants**

The design of all the technological plants for the LUNA-MV facility (i.e. electric power, cooling, venting, safety systems, internal and external connectivity, etc) has been initially defined by the LNGS technical division and then detailed in the final and constructive design by the Society STAIN srl, selected through a public tender. As for the previous point, the works on the plants will anyway start only after the completion of the accelerator room and they should be anyway concluded by December 2018.

References

[1] J. J. He *et al.*, Phys. Lett. B **725** (2013) 287

[2] V. Mossa, Eur. Phys. J. Web of Conferences **165** (2018) 01038

[3] R. Cooke et al., Astrophys. J. 781, 31 (2014)

[4] E. Di Valentino *et al.*, Phys. Rev. D **90** (2014) 023543

[5] L.E. Marcucci et al., J. Phys. G43, 023002 (2016)

[6] F. Cavanna et al., Phys. Rev. Lett. **115** (2015) 252501

[7] R. Depalo et al , Phys. Rev. C, **94** (2016) 1-13

[8] C. Angulo et al., Nucl. Phys. A **656** (1999) 3

[9] A. L. Sallaska et al., Astrophys. J. Suppl. Ser. **207** (2013) 18

[10] A. Slemer et al., MNRAS, **465**(4) (2016) 4817 - 4837

[11] F. Ferraro et al., Eur. Phys. J A **54** (2018) 44-54

[12] A. Best et al. NIM A **812** (2016), 1

7   List of Publications

1. *Neon and Sodium ejecta from intermediate mass stars: The impact of the new LUNA rate for the $^{22}Ne(p,\gamma)^{23}Na$*
A. Slemer, P. Marigo, D. Piatti, M. Aliotta, D. Bemmerer, A. Best, A. Boeltzig, A. Bressan, C. Broggini, C.G. Bruno, A. Caciolli, F. Cavanna, P. Corvisiero, T. Davinson, R. Depalo, A. Di Leva, Z. Elekes, F. Ferraro, A. Formicola, Zs. Fülöp, G. Gervino, A. Guglielmetti, C. Gustavino, Gy. Gyürky, G. Imbriani, M. Junker, R. Menegazzo, V. Mossa, F. R. Pantaleo, P. Prati, O. Straniero, T. Szücs, M. P. Takács, D. Trezzi (LUNA Collaboration)
Monthly Notices of the Royal Astronomical Society 465 (2016) 4817

2. *Big Bang 6-Lithium Nucleosynthesis studied deep underground*
D. Trezzi, M. Anders, M. Aliotta, A. Bellini, D. Bemmerer, C. Broggini, A. Caciolli, P. Corvisiero, H. Costantini, T. Davinson, Z. Elekes, M. Erhard, A. Formicola, Zs. Fülöp, G. Gervino, A. Guglielmetti, C. Gustavino, Gy. Gyürky, M. Junker, A. Lemut, M. Marta, C. Mazzocchi, R. Menegazzo, P. Prati, C. Rossi Alvarez, D. A. Scott, E. Somorjai, O. Straniero, T. Szücs (LUNA Collaboration)
Astroparticle Physics 89 (2017) 57

3. *Origin of meteoritic stardust unveiled by new proton-capture rate on oxygen-17*
M. Lugaro, A. Karakas, C.G. Bruno, M. Aliotta, L.R. Nittler, D. Bemmerer, A. Best, A. Böltzig, C. Broggini, A. Caciolli, F. Cavanna, G.F. Ciani, P. Corvisiero, S. Cristallo, T. Davinson, R. Depalo, A. Di Leva, Z. Elekes, F. Ferraro, A. Formicola, Zs. Fülöp, G. Gervino, A. Guglielmetti, C. Gustavino, Gy. Gyürky, G. Imbriani, M. Junker, R. Menegazzo, V. Mossa, F. R. Pantaleo, D. Piatti, P. Prati, D.A. Scott, O. Straniero, F. Strieder, T. Szücs, M. P. Takács, D. Trezzi (LUNA Collaboration)
Nature Astronomy 1 (2017) 0027

4. *The impact of the revised $^{17}O(p,\alpha)^{15}N$ reaction rate on the ^{17}O stellar abundances and yields* O. Straniero, C.G. Bruno, M. Aliotta, A. Best, A. Boeltzig, D. Bemmerer, C. Broggini, A. Caciolli, F. Cavanna, G.F. Ciani, P. Corvisiero, S. Cristallo, T. Davinson, R. Depalo, A. Di Leva, Z. Elekes, F. Ferraro, A. Formicola, Zs. Fülöp, G. Gervino, A. Guglielmetti, C. Gustavino, Gy. Gyürky, G. Imbriani, M. Junker, R. Menegazzo, V. Mossa, F. R. Pantaleo, D. Piatti, L. Piersanti, P. Prati, E. Somorjai, F. Strieder, T. Szcs, M. P. Takcs, D. Trezzi (LUNA Collaboration)
Astronomy and Astrophysics 598 (2017) A128

8 Conference Proceedings

1. F. Cavanna, R. Depalo, *Three New Low-Energy resonances in the $^{22}Ne(p,\gamma)^{23}Na$ reaction*, Nuclei in the Cosmos XIV, Toki Messe, Niigata, Japan
Proceedings of the 14th International Symposium on Nuclei in the Cosmos (2016)

2. V. Mossa, *Study of the $^2H(p,\gamma)^3He$ reaction in the Big Bang Nucleosynthesis energy range at LUNA*
EPJ Web of Conferences 165 (2017) 01038

3. A. Guglielmetti, *Nuclear Astrophysics and Luna MV*
PoS(NEUTEL2017)(2017) 025

4. G. F. Ciani, A. Best, L. Csedreki, Gy. Gyürky, I. Kochanek *Target characterizations for direct measurement of the $^{13}C(\alpha,n)^{16}O$ reaction at LUNA 400*
EPJ (European Physical Journal) Web of Conferences (2017) 165 01012

5. L. Csedreki, G. F. Ciani, I. Kochanek, A. Best *Introduction of the new LUNA experimental setup for high precision measurement of the $^{13}C(\alpha,n)^{16}O$ reaction for astrophysical purposes*
EPJ (European Physical Journal) Web of Conferences 165 (2017) 01017

6. C. Abia, O. Straniero, P. Ventura *Isotopic ratios of C, O and light element abundances in AGB stars undergoing Hot Bottom Burning*
MemSAIt 88 (2017) 360

7. *A. Caciolli* Nuclear Astrophysics in underground laboratories: the LUNA experiment
EPJ Web of Conferences Volume 163 (2017) 00009

8. C.G. Bruno *Underground Study of the $^{17}O(p,\alpha)^{14}N$ Reaction at UNA*
JPS Conf. Proc 14, 020401 (2017)

9. *M. Lugaro, A. I. Karakas, D. A. Garca-Hernndez, L. R. Nittler, and The LUNA Collaboration,* Cosmic chemistry from AGB stars and its dependence on the initial stellar mass
Memorie della Societa Astronomica Italiana, 88 (2017) 237

10. S. Zavatarelli *Neutrino physics and nuclear astrophysics: the LUNA MV project at Gran Sasso*
PoS(EPS-HEP2017) (2017) 148

11. *A. Boeltzig* ^{23}Na(p,γ)^{24}Mg Cross Section Measurements
EPJ Web of Conferences 165 (2017) 01006

12. A. Boeltzig *Status of Direct $^{23}Na(p,\gamma)^{24}Mg$ and $^{18}O(p,\gamma)^{19}F$ Cross Section Measurements Underground at LUNA*
JPS Conf. Proc. 14 (2017) 020409

13. *F. Pantaleo* Direct cross section measurement for the ^{18}O(p,γ)^{19}F reaction at astrophysical energies at LUNA
EPJ Web of Conferences 165 (2017) 01040

14. M. Junker *Experiences and Prospects of Nuclear Astrophysics in Underground Laboratories*
WORLD SCIENTIFIC (2017) 464-471

15. *F. Ferraro* Low-Background, High-Efficiency Setup for the Study of ^{22}Ne(p,γ)^{23}Na Reaction at Low Energy
   Proceedings of the 14th International Symposium on Nuclei in the Cosmos (NIC2016) (2017)

16. F. Ferraro *Newly Discovered Low Energy Resonances in the ^{22}Ne(p, γ)^{23}Na at Luna
   The 26th International Nuclear Physics Conference (2017)*

9   Invited talks

1. A. Caciolli, FUSION17, Hobart-Australia, 20-24 February 2017

2. A. Guglielmetti, XVII INTERNATIONAL WORKSHOP NEUTRINO TELESCOPES, Venezia-Italy, 13-17 March 2017

3. A. Guglielmetti, SCUOLA DI OTRANTO (for PhD students), Otranto-Italy, 26-31 May 2017

4. A. Guglielmetti, SIF, Trento- Italy, 11-15 September 2017

5. A. Guglielmetti, Ages^2: taking stellar ages to the next power, Elba (IT), 18-22 September 2017

6. O. Straniero, 14th Russbach school on Nuclear Astrophysics, Russbach (Austria), 12-18 March 2017

7. O. Straniero, 9th European Summer School on Experimental Nuclear Astrophysics (Santa Tecla School), Acireale (Italy) 17-24 September 2017

8. M. Aliotta, 55th International Winter Meeting on Nuclear Astrophysics, Bormio (Italy), 23-27 January 2017

9. M. Aliotta, Workshop on Nuclear Astrophysics at Dresden Felsenkeller, Dresden (Germany), 26-28 June 2017

10. M. Aliotta, BRIDGCE Workshop, Edinburgh (UK), 4-5 September 2017

11. M. Lugaro, Meeting of the MTA CSFK, Budapest (Hungary), 15 February 2017

12. M. Lugaro, Meeting of the MTA Department of Physics, Budapest (Hungary), 11 May 2017

13. M. Lugaro, The AGB-Supernovae mass transition conference, Roma (Italy), 27-31 March 2017

14. F. Cavanna, CGS16, Shanghai (China), 18-22 September 2017

15. F. Ferraro, GIANTS IX, Bologna (IT), 5-6 October 2017

16. G. Imbriani, Gordon Research Conference at Colby-Sawyer College New London, NH, USA 19-23 June 2017

17. G. Imbriani, Towards the ANDES laboratory flag-ship and further experiments Buenos Aires, Argentina 29-30 June 2017

18. C.G. Bruno, GIANTS IX, Bologna (IT), 5-6 October 2017

19. G.F. Ciani, GIANTS IX, Bologna (IT), 5-6 October 2017

20. A. Best, GIANTS IX, Bologna (IT), 5-6 October 2017

21. A. Best, 9th European Summer School on Experimental Nuclear Astrophysics (Santa Tecla School), Acireale (Italy) 17-24 September 2017

22. M. Aliotta, 9th European Summer School on Experimental Nuclear Astrophysics (Santa Tecla School), Acireale (Italy) 17-24 September 2017

23. R. Depalo, Particles and Nuclei International Conference 2017 (PANIC2017) Beijing (China) 1-5 September 2017

24. R. Depalo, GIANTS IX, Bologna (IT), 5-6 October 2017

25. C. Broggini, 9th European Summer School on Experimental Nuclear Astrophysics (Santa Tecla School), Acireale (Italy) 17-24 September 2017

26. A. Formicola, NPA8 Catania(Italy), 18-23 June2107

27. A. Formicola, NuPhys2017: Prospects in Neutrino Physics. London (UK) 20-22 December 2017

28. A. Formicola, PISA Summer School, Pisa (Italy), 24-28 July 2017

29. P. Prati, TAUP 2017 - XV International Conference on Topics in Astroparticle and Underground Physics, Sudbury, ON, Canada, 24 - 28 July 2017

30. P. Prati, Workshop on Nuclear Astrophysics at the Dresden Felsenkeller, Dresden (Germany), 26-28 June 2017

31. P. Prati, TNPI2017 - XVI Conference on Theoretical Nuclear Physics in Italy, Cortona (Italy), 3-5 October 2017

32. P. Prati, ISTROS, Casta-Papiernicka Centre, Slovacchia, 14-19 May 2017

10   Contributed talk

1. O. Straniero, 13th Patras Workshop on Axions, WIMPs and WISPs Thessaloniki (Greece), 11-19 May

2. C.G. Bruno, BRIDGCE Workshop, Edinburgh (UK), 4-5 September 2017

3. F.R. Pantaleo, Nuclear Physics in Astrophysics VIII, Catania (Italy) 18-23 June 2017

4. V. Mossa, Nuclear Physics in Astrophysics VIII, Catania (Italy) 18-23 June 2017

5. D. Bemmerer, German Physical Society, Spring meeting Münster (Germany) 20-24 March 2017

6. L. Csedreki, Seminar in MTA Atomki, Debrecen (Hungary) 06 September 2017

7. L. Csedreki, Particle and astroparticle physics autumn program 2017, Assergi (Italy), 11 October 2017

8. F. Ferraro, XXXV Mazurian Lakes Conference on Physics Piaski, (Poland), 3-9 September 2017

9. T. Chillery, 9th European Summer School on Experimental Nuclear Astrophysics (Santa Tecla School), Acireale (Italy) 17-24 September 2017

11 PhD Theses

Direct measurement of the $^{22}Ne(p,\gamma)^{23}Na$ reaction cross section at astrophysical energies
Federico Ferraro, PhD thesis
Università degli Studi di Genova, March 2017
Supervisors: Prof. Paolo Prati
Referee: PD. Dr. Daniel Bemmerer, Prof. Paola Marigo

Hydrogen burning: Study of the ^{22}Ne$(p,\gamma)^{23}$Na, ^{3}He$(\alpha,\gamma)^{7}$Be and ^{7}Be$(p,\gamma)^{8}$B reactions at ultra-low energies
Marcell P. Takács, PhD thesis
Technische Universität Dresden, September 2017
Supervisors: PD. Dr. Daniel Bemmerer, Prof. Kai Zuber

The XENON Project

E. Aprile[a*], J. Aalbers[b], F. Agostini[cd], M. Alfonsi[e]

F. D. Amaro[f], M. Anthony[a], F. Arneodo[g], P. Barrow[h], L. Baudis[h]

B. Bauermeister[i], M. L. Benabderrahmane[g], T. Berger[k]

P. A. Breur[b], A. Brown[b], E. Brown[k], S. Bruenner[l]

G. Bruno[c], R. Budnik[m], L. Bütikofer[n], J. Calvén[i], J. M. R. Cardoso[f]

M. Cervantes[o], D. Cichon[l], D. Coderre[n], A. P. Colijn[b]

J. Conrad[i], J. P. Cussonneau[p], M. P. Decowski[b], P. de Perio[a], P. Di Gangi[d]

A. Di Giovanni[g], S. Diglio[p], G. Eurin[l], J. Fei[q], A. D. Ferella[i]

A. Fieguth[r], W. Fulgione[cs], A. Gallo Rosso[c], M. Galloway[h], F. Gao[a]

M. Garbini[d], C. Geis[e], L. W. Goetzke[a], L. Grandi[t], Z. Greene[a]

C. Grignon[e], C. Hasterok[l], E. Hogenbirk[b], R. Itay[m], B. Kaminsky[n]

S. Kazama[h], G. Kessler[h], A. Kish[h], H. Landsman[m], R. F. Lang[o]

D. Lellouch[m], L. Levinson[m], Q. Lin[a], S. Lindemann[nl]

M. Lindner[l], F. Lombardi[q], J. A. M. Lopes[f], A. Manfredini[m], I. Maris[g]

T. Marrodán Undagoitia[l], J. Masbou[p], F. V. Massoli[d]

D. Masson[o], D. Mayani[h], M. Messina[ga], K. Micheneau[p]

A. Molinario[c], K. Morå[i], M. Murra[r], J. Naganoma[v], K. Ni[q]

U. Oberlack[e], P. Pakarha[h], B. Pelssers[i], R. Persiani[p]

F. Piastra[h], J. Pienaar[to], V. Pizzella[l], M.-C. Piro[k], G. Plante[a]

N. Priel[m], D. Ramírez García[ne], L. Rauch[l]

S. Reichard[oh], C. Reuter[o], A. Rizzo[a], N. Rupp[l], R. Saldanha[t]

J. M. F. dos Santos[f], G. Sartorelli[d], M. Scheibelhut[e]

S. Schindler[e], J. Schreiner[l], M. Schumann[n], L. Scotto Lavina[u]

M. Selvi[d], P. Shagin[v], E. Shockley[t], M. Silva[f]

H. Simgen[l], M. v. Sivers[n], A. Stein[w], D. Thers[p]

A. Tiseni[b], G. Trinchero[s], C. Tunnell[t], M. Vargas[r]

H. Wang[w], Z. Wang[c], Y. Wei[qh], C. Weinheimer[r]

C. Wittweg[r], J. Wulf[h], J. Ye[q], Y. Zhang.[a]   (The XENON Collaboration)

[a]Physics Department, Columbia University, New York, NY 10027, USA
[b]Nikhef and the University of Amsterdam, Science Park, 1098XG Amsterdam, Netherlands
[c]INFN-Laboratori Nazionali del Gran Sasso and Gran Sasso Science Institute, 67100 L'Aquila, Italy
[d]Department of Physics and Astrophysics, University of Bologna and INFN-Bologna, 40126 Bologna, Italy
[e]Institut für Physik & Exzellenzcluster PRISMA, Johannes Gutenberg-Universität Mainz, 55099 Mainz, Germ
[f]LIBPhys, Department of Physics, University of Coimbra, 3004-516 Coimbra, Portugal
[g]New York University Abu Dhabi, Abu Dhabi, United Arab Emirates
[h]Physik-Institut, University of Zurich, 8057 Zurich, Switzerland
[i]Oskar Klein Centre, Department of Physics, Stockholm University, AlbaNova, Stockholm SE-10691, Sweden
[k]Department of Physics, Applied Physics and Astronomy, Rensselaer Polytechnic Institute, Troy, NY 12180, U
[l]Max-Planck-Institut für Kernphysik, 69117 Heidelberg, Germany
[m]Department of Particle Physics and Astrophysics, Weizmann Institute of Science, Rehovot 7610001, Israel
[n]Physikalisches Institut, Universität Freiburg, 79104 Freiburg, Germany
[o]Department of Physics and Astronomy, Purdue University, West Lafayette, IN 47907, USA
[p]SUBATECH, IMT Atlantique, CNRS/IN2P3, Université de Nantes, Nantes 44307, France
[q]Department of Physics, University of California, San Diego, CA 92093, USA
[r]Institut für Kernphysik, Westfälische Wilhelms-Universität Münster, 48149 Münster, Germany
[s]INFN-Torino and Osservatorio Astrofisico di Torino, 10125 Torino, Italy
[t]Department of Physics & Kavli Institute of Cosmological Physics, University of Chicago, Chicago, IL 60637, U
[u]LPNHE, Université Pierre et Marie Curie, Université Paris Diderot, CNRS/IN2P3, Paris 75252, France
[v]Department of Physics and Astronomy, Rice University, Houston, TX 77005, USA
[w]Physics & Astronomy Department, University of California, Los Angeles, CA 90095, USA

---

[*]Spokesperson

Abstract

During 2017, the XENON collaboration continued their strong scientific program in the search for dark matter particles. Analysis of data from the XENON100 detector was concluded with final analyses being published. A first analysis of data from the XENON1T experiment yielded world-best limits on WIMP-nucleus cross-sections and was published in Physical Review Letters. Data taking with XENON1T continued throughout the entire year to improve the sensitivity to rare events even further. In parallel to analyzing XENON1T data, the collaboration also refined the design of the upgrade XENONnT which will start in 2018.

1   Introduction

The XENON collaboration operates a series of experiments at the Gran Sasso laboratory to search for dark matter particles in our Milky Way and for interactions from other rare processes. The experiments use dual-phase liquid xenon time-projection chambers (TPCs) which are particularly well-suited to search for one of the most compelling dark matter candidate particle, the Weakly Interacting Massive Particle (WIMP), covering a broad range of parameters. Starting with the XENON10 experiment more than a decade ago, the collaboration has successively built a series of larger and more sensitive detectors. The XENON100 experiment was the worlds most sensitive direct detection dark matter experiment for a number of years. The results from final data analyses using data from XENON100 were published in 2017. After about three years of construction, first data from the successor XENON1T experiment was taken until an earthquake in early 2017 briefly interrupted data taking. This first data was subsequently analyzed and published, again resulting in world-best limits on the WIMP-nucleon cross-section. Data taking swiftly resumed and continued in stable background data taking mode throughout the year, interleaved only by various calibration campaigns. Results from this data will be published in 2018. In parallel to the XENON1T operations and data analysis effort, the design of a rapid upgrade called XENONnT was progressing well and will enable to improve the sensitivity of this experiment by yet another order of magnitude, starting in 2019.

2   The XENON Collaboration

The XENON collaboration grew again and now counts more than 160 members from 27 institutions. The collaboration was strengthened with the addition of the LAL group, led by Dr. Carla Macolino, the INFN-Napoli group led by Prof. Michele Iacovacci, and Prof. Guido Zavattini from INFN-Ferrara. Key members of the Japanese XMASS collaboration have joined the XENON collaboration and will contribute to the realization of the XENONnT upgrade. In particular groups joined from the University of Tokyo, led by Prof. Shigetaka Moriyama and Prof. Kai Martens, from Nagoya University, led by Prof. Yoshitaka Itow, and from Kobe University, led by Prof. Kentaro Miuchi.

3   XENON100

The XENON collaboration continued to analyze data from the XENON100 experiment in the context of various dark matter models. Dedicated publications describe analyses and results in the search for bosonic super-WIMPs, magnetic inelastic dark matter, and for WIMPs scattering inelastically off the xenon target. Another publication interprets the results from XENON100 in the context of dark matter effective field theories. Further publications include an analysis of

Figure 1: The XENON experiment underground in Hall B of the Gran Sasso lab. On the left the water tank is visible with an attached rendering of the inside, including the heart of the detector at its center. On the right the three-story service building is visible.

the discrimination of electronic and nuclear recoils in liquid xenon, as well as a paper describing the intrinsic background in this experiment that is due to Radon and Krypton. Data taking with XENON100 has since ceased and the experiment is mostly decommissioned, but not before the collaboration could use this detector to demonstrate the online removal of radon using a dedicated cryogenic distillation setup.

4   First Results from XENON1T

A description of the XENON1T experimental setup was published in the European Physics Journal, and more detail on the careful screening and selection of construction materials was given in a dedicated publication. The 2017 highlight from the XENON1T collaboration certainly was the publication of the first dark matter search results using this new detector, in Physical Review Letters. This publication was a cumulation of several months of analysis work by a large team of graduate students and postdocs from the XENON collaboration.

The dark matter analysis was performed as a blind analysis, where the signal region was inaccessible to the analysts up until the final stages. This analysis not only demonstrated that the full experiment, from its hardware to the data analysis chain, met the design requirements, but also that the data coming from the detector is of very high quality. As expected, no WIMPs were found in this initial 34.2-day Science Run 0 data-set, spanning the data taking period from November 2016 up to the January 18, 2017 earthquake. With a fiducial mass of 1042 kg, the exposure was sufficient for XENON1T to become the most sensitive direct detection dark matter detector in the world and allowed the collaboration to set stringent dark matter limits. In the
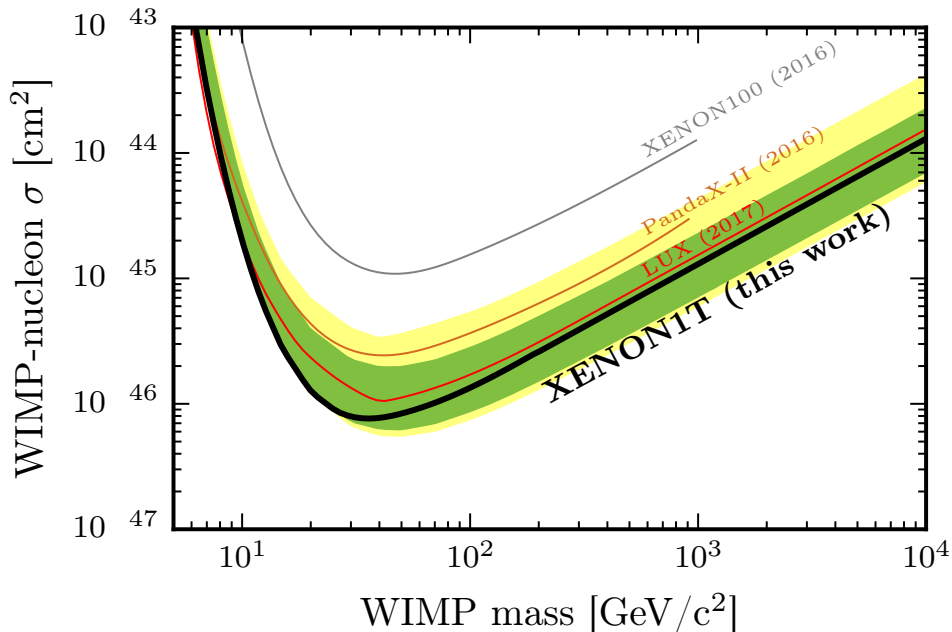
Figure 2: The spin-independent WIMP-nucleon cross section limits derived from XENON1T Science Run 0 as a function of WIMP mass at 90% confidence level (black). In green and yellow are the 1- and 2 sigma sensitivity bands. Results from LUX (red), PandaX-II (brown), and XENON100 (gray) are shown for reference.

[5 to 40] keV$_{nr}$ energy range that is of interest for WIMP dark matter searches, the detector shows an unprecedented low background of $(1.93 \pm 0.25) \times 10^4$ events/(kg×day×keV$_{ee}$). These first exclusion limits on the spin-independent WIMP-nucleon interaction cross section have a minimum of 7.7×10^{47} cm^2 for a 35-GeV WIMP, at 90% confidence level.

5   Continued Data Taking with XENON1T

The XENON collaboration continued acquiring data with XENON1T throughout 2017. Most of the data was background data that is used to search for signals from dark matter and other rare events. Other data include various calibration campaigns. Those include internal radioactive sources that are mixed directly in the liquid xenon, to monitor for example the purity of the target and stability of the detector.

6   Novel Neutron Calibration

Another first for the Gran Sasso lab in 2017 was the operation of a deuterium-deuterium plasma fusion generator as a neutron calibration source for the XENON1T experiment. Neutrons with energies between 2.2 MeV and 2.7 MeV are produced by the generator, but in contrast to the other neutron sources usually used in the Gran Sasso lab, here, the neutron flux can be tuned to the desired value by adjusting the generator voltage and current, and thus can be completely turned off. This new source has great benefits for operation in a low-radioactivity underground laboratory such as LNGS. The particular generator was modified by the manufacturer to achieve
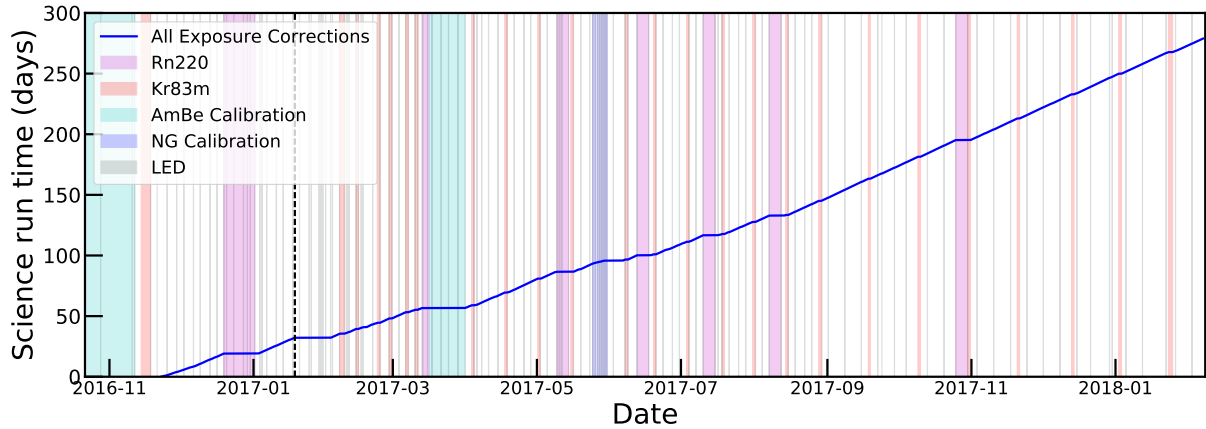
Figure 3: XENON1T started science data-taking in October 2016 and continued until January 18, 2017 when a magnitude 5.7 earthquake temporarily disrupted detector operation. After a brief down time, the detector resumed science data taking on February 2, 2017 and continued until February 24, 2018, marking over one year of stable science data. The detector usually collects data in dark matter search mode, but also requires calibration data where the detector response is measured given a known particle type at a known energy. The calibration periods are indicated by colored boxes indicating data collected in the presence of various sources. The blue line is the accumulated dark matter exposure versus real time.

stable operation conditions even at very low emission rates of about 10 neutrons per second. The generator is operated directly inside the water tank of XENON1T, adjacent to its cryostat. The water-shield of at least 5 m in all directions reduces the neutron flux by a factor of 10^5 to completely negligible levels outside of the water tank.
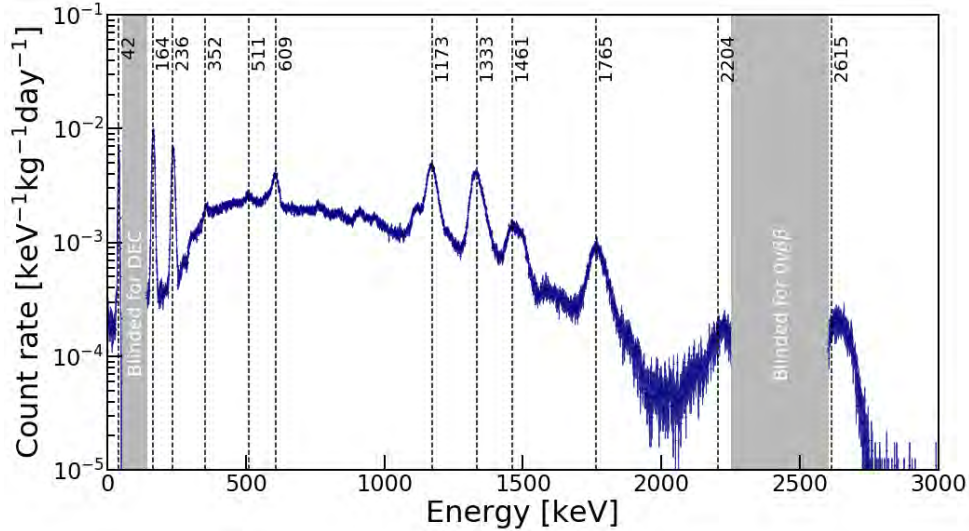
Figure 4: The energy spectrum recorded by XENON1T. The small portion of data in the very left of the plot next to the first grey-shaded region is relevant to the standard dark matter search due to the low expected energy depositions. The following grey region is blinded, which means it has deliberately been made inaccessible to the analyzers, since it might contain traces of a rare nuclear decay of xenon-124 that has not been observed until now. The large region from about 100-2300 keV contains multiple peaks from mono-energetic γ-lines of radioactive isotopes contained in the detector materials. The peaks are sitting on a continuous pedestal which is created by γ-rays depositing only part of their total energy due to Compton scattering inside or outside the detector, β decays of radioisotopes inside the detector, and the two-neutrino double β-decay of xenon-136. The latter produces a continuous energy spectrum over the whole energy range that ends at 2458 keV. The decay is rare, but becomes relevant due to the large amount of the xenon-136 isotope in the detector and the relative smallness of other background contributions. Xenon-136 is also responsible for the second gray-shaded region at high energies which might contain an experimental signature of the neutrinoless double β-decay of this isotope. The observation of this decay would be a gateway to new physics and complements the physics program of XENON1T. Overall, this measured spectrum is in excellent agreement with the design specifications and indicates the various energy ranges for a variety of science channels.
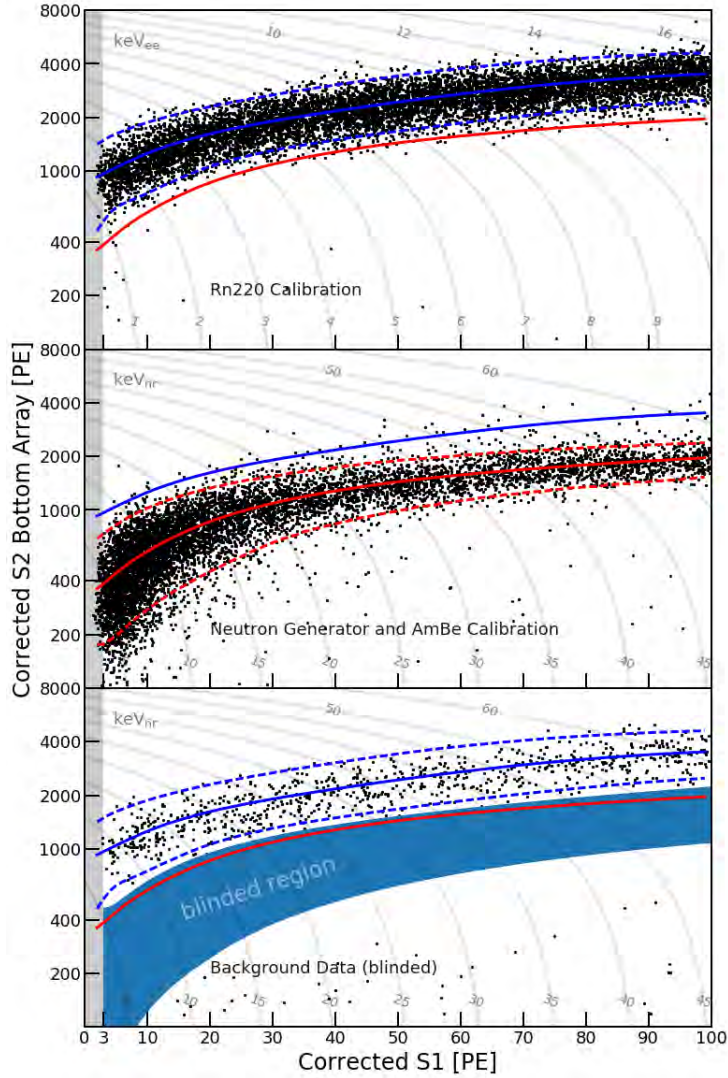
Figure 5: After collecting data for one year, all identified interactions are subjected to several selection requirements in order to suppress known sources of non-physical background and poorly reconstructed events. These plots show the remaining interactions. The radon-220 calibration data shows the detector response to electronic recoils while the neutron generator data shows the response to (WIMP-like) nuclear recoils. At the time of writing, the signal region is still blinded in the background data and will only be revealed once the analysis and physical interpretations are fixed.

7 Reduction of Radioactive Backgrounds

Using the principle of cryogenic distillation, the concentration of natural krypton in the liquid xenon was reduced while the detector was in operation. This reduced the ^{nat}Kr concentration from (2.60 ± 0.05) ppt [mol/mol] at the beginning of Science Run 0 to (0.36 ± 0.06) ppt one month after the end of it. This makes the intrinsic background in XENON1T that can be attributed to the krypton-85 isotope completely subdominant and pushes it even below the electronic recoil signal that is expected from solar neutrinos. The background rate from lead-214, itself a daughter of the radon-222 decay chain, was $(0.8-1.9)\times10^4$ events/(kg×day×keV$_{ee}$) in the low-energy range that is of interest for WIMP searches. These bounds were set using in-situ alpha-spectroscopy on polonium-218 and polonium-214 isotopes. The radon-222 concentration was reduced by 20% using the krypton distillation column in inverse mode, as described in a dedicated publication. The measured radon-222 concentration of 10 μBq matches the design expectations of XENON1T, as assumed in the original sensitivity predictions for XENON1T.

8 XENONnT

The preparation of the XENONnT upgrade, aiming at a factor 10 improvement in sensitivity compared to XENON1T, was ongoing throughout 2017. A series of milestones was reached during 2017, including the delivery of all Hamamatsu R11410-21 photomultiplier tubes needed for the upgrade, as well as the procurement of the total of 8000 kg of Xenon gas. Most of the required low-background materials have been identified using the screening facilities of the collaboration, and additional electronics was purchased as well, allowing for the construction of this upgrade to start in 2018.

9 Conclusions

The XENON project continues to set standards for the field of direct dark matter detection, both in terms of analysis innovations and its unprecedented sensitivity. With the XENON1T experiment at the Gran Sasso lab, the collaboration now again operates the most sensitive search for WIMP dark matter. With its analyses and detectors, the collaboration thus operates at the forefront of the quest to unravel one of the most pressing questions in contemporary physics: What is our universe made of?

10 List of Publications

1. The XENON Collaboration: E. Aprile et al., *Signal Yields of keV Electronic Recoils and Their Discrimination from Nuclear Recoils in Liquid Xenon*, arXiv:1709.10149, submitted to Physical Review D (2017).

2. The XENON Collaboration: E. Aprile et al.,*Search for Bosonic Super-WIMP Interactions with the XENON100 Experiment*, Physical Review D **96** (2017) 122002, doi:10.1103/PhysRevD.96.122002, arXiv:1709.02222.

3. The XENON Collaboration: E. Aprile et al., *The XENON1T Dark Matter Experiment*, European Physics Journal C (2017) **77**:881, doi:10.1140/epjc/s10052-017-5326-3, arXiv:1708.07051, (2017).

4. The XENON Collaboration: E. Aprile et al., *First Dark Matter Search Results from the XENON1T Experiment*, Physical Review Letters **119** (2017), 181301, `doi:10.1103/PhysRevLett.119.1813` `arXiv:1705.06655`.

5. The XENON Collaboration: E. Aprile et al., *Search for WIMP Inelastic Scattering off Xenon Nuclei with XENON100*, Physical Review D **96** (2017) 022008, `doi:10.1103/PhysRevD.96.022008`, `arXiv:1705.05830`.

6. The XENON Collaboration: E. Aprile et al., *Effective field theory search for high-energy nuclear recoils using the XENON100 dark matter detector*, Physical Review D **96** (2017), 042004, `doi:10.1103/PhysRevD.96.042004`, `arXiv:1705.02614`.

7. The XENON Collaboration: E. Aprile et al., *Material radioassay and selection for the XENON1T dark matter experiment*, European Physical Journal C **77** (2017) 890, `doi:10.1140/epjc/s10052` `arXiv:1705.01828`.

8. The XENON Collaboration: E. Aprile et al., *Search for magnetic inelastic dark matter with XENON100*, Journal of Cosmology and Astroparticle Physics **10** (2017) 039, `doi:10.1088/1475-7516/2017/10/039`, `arXiv:1704.05804`.

9. The XENON Collaboration: E. Aprile et al., *Online ^{222}Rn removal by cryogenic distillation in the XENON100 experiment*, The European Physical Journal C (2017) **77**:358, `doi:10.1140/epjc/s10052-017-4902-x`, `arXiv:1702.06942`.

THE PIERRE AUGER OBSERVATORY

G. A. Anastasi[a,c], A.F. Grillo[a,†], G. Morlino[a,c],
S. Petrera[a,c], V. Rizi[a,b], F. Salamida[a,b]
for the Pierre Auger Collaboration

[a] INFN Laboratori Nazionali del Gran Sasso, Assergi (AQ), Italy
[b] INFN and Department of Physical and Chemical Sciences,
University of L'Aquila, L'Aquila, Italy
[c] GSSI, Gran Sasso Science Institute, L'Aquila, Italy
[†] deceased

Abstract

The Pierre Auger Project is an international Collaboration involving about 450 scientists from 16 countries, with the objective of studying the highest energy cosmic rays. Recent results from the Collaboration as well as further developments in the detector are presented in this report.

1   Introduction

Ultra-high energy cosmic rays are of intrinsic interest as their origin and nature are unknown. It is quite unclear where and how particles as energetic as $\approx 10^{20}$ eV are accelerated. Over 40 years ago it was pointed out that if the highest energy particles are protons then a fall in the flux above an energy of about 4×10^{19} eV is expected because of energy losses by the protons as they propagate from distant sources through the photon background radiation. At the highest energies the key process is photo-pion production in which the proton loses part of its energy in each creation of a Δ resonance. This is the Greisen–Zatsepin–Kuzmin (GZK) effect. It follows that at 10^{20} eV any proton observed must have come from within about 50 Mpc and on this distance scale the deflections by intervening magnetic fields in the galaxy and intergalactic space are expected to be so small that point sources should be observed. If nuclei are propagated from sources their photo-disintegration in the photon background field plays a role similar to the GZK effect in the depletion of the flux above 10^{20} eV and the limitation of the CR horizon, but the angular correlation with the sources is expected weaker because of the higher charges. $3 \times 9''$ hemispherical photomultipliers. The fluorescence detectors (FD) are designed to record the faint ultra-violet light emitted as the shower traverses the atmosphere. Each telescope images a portion of the sky of $30°$ in azimuth and $1°$–$30°$ in elevation using a spherical mirror of 3 m^2 effective area to focus light on to a camera of 440×18 cm^2 hexagonal pixels, made of photomultipliers complemented with light collectors, each with a field of view of $1.5°$ diameter. 3 High Elevation Auger Telescopes (HEAT) located at one of the fluorescence sites are dedicated to the fluorescence observation of lower energy showers. The Observatory also comprises a sub array of 124 radio sensors (AERA, Auger Engineering Radio Array) working in the MHz range and covering 6 km^2, a sub Array of 61 radio sensors (EASIER, Extensive Air Shower Identification with Electron Radiometer) working in the GHz range and covering 100 km^2, and two GHz imaging radio telescopes AMBER and MIDAS. A review of main results from the Pierre Auger Observatory is presented with a particular focus on the energy spectrum measurements, the mass composition studies, the arrival directions analyses and the search for neutral cosmic messengers. The measurement of the energy spectrum of UHECRs, the inference on their mass composition and the analysis of their arrival directions bring different information, complementary and supplementary one to the other, with respect to their origin. Despite the results reached by Auger, the understanding of the nature of UHECRs and of their origin remains an open science case that the Auger collaboration is planning to address with the AugerPrime project [2] to upgrade the Observatory.

2   Recent results from the Pierre Auger Observatory

2.1   Cosmic Ray Spectrum measurements

The measurement of the flux of UHECRs has been one of the first outcomes of Auger data [3, 4, 5]. Two spectral features have been established beyond doubt: the hardening in the spectrum at about 5×10^{18} eV (the so-called ankle), and a strong suppression of the flux at the highest energies, starting at about 4×10^{19} eV. The all-particle flux of cosmic rays presented at ICRC 2017 [6] is an update of such measurement, being based on an exposure exceeding 67,000 km^2 sr yr, accumulated since January 2004 until December 2016. Four independent energy spectra (Fig. 1, left) are obtained: two data sets from the SD-1500 m, respectively vertical and horizontal (zenith angles above $60°$) events; one from the SD-750 m; the last one from events detected by the FD simultaneously with at least one detector of the SD 1500. The SD-1500 m vertical data

are crucial above the energy of full trigger efficiency of 3×10^{18} eV up to the highest energies, with horizontal events contributing above 4×10^{18} eV and providing an independent measurement in this energy range. Data from the SD-750 m allow for the determination of the energy spectrum down to 10^{17} eV. Hybrid data bridge those from the two SDs, between 10^{18} eV and $10^{19.6}$ eV. The four spectra, in agreement within uncertainties, are combined into a unique one (Fig. 1, right) through a likelihood function defined in such a way to fit all the data sets globally. The result is emblematic of the power of using multiple detectors.

The evident features are quantified by fitting a model that describes the spectrum with two power-laws around the ankle, the second of which includes a smooth suppression at the highest energies. The ankle is found to be at $E_{\mathrm{ankle}} = (5.08 \pm 0.06 \pm 0.8) \times 10^{18}$ eV. The spectral slope below the ankle is $\gamma_1 = 3.293 \pm 0.002 \pm 0.05$, and above the ankle is $\gamma_2 = 2.53 \pm 0.02 \pm 0.1$. The energy at which the integral spectrum drops by a factor of two below what would be the expected with no steepening is $E_{1/2} = (22.6 \pm 0.8 \pm 4.0) \times 10^{18}$ eV. The obtained parameters are in good agreement with those previously shown in [7].

2.2 Mass composition studies

The composition of cosmic rays in the energy range of 0.1 to 1 EeV is the key for identifying a possible transition from galactic to extra-galactic sources and for understanding the features in the energy spectrum, such as the ankle and the flux suppression. This study has been addressed by the Collaboration through the measurement of the depth of the shower maximum, X_{max}, one of the most robust mass-sensitive EAS observables. The measurement published in [8] (relying on hybrid events above $10^{17.8}$ eV collected by the standard FD telescopes) has been extended in [9] down to $10^{17.2}$ eV using data collected with HEAT in coincidence with the closest FD, Coihueco (so-called HeCo data set) and updated in the last ICRC conference [10].

The determination of the primary composition is performed by comparing the measured X_{max} distributions of EAS with expectations according to high energy hadronic interaction models. The analysis is based on a selected set of hybrid events, recorded during stable runs and good atmospheric conditions. In addition to these selection criteria a set of fiducial FoV cuts are applied to reduce to a minimum the detector effects in the sampled Xmax distributions. The total number of events that passed all cuts (quality and FoV cuts) is 16778 and 25688 for
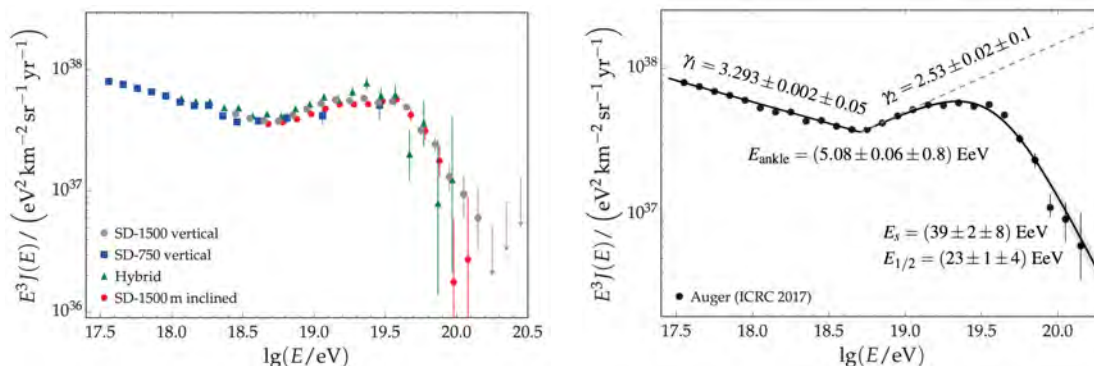

Figure 1: Left: The four energy spectra derived from SD and hybrid data. The systematic uncertainty on the energy scale is 14%. Right: The combined energy spectrum, fitted with a flux model and the related fitting parameters (see text). As in the left panel, only statistical uncertainties are shown. Images from [6].

HeCo and Standard-FD data sets respectively.

The resulting $\langle X_{\max}\rangle$ and $\sigma(X_{\max})$ is shown in Fig. 2, left and right, respectively, as a function of energy. Data are confronted to simulations, for proton and iron primaries, performed using three hadronic interaction models that were found to agree with recent LHC data. Between $10^{17.2}$ and $10^{18.3}$ eV, $\langle X_{\max}\rangle$ increases by around (79 ± 1) g cm^{-2} per decade of energy; around $10^{18.3}$ eV, the rate of change of $\langle X_{\max}\rangle$ becomes significantly smaller ((26 ± 2) g cm^{-2}/decade). These two values, consistent with those found with FD data alone [8], allow to extend the inferences on the evolution of the average mass composition down to 10^{17} eV. As the first value is larger than the one expected for a constant mass composition (~ 60 g cm^{-2}/decade), it indicates that the mean primary mass is getting lighter all the way from 10^{17} to $10^{18.3}$ eV. Above this energy, the trend inverts and the composition becomes heavier. The fluctuations of $X_{\max}$ start to decrease above the same energy $\sim 10^{18.3}$ eV, being rather constant below.

2.3 Photons and neutrinos diffuse search

Both neutrinos and photons are sought for in the flux of UHECRs detected by Auger. The neutrino search is performed by studying very inclined showers and earth-skimming ones [11]. The criteria are based on the characteristics expected for "young" showers initiated by neutrinos, developing deeper in the atmosphere, compared to "old" ones from inclined hadronic showers, having their electromagnetic component fully absorbed before reaching the detectors. Also photon showers develop deep in the atmosphere, but a key difference is the lower average number of muons in photon-induced air showers compared to those initiated by hadrons of the same primary energy.

SD events on the one hand, and hybrid events on the other hand have been analyzed, to cover the energy range above 1 EeV. Assuming a differential flux $dN(E) = kE^2$ for both neutrinos and photons, stringent upper limits to their flux can be derived. The Auger limits on neutrinos (Fig.3 left panel) outperform those from IceCube and ANITA, and also the Waxman-Bahcall limit; in
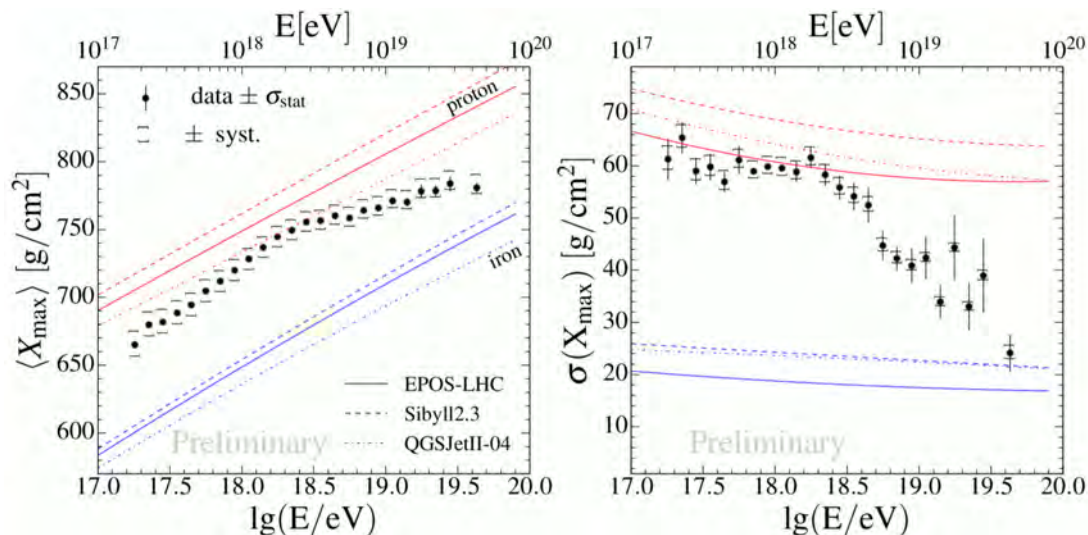

Figure 2: The mean (left) and the standard deviation (right) of the measured $X_{\max}$ distributions as a function of energy compared to air-shower simulations for proton and iron primaries. Images from [10].

the range 10^{17} - 10^{19} eV they are challenging the contribution from cosmogenic-neutrino models [12]. The limits to the integral photon flux are shown in Fig.3 right panel. So far, the extensive searches for UHE photons at the Pierre Auger Observatory have not yielded an unambiguous detection, but the upper limits on the diffuse flux of photons presented in [13] are the most stringent limits to date, severely constraining top-down models for the origin of UHE cosmic rays.

2.4 Targeted search of neutrinos

The detection of gravitational waves started by the Advanced Ligo Collaboration has triggered a targeted search for coincidence events that would complement these observations. Even if the directionality of the neutrino exposure makes the effectivity of the search quite dependent on the event position, an upper bound to the flux of UHE neutrinos and on the related energy budget can be obtained. These limits help to constrain all kinds of models as part of a multi-messenger approach.

A search [12] has been made for EeV events in the data collected with the Observatory and correlated in time and position with gravitational wave events. In particular, on 2017 August 17 a binary neutron star coalescence candidate (later designated GW170817) was observed through gravitational waves by the Advanced LIGO and Advanced Virgo detectors [14]. Subsequently, ultra-violet, optical, and infrared emission was observed from the merger, consistent with kilonova/macronova emission.

Auger performed a search for UHE neutrinos with its SD in a time window of ± 500 s centered at the merger time of GW170817, as well as in a 14-day period after it. Remarkably, the position of the optical counterpart was visible from Auger in the field of view of the Earth-skimming channel during the whole ± 500 s window as shown in Fig. 4. Inclined showers passing the Earth-skimming selection (neutrino candidates) were not found in this time window, nor in the 14-day period. However, the absence of candidates allows to constrain the fluence in UHE neutrinos from GW170817 (reported in [15]), assuming they are emitted steadily and with an E^{-2} spectrum.
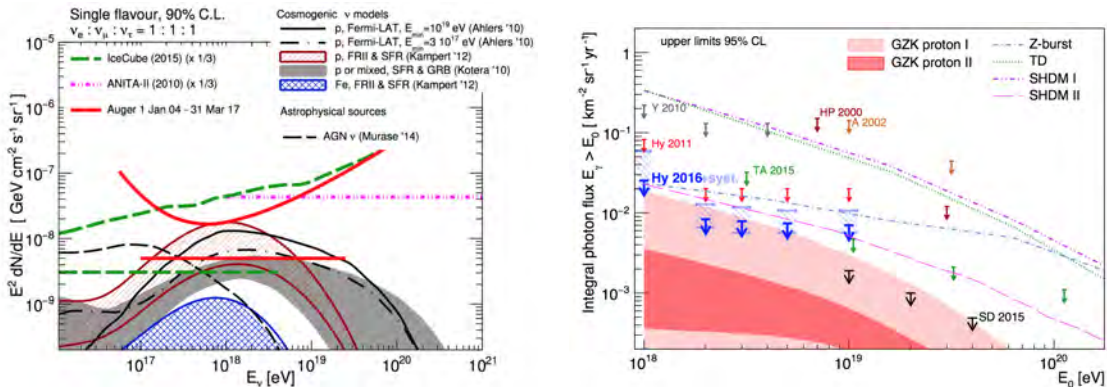

Figure 3: Left: Integral upper limit (at 90% C.L.) for a diffuse neutrino flux, given as a normalization (straight red line) and differential upper limit (see [12] for details). Right: Upper limits on the integral photon flux (95% C.L.) (see [13] for details).

2.5 Anisotropy searches

Besides the measurement of the cosmic ray spectrum and the determination of the primary composition, the analysis of the arrival direction distribution provides a crucial handle for the studies about the origin and nature of the ultra-high energy cosmic rays. It is difficult to locate the sources of cosmic rays, as they are charged particles and thus interact with the
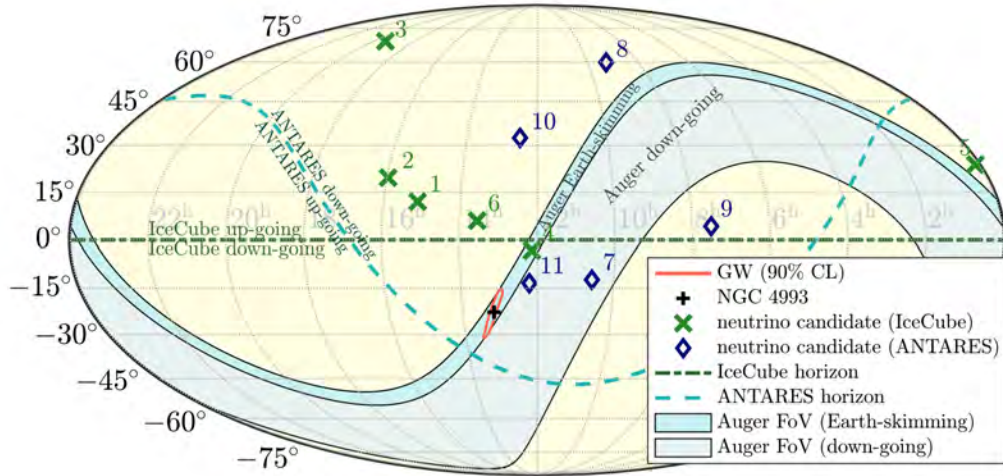

Figure 4: Localizations and sensitive sky areas at the time of the event GW170817 in equatorial coordinates: GW 90% credible-level localization (red contour), direction of NGC 4993 oprtical counterpart (black plus symbol), directions of IceCubes and ANTARESs neutrino candidates within 500 s of the merger (green crosses and blue diamonds, respectively), ANTARESs horizon separating down-going (north of horizon) and up-going (south of horizon) neutrino directions (dashed blue line), and Augers fields of view for Earth-skimming (darker blue) and down-going (lighter blue) directions. Image from [15].
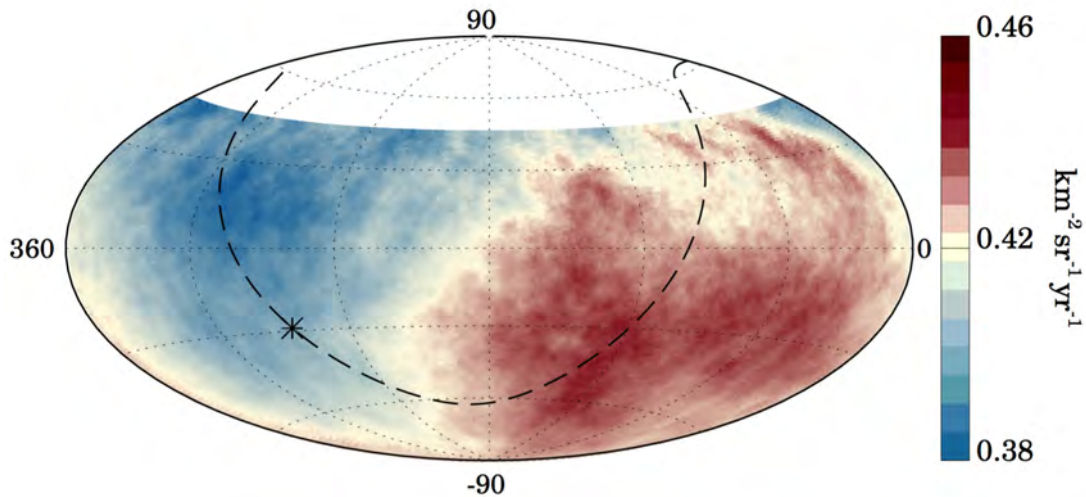

Figure 5: Sky map in equatorial coordinates, using a Hammer projection, of the cosmic-ray flux above 8 EeV smoothed with a 45° top-hat function. The Galactic center is marked with an asterisk and the Galactic plane is shown by a dashed line. Image from [21].

magnetic fields in our galaxy and the intergalactic medium that lies between the sources and Earth. However, even if particles from individual sources are strongly deflected, it remains possible that anisotropies in the distribution of their arrival directions will be detectable on large angular scales. Previous large-scale studies [16, 17, 18, 19] have been performed down to the lowest energies accessible by the Observatory ($\sim 10^{16}$ eV). Nevertheless, the updated analysis [20, 21] considers showers with energies above 4 EeV, in particular the bins 4 EeV < E < 8 EeV and E $\geq$ 8 EeV (median energies 5.0 EeV and 11.5 EeV). The standard approach to study the distribution at large angular scales of the arrival directions is to perform a harmonic analysis over the distributions in right ascension (α) and in the azimuthal angle (ϕ). In fact, in the presence of a three-dimensional dipole, the analysis in right ascension is sensitive only to its component orthogonal to the rotation axis of Earth. Instead, the dipole component in the direction of the rotation axis of Earth induces a modulation in the azimuthal distribution of the arrival directions at the array.

For 4 EeV < E < 8 EeV, the dipole amplitude is again not statistically significant. For energies above 8 EeV, the total dipole amplitude is d = $6.5^{+1.3}_{-0.9}$% pointing toward (l, b) = (233°, 13°) in Galactic coordinates. This dipolar pattern can be clearly seen in the flux map in Fig. 5. To establish whether the departures from a perfect dipole are just statistical fluctuations or indicate the presence of additional structures at smaller angular scales would require at least twice as the events selected for this analysis.

By comparing the results in [21] with phenomenological predictions, the magnitude and direction of the anisotropy support the hypothesis of an extragalactic origin for the highest-energy cosmic rays, rather than sources within the Galaxy. In general, models proposing a Galactic origin up to the highest observed energies are in increasing tension with observations. In this sense, the constraint obtained here on the dipole amplitude for 4 EeV < E < 8 EeV further disfavors a predominantly Galactic origin. This tension could be alleviated if cosmic rays at a few EeV were dominated by heavy nuclei such as iron, but this would be in disagreement with the lighter composition inferred observationally at these energies. Furthermore, the anisotropy observed in events with E $\geq$ 8 EeV is better explained in terms of an extragalactic origin, since the direction of the three-dimensional dipole determined above 8 EeV lies $\sim$ 125° from the Galactic center. Finally, above 40 EeV, where the propagation should become less diffusive, there are no indications of anisotropies associated with either the Galactic center or the Galactic plane.

3   The Pierre Auger Observatory Upgrade: AugerPrime

To answer many questions still open in the UHECR field, the Observatory has started a major upgrade, called AugerPrime [2]. The main goal of AugerPrime is to improve the mass composition sensitivity of the surface detectors to explore energies above 10^{19} eV where the fluorescence detector is not adequate due to its limited duty cycle ($\sim$15%).

The upgrade program will include more powerful SD electronics, an extension of the dynamic range with an additional PMT installed in the water-Cherenkov detectors and above-all the installation of a new detector above each of the existing tanks. This Surface Scintillator Detector (SSD) consists of a plane of plastic scintillator (a box of area 3.8 m × 1.3 m) that will be triggered by the larger WCD below it (Fig. 6).

A thin scintillation detector, which is mounted above the larger WCD, provides a robust and well-understood scheme for particle detection that is sufficiently complementary to the water-

Cherenkov technique and permits a good measurement of the density of muons. The availability of muon information on an event-by-event basis will permit an estimation of the primary mass and also the selection of a sub-sample of events in the cutoff region enriched with light elements, increasing the capacity of the Observatory to identify potential sources of UHECRs.

The first twelve stations of AugerPrime were assembled in Europe and deployed at the Pierre Auger Observatory in September 2016 [22]. This Engineering Array has been in continuous data taking mode since begin of October 2016 and has collected more that 30000 local triggers. In this way the performance of the upgraded stations has been monitored, producing signals that are in good agreement with expectations.

4 Activity of the L'Aquila–Gran Sasso Group

The activity of the group proceed in the following main lines:

- Development of a Monte Carlo code (*SimProp*) for the propagation of UHECR nuclei in extragalactic space, and its use for the study of physical observables [23].

- Development and operation of the Raman Lidar system for an enhanced atmospheric test beam within the Pierre Auger Observatory.

- Study of Lorentz invariance violation from the point of view of the effects on UHECR propagation and interactions of particles in atmosphere [24].

- Development of an updated air shower reconstruction procedure based on the paradigm of air shower Universality [25, 26].

- Participation to the Auger-Telescope Array joint Spectrum working group.

4.1 Talks

- <u>F. Salamida</u> for the Pierre Auger Collaboration, "Highlights from the Pierre Auger Observatory", PSF2017, 10-14 July 2017, Trieste, Italy
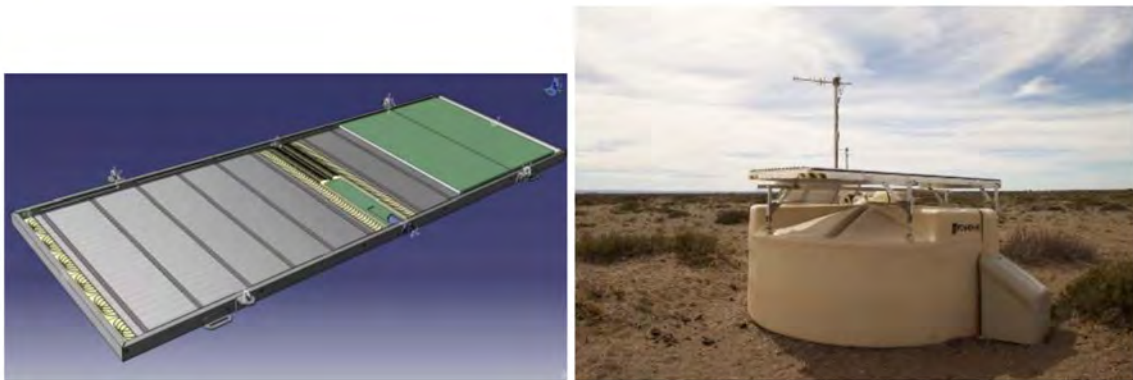

Figure 6: Left: the layout of the Surface Scintillator Detector (SSD); Right: One station of the AugerPrime Engineering Array. Image from [22].

References

[1] A. Aab *et al.* [Pierre Auger Collaboration], Nucl. Instrum. Meth. A **798** (2015) 172 doi:10.1016/j.nima.2015.06.058 [arXiv:1502.01323 [astro-ph.IM]].

[2] A. Aab *et al.* [Pierre Auger Collaboration], arXiv:1604.03637 [astro-ph.IM].

[3] J. Abraham *et al.* [Pierre Auger Collaboration], Phys. Rev. Lett. **101**, 061101 (2008) doi:10.1103/PhysRevLett.101.061101 [arXiv:0806.4302 [astro-ph]].

[4] J. Abraham *et al.* [Pierre Auger Collaboration], Phys. Lett. B **685**, 239 (2010) doi:10.1016/j.physletb.2010.02.013 [arXiv:1002.1975 [astro-ph.HE]].

[5] A. Aab *et al.* [Pierre Auger Collaboration], JCAP **1508**, 049 (2015) doi:10.1088/1475-7516/2015/08/049 [arXiv:1503.07786 [astro-ph.HE]].

[6] Francesco Fenu, for the Pierre Auger Collaboration, "The cosmic ray energy spectrum measured using the Pierre Auger Observatory", ICRC 2017

[7] I. Valiño, for the Pierre Auger Collaboration, "The flux of ultra-high energy cosmic rays after ten years of operation of the Pierre Auger Observatory", ICRC 2015, [arXiv:1509.03732[astro-ph.HE]].

[8] A. Aab *et al.* [Pierre Auger Collaboration], Phys. Rev. D **90**, no. 12, 122005 (2014) doi:10.1103/PhysRevD.90.122005 [arXiv:1409.4809 [astro-ph.HE]].

[9] A. Porcelli, for the Pierre Auger Collaboration, "Measurements of $X_{\max}$ above 10^{17} eV with the fluorescence detector of the Pierre Auger Observatory", ICRC 2015, [arXiv:1509.03732[astro-ph.HE]].

[10] J. Bellido, for the Pierre Auger Collaboration, "Depth of maximum of air-shower profiles at the Pierre Auger Observatory: Measurements above 10 17.2 eV and Composition Implications", ICRC 2017

[11] A. Aab *et al.* [Pierre Auger Collaboration], "Improved limit to the diffuse flux of ultrahigh energy neutrinos from the Pierre Auger Observatory," Phys. Rev. D **91**, no. 9, 092008 (2015) doi:10.1103/PhysRevD.91.092008 [arXiv:1504.05397 [astro-ph.HE]].

[12] E. Zas, for the Pierre Auger Collaboration, "Searches for neutrino fluxes in the EeV regime with the Pierre Auger Observatory : UHE neutrinos at Auger", ICRC 2017

[13] M. Niechciol, for the Pierre Auger Collaboration, "Diffuse and targeted searches for ultra-high-energy photons using the hybrid detector of the Pierre Auger Observatory: Auger photon searches", ICRC 2017

[14] LIGO Scientific and Virgo and Fermi GBM and INTEGRAL and IceCube and IPN and Insight-Hxmt and ANTARES and Swift and Dark Energy Camera GW-EM and Dark Energy Survey and DLT40 and GRAWITA and Fermi-LAT and ATCA and ASKAP and OzGrav and DWF (Deeper Wider Faster Program) and AST3 and CAASTRO and VINROUGE and MASTER and J-GEM and GROWTH and JAGWAR and CaltechNRAO and TTU-NRAO and NuSTAR and Pan-STARRS and KU and Nordic Optical Telescope and ePESSTO and GROND and Texas Tech University and TOROS and BOOTES and MWA and CALET and IKI-GW Follow-up and H.E.S.S. and LOFAR and LWA and

HAWC and Pierre Auger and ALMA and Pi of Sky and DFN and ATLAS Telescopes and High Time Resolution Universe Survey and RIMAS and RATIR and SKA South Africa/MeerKAT Collaborations and AstroSat Cadmium Zinc Telluride Imager Team and AGILE Team and 1M2H Team and Las Cumbres Observatory Group and MAXI Team and TZAC Consortium and SALT Group and Euro VLBI Team and Chandra Team at McGill University, Astrophys. J. **848** (2017) no.2, L12 doi:10.3847/2041-8213/aa91c9 [arXiv:1710.05833 [astro-ph.HE]].

[15] A. Albert *et al.* [ANTARES and IceCube and Pierre Auger and LIGO Scientific and Virgo Collaborations], Astrophys. J. **850** (2017) no.2, L35 doi:10.3847/2041-8213/aa9aed [arXiv:1710.05839 [astro-ph.HE]].

[16] P. Abreu *et al.* [Pierre Auger Collaboration], Astrophys. J. Suppl. **203**, 34 (2012) doi:10.1088/0067-0049/203/2/34 [arXiv:1210.3736 [astro-ph.HE]].

[17] A. Aab *et al.* [Pierre Auger Collaboration], Astrophys. J. **802**, no. 2, 111 (2015) doi:10.1088/0004-637X/802/2/111 [arXiv:1411.6953 [astro-ph.HE]].

[18] A. Aab *et al.* [Telescope Array and Pierre Auger Collaborations], Astrophys. J. **794**, no. 2, 172 (2014) doi:10.1088/0004-637X/794/2/172 [arXiv:1409.3128 [astro-ph.HE]].

[19] I. Al Samarai for the Pierre Auger Collaboration, "Indications of anisotropy at large angular scales in the arrival directions of cosmic rays detected at the Pierre Auger Observatory", ICRC 2015, [arXiv:1509.03732[astro-ph.HE]].

[20] O. Taborda, for the Pierre Auger Collaboration, "Dipolar anisotropy of cosmic rays above 8 EeV", ICRC 2017

[21] A. Aab *et al.* [Pierre Auger Collaboration], Science **357** (2017) no.6537, 1266 doi:10.1126/science.aan4338 [arXiv:1709.07321 [astro-ph.HE]].

[22] D. Martello, for the Pierre Auger Collaboration, "The Pierre Auger Observatory Upgrade", ICRC 2017

[23] A. Aab *et al.* [Pierre Auger Collaboration], JCAP **1704** (2017) no.04, 038 Erratum: [JCAP **1803** (2018) no.03, E02] doi:10.1088/1475-7516/2018/03/E02, 10.1088/1475-7516/2017/04/038 [arXiv:1612.07155 [astro-ph.HE]].

[24] D. Boncioli *et al.*, PoS ICRC **2015** (2016) 521 [arXiv:1509.01046 [astro-ph.HE]].

[25] M. Ave, R. Engel, M. Roth and A. Schulz, Astropart. Phys. **87** (2017) 23. doi:10.1016/j.astropartphys.2016.11.008

[26] M. Ave, M. Roth and A. Schulz, Astropart. Phys. **88** (2017) 46. doi:10.1016/j.astropartphys.2017.01.003

5   List of Publications

1. P. Homola *et al.* [Pierre Auger Collaboration], arXiv:1804.05613 [astro-ph.IM].

2. A. Aab *et al.* [Pierre Auger Collaboration], Astrophys. J. **853** (2018) L29 doi:10.3847/2041-8213/aaa66d [arXiv:1801.06160 [astro-ph.HE]].

3. M. G. Aartsen *et al.* [IceCube and Pierre Auger and Telescope Array Collaborations], arXiv:1801.01854 [astro-ph.HE].

4. A. Aab *et al.* [Pierre Auger Collaboration], Phys. Rev. D **96** (2017) no.12, 122003 doi:10.1103/PhysRevD.96.122003 [arXiv:1710.07249 [astro-ph.HE]].

5. A. Albert *et al.* [ANTARES and IceCube and Pierre Auger and LIGO Scientific and Virgo Collaborations], Astrophys. J. **850** (2017) no.2, L35 doi:10.3847/2041-8213/aa9aed [arXiv:1710.05839 [astro-ph.HE]].

6. B. P. Abbott *et al.* [LIGO Scientific and Virgo and Fermi GBM and INTEGRAL and IceCube and IPN and Insight-Hxmt and ANTARES and Swift and Dark Energy Camera GW-EM and Dark Energy Survey and DLT40 and GRAWITA and Fermi-LAT and ATCA and ASKAP and OzGrav and DWF (Deeper Wider Faster Program) and AST3 and CAASTRO and VINROUGE and MASTER and J-GEM and GROWTH and JAGWAR and CaltechNRAO and TTU-NRAO and NuSTAR and Pan-STARRS and KU and Nordic Optical Telescope and ePESSTO and GROND and Texas Tech University and TOROS and BOOTES and MWA and CALET and IKI-GW Follow-up and H.E.S.S. and LOFAR and LWA and HAWC and Pierre Auger and ALMA and Pi of Sky and DFN and ATLAS Telescopes and High Time Resolution Universe Survey and RIMAS and RATIR and SKA South Africa/MeerKAT Collaborations and AstroSat Cadmium Zinc Telluride Imager Team and AGILE Team and 1M2H Team and Las Cumbres Observatory Group and MAXI Team and TZAC Consortium and SALT Group and Euro VLBI Team and Chandra Team at McGill University], Astrophys. J. **848** (2017) no.2, L12 doi:10.3847/2041-8213/aa91c9 [arXiv:1710.05833 [astro-ph.HE]].

7. A. Aab *et al.* [Pierre Auger Collaboration], Science **357** (2017) no.6537, 1266 doi:10.1126/science.aan4338 [arXiv:1709.07321 [astro-ph.HE]].

8. F. Acero *et al.*, arXiv:1709.03483 [astro-ph.HE].

9. A. Aab *et al.* [Pierre Auger Collaboration], Astropart. Phys. **95** (2017) 44 doi:10.1016/j.astropartphys.2017.09 [arXiv:1709.01537 [astro-ph.IM]].

10. A. Aab *et al.* [Pierre Auger Collaboration], arXiv:1708.06592 [astro-ph.HE].

11. L. Wiencke *et al.*, JINST **12** (2017) no.03, P03008 doi:10.1088/1748-0221/12/03/P03008 [arXiv:1704.04417 [astro-ph.IM]].

12. A. Aab *et al.* [Pierre Auger Collaboration], JINST **12** (2017) no.03, P03002 doi:10.1088/1748-0221/12/03/P03002 [arXiv:1703.06193 [astro-ph.IM]].

13. A. Aab *et al.* [Pierre Auger Collaboration], JINST **12** (2017) no.02, P02006 doi:10.1088/1748-0221/12/02/P02006 [arXiv:1702.02835 [astro-ph.IM]].

14. A. Aab *et al.* [Pierre Auger Collaboration], JINST **12** (2017) no.10, T10005 doi:10.1088/1748-0221/12/10/T10005 [arXiv:1702.01392 [astro-ph.IM]].

The Pierre Auger Collaboration

A. Aab[75], P. Abreu[67], M. Aglietta[49,48], I.F.M. Albuquerque[18], J.M. Albury[12], I. Allekotte[1], A. Almela[8,11], J. Alvarez Castillo[63], J. Alvarez-Muñiz[74], G.A. Anastasi[40,42], L. Anchordoqui[81],

B. Andrada[8], S. Andringa[67], C. Aramo[46], N. Arsene[69], H. Asorey[1,26], P. Assis[67], G. Avila[9,10], A.M. Badescu[70], A. Balaceanu[68], F. Barbato[56,46], R.J. Barreira Luz[67], K.H. Becker[33], J.A. Bellido[12], C. Berat[32], M.E. Bertaina[58,48], X. Bertou[1], P.L. Biermann[b], J. Biteau[30], S.G. Blaess[12], A. Blanco[67], J. Blazek[28], C. Bleve[52,44], M. Boháčová[28], C. Bonifazi[23], N. Borodai[64], A.M. Botti[8,35], J. Brack[f], T. Bretz[37], A. Bridgeman[34], F.L. Briechle[37], P. Buchholz[39], A. Bueno[73], S. Buitink[75], M. Buscemi[54,43], K.S. Caballero-Mora[62], L. Caccianiga[55], L. Calcagni[4], A. Cancio[11,8], F. Canfora[75,77], J.M. Carceller[73], R. Caruso[54,43], A. Castellina[49,48], F. Catalani[16], G. Cataldi[44], L. Cazon[67], J.A. Chinellato[19], J. Chudoba[28], R.W. Clay[12], A.C. Cobos Cerutti[7], R. Colalillo[56,46], A. Coleman[86], L. Collica[48], M.R. Coluccia[52,44], R. Conceição[67], G. Consolati[45,50], F. Contreras[9,10], M.J. Cooper[12], S. Coutu[86], C.E. Covault[79], S. D'Amico[51,44], B. Daniel[19], S. Dasso[5,3], K. Daumiller[35], B.R. Dawson[12], J.A. Day[12], R.M. de Almeida[25], S.J. de Jong[75,77], G. De Mauro[75,77], J.R.T. de Mello Neto[23,24], I. De Mitri[52,44], J. de Oliveira[25], V. de Souza[17], J. Debatin[34], O. Deligny[30], M.L. Díaz Castro[19], F. Diogo[67], C. Dobrigkeit[19], J.C. D'Olivo[63], Q. Dorosti[39], R.C. dos Anjos[22], M.T. Dova[4], A. Dundovic[38], J. Ebr[28], R. Engel[35], M. Erdmann[37], C.O. Escobar[d], A. Etchegoyen[8,11], H. Falcke[75,78,77], J. Farmer[87], G. Farrar[84], A.C. Fauth[19], N. Fazzini[d], F. Feldbusch[36], F. Fenu[58,48], L.P. Ferreyro[8], B. Fick[83], J.M. Figueira[8], A. Filipčič[72,71], M.M. Freire[6], T. Fujii[87,g], A. Fuster[8,11], R. Gaïor[31], B. García[7], H. Gemmeke[36], A. Gherghel-Lascu[68], P.L. Ghia[30], U. Giaccari[23,14], M. Giammarchi[45], M. Giller[65], D. Głas[66], C. Glaser[37], J. Glombitza[37], G. Golup[1], M. Gómez Berisso[1], P.F. Gómez Vitale[9,10], N. González[8,35], I. Goos[1,35], A. Gorgi[49,48], M. Gottowik[33], T.D. Grubb[12], F. Guarino[56,46], G.P. Guedes[20], E. Guido[48,58], R. Halliday[79], M.R. Hampel[8], P. Hansen[4], D. Harari[1], T.A. Harrison[12], V.M. Harvey[12], A. Haungs[35], T. Hebbeker[37], D. Heck[35], P. Heimann[39], A.E. Herve[34], G.C. Hill[12], C. Hojvat[d], E.M. Holt[34,8], P. Homola[64], J.R. Hörandel[75,77], P. Horvath[29], M. Hrabovský[29], T. Huege[35,c], J. Hulsman[8,35], A. Insolia[54,43], P.G. Isar[69], I. Jandt[33], J.A. Johnsen[80], M. Josebachuili[8], J. Jurysek[28], A. Kääpä[33], K.H. Kampert[33], B. Keilhauer[35], N. Kemmerich[18], J. Kemp[37], H.O. Klages[35], M. Kleifges[36], J. Kleinfeller[9], R. Krause[37], N. Krohm[33], D. Kuempel[33], G. Kukec Mezek[71], N. Kunka[36], A. Kuotb Awad[34], B.L. Lago[15], D. LaHurd[79], R.G. Lang[17], R. Legumina[65], M.A. Leigui de Oliveira[21], V. Lenok[35], A. Letessier-Selvon[31], I. Lhenry-Yvon[30], D. Lo Presti[54,43], L. Lopes[67], R. López[59], A. López Casado[74], R. Lorek[79], Q. Luce[30], A. Lucero[8], M. Malacari[87], M. Mallamaci[55,45], D. Mandat[28], P. Mantsch[d], A.G. Mariazzi[4], I.C. Mariş[13], G. Marsella[52,44], D. Martello[52,44], H. Martinez[60], O. Martínez Bravo[59], H.J. Mathes[35], S. Mathys[33], J. Matthews[82], G. Matthiae[57,47], E. Mayotte[33], P.O. Mazur[d], C. Medina[80], G. Medina-Tanco[63], D. Melo[8], A. Menshikov[36], K.-D. Merenda[80], S. Michal[29], M.I. Micheletti[6], L. Middendorf[37], L. Miramonti[55,45], B. Mitrica[68], D. Mockler[34], S. Mollerach[1], F. Montanet[32], C. Morello[49,48], G. Morlino[40,42], M. Mostafá[86], A.L. Müller[8,35], M.A. Muller[19,e], S. Müller[34,8], R. Mussa[48], L. Nellen[63], P.H. Nguyen[12], M. Niculescu-Oglinzanu[68], M. Niechciol[39], L. Niemietz[33], D. Nitz[83,h], D. Nosek[27], V. Novotny[27], L. Nožka[29], A Nucita[52,44], L.A. Núñez[26], F. Oikonomou[86], A. Olinto[87], M. Palatka[28], J. Pallotta[2], P. Papenbreer[33], G. Parente[74], A. Parra[59], T. Paul[81], M. Pech[28], F. Pedreira[74], J. Pękala[64], R. Pelayo[61], J. Peña-Rodriguez[26], L.A.S. Pereira[19], M. Perlin[8], L. Perrone[52,44], C. Peters[37], S. Petrera[40,42], J. Phuntsok[86], T. Pierog[35], M. Pimenta[67], V. Pirronello[54,43], M. Platino[8], J. Poh[87], B. Pont[75], C. Porowski[64], R.R. Prado[17], P. Privitera[87], M. Prouza[28], A. Puyleart[83], E.J. Quel[2], S. Querchfeld[33], S. Quinn[79], R. Ramos-Pollan[26], J. Rautenberg[33], D. Ravignani[8], M. Reininghaus[35], J. Ridky[28], F. Riehn[67], M. Risse[39], P. Ristori[2], V. Rizi[53,42], W. Rodrigues de Carvalho[18], G. Rodriguez Fernandez[57,47], J. Rodriguez Rojo[9], M.J. Roncoroni[8], M. Roth[35], E. Roulet[1], A.C. Rovero[5], P. Ruehl[39], S.J. Saffi[12], A. Saftoiu[68], F. Salamida[53,42], H. Salazar[59], A. Saleh[71], G. Salina[47], F. Sánchez[8], P. Sanchez-Lucas[73], E.M. Santos[18], E. Santos[28], F. Sarazin[80], R. Sarmento[67], C. Sarmiento-Cano[8], R. Sato[9], M. Schauer[33], V. Scherini[44], H. Schieler[35], M. Schimassek[34], M. Schimp[33], D. Schmidt[35,8], O. Scholten[76,c], P. Schovánek[28], F.G. Schröder[34], S. Schröder[33], A. Schulz[34], J. Schumacher[37], S.J. Sciutto[4], A. Segreto[41,43], R.C. Shellard[14],

141

G. Sigl[38], G. Silli[8,35], O. Sima[68,i], R. Šmída[37], G.R. Snow[88], P. Sommers[86], J.F. Soriano[81], J. Souchard[32], R. Squartini[9], D. Stanca[68], S. Stanič[71], J. Stasielak[64], P. Stassi[32], M. Stolpovskiy[32], F. Strafella[52,44], A. Streich[34], F. Suarez[8,11], M. Suárez-Durán[26], T. Sudholz[12], T. Suomijärvi[30], A.D. Supanitsky[5], J. Šupík[29], J. Swain[85], Z. Szadkowski[66], A. Taboada[35], O.A. Taborda[1], C. Timmermans[77,75], C.J. Todero Peixoto[16], B. Tomé[67], G. Torralba Elipe[74], P. Travnicek[28], M. Trini[71], M. Tueros[4], R. Ulrich[35], M. Unger[35], M. Urban[37], J.F. Valdés Galicia[63], I. Valiño[74], L. Valore[56,46], P. van Bodegom[12], A.M. van den Berg[76], A. van Vliet[75], E. Varela[59], B. Vargas Cárdenas[63], R.A. Vázquez[74], D. Veberič[35], C. Ventura[24], I.D. Vergara Quispe[4], V. Verzi[47], J. Vicha[28], L. Villaseñor[59], S. Vorobiov[71], H. Wahlberg[4], O. Wainberg[8,11], D. Walz[37], A.A. Watson[a], M. Weber[36], A. Weindl[35], M. Wiedeński[66], L. Wiencke[80], H. Wilczyński[64], M. Wirtz[37], D. Wittkowski[33], B. Wundheiler[8], L. Yang[71], A. Yushkov[28], E. Zas[74], D. Zavrtanik[71,72], M. Zavrtanik[72,71], L. Zehrer[71], A. Zepeda[60], B. Zimmermann[36], M. Ziolkowski[39], Z. Zong[30], F. Zuccarello[54,43]

[1] Centro Atómico Bariloche and Instituto Balseiro (CNEA-UNCuyo-CONICET), San Carlos de Bariloche, Argentina

[2] Centro de Investigaciones en Láseres y Aplicaciones, CITEDEF and CONICET, Villa Martelli, Argentina

[3] Departamento de Física and Departamento de Ciencias de la Atmósfera y los Océanos, FCEyN, Universidad de Buenos Aires and CONICET, Buenos Aires, Argentina

[4] IFLP, Universidad Nacional de La Plata and CONICET, La Plata, Argentina

[5] Instituto de Astronomía y Física del Espacio (IAFE, CONICET-UBA), Buenos Aires, Argentina

[6] Instituto de Física de Rosario (IFIR) – CONICET/U.N.R. and Facultad de Ciencias Bioquímicas y Farmacéuticas U.N.R., Rosario, Argentina

[7] Instituto de Tecnologías en Detección y Astropartículas (CNEA, CONICET, UNSAM), and Universidad Tecnológica Nacional – Facultad Regional Mendoza (CONICET/CNEA), Mendoza, Argentina

[8] Instituto de Tecnologías en Detección y Astropartículas (CNEA, CONICET, UNSAM), Buenos Aires, Argentina

[9] Observatorio Pierre Auger, Malargüe, Argentina

[10] Observatorio Pierre Auger and Comisión Nacional de Energía Atómica, Malargüe, Argentina

[11] Universidad Tecnológica Nacional – Facultad Regional Buenos Aires, Buenos Aires, Argentina

[12] University of Adelaide, Adelaide, S.A., Australia

[13] Université Libre de Bruxelles (ULB), Brussels, Belgium

[14] Centro Brasileiro de Pesquisas Fisicas, Rio de Janeiro, RJ, Brazil

[15] Centro Federal de Educação Tecnológica Celso Suckow da Fonseca, Nova Friburgo, Brazil

[16] Universidade de São Paulo, Escola de Engenharia de Lorena, Lorena, SP, Brazil

[17] Universidade de São Paulo, Instituto de Física de São Carlos, São Carlos, SP, Brazil

[18] Universidade de São Paulo, Instituto de Física, São Paulo, SP, Brazil

[19] Universidade Estadual de Campinas, IFGW, Campinas, SP, Brazil

[20] Universidade Estadual de Feira de Santana, Feira de Santana, Brazil

[21] Universidade Federal do ABC, Santo André, SP, Brazil

[22] Universidade Federal do Paraná, Setor Palotina, Palotina, Brazil

[23] Universidade Federal do Rio de Janeiro, Instituto de Física, Rio de Janeiro, RJ, Brazil

[24] Universidade Federal do Rio de Janeiro (UFRJ), Observatório do Valongo, Rio de Janeiro, RJ, Brazil

[25] Universidade Federal Fluminense, EEIMVR, Volta Redonda, RJ, Brazil

[26] Universidad Industrial de Santander, Bucaramanga, Colombia

[27] Charles University, Faculty of Mathematics and Physics, Institute of Particle and Nuclear Physics, Prague, Czech Republic

[28] Institute of Physics of the Czech Academy of Sciences, Prague, Czech Republic

[29] Palacky University, RCPTM, Olomouc, Czech Republic

[30] Institut de Physique Nucléaire d'Orsay (IPNO), Université Paris-Sud, Univ. Paris/Saclay, CNRS-IN2P3, Orsay, France

[31] Laboratoire de Physique Nucléaire et de Hautes Energies (LPNHE), Universités Paris 6 et Paris 7, CNRS-IN2P3, Paris, France

[32] Univ. Grenoble Alpes, CNRS, Grenoble Institute of Engineering Univ. Grenoble Alpes, LPSC-IN2P3, 38000 Grenoble, France, France

[33] Bergische Universität Wuppertal, Department of Physics, Wuppertal, Germany

[34] Karlsruhe Institute of Technology, Institute for Experimental Particle Physics (ETP), Karlsruhe, Germany

[35] Karlsruhe Institute of Technology, Institut für Kernphysik, Karlsruhe, Germany

[36] Karlsruhe Institute of Technology, Institut für Prozessdatenverarbeitung und Elektronik, Karlsruhe, Germany

[37] RWTH Aachen University, III. Physikalisches Institut A, Aachen, Germany

[38] Universität Hamburg, II. Institut für Theoretische Physik, Hamburg, Germany

[39] Universität Siegen, Fachbereich 7 Physik – Experimentelle Teilchenphysik, Siegen, Germany

[40] Gran Sasso Science Institute, L'Aquila, Italy

[41] INAF – Istituto di Astrofisica Spaziale e Fisica Cosmica di Palermo, Palermo, Italy

[42] INFN Laboratori Nazionali del Gran Sasso, Assergi (L'Aquila), Italy

[43] INFN, Sezione di Catania, Catania, Italy

[44] INFN, Sezione di Lecce, Lecce, Italy

[45] INFN, Sezione di Milano, Milano, Italy

[46] INFN, Sezione di Napoli, Napoli, Italy

[47] INFN, Sezione di Roma "Tor Vergata", Roma, Italy

[48] INFN, Sezione di Torino, Torino, Italy

[49] Osservatorio Astrofisico di Torino (INAF), Torino, Italy

[50] Politecnico di Milano, Dipartimento di Scienze e Tecnologie Aerospaziali , Milano, Italy

[51] Università del Salento, Dipartimento di Ingegneria, Lecce, Italy

[52] Università del Salento, Dipartimento di Matematica e Fisica "E. De Giorgi", Lecce, Italy

[53] Università dell'Aquila, Dipartimento di Scienze Fisiche e Chimiche, L'Aquila, Italy

[54] Università di Catania, Dipartimento di Fisica e Astronomia, Catania, Italy

[55] Università di Milano, Dipartimento di Fisica, Milano, Italy

[56] Università di Napoli "Federico II", Dipartimento di Fisica "Ettore Pancini", Napoli, Italy

[57] Università di Roma "Tor Vergata", Dipartimento di Fisica, Roma, Italy

[58] Università Torino, Dipartimento di Fisica, Torino, Italy

[59] Benemérita Universidad Autónoma de Puebla, Puebla, México

[60] Centro de Investigación y de Estudios Avanzados del IPN (CINVESTAV), México, D.F., México

[61] Unidad Profesional Interdisciplinaria en Ingeniería y Tecnologías Avanzadas del Instituto Politécnico Nacional (UPIITA-IPN), México, D.F., México

[62] Universidad Autónoma de Chiapas, Tuxtla Gutiérrez, Chiapas, México

[63] Universidad Nacional Autónoma de México, México, D.F., México

[64] Institute of Nuclear Physics PAN, Krakow, Poland

[65] University of Łódź, Faculty of Astrophysics, Łódź, Poland

[66] University of Łódź, Faculty of High-Energy Astrophysics,Łódź, Poland

[67] Laboratório de Instrumentação e Física Experimental de Partículas – LIP and Instituto Superior Técnico – IST, Universidade de Lisboa – UL, Lisboa, Portugal

[68] "Horia Hulubei" National Institute for Physics and Nuclear Engineering, Bucharest-Magurele,

Romania

[69] Institute of Space Science, Bucharest-Magurele, Romania

[70] University Politehnica of Bucharest, Bucharest, Romania

[71] Center for Astrophysics and Cosmology (CAC), University of Nova Gorica, Nova Gorica, Slovenia

[72] Experimental Particle Physics Department, J. Stefan Institute, Ljubljana, Slovenia

[73] Universidad de Granada and C.A.F.P.E., Granada, Spain

[74] Instituto Galego de Física de Altas Enerxías (I.G.F.A.E.), Universidad de Santiago de Compostela, Santiago de Compostela, Spain

[75] IMAPP, Radboud University Nijmegen, Nijmegen, The Netherlands

[76] KVI – Center for Advanced Radiation Technology, University of Groningen, Groningen, The Netherlands

[77] Nationaal Instituut voor Kernfysica en Hoge Energie Fysica (NIKHEF), Science Park, Amsterdam, The Netherlands

[78] Stichting Astronomisch Onderzoek in Nederland (ASTRON), Dwingeloo, The Netherlands

[79] Case Western Reserve University, Cleveland, OH, USA

[80] Colorado School of Mines, Golden, CO, USA

[81] Department of Physics and Astronomy, Lehman College, City University of New York, Bronx, NY, USA

[82] Louisiana State University, Baton Rouge, LA, USA

[83] Michigan Technological University, Houghton, MI, USA

[84] New York University, New York, NY, USA

[85] Northeastern University, Boston, MA, USA

[86] Pennsylvania State University, University Park, PA, USA

[87] University of Chicago, Enrico Fermi Institute, Chicago, IL, USA

[88] University of Nebraska, Lincoln, NE, USA

[a] School of Physics and Astronomy, University of Leeds, Leeds, United Kingdom

[b] Max-Planck-Institut für Radioastronomie, Bonn, Germany

[c] also at Vrije Universiteit Brussel, Brussels, Belgium

[d] Fermi National Accelerator Laboratory, USA

[e] also at Universidade Federal de Alfenas, Poços de Caldas, Brazil

[f] Colorado State University, Fort Collins, CO, USA

[g] now at Institute for Cosmic Ray Research, University of Tokyo

[h] also at Karlsruhe Institute of Technology, Karlsruhe, Germany

[i] also at University of Bucharest, Physics Department, Bucharest, Romania

Cosmic Silence

L. Satta[a], E. Bortolin[b], C. De Angelis[b], G. Esposito[b], C. Quattrini[b], C. Nuccetelli[b], M. A. Tabocchini[a,b,*], E. Alesse[c], M. Balata[d], L. Ioannuci[d], A. Esposito[e], O. Frasciello[e], M. Chiti[e], G. Cenci[a,f], F. Cipressa[a,f] PF. Morciano[f] A. Porrazzo[f]

[a]Museo Storico della Fisica e Centro Studi e Ricerche Enrico Fermi

[b]Istituto Superiore di Sanitá, Technology and Health Department, and INFN-Roma1, 00161 Roma, Italy

[c]LAquila University, Department of Biotechnological and Applied Clinical Sciences

[d]INFN - Gran Sasso National Laboratory

[e]INFN - Frascati National Laboratory

[f]La Sapienza University of Rome, "C. Darwin" Department of Biology and Biotechnologies

[(*)] Spokepersons

Abstract

Deep underground laboratories (DULs), originally created to host particle, astroparticle or nuclear physics experiments, are increasingly used for underground biology experiments. Among these DULs is the Gran Sasso National Laboratory (LNGS), where the majority of radiobiological data have been collected so far. Here we focus on the recent results obtained using the model system *Drosophila melanogaster*, which provided the first evidence at the organism level of the influence of the radiation environment in modulating life span, fertility and response to genotoxic stress. In particular, we describe the results of the first experiments aimed at understanding the molecular mechanisms underlying these effects. We also report on the status of the physical characterization of the radiation field in the different experimental sites.

1 Introduction

The limited understanding of the biological effects induced by ionizing radiation at low dose/dose rate continues to be the major challenge in predicting radiation risk to human health. Several *in vitro* radiobiological studies have been performed at Gran Sasso National Laboratory (LNGS) in order to increase the knowledge in this research area [1-6]. The overall message derived from these studies is that environmental radiation is necessary to trigger mechanisms that increase the ability to respond to stress. Recently, we obtained the first evidence of a differential response below and above ground at the organism level using the fruit fly *Drosophila melanogaster* as a model organism. We have reported a comparative data set on lifespan, fertility and response

to genotoxic stress in different *Drosophila* strains that were raised in parallel at the Gran Sasso National Laboratory (LNGS) and in the reference laboratory at LAquila University [7]. Our study has shown that the permanence in a strongly reduced radiation environment can indeed affect *Drosophila* development and, depending on the genetic background, may affect viability for several generations even when flies are moved back to the reference radiation environment. Of further relevance is that changes in *Drosophila* growth and development are observed as soon as after 2 weeks of permanence underground, giving suggestions for possible mechanisms involved.

2 The FLYINGLOW project

A few years ago, in the framework of a collaboration between INFN, ISS, Rome University and Centro Fermi, we launched the FLYINGLOW project, a research program meant to determine whether the LNGS underground environment could affect different life parameters associated with *Drosophila melanogaster*, a well-established model organism. The recently reported results [7] indicated that the reduction of environmental radiation affects developmental parameters of *Drosophila*, providing for the first time evidence of the influence of radiation background in a complex organism. We compared different developmental parameters, such as life span, fertility and motility activity, between control flies maintained for different generations at the LNGS (LRE) and at the reference Laboratory at LAquila University (RRE), located very close to the LNGS. We found that the median life span of independent populations, consecutively raised and maintained for several generations at LRE, was significantly increased with respect to that of reference (RRE) wild-type populations, indicating that reduction of natural background radiation alters the survival ratio. Interestingly, the positive effect on lifespan was observed as early as after one generation time (1015 days) and the extension rate remained constant as well, even after several generations. These results indicated that a short time of permanence underground was sufficient to obtain a significant effect on the biology of a complex organism. Moreover, this finding ruled out the possibility that this effect could be caused by potential LNGS-induced mutations that suppressed normal aging, as they would have required a much longer time to get fixed in the population. The molecular mechanisms underlying the effect on life span are still unclear. However, a comparative analysis of heterochromatin domains in body wall muscle fibers between LRE and RRE in 40-day-old adult flies provided some clues. It has been reported that heterochromatin levels, as revealed by the presence of Heterochromatin Protein 1a (HP1a) foci, in *Drosophila* muscular nuclei, gradually decline with aging and can account for age-related muscle degeneration (sarcopenia) [8]. Consistently, we found that HP1 localization at the chromocenter of muscular cells from 40-day-old adult flies kept at RRE, was dramatically reduced with respect to those from young adult flies (Fig. 1). This finding might present an intriguing notion that LRE could prolong life span by preventing heterochromatin decline, which in turns prevents muscle fragility.

While LRE prolongs the life span, it also strongly limits the reproductive capacity of both male and female flies. Fertility tests that were performed on both wild-type Oregon male and female adults from the same generation time have indeed shown that LNGS background radiation reduces the fertility of both male and female adults by 30%. Interestingly, as with the effect on lifespan, the fertility reduction was observed in flies as soon as they were raised at the LNGS for two generations, and more importantly the rate of reduced fertility remained almost unchanged along different generations. This latter evidence excluded the possibility that the reduction in
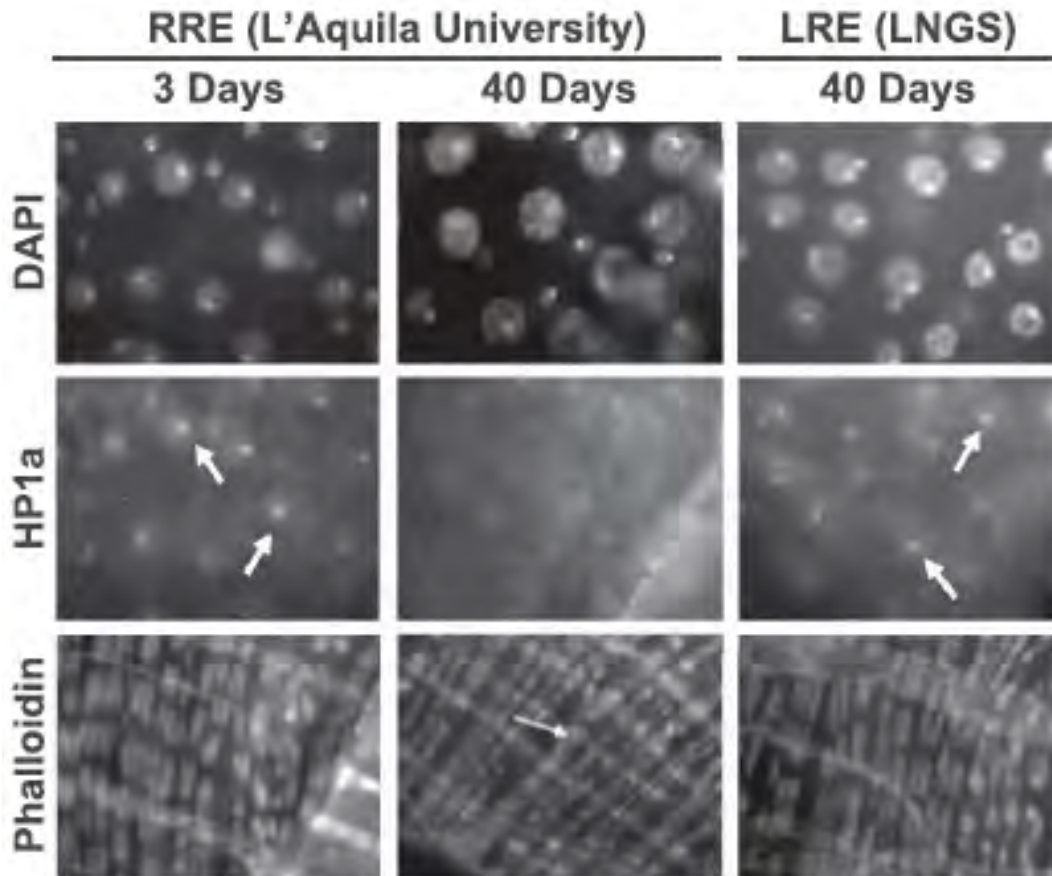
Figure 1: Age-dependent loss of heterochromatin is prevented by low-radiation enviroment (LRE). Gut tissues from young (3-day-old) and old (40-day-old) reference radiation environment (RRE) female flies and from old (40-day-old) low-radiation enviroment (LRE) female flies were dissected and stained with anti-HP1 to visualize the heterochromatin domains and phalloidin-fluorescein to reveal the longitudinal and circular intestinal body wall muscle fibers. Note the presence of marked HP1-enriched foci in the young RRE gut, which appear more diffuse in the old RRE gut but still prominent in old LRE gut (arrows). The phalloidin staining reveals that muscle fibers in old LRE flies are indistinguishable from that of young RRE flies, whereas, as expected, their morphology appears degenerated in old RRE flies. (*Morciano et al., Radiat Res in press*)

fertility was a consequence of the induction of spontaneous mutations, which could eventually affect fertility progressively as the generation time increases. We can speculate that the LRE-induced decrease in fertility is related to the general effect of low-radiation background on DNA repair. Indeed, proper DNA repair plays a pivotal role in the complete execution of specific biological processes in Drosophila, including male and female meiosis [9, 10]. Thus, it is conceivable that both spermatogenesis and oogenesis may be particularly influenced by reduced radiation background. From this perspective, a prolonged lifespan extension is not quite unexpected, since it could reflect the obligate trade-off between survival and reproduction that underlies the widespread cost of reproduction [11]. Moreover, we found that flies bearing the *5190* mutant

allele in the ATM-encoding tefu gene, that are normally semilethal when homozygous (i.e., only rare adults are found at RRE), generated a number of homozygous adults was much higher (20%) than that observed at RRE (1:3%), indicating that LRE conditions positively selected the survival of flies with little ATM protein. This finding might present an intriguing notion that LRE could prolong life span by preventing heterochromatin decline, which in turns prevents muscle fragility. We observed that the frequency of *tefu* homozygotes remained high when LRE *tefu* mutant lines were moved and kept at RRE for two more generations, indicating that the LRE-induced positive selection of ATM defective flies is retained in a trans-generational manner. Given that trans-generational inheritance is mainly regulated by epigenetics mechanisms [12], it would be interesting to unravel which type of LRE-induced epigenetic change underlies the suppression of lethality of *tefu* homozygotes.

3 Update on the physical characterization in the different experimental sites

The dosimetric characterization of the different experimental sites is crucial for the interpretation of results. We have carried out further measurements of the gamma component in the experimental site where Drosophila lines are maintained, using thermoluminescence dosimeters, specifically TLD-700H. We found that the dose rate values due to gamma component of the radiation background inside the underground laboratory and at LAquila University are about $20nGy/h$ and $75nGy/h$, respectively. These TLD data were confirmed by measurements carried out with Reuter Stokes and plastic scintillator (Automess). An important aspect of the experimental set up is to stabilize as much as possible the Radon concentration inside the COSMIC SILENCE facility where the biological experiments are carried out. This facility is provided with temperature, humidity and light control systems as well as with a ventilation system that supplies fresh air, continuously collected directly from the external environment. Ventilation is fundamental for the reduction of Radon in the experimental site. We increased the air exchange number and the air flow in order to bring the Radon concentration inside the COSMIC SILENCE facility close to the value of the external reference environment. We measured $(10 - 20Bq/m3)$, i.e. a condition that allow us to conclude that Radon concentration has been stabilized at the minimum level. Besides the careful control of the environmental parameters (presence of Radon, temperature, pressure, relative humidity), the major problem when parallel underground and aboveground experiments are carried out is related to the identification of other possible systematic confounding factors. They have been widely evaluated, specifically for the different biological systems used since the beginning of our investigation. In particular, for cultured cells as well as for fruit flies, all the reagents (culture media, buffers, chemicals,) used during the sample growth and manipulations were the same. Moreover, the same operator was in charge for all the experiments carried out with *Drosophila*. With this approach we are confident to minimize all the possible sources of variability that, at the best of our knowledge, can affect the experimental results.

Perspectives

The determination of whether low-radiation background could affect life and development of multicellular and complex organisms remains a high priority task in most underground laboratory agendas [13-17]. At the LNGS we have successfully started to address this complex question using *Drosophila melanogaster* as model system. So far our study has provided the first evidence

in organisms of how reducing normal environmental radiation could perturb basic biological processes such as lifespan and fertility and sheds more light on how normal environmental radiation variation had contribute to evolution. Our purpose is to get more insights on the physical and biological mechanisms underlying the observed effects. For radiation protection purposes, underground experiments can be nicely complemented with above ground studies at increasing dose rate. This can be done by choosing different reference sites above ground and/or using radiation facilities specifically designed for low-dose/dose-rate studies, such the LIBIS facility designed and set up at the ISS [18].

Acknowledgements

References

1. L. Satta, G. Augusti-Tocco, R. Ceccarelli, A. Esposito, M. Fiore, P. Paggi, I. Poggesi, R. Ricordy, G. Scarsella, E. Cundari. *Low environmental radiation background impairs biological defence of the yeast Saccharomyces cerevisiae to chemical radiomimetic agents.* Mutat. Res. 347(3-4):129-33, 1995

2. L. Satta, F. Antonelli, M. Belli, O. Sapora, G. Simone, E. Sorrentino, M.A. Tabocchini, F. Amicarelli, C. Ara, M.P. Cer, S. Colafarina, L. Conti Devirgiliis, A. De Marco, M. Balata, A. Falgiani, S. Nisi. *Influence of a low background radiation environment on biochemical and biological responses in V79 cells.* Radiat. Environ. Biophys. 41 (3):217-24, 2002

3. M.C. Carbone, M. Pinto, F. Antonelli, F. Amicarelli, M. Balata, M. Belli, L. Conti Devirgiliis, L. Ioannucci, S. Nisi, O. Sapora, et al. *The Cosmic Silence Experiment: on the putative adaptive role of environmental ionizing radiation.* Radiat. Environ. Biophys. 48:189-196, 2009

4. M.C. Carbone, M. Pinto, F. Antonelli, F. Amicarelli, M. Balata, M. Belli, L. Conti Devirgiliis, O. Sapora, G. Simone, E. Sorrentino, M.A. Tabocchini, L. Satta. *Effects of deprivation of background environmental radiation on cultured human cells.* Il Nuovo Cimento 4:469-477, 2010

5. E. Fratini, C. Carbone, D. Capece, G. Esposito, G. Simone, M.A. Tabocchini, M. Tomasi, M. Belli, L. Satta. *Low-radiation environment affects the development of protection mechanisms in V79 cells.* Radiat. Environ. Biophys. 54(2):183-94, 2015

6. E. Fratini, M.F. Fischietti, G. Simone, E. Bortolin, C. De Angelis, G. Esposito, P. Fattibene, C. Nuccetelli, C. Quattrini, M. A. Tabocchini, E. Alesse, A. Tessitore, F. Zazzeroni, M. Balata, L. Ioannuci, A. Esposito, M. Chiti, O. Frasciello, L. Satta, M. Pavan, G. Cenci. Cosmic Silence. *LNGS Annual Report* 202-212, 2015

7. P. Morciano, R. Iorio, D. Iovino, F. Cipressa, G. Esposito, A. Porrazzo, L. Satta, E. Alesse, M.A. Tabocchini and G. Cenci. 2017. *Effects of reduced natural background radiation on* Drosophila *melanogaster growth and development as revealed by the FLYINGLOW program.* Journal of Cellular Physiology (doi: 10.1002/jcp.25889. [Epub ahead of print].

8. K. Larson, S-J. Yan , A. Tsurumi , J. Liu , J. Zhou, K. Gaur, et al. *Heterochromatin formation promotes longevity and represses ribosomal RNA synthesis.* PLoS Genet 2012; 8:e1002473.

9. H. Blanton , J. Sekelsky. *Unique invasions and resolutions: DNA repair proteins in meiotic recombination in Drosophila melanogaster.* Nat. Rev. Genetic Cytogenet Genome Res 2004; 107:1729.

10. G.Peretz, LG. Arie , A. Bakhrat, U. Abdu. *The Drosophila hus1 gene is required for homologous recombination repair during meiosis.* Mech Dev 2009; 126:67786

11. AI. Barnes , S. Wigby , JM. Boone, L. Partridge, T. Chapman. *Feeding, fecundity and lifespan in female Drosophila melanogaster.* Proc Biol Sci 2008; 275:167583

12. V. Serobyan , RJ. Sommer. *Developmental systems of plasticity and trans-generational epigenetic inheritance in nematodes.* Curr Opin Genet Dev 2017; 45:517

13. GB. Smith , Y. Grof, A. Navarrette, RA. Guilmette. *Exploring biological effects of low level radiation from the other side of background.* Health Phys 2011; 100:2635.

14. N. Lampe, V. Breton, D. Sarramia, T. Sime-Ngando, DG. Biron. *Understanding low radiation background biology through controlled evolution experiments.* Evol Appl 2017; 10: 65866. (https://doi.org/10.1111/eva.12491)

15. C . Thome, S. Tharmalingam, J. Pirkkanen, A. Zarnke, T. Laframboise, DR. Boreham *The REPAIR Project: examining the biological impacts of sub-background radiation exposure within SNOLAB, a deep underground laboratory.* Radiat Res 2017;188:4704.

16. N . Lampe, P . Marin, J. Castor, G. Warot, S. Incerti, L. Maigne, et al. *Background study of absorbed dose in biological experiments at the Modane Underground Laboratory.* EPJ Web of Conferences 2016; 124, 00006. (https://bit.ly/2rKWP32)

17. J .Liu, T. Ma, Y. Liu, J. Zou, M. Gao, R. Zhang, J. Wu, S. Liu, H. Xie *History, advancements, and perspective of biological research in deepunderground laboratories: A brief review.* Environmental Internatuional. 120 (2018) 207-214

18. G. Esposito, P. Anello, I. Pecchia, M.A. Tabocchini, A.Campa.*Facility for gamma irradiations of cultured cells at low dose rates: design, physical characteristics and functioning.* Appl. Radiat. Isot. 115: 227-234, 2016

List of publications and international meetings presentations

- P. Morciano, R. Iorio, D. Iovino, F. Cipressa, G. Esposito, A. Porrazzo, L. Satta, E. Alesse, M.A. Tabocchini and G. Cenci. 2017. *Effects of reduced natural background radiation on* Drosophila *melanogaster growth and development as revealed by the FLYINGLOW program.* Journal of Cellular Physiology (doi: 10.1002/jcp.25889. [Epub ahead of print March 2017].

- A. Cicconi, E. Micheli, F. Vern, A. Jackson , A. Gradilla, F. Cipressa, D. Raimondo, G. Bosso, J. Wakefield, L. Ciapponi, G. Cenci, M. Gatti, S. Cacchione, G. Raffa. (2016). The *Drosophila* telomere-capping protein Verrocchio binds single-stranded DNA and protects telomeres from DNA damage response. *Nucleic Acid Research* 2017 45:3068-3085.

- P. Morciano, F. Cipressa, A. Porrazzo, G. Esposito, M.A. Tabocchini,G. Cenci. Fruit Flies Provide New Insights in Low-Radiation Background Biology at the INFN Underground Gran Sasso National Laboratory (LNGS). *Radiat Res. (in press).*

- L. Graziadio, V. Palumbo, F. Cipressa, B.C. Williams, G. Cenci, M. Gatti, M.L. Goldberg, S. Bonaccorsi. Phenotypic characterization of diamond (dind), a Drosophila gene required for multiple aspects of cell division. *Chromosoma (in press).*

- M.A.Tabocchini. Radiobiological evidence challenging the LNT model for cancer risk extrapolation. *5 Congreso Conjunto 21 SEPM/16 SEPR, Girona, Spain, 13-16 Junio 2017*

- M.A.Tabocchini. The underground biology at the INFN Gran Sasso National Laboratory. *Fifth Internation Workshop for the Design of the ANDES Underground Laboratory. Buenos Aires, Argentina, 29-30 June 2017*

- F. Cipressa, A. Porrazzo, P. Morciano, G. Esposito, M.A. Tabocchini, G. Cenci. Low doses of gamma irradiation enhance the efficiency of DNA repair in Drosophila melanogaster. *2nd European Radiological Protection Week, Paris, 10-12 October 2017*

GINGER

The G-GranSasso collaboration

The GINGER (Gyroscopes IN GEneral Relativity) experiment foresees the realization of an underground-installed array of large-frame Ring Laser Gyroscopes (RLGs) aimed at measuring the rotational motion of the Earth with unprecedented sensitivity and long-term stability. The scientific target of the experiment is to investigate General Relativity phenomena, in particular the Lense-Thirring effect with a relative precision of 1%, presently not attainable by other methods.

In view of the array realization, the experiment is presently in the stage of validation of the site and of the methods. To this aim, a single RLG, called GINGERino, is in operation at LNGS and, in parallel, a smaller-size instrument, called GP-2, is running at INFN Pisa as a test-bench for implementing and assessing technical improvements.

Results acquired in 2017 are relevant for the progress of different R&D activities, ranging through performance improvements of the apparatus to refinements of the overall project in view of its challenging scientific objectives. Furthermore, the uninterrupted operation of GINGERino for over 90 days since May 2017 enabled collecting rotational motion data of great interest within the frame of geoscience.

1   Introduction

The experiment G-GranSasso is based on a heterolithic Ring Laser Gyroscope (RLG) with 3.6 m side length, called GINGERino, installed underground at LNGS. An RLG is an extremely sensitive instrument for measuring rotational motion and, at present, it provides the most accurate method for determining the absolute angular velocity in Earth based apparatus, with a noise floor on the order of 10^{-10} (rad/s)/$\sqrt{\text{Hz}}$. Thanks to the underground location and the subsequent strong suppression of anthropic noise and fluctuations of the operating conditions, such as temperature and pressure, GINGERino represents a unique device for assessing the ultimate potential of RLGs.

Main goal of the experiment was to investigate the feasibility of a larger experiment called GINGER, an array of RLGs comprising a minimum of three large area gyroscopes to be installed underground, suitably oriented each other in order to measure all components of Earth rotational velocity. The scientific aim is to enable on Earth measurements of the Lense-Thirring effect at a targeted precision of 1%, presently not attainable by other methods.

Further to progressing towards GINGER, a task involving careful characterization of the RLG and the deployment of a range of technical improvements, the availability of GINGERino and its uninterrupted operation since May 2017 made possible to collect reliable data on Earth angular velocity and its variations associated with, e.g., seismic events. Owing to their sensitivity and long term stability, such data stimulate a very large interest within the frame of geoscience.

The presentation of the activities carried out in 2017 is therefore broken in different sections, addressing technical improvements, analysis of data collected in 90-day uninterrupted operation, progress towards GINGER.

2   Technical improvements

GINGERino consists of a granite slab connected at its center to a reinforced concrete structure, representing a mechanical link with the Earth. Mirrors and vacuum pipes needed to realize the RLG, as well as the HeNe discharge required for laser radiation, are mechanically connected to the granite slab realizing a heterolithic structure. The ring cavity has a square shape with 3.6 m long sides and the orientation of the RLG plane is orthogonal to the the local vertical direction.

According to the general strategy of the experiment, and also accounting for the cumbersome access to the underground site, technical improvements have been realized and tested at INFN Pisa, where a smaller size RLG, called GP-2, is in operation. Main technical improvements considered in 2017 are listed here in the following, along with their progress status.

2.1   New data acquisition system and remote control

The original GINGERino relies, for data acquisition, on a National Instruments PXI system. While still in operation, and actually able to ensure uninterrupted and unattended data acquisition for more than 90 days (see the next section), the system presents several limitations. Signals pertaining to RLG operation (the Sagnac beating signal, two monobeam intensity signals for the radiation propagating clockwise and counter-clockwise in the ring, an intensity monitor for the laser discharge, looking at the plasma fluorescence) are acquired at the fast rate of 5 kHz. Environmental data (output of a 3-axis tiltmeter mounted on top of the RLG structure, temperature, eventually air pressure and flow) were expected to be acquired at the slow rate of 1 Hz, owing to the response time of the involved sensors. The slow rate acquisition showed problems of synchronization leading, for instance, to unavailable temperature data for the uninterrupted 90 day acquisition run discussed in the next section.

A new data acquisition system, based on D/A cards mounted on-board of an industrial-grade computer, has been designed, realized and tested to a large extent. It foresees accurate synchronization of a commercial Rb-clock with the pulse-per-second (PPS) signal available in the underground lab and acquisition of all environmental data channels. Fast-rate data will be acquired for redundancy on both systems, the old PXI and the new computer-based one. Once completely tested, the system will be mounted at the underground site (installation foreseen before summer 2018).

Another relevant issue that will be addressed by the new system is the remote control of the RLG operation. In the case of power failures, the present setup requires the presence of an operator for the electrical discharge of the laser to be switched-on and regulated to the very low-current regime needed for single mode operation of the source. A remotely actuated system based on a capacitive spark discharge current control has been designed and realized at INFN Pisa. The system will be also fitted to GINGERino along with the new data acquisition device.

2.2   Measurement of diagonal lengths and control of geometry

Because of its heterolithic structure, GINGERino may suffer from fluctuations of the geometry. They can affect the sensitivity, since, in a RLG, the scaling factor k_S connecting the frequency of the Sagnac beat note and the angular velocity depends on area A and perimeter P of the ring cavity according to

$$k_S = \frac{4A}{\lambda P} \cos \theta \, , \tag{1}$$

with λ the laser wavelength (633 nm, in our case) and θ the angle of the rotational axis with the normal to ring plane.

While the results presented in the next section suggest that such fluctuations play an almost negligible role in long-term runs performed at the underground site, efforts in 2017 have been devoted also to project, realize and test methods for stabilizing the geometry, with the main goal to further improve sensitivity and long-term stability. The involved technique is based on the continuos monitor and feedback-control of lengths for the two ring diagonals, carried out with a metrological system referenced to a stabilized laser with a linewidth of the order of 100 kHz fwhm.

The stabilization requires the ability to displace the mirrors through piezo-electric actuators. Furthermore, a rather complex experimental setup is needed in order to produce stabilized-frequency laser radiation, to modulate it with acousto-optic and electro-optic modulators (AOM and EOM, respectively) and to distribute it to two distinct Fabry-Prot cavities aligned along the ring diagonals and using the ring mirrors. Realization and test of the system have been carried out on the GP-2 at INFN Pisa. The results will be eventually useful to further enhance long-term stability of GINGER.
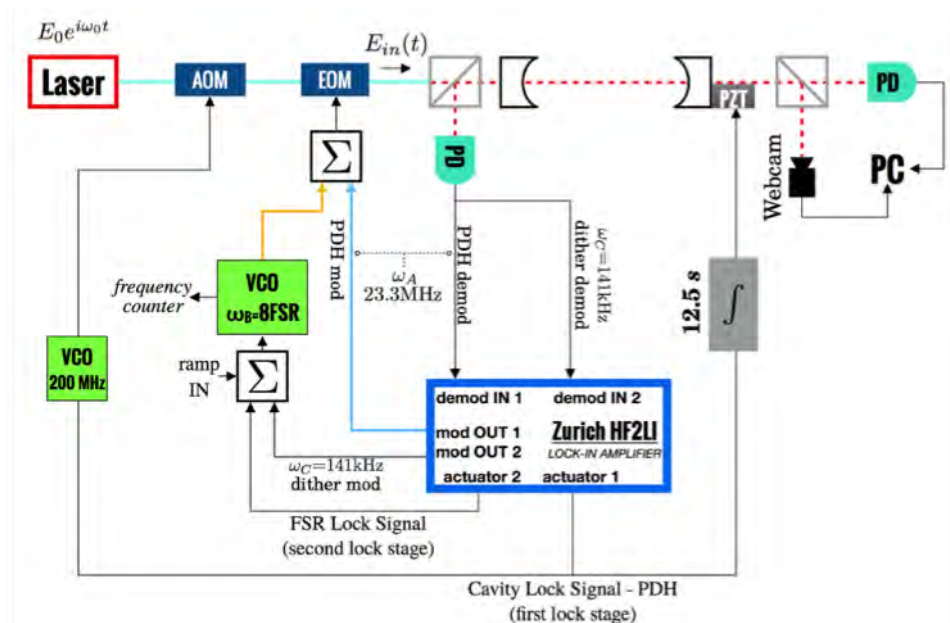
Figure 1: Overview of the setup installed in GP-2 for measuring and stabilizing the ring diagonal lengths [1]: the setup is duplicated for the two diagonals.

Figure 1 [1] shows a general overview of the system. A Pound-Drever-Hall setup is used to lock the laser on the Fabry-Pérot (FP) frequency through EOM modulation, while independent locking at a higher harmonic of the FP free-spectral range allows measuring its length, i.e., the length of the ring diagonal. Actuation is then accomplished by acting on piezo-electric translators after time integration in the 10 s range, required to match with the small band-pass of the translators.

Quite interesting results have been achieved already by running GP-2 for short periods (14 hours, without and with the diagonal length control). Due to the small size of the ring cavity and to the installation in a noisy environment, strongly affected by anthropic activities and with poor temperature stabilization, GP-2 operates with a definitely worse signal-to-noise ratio than GINGERino. Nonetheless, as shown in Fig. 2, reporting the distribution of the length measurements for the two diagonals integrated over 14 hours, along with Gaussian best-fits, the

measurement accuracy was very good. In particular, the uneven length of the two diagonals was ascertained with an estimated uncertainty of 130 nm over 1 hour of measurements. Such results make active length stabilization in GINGER a very appealing perspective, worth to be further pursued.
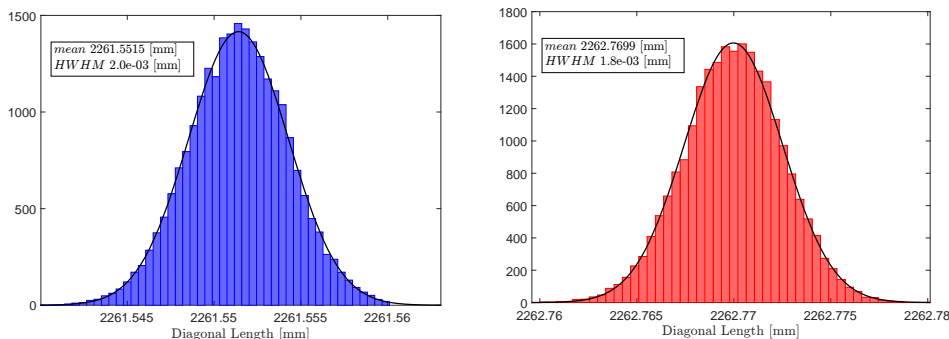

Figure 2: Distribution of measured lengths for the two diagonals on a measurement duration of 14 hours. Black lines represent the results of best-fit to Gaussian functions (parameters reported in the legends). The two diagonals differ each other in length for around 1.2 mm.

2.3   Mirror quality and backscattering reduction

Quality of the cavity mirror is of paramount importance to achieve the design sensitivity on angular motion. The main issue here is the occurrence of backscattering, an effect leading to mix clockwise and counter-clockwise radiation reflected by the cavity mirrors. Mirrors used in the RLG must show extremely specific features in terms of low transmission at the operation wavelength (a few tens of ppm), in order to increase the cavity finesse, and ultra-low scattering (targeted below 5 ppm), in order to reduce spurious diffusion of light responsible for backscattering. Such a combination of properties is quite uncommon in optics and, further to making challenging the search for suitable mirrors, imposes care in designing and realizing suitable quantitative testing procedures.

To this aim, the test setup already installed in the clean room of INFN Pisa, as required for avoiding fast surface contamination of the reflecting surfaces, has been used to assess the properties of batches of mirrors coming from different providers. The setup enables ringdown measurements on a test cavity, leading to an accuracy estimated on the order of a few ppm in both scattering and transmission data. Replacement of the cavity mirror of GINGERino, already planned for 2018, will be accomplished as soon as mirrors with the required optical properties will be available.

As far as issues related to mirrors are concerned, in 2017 collaborations have been initiated with scientific groups suffering from similar issues while being involved in different experiments. In particular the proposal for a joint PhD ("Doctorate in co-tutelle") has been filed with Université Paul Sabatier and LNCMI/CNRS, Toulouse, aimed at modeling effects played by the eventual birefringence (differential reflectivity for different polarization components) and at understanding the physical mechanisms leading to mirror imperfections at the local scale.

Backscattering can obviously stem from any unwanted reflection from in-cavity components. Since the discharge for laser operation takes place inside a pyrex capillary (4 mm diameter), contributions to backscattering can also come from diffusion of the laser light by the edge of the capillary. According to simulations, the problem can in principle be mitigated by placing

small-diameter irises in the optical path, in both clockwise and counter-clockwise radiation, in order to suppress spurious reflection and diffusion of light. During 2017, a setup for iris mounting featuring in-vacuum adjustment of position and size has been designed and the relevant vacuum-compatible components purchased. Installation will be obviously made on the GP-2 apparatus and the operation will be carefully assessed prior to validating the use of the designed system with GINGERino.

3 Long-term uninterrupted operation

During 2017, GINGERino has been in continuous, uninterrupted and unattended operation for a long period, amounting to more than 90 days. Moreover, the duty-cycle of the measurements was very large (above 95% of the total operation time) if compared with typical performance of other large-frame RLGs in the world (e.g., "G" at Wetzell and ROMY at LMU, Germany).

Figure 3 [2] shows the Sagnac frequency measured in the whole period.
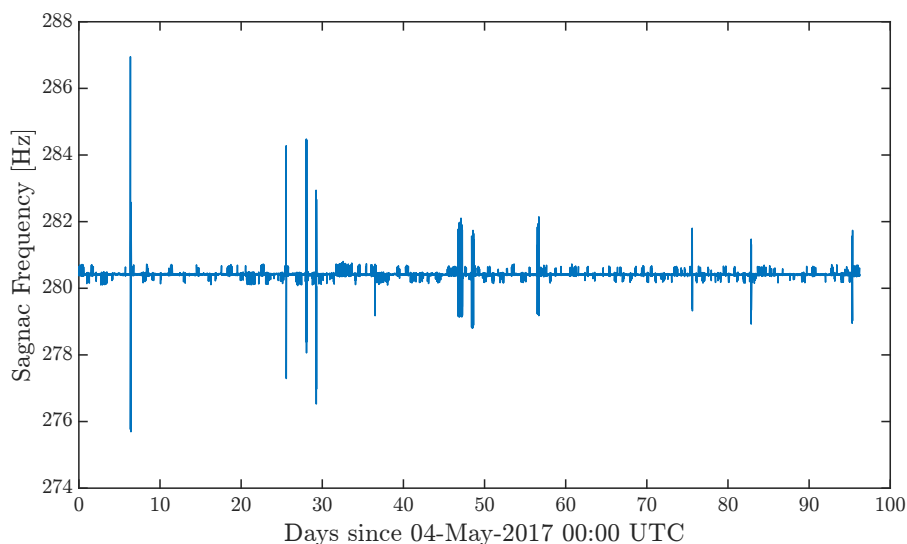
Figure 3: Sagnac frequency measured during the uninterrupted operation of GINGERino starting on May 2017 [2]. The frequency is centered around the $\simeq 280$ Hz value in agreement with the design of the RLG.

Having a data set extending over a long period is extremely relevant for various motivations. First of all, this is a demonstration of the long term stability of the apparatus, which cannot be otherwise ascertained. Moreover, such a long term stability is significant for assessing the operation of the RLG as a sensor for Earth rotational motion in the ultra-low frequency range. Presently, data relevant within this frame, for instance the evaluation of the "Length Of Day" (LOD), are determined via indirect observations, such as the Very Large Base Interferometer (VLBI) network, and made available to the scientific community at a very low rate after data processing. On the contrary, RLG data can be acquired continuously and the information evaluated right after a fast and simple data analysis procedure.

Neglecting relativistic corrections (de Sitter and Lense-Thirring precession terms), the Sagnac beating frequency f_S measured by a single RLG is proportional to the projection along the ring normal of the actual rotation velocity $\vec{\Omega}$ at the site of the instrument. Besides Earth angular

156

velocity $\vec{\Omega}_E$, $\vec{\Omega}$ contains contribution from anthropic and top soil motion, both negligible underground, and from $\vec{\delta\omega}$, which represents the local variations of the angular velocity measured at the instrument site. Such variations, which have a seismic nature, cannot be directly measured by conventional instruments for seismology. In fact, seismometer and strain-meters are not able to discriminate angular from linear motion.

Therefore, a RLG represents an extremely precious tool for seismology. Moreover, the underground location at LNGS and the occurrence of frequent seismic events in a radius of few hundreds km, make GINGERino a unique seismological observatory, potentially able to provide relevant insight onto geophysics and geodesic issues. As already demonstrated in the past, GINGERino is in fact sensitive on both tele-seismic and local seismic events: Fig. 4 shows two representative data sets.
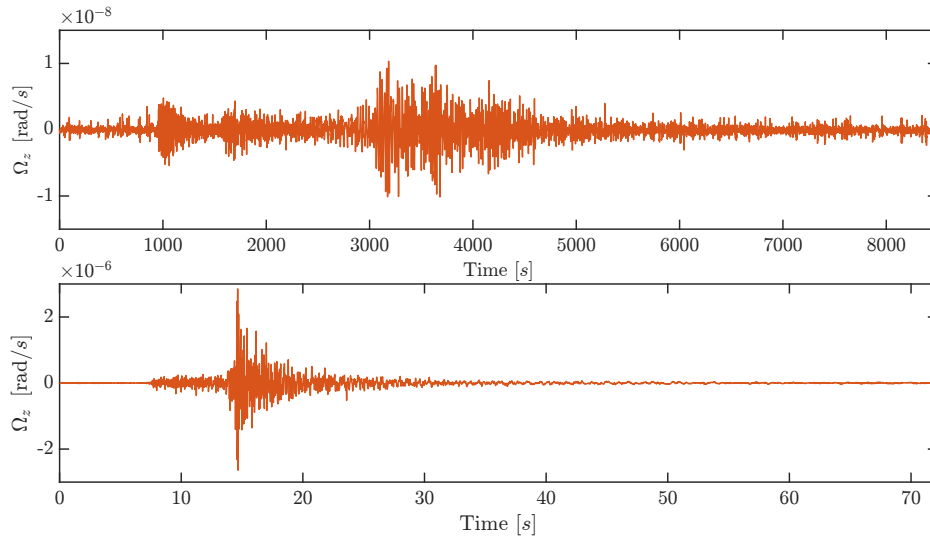
Figure 4: Variations of the angular velocity measured during a tele-seismic (M 7.6 earthquake in Kamchatka, Russia, July 18, 2017 - top panel) and a regional seismic event (Mw 4.0 earthquake in Rieti, Italy, October 16, 2016 - bottom panel).

The opportunity to use GINGERino as an advanced and extremely accurate tool for geoscience prompted the need for developing suitable data analysis procedures, in line with activities already started in the past. From one hand, due to the complex array of phenomena involved in seismic events, this required contributions from experts in seismology aiming at comparing our data with those acquired by other techniques. Within this frame, during 2017 collaboration with INGV, Italy, and LMU, Germany, has been further reinforced, the latter being based also on the activity of Andreino Simonelli, who earned a joint PhD diploma at LMU. Moreover, the collaboration has entered a proposal for a Marie Curie - International Training Network activity (coordinator C. Hadziioannou, Hamburg University) within EU-H2020 which, once funded, will grant a PhD position devoted to data analysis.

On the other hand, the long-term uninterrupted operation and the consequent availability of large and reliable data sets enabled analyzing the behavior of GINGERino at the very low frequency range, where geodetic phenomena (e.g., polar motion, solid tides) of very large relevance occur on different time scales. Results of the efforts carried out in 2017 are well summarized in Fig. 5 showing the Allan deviation calculated over raw and duly manipulated [2] data. The plot reports also the contribution of simulated geodesic effects and the line corresponding to the

quantum noise limit. It can be inferred that, while in the short time scale the actual signal-to-noise ratio is less than one order of magnitude larger than the quantum noise, on the long time scale the deviation is more pronounced, as expected because of the presence of various disturbances. Provisions exist to significantly improve the behavior in the next year, thanks to the implementation of the technical strategies discussed in Section 2 (or of a part of them) and to the development of more accurate data analysis procedures, using, e.g., intelligent frequency filtering.
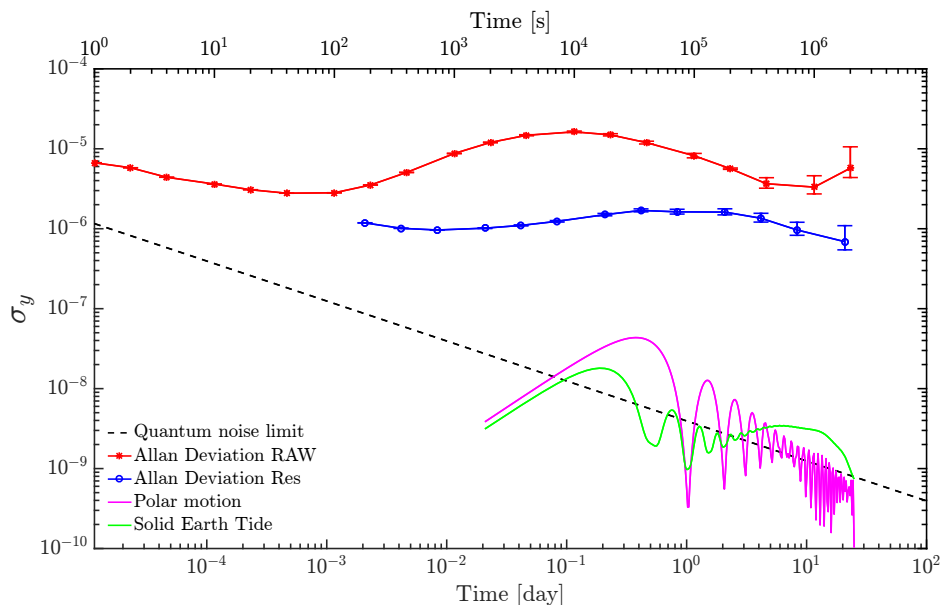
Figure 5: Allan deviation calculated over raw (blue) and manipulated (red) data [2]. Simulated effects of polar motion (magenta) and solid Earth tides (green) are also shown. The dashed line represents the quantum noise limit theoretically evaluated for GINGERino.

4   Progress towards GINGER and conclusions

Further to being relevant in the field of metrology and geoscience, all results acquired during 2017, joined with those gathered in in previous years, set the basis for a more defined picture of the foreseen array of RLG included in the GINGER project. The project is now part of a FISR proposal submitted by INGV and endorsed by INFN.

A somehow simplified design of the array, based on the proposal of [3], has been identified, as pictorially sketched in Fig. 6. A careful activity has been started in 2017 aimed at defining details of the mechanics. Major guidelines for this activity are: (i) search for improved robustness and ease of alignment; (ii) clear mounting procedure based on suitable fiducial markers; (iii) implementation of active geometry control, of backscattering suppression and improved mirrors, according to the results of the R&D activity.

Further details of the mechanical project will be defined in the next year, when identification of the possible location of the experiment in LNGS will also be finalized.
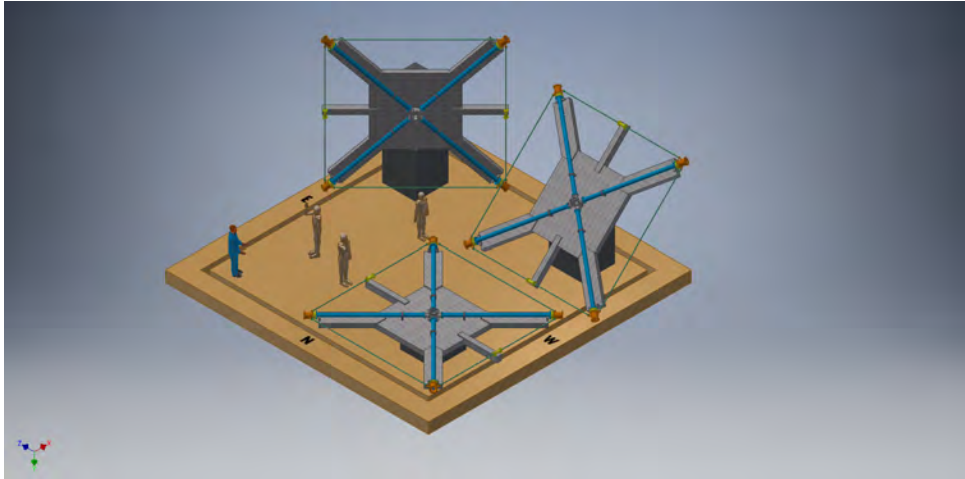
Figure 6: Pictorial sketch of the RLG array foreseen in the GINGER project.

References

[1] F. Stefani, et al., Long term stabilization of large frame laser gyroscopes, to be published on Proceedings of European Frequency and Time Forum, EFTF2018, IEEE Proceedings.

[2] J. Belfi, et al., Analysis of 90 days operation of the gyroscope GINGERINO, Optics Letters, submitted (2018).

[3] A. Di Virgilio, et al, GINGER: a feasibility study, Eur. Phys. J. Plus, 132, 157 (2017).

VIP

C.Curceanu (spokesperson) [a], S. Bartalucci[a], M. Bazzi[a],
M. Benfatto[a], S. Bertolucci[b], C. Berucci[a,c],
A.M. Bragadireanu[a,d], M. Cargnelli[a,c], A. Clozza[a],
J-P Egger[e], C. Guaraldo[a], M. Iliescu[a], M. Laubenstein[f],
J. Marton[a,c], S.Di Matteo[g], E. Milotti[h],
G. Modestino[a], L. De Paolis[a], A. Pichler[a,c],
D. Pietreanu[a,d], K. Piscicchia[a,i], A. Scordo[a],
H. Shi[a], D. Sirghi[a,d], F. Sirghi[a,d],

L. Sperandio[a], O. Vazquez Doce[j], E. Widmann[c], J. Zmeskal[a,c]

[a] INFN, Laboratori Nazionali di Frascati, CP 13, Via E. Fermi 40,
I-00044, Frascati (Roma), Italy
[b] University and INFN Bologna, Via Irnerio 46, I-40126, Bologna, Italy
[c] The Stefan Meyer Institute for Subatomic Physics, Boltzmanngasse 3, A-1090 Vienna, Austria
[d] "Horia Hulubei"National Institute of Physics and Nuclear Engineering,
Str. Atomistilor no. 407,P.O. Box MG-6, Bucharest - Magurele, Romania
[e] Institut de Physique, Université de Neuchâtel, 1 rue A.-L. Breguet,
CH-2000 Neuchâtel, Switzerland
[f] INFN, Laboratori Nazionali del Gran Sasso, S.S. 17/bis, I-67010 Assergi (AQ), Italy
[g] Institut de Physique UMR CNRS-UR1 6251, Université de Rennes1, F-35042 Rennes, France
[h] Dipartimento di Fisica, Università di Trieste and INFN,
Sezione di Trieste, Via Valerio, 2, I-34127 Trieste, Italy
[i] Museo Storico della Fisica e Centro Studi e Ricerche "Enrico Fermi", Roma, Italy
[j] Excellence Cluster Universe, Technische Universität München, Garching, Germany

Abstract

By performing X-rays measurements in the "cosmic silence" of the underground laboratory of Gran Sasso, LNGS-INFN, we test a basic principle of quantum mechanics: the Pauli Exclusion Principle (PEP), for electrons by searching for atomic transitions in copper prohibited by PEP with respect to the previous VIP experiment. VIP2 uses Silicon Drift Detectors (SDDs) to measure the X rays emmited in the copper target and a veto system (scintillators read by SiPM) to reduce background.

1 The VIP scientific case and the experimental method

Within VIP an experimental test on the Pauli Exclusion Principle is being performed, together with feasibility tests on other fundamental physics principles (collapse model).

The Pauli Exclusion Principle (PEP), a consequence of the spin-statistics connection, plays a fundamental role in our understanding of many physical and chemical phenomena, from the periodic table of elements, to the electric conductivity in metals and to the degeneracy pressure which makes white dwarfs and neutron stars stable. Although the principle has been spectacularly confirmed by the huge number and accuracy of its predictions, its foundation lies deep in the structure of quantum field theory and has defied all attempts to produce a simple proof. Given its basic standing in quantum theory, it is appropriate to carry out high precision tests of the PEP validity and, indeed, mainly in the last 20 years, several experiments have been performed to search for possible small violations. Many of these experiments are using methods which are not obeying the so-called Messiah-Greenberg superselection rule. Moreover, the indistinguishability and the symmetrization (or antisymmetrization) of the wave-function should be checked independently for each type of particles, and accurate tests were and are being done.

The VIP (VIolation of the Pauli Exclusion Principle) experiment, an international Collaboration among 10 Institutions of 6 countries, has the goal to either dramatically improve the previous limit on the probability of the violation of the PEP for electrons, ($P < 1.7$ x 10^{-26} established by Ramberg and Snow: *Experimental limit on a small violation of the Pauli principle*, Phys. Lett. **B 238** (1990) 438) or to find signals from PEP violation.

The experimental method consists in the introduction of electrons into a copper strip, by circulating a current, and in the search for X-rays resulting from the forbidden radiative transition that occurs if some of the new electrons are captured by copper atoms and cascade down to the 1s state already filled by two electrons with opposite spins (Fig. 1.)
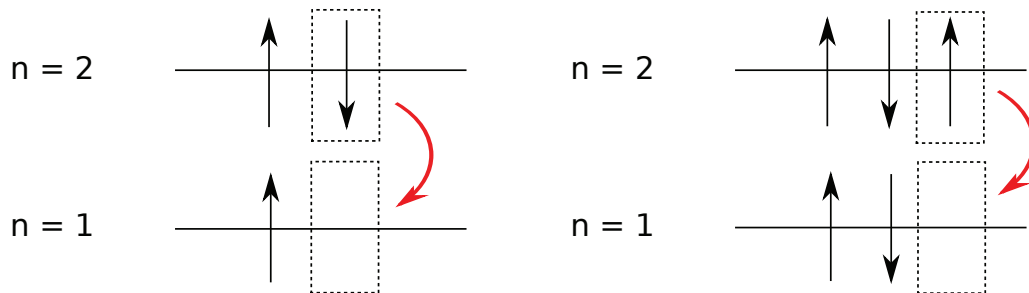

Figure 1: *Normal 2p to 1s transition with an energy around 8 keV for Copper (left) and Pauli-violating 2p to 1s transition with a transition energy around 7,7 keV in Copper (right).*

The energy of PEP violating $2p \rightarrow 1s$ transition differs from the normal K_α transition one by about 300 eV (7.729 keV instead of 8.040 keV) providing an unambiguous signal of the PEP violation. The measurement alternates periods without current in the copper strip, in order to evaluate the X-ray background in conditions where no PEP violating transitions are expected to occur, with periods in which current flows in the conductor, thus providing "new" electrons, which might violate PEP. The rather straightforward analysis consists in the evaluation of the statistical significance of the normalized subtraction of the two spectra in the region of interest (if no signal is seen). A more complex statistical analysis (Bayesian) is also being implemented.

The experiment is being performed at the LNGS underground Laboratories, where the X-ray background, generated by cosmic rays, is strongly reduced.

The VIP group is considering also the extension of its scientific program to the study of other items of the fundamental physics, such as collpase models. Encouraging preliminary results were obtained.

2   The VIP and VIP2 apparata

The first VIP setup was realized in 2005, starting from the DEAR setup, reutilizing the CCD (Charge Coupled Devices) as X-ray detectors, and consisted of a copper cylinder, were current was circulated, 4.5 cm in radius, 50 μm thick, 8.8 cm high, surrounded by 16 equally spaced CCDs of type 55.

The CCDs were placed at a distance of 2.3 cm from the copper cylinder, grouped in units of two chips vertically positioned. The setup was enclosed in a vacuum chamber, and the CCDs cooled to 165 K by the use of a cryogenic system. The VIP setup was surrounded by layers of copper and lead to shield it against the residual background present inside the LNGS laboratory, see Fig. 2.

Figure 2: The VIP setup at the LNGS laboratory during installation.

The DAQ alternated periods in which a 40 A current was circulated inside the copper target with periods without current, representing the background.

VIP was installed at the LNGS Laboratory in Spring 2006 and was taking data until Summer 2010. The probability for PEP Violation was found to be: $\beta^2/2 < 4.6 \times 10^{-29}$.

In 2011 we started to prepare a new version of the setup, VIP2, which was finalized and installed at the LNGS-INFN in November 2015 and with which we will gain a factor about 100 in the probability of PEP violation in the coming years (see Table 1).

3   Activities in 2017

3.1   VIP2 - a new high sensitivity experiment

In order to achieve a signal/background increase which will allow a gain of two orders of magnitude for the probability of PEP violation for electrons, we built a new setup with a new target, a new cryogenic system and we use new detectors with timing capability and an active veto system. As X-ray detectors we use spectroscopic Silicon Drift Detectors (SDDs) which have an even better energy resolution than CCDs and provide timing capability which allow to use anti-coincidence provided by an active shielding.
The VIP2 system is providing:

Table 1: List of expected gain factors of VIP2 in comparison to VIP (given in brackets).

Changes in VIP2	value VIP2(VIP)	expected gain
acceptance	12%	12
increase current	100A (50A)	2
reduced length	3 cm (8.8 cm)	1/3
total linear factor		8
energy resolution	170 eV(340 eV)	4
reduced active area	6 cm^2(114 cm^2)	20
better shielding and veto		5-10
higher SDD efficiency		1/2
background reduction		200-400
overall gain		**∼120**

1. signal increase with a more compact system with higher acceptance and higher current flow in the new copper strip target;

2. background reduction by decreasing the X-ray detector surface, more compact shielding (active veto system and passive), nitrogen filled box for radon radiation reduction.

In the Table 1 the numerical values for the improvements in VIP2 are given which will lead to an expected overall improvement of a factor about 100.

3.2   Status of VIP2 in 2017

In the VIP2 apparatus six SDDs units, with a total active area of 6 cm^2 each are mounted close to the Cu target. Moreover, an active shielding system (veto) was implemented, to reduce the background in the energy region of the forbidden transition. These systems will play an important role to improve the limit for the violation of the PEP by two orders of magnitude with the new data which are presently coming by running the VIP2 experiment at LNGS.

In November 2015, the VIP2 setup was installed at Gran Sasso. In the years 2016 and 2017, data with the VIP2 detector system at the LNGS without shielding were taken. In Figure 3 the VIP2 setup as installed at LNGS is shown.

Data with 100 Ampere DC current applied to the copper strip was collected together with the data collected without current.

Preliminary data analyses "a la VIP": two types of preliminary data referring to the first period of data taking (data from 2016) were performed: one "a la VIP", i.e. using exactly the same procedure as the one used in VIP (subtracted spectra: with and without current). The result which was obtained was published in the review: Entropy, 2017, 19, p. 300. The obtained calibrated energy spectra for all 6 SDDs are shown in Fig. 4 and their analysis allowed to extract a limit on the probability for PEP violation as:

$$\frac{\beta^2}{2} \leq \frac{3 \times 66}{4.7 \times 10^{30}} = 4.2 \times 10^{-29}. \tag{1}$$

which is slightly better (10% than the one for VIP). To be underlined that the limit was obtained after two months of data taking, while the VIP one corresponds to 4 years of data taking.
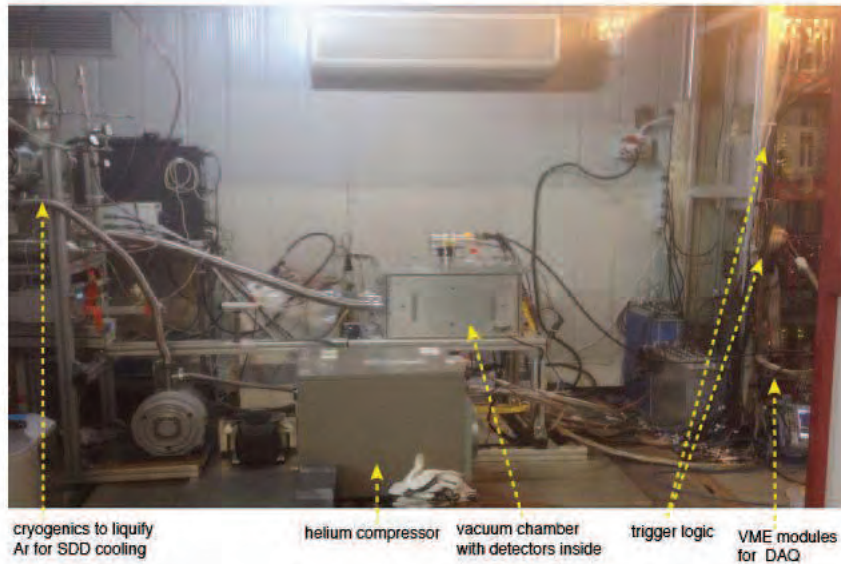
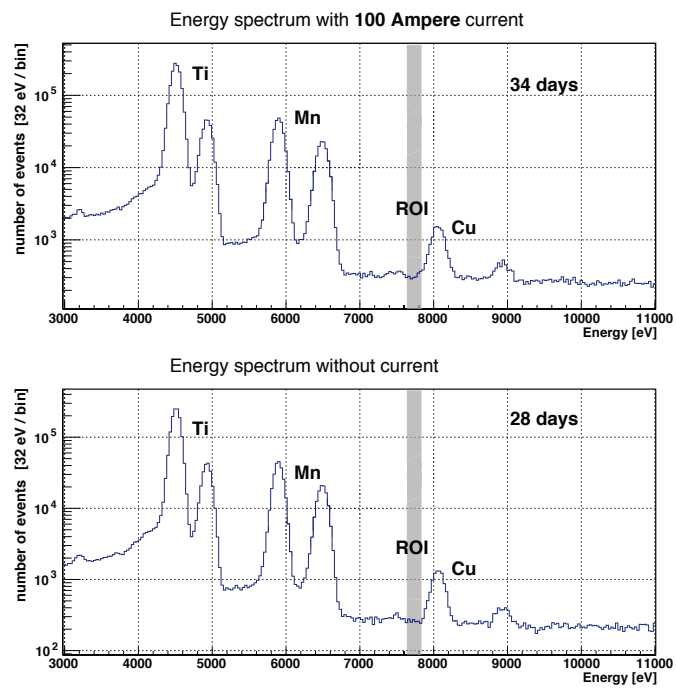Figure 3: *A picture of the VIP-2 setup installed at LNGS .*

Figure 4: *The energy spectra from all the SDDs, for data with and without applied DC current to the copper strip, taken during the physics run in late 2016 at the LNGS.*

Preliminary data analyses with a new method: the same set of data analysed by using a different method, i.e. a simultaneous fit of the "signal" and background spectra, in order to use all the information available for the background shape from the data. The obtained spectra are shown in Fig 5, together with the simultaneous fitting functions, from where a limit of the probability of PEP violation was extracted to be:

$$\frac{\beta^2}{2} \leq \frac{3 \times 67}{8.1 \times 10^{30}} = 3.2 \times 10^{-29}. \tag{2}$$
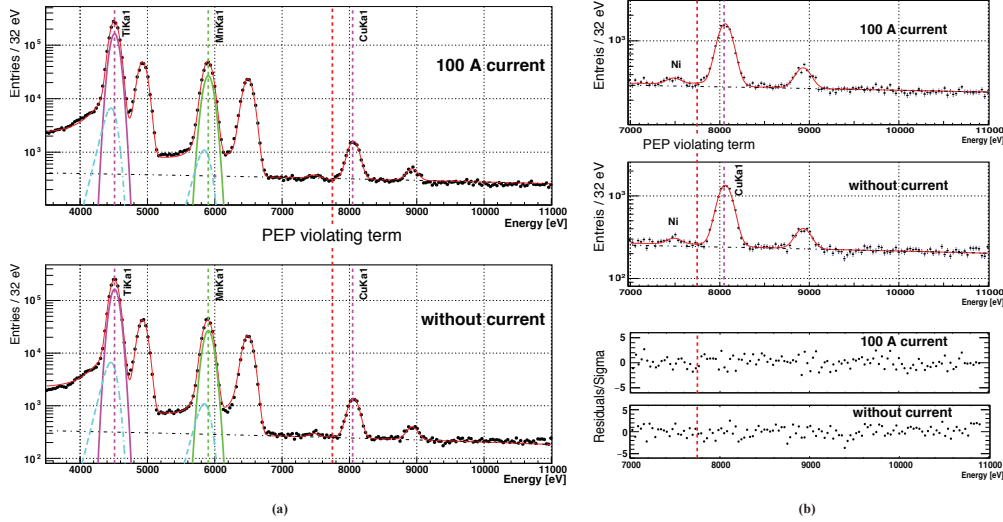
Figure 5: *A global chi-square function was used to fit simultaneously the spectra with and without 100 A current applied to the copper conductor. The energy position for the expected PEP violating events is about 300 eV below the normal copper $K_{\alpha 1}$ transition. The Gaussian function and the tail part of the $K_{\alpha 1}$ components and the continuous background from the fit result are also plotted. (a) : the fit to the wide energy range from 3:5 keV to 11 keV; (b) : the fit and its residual for the 7 keV to 11 keV range where there is no background coming from the calibration source.*

A paper describing the new analysis and the obtained results was recently (April 2018) accepted for publication in EPJ C.

3.3 Workshops organization

In 2017 the following events related to the physics of VIP, and, more generally, to quantum mechanics, were organized:

1. Workshop Quantum Foundation, "The physics of "what happens" and the measurement problem", 24-26 May, 2017, Frascati, Italy.

2. Workshop Quantum Foundation, "New frontiers in testing quantum mechanics from underground to the space", 29 November-1 December, 2017, Frascati, Italy.

4 Activities in 2018

In 2018 we will be in data taking with VIP2 at LNGS-INFN. The 2016 and 2017 data analysis will be finalized and published. We are, as well, going to continue the studies on fundamental physics, in particular on the collapse model by measurements of X rays spontaneously emitted in the continuous spontaneous localization (CSL) model.

5 List of Publications

1. Catalina Curceanu *et al*, Quantum mechanics under X-rays in the Gran Sasso underground laboratory, Int. J. Quant .Inf. **15** (2017) no.08, 1740004.

2. J. Marton *et al*, VIP2 at Gran Sasso - Test of the validity of the spin statistics theorem for electrons with X-ray spectroscopy, arXiv:1711.01309.

3. Catalina Curceanu *et al*, Test of the Pauli Exclusion Principle in the VIP-2 underground experiment, Entropy **19** (2017) no.7, 300.

4. J. Marton *et al*, Underground test of quantum mechanics - the VIP2 experiment, arXiv:1703.10055 [quant-ph].

5. Catalina Curceanu *et al* , Underground tests of quantum mechanics. Whispers in the cosmic silence?, J. Phys. Conf. Ser. **880** (2017) no.1, 012045.

6. J. Marton *et al*, VIP-2 at LNGS: An experiment on the validity of the Pauli Exclusion Principle for electrons, J. Phys. Conf. Ser. **873** (2017) no.1, 012018.

7. K. Piscicchia, *et al*, CSL Collapse Model Mapped with the Spontaneous Radiation, Entropy 2017, 19(7), 319.